

学位論文

Studies on New Charge Selective and Conductive Interfaces in
Organic-Inorganic Thin-film Photovoltaics

(有機無機薄膜太陽電池における新規電荷選択及び輸送界面の研究)

平成 27 年 12 月博士(理学)申請

東京大学大学院理学系研究科

化学専攻

田日 (JEON, I1)

Acknowledgement

First and foremost, I would like to express my special appreciation to my supervisors, professor Tetsuya Hasegawa and professor Yutaka Matsuo.

To Professor Hasegawa, I sincerely thank you for accepting me to your group and for the financial support throughout the course. I could not have achieved this without your munificent help. I will not forget the generosity you have shown me.

To Professor Matsuo, I earnestly thank you for being a tremendous mentor both academically and psychologically. Looking back, when I first contacted you in 2012, I could never imagine my Ph.D. would turn out this productive and satisfactory. Your sagacious advice and guidance throughout the course have been the key compositions in my Ph.D. pursuit. The passion you have for the research was contagious and motivational for me, even during the tough times of our laboratory. I appreciate for the excellent example you have showcased as a successful scientist and a principal investigator.

The members of Matsuo group have contributed immensely to my professional and personal life in Tokyo too. They have been a source of friendships as well as fruitful advice. I am especially grateful for the Japanese I learnt from them and now I can blend in with any Japanese. These members who stuck it out together in Miraikan with me are Nakagawa Takafumi, Okada Hiroshi, Tsuyoshi Suzuki, Hiroki Kawakami, Sato, and Keisuke.

I would like to also acknowledge honorary group members of Hasegawa laboratory: Kojima Shungo, who has helped be with every bits of Tokyo life, including 2-years-consecutive tuition exemptions for which I owe him a great number of ramen bowls. I also would like to thank other members for helping me out: Tsukasa Katayama, Thantip S. Krasienapibal, Soichiro Nakao, Prof. Yasushi Hirose, and Daisuke Ogawa.

I also would like to thank Clement L. Delacou, Dr. Kehang Cui, Takaaki Chiba, Ju Zheng, Prof. Sasa Zeljkovic, Dr. James W. Ryan, and all other unmentioned past and present group members that I have had the pleasure working with.

My time in Tokyo was enjoyable with the friends I made in Japan, who are now part of my life. Although, I could not spend much time together, because of ostensibly busy schedule of mine, I regard them very special: Christian Business Committee members including Kaicho, Kanehara-san, Ikeda-san, Oosugi-san, Kojima-san, Kunho Kim; Maki-san and Abe-san, who are my Japanese tutors and friends; Elite Academy and ISA for being the bread and butter; David Oppenheimer, an alumnus of Oxford university residing in Japan; Matt Shannon; Dustin Bullock; all of the students I gave private lessons to: Tadashi in Dartmouth, Nana in Princeton, Hey-Soo in UCLA, Hei-Jong, Yuri, Rino, and Mikio.

Above all, I would like to thank my family for all their love and support. Super-duper ineffable thanks to my mum, and dad. Your prayers and encouragement sustained me thus far. And my true love, SY, your faithful support and prayer during the late stages of the Ph.D. were tremendously reassuring. Lastly, I thank my expected son in advance for coming out duly to this world, not to disturb his dad's Ph.D programme.

Finally I thank God. I have experienced your guidance everyday during the course. Thank you, Lord.

Scientific Contributions

Publications

- (13) ‘Stability of Diketopyrrolopyrrole Small-molecule Inverted Organic Solar Cells’
Il Jeon, Ryohei Sakai, Takafumi Nakagawa, Hiroki Setoguchi, Yutaka Matsuo*
Organic Electronics, May **2016** in print
- (12) ‘Multifunctionalization of C₇₀ at the two polar regions with a high regioselectivity via oxazolinization and benzylation reactions’
Shu-Hui Li, Zong-Jun Li, Takafumi Nakagawa, Il Jeon, Zheng Ju, Yutaka Matsuo* and Xiang Gao*
Chemistry of Letters May **2016** in print
- (11) ‘Enhancement of Low-field Magnetoresistance in Self-Assembled Epitaxial La_{0.67}Ca_{0.33}MnO₃:NiO and La_{0.67}Ca_{0.33}MnO₃:Co₃O₄ Composite Films via Polymer-Assisted Deposition’
Meng Zhou^{1st}, Yuling Li^{1st}, Il Jeon^{1st}, Xuebin Zhu, Xianwu Tang, Haiyan Wang, Ling Fei, Yuping Sun, Shuguang Deng, Guifu Zou, Hongmei Luo, Yutaka Matsuo
Scientific Report **2016** in print
- (10) ‘Enhancement of Open-circuit Voltage and Efficiency using the 58- π Silylmethyl Fullerenes in Small Molecule Organic Solar Cells’
Il Jeon^{1st}, Clement Delacou^{1st}, Takafumi Nakagawa, Yutaka Matsuo*
Chemistry- An Asian Journal 1861-471X February **2016** (invited)
- (9) ‘Enhancement of Fill Factor in Air-processed Inverted Organic Solar Cells using Self-Assembled Monolayer of Fullerene Catechol’
Il Jeon, Yutaka Matsuo*
Japanese Journal of Applied Physics **2016** submitted
- (8) ‘Metal-free and Window-like Transparent Organic Solar Cells with P-dopant Enhanced Carbon Nanotube Electrodes and Novel Transfer Methodologies’
Il Jeon, Clement Delacou, Antti Kaskela, Esko I. Kauppinen, Shigeo Maruyama, Yutaka Matsuo*
Scientific Reports **2016**
- (7) ‘Indium-free Inverted Organic Solar Cell Fabrication using Niobium Doped Titanium Oxide possessing an Integrated Dual-function of Electrode and

- Electron-transporter’
Il Jeon, Shoichiro Nakao, Yasushi Hirose, Tetsuya Hasegawa, Yutaka Matsuo*
Advanced Electronic Materials 1500341 January **2016**
- (6) ‘Single-walled Carbon Nanotube Film as Electrode in Indium-free Planar Heterojunction Perovskite Solar Cells: Investigation of Electron-blocking Layers and Dopants’
Il Jeon, Takaaki Chiba, Clement Delacou, Yunlong Guo, Antti Kaskela, Olivier Reynaud, Esko I. Kauppinen, Shigeo Maruyama, Yutaka Matsuo*
Nano Letters 15, 6665–6671 August **2015**
- (5) ‘Direct and Dry-Deposited Single-Walled Carbon Nanotube Films Doped with MoO_x as Electron-Blocking Transparent Electrodes for Flexible Organic Solar Cells’
Il Jeon, Kehang Cui, Anton Anisimov, Albert Nasibulin, Esko I. Kauppinen, Shigeo Maruyama*, Yutaka Matsuo*
Journal of the American Chemical Society 137 (25), 7982-7985 June **2015**
- (4) ‘Vertical Phase Separation and Light-soaking Effect Improvements by Photoactive Layer Spin Coating Initiation Time Control in Air-processed Inverted Organic Solar Cells’
Il Jeon, Yutaka Matsuo*
Solar Energy Materials and Solar Cells 140, 335-343 September **2015**
- (3) ‘Multilayered MoS₂ Nanoflakes Bound to Carbon Nanotubes as Electron Acceptors in Bulk Heterojunction Inverted Organic Solar Cells’
Il Jeon, Dai Kutsuzawa, Yu Hashimoto, Takashi Yanase, Taro Nagahama, Toshihiro Shimada, Yutaka Matsuo*
Organic Electronics 17, 275–280 February **2015**
- (2) ‘Air-Processed Inverted Organic Solar Cells Utilizing a 2-Aminoethanol-Stabilized ZnO Nanoparticle Electron Transport Layer That Requires No Thermal Annealing’
Il Jeon, James W. Ryan, Tafu Nakazaki, Kee Sheng Yeo, Yuichi Negishi, Yutaka Matsuo*
Journal of Material Chemistry A 2,18754-18760 September **2014**
- (1) ‘Mixture of [60] and [70] PCBM giving morphological stability in organic solar cells’
Yoshihide Santo, Il Jeon, Kee Sheng Yeo, Takafumi Nakagawa, Yutaka Matsuo*
Applied Physics Letters 103 (7), 073306-4 August **2013**

Conferences – Oral Presentations

- (8) ‘Single-walled Carbon Nanotube Film as anode in Flexible Indium-free Planar Heterojunction Perovskite Solar Cells’
OIl Jeon, Takaaki Chiba, Clement Delacou, Esko Kauppinen, Shigeo Maruyama, Yutaka Matsuo
International Conference on Solid State Devices and Materials 2015 (2015. 09. 28) C-1-5, 15 minutes, Sapporo
- (7) ‘Indium-Free Flexible Planar Heterojunction Perovskite Solar Cells using Single-walled Carbon Nanotube film as Electrode, and Investigation of Hole-transporting Layers and Dopants thereof’
OIl Jeon, Takaaki Chiba, Clement Delacou, Esko Kauppinen, Shigeo Maruyama, Yutaka Matsuo
The 48th Fullerenes-Nanotubes-Graphene General Symposium (2015. 09. 09) 3-6, 15 minutes, Kita-Kyushu
- (6) ‘Single-Walled Carbon Nanotubes and Graphene as Hole Transport Layer and Electrode for Solar Cells’
OShigeo Maruyama, Kehang Cui, Takaaki Chiba, Il Jeon, Xiao Chen, Rong Xiang, Shohei Chiashi, Esko I. Kauppinen, Yutaka Matsuo
WONTON (2015) 20 minutes, Invited Talk, Banz
- (5) ‘Single-Walled Carbon Nanotubes and Graphene As Highly Efficient Hole Collecting and Transport Layer for Solar Cells’
OShigeo Maruyama, Kehang Cui, Takaaki Chiba, Il Jeon, Xiao Chen, Rong Xiang, Shohei Chiashi, Yutaka Matsuo
227th ECS Meeting (2015. 05. 27) 20 minutes, Chicago
- (4) ‘Highly Efficient and Flexible Organic Solar Cells Using Single-Walled Carbon Nanotube Films Doped with Strong and Safe MoO_x Dopant’
OIl Jeon, Kehang Cui, Albert Nasibulin, Esko I. Kauppinen, Shigeo Maruyama, Yutaka Matsuo
Japanese Society of Applied Physics (2015. 03. 12) 12p-D6-10 15 minutes, Tokyo
- (3) ‘Direct- and Dry-Deposited Single-Walled Carbon Nanotube Films Doped with MoO_x as Electron-Blocking Transparent Electrodes for Efficient Flexible Organic Solar Cells’
OIl Jeon, Kehang Cui, Anton Anisimov, Albert Nasibulin, Esko I. Kauppinen, Shigeo Maruyama, Yutaka Matsuo
The 47th Fullerenes-Nanotubes-Graphene General Symposium (2015. 02. 23) 15 minutes, Tokyo
- (2) ‘A Novel Ligand-free ZnO Particle for Solution-processed Inverted Organic

Solar Cell'

Oll Jeon, James W. Ryan, Kee Sheng Yeo, Tafu Nakazaki, Yuichi Negishi, Yutaka Matsuo

Material Research Societies – Japan (2013.12.09) 2-1-A 15 minutes, Yokohama

- (1) 'The Evaluation of Stability and Structure of Organic Solar Cell Using Mixed PCBM'
Oll Jeon, Yoshihide Santo, Kee Sheng Yeo, Takafumi Nakagawa, Yutaka Matsuo
Japanese Society of Applied Physics (2013. 07. 01) 17a-A12-7 15 minutes, Kyoto

Conferences – Poster Presentations

- (10) 'フレキシブル有機太陽電池作成のための新規単層カーボンナノチューブ膜の開発'
Oll Jeon, Cui Kehang, Kaupinnen Esko, Shigeo Maruyama, Yutaka Matsuo
Chemical Society of Japan 2015 (2015. 10. 13) P1-126, Tohoku
- (9) 'Metal-free Transparent Organic Solar Cell using Dopant Enhanced Carbon Nanotube Electrode and its Transfer Methodologies'
Oll Jeon, Clement Delacou, Esko Kauppinen, Shigeo Maruyama, Yutaka Matsuo
The 48th Fullerenes-Nanotubes-Graphene General Symposium (2015. 09. 07) P1-8, Kita-kyushu
- (8) 'Single-walled Carbon Nanotube Film as Electrode in Indium-Free Planar Heterojunction Perovskite Solar Cells: Investigation of Hole-transporting Layers, Dopants, and Flexible Application'
Oll Jeon, Takaaki Chiba, Clement Delacou, Esko I. Kauppinen, Shigeo Maruyama, Yutaka Matsuo
Nano Tube 15 (2015. 07. 01) P385, Nagoya
- (7) 'Vertical Phase Separation and Light-Soaking Improvements by Active Layer Spin Coating Initiation Time Control in Air-Processed Inverted Organic Solar Cells'
Oll Jeon, Yutaka Matsuo
Japanese Society of Applied Physics (2015. 03. 12) P13-2, Tokyo
- (6) 'Record-High Efficient SWCNT OSCs: Doping and Electron Blocking Dual-Function of MoO_x'
Oll Jeon, Kehang Cui, Albert Nasibulin, Esko I. Kauppinen, Shigeo

- Maruyama, Yutaka Matsuo
The 47th Fullerenes-Nanotubes-Graphene General Symposium (2014. 09. 05)
P3-1, Nagoya
- (5) ‘Towards Flexible Inverted Solar Cells: Annealing-free ZnO film formation as an Electron Selective Layer’
Oll Jeon, James W. Ryan, Kee Sheng Yeo, Tafu Nakazaki, Yuichi Negishi, Yutaka Matsuo
NIMS (National Institute for Materials Science) Conference 2014 – (2014.07.02) P143, Tsukuba
- (4) ‘Chemical Vapor Deposition of MoS₂ on Carbon Nanotube for Organic Thin Film Solar Cells’
Oll Jeon, Dai Kutsuzawa, Yu Hashimoto, Takashi Yanase, Taro Nagahama, Toshihiro Shimada, Yutaka Matsuo
The 46th Fullerenes-Nanotubes-Graphene General Symposium (2014. 03. 05)
P3-23, Tokyo
- (3) ‘A Novel Ligand-free ZnO Particle for Fullerene:Polymer Inverted Organic Solar Cell’
Oll Jeon, James W. Ryan, Kee Sheng Yeo, Tafu Nakazaki, Yuichi Negishi, Yutaka Matsuo
The 46th Fullerenes-Nanotubes-Graphene General Symposium (2014. 03. 04)
P2-3, Tokyo
- (2) ‘[60]PCBM と [70]PCBM の混合物の利用による有機薄膜太陽電池特性の向上’
Oll Jeon, Yoshihide Santo, Kee Sheng Yeo, Takafumi Nakagawa, Yutaka Matsuo
Chemical Society of Japan 2013 P7-95, Tohoku
- (1) ‘Stability Enhancement of Inverted OPV by using Mixed PCBM via control of Nano-surface Morphology’
Oll Jeon, Yoshihide Santo, Kee Sheng Yeo, Takafumi Nakagawa, Yutaka Matsuo
The 24th Symposium of Physical Organic Chemistry 2013 P2-24, Tokyo

Patents

- (2) ‘Niobium doped titanium oxide organic thin-film solar cells (ニオブドーパ酸化チタンを用いた有機薄膜太陽電池)’
Yutaka Matsuo, Tetsuya Hasegawa, Il Jeon et al., JP 2015-034346

- (1) ‘Carbon Nanotube Organic Solar Cells (カーボンナノチューブ有機太陽電池)’
Yutaka Matsuo, Shigeo Maruyama, Il Jeon et al., JP 2014-178204

Studies on New Charge Selective and Conductive Interfaces in Organic-Inorganic Thin-film Photovoltaics

IL JEON

Department of Chemistry
Graduate School of Science
The University of Tokyo

ABSTRACT

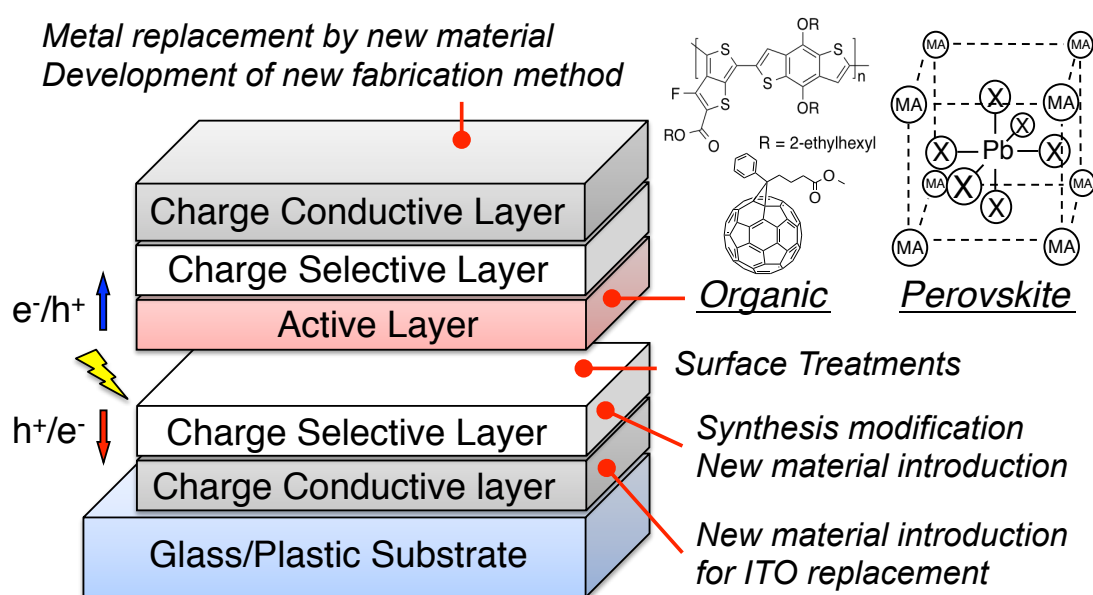
Global warming and nuclear disasters in recent times have urged the society to look towards alternative energy sources, which are pollution-free, infinite, and viable in mass-production. As a result, there has been a remarkable upshift in development of the solar cell research among scientists. Experts forecast that, with technology assuring large-scale, solar cells can contribute nearly a third of electricity consumption worldwide between now and 2030.

Although already-industrialised silicon solar cells possess notably high power conversion efficiencies, they have a combination of disadvantages including heavy weight and high cost which made difficult for them to supersede the conventional energy sources. Opportunities exist for photovoltaics that promise substantial reduction in manufacturing costs and superior functionalities such as flexibility while retaining descent efficiencies. There are two novel technologies that satiate tantalising prospects on these fronts: organic solar cells and lately emerging mixed organic–inorganic halide perovskite solar cells.

Solar cell devices are mainly composed of active layer, charge selective layer, and charge conductive layer. The active layer absorbs light and generates excitons; the choice of materials for this layer determines the type of solar cells. The charge selective layers are placed above and below the active layer to filter out any unwanted charges followed by the conductive layers, which then extract those filtered charges. The charge selective and conductive layers are the two common essential layers in all

types of solar cells. Focusing on these two layers and their interfaces is crucial in solar cell technologies and gaining ground in the energy competition via scientific breakthroughs.

In this thesis, new materials for charge selective/conductive layers in photovoltaic devices were introduced and their interfaces were studied by various approaches (Insetted Figure). They include numerous novel materials, modification of already existing layers, changing fabrication methods, surface treatments and so forth. The investigation in this dissertation starts from the charge conductive layer (electrode) way up to the interface between the charge selective layer and the active layer. Both organic and perovskite solar cells have been utilised here, because neither of them drops as less promising. Since two systems have been used, it was possible to explore common traits shared by both systems, as well as different behaviours unique to each system.



Inset Figure. Illustration of focuses of the research in this thesis

Quick glances at some of the researches done in this work are the following:

- Inflexible and expensive conventional indium tin oxide electrode was replaced by earth-abundant and mechanically resilient carbon nanotubes. Diverse methodologies were employed to improve the properties of carbon nanotubes and led to power conversion efficiencies of around 80% to those of the indium tin oxide counterparts in both organic and perovskite solar cells. Moreover, their flexible

applications were successfully demonstrated. In addition to the bottom indium tin oxide electrode, top metal electrode was also replaced to produce window-like transparent solar cells.

- Conductive niobium (2%)-doped titanium oxide film was found to turn its surface layer into a semiconducting and hole-blocking layer upon UV-ozone treatment. This means that the film can now function as both a charge conductor and a selective layer, making the solar cell fabrication simpler and cheaper.
- ZnO quantum dots were synthesised and stabilised by 2-aminoethanol. They were then spin-coated and used in solar cell fabrication directly without usually required thermal annealing. Yet, they performed as good as the conventional ZnO film. Furthermore, sputtering ZnO technique was studied, and found that the sputtered ZnO film gives better performance than the conventional film.
- Surface of the hole-blocking layers in inverted organic solar cells was modified by catechol derivatives or anthracene derivatives. Charged ends of the chemical compounds were adsorbed firmly to the surface of the charge selective layers, inducing a thin layer of fullerenes to enhance the charge extraction. The same effect was observed without use of the surface modifiers when a technique called ‘Waiting effect’ was applied. Literally waiting before spin-coating an active layer solution as drop-cast on the substrate promoted a vertical separation of donor and acceptor species in the active layer.
- MoS₂ nano-flakes were deposited on carbon nanotubes by chemical vapour deposition technique. MoS₂ does not interact directly with P3HT, whereas carbon nanotubes can form π - π bonds with P3HT. Therefore, MoS₂ stuck to carbon nanotubes could form a bulk heterojunction for the first time and function as electron acceptors in solar cell devices.

Different materials and interfaces in the charge selective/conductive layers have been studied in depth. Their applications were successful in terms of enhancement in power conversion efficiency and endowing novel functionalities. Researches here are exceptionally useful in a way that they are applicable not only in photovoltaics, but in other electronic devices as well.

Keywords: *Interface, Solar cell, Electrode, Cathode, Anode, Charge conductive layer, Electron blocking layer, Hole blocking layer, Charge selective layer, Carbon nanotube, Graphene, TiO_x, ZnO, MoS₂, MoO₃, Chemical vapour deposition, Spin coating, Light soaking effect,*

TABLE OF CONTENTS

Chapter 1 – INTRODUCTION TO THESIS

1.0 Background.....	23
1.0.1 Inspiration.....	23
1.0.1.1 Energy crisis.....	23
1.0.1.2 Solar cells.....	23
1.0.2 Agenda and Layout of this Thesis.....	26
1.0.2.1 Agenda.....	26
1.0.2.2 Layout.....	27
1.1 Organic Solar Cell.....	29
1.1.1 History and Overview.....	29
1.1.2 Photoactive Material Developments.....	31
1.1.3 Photoactive Materials and Interface.....	32
1.1.3.1 Vertical phase separation.....	32
1.1.3.2 Interface of the photoactive layer.....	33
1.2 Perovskite Solar Cell.....	34
1.2.1 History and Overview.....	34
1.2.1.1 History.....	34
1.2.1.2 Overview.....	35
1.2.2 Photoactive Materials and Interface.....	36
1.3 Photovoltaic Parameters.....	37
1.4 Charge Selective Layers.....	39
1.4.1 Charge Selective Layers in Organic Solar Cells.....	39
1.4.1.1 Anode and the interface.....	39
1.4.1.2 Cathode and the interface.....	39
1.4.1.3 TiO _x and ZnO _x electron-transporting layers.....	40
1.4.1.4 Surface treatments on electron-transporting layers.....	40
1.4.2 Charge Selective Layers in Perovskite Solar Cells.....	41
1.5 Charge Conductive Layers and the Interface.....	41
1.5.1 Alternatives to Indium Tin Oxide.....	41
1.5.2 Single-walled Carbon Nanotubes.....	42

Chapter 2 – EXPERIMENTAL AND ANALYSES

2.1 Device Fabrications.....	44
2.1.1 Organic Solar cell Fabrications.....	45
2.1.1.1 Organic solar cell normal device architecture.....	45
2.1.1.2 Organic solar cell inverted device architecture.....	46
2.1.1.3 P3HT:mix-PCBM solution preparation.....	46
2.1.1.4 PTB7:PC ₇₁ BM solution preparation.....	47
2.1.2 Perovskite Solar Cell Fabrications.....	47
2.1.2.1 Perovskite solar cell normal device architecture.....	48
2.1.2.2 Perovskite solar cell inverted device architecture.....	48
2.1.2.3 Perovskite solution preparation.....	48
2.1.3 SWNT Preparations.....	49
2.1.3.1 Aerosol SWNT.....	49
2.1.3.2 SWNT electrode.....	49
2.2 Characterisations.....	50
2.2.1 Device Characterisations.....	50
2.2.1.1 Current-voltage characterisation.....	50
2.2.1.2 Incident photon to current efficiency (IPCE).....	50
2.2.1.3 Space-charge limited current (SCLC).....	50
2.2.1.4 Impedance measurement.....	51
2.2.2 Material Characterisations.....	51
2.2.2.1 UV-vis absorption.....	51
2.2.2.2 Photoluminescence.....	51
2.2.2.3 Atomic force microscopy (AFM).....	51
2.2.2.4 Scanning electron microscopy (SEM).....	52
2.2.2.5 Transmission electron microscopy (TEM).....	53
2.2.2.6 X-ray photoelectron spectroscopy (XPS).....	53
2.2.2.7 X-ray powder diffraction (XRD).....	53
2.2.2.8 Photoelectron yield spectroscopy (PYS) and Kevin probe.....	53
2.2.2.9 Raman spectroscopy.....	53
2.2.2.10 Auger electron microscope (AES).....	53
2.2.2.11 Water contact angle test.....	54
2.2.2.12 Profilometer.....	54
2.2.2.13 Four-probe measurement.....	54

Chapter 3 – SINGLE-WALLED CARBON NANOTUBES AS THE CONDUCTIVE LAYER IN FLEXIBLE ORGANIC SOLAR CELLS

3.1 Summary.....	55
3.2 Introduction.....	56
3.3 Experimental Procedures.....	56
3.3.1 Device Fabrications.....	56
3.3.2 Characterisations.....	57
3.4 Results and Discussion.....	57
3.5 Conclusion.....	68

Chapter 4 – SINGLE-WALLED CARBON NANOTUBES AS THE CONDUCTIVE LAYER IN FLEXIBLE PLANAR HETEROJUNCTION PEROVSKITE SOLAR CELLS

4.1 Summary	69
4.2 Introduction	70
4.3 Experimental Procedures.....	70
4.3.1 Device Fabrications.....	70
4.3.2 Characterisations.....	71
4.4 Results and Discussion.....	71
4.5 Conclusion.....	84

Chapter 5 – DOUBLE-WALLED CARBON NANOTUBES AS THE CONDUCTIVE LAYER IN FLEXIBLE ORGANIC SOLAR CELLS

5.1 Summary.....	85
5.2 Introduction.....	86
5.3 Experimental Procedures.....	87
5.3.1 Device Fabrications.....	87
5.3.2 Characterisations.....	87
5.4 Results and Discussion.....	88
5.5 Conclusion.....	91

Chapter 6 – SINGLE-WALLED CARBON NANOTUBES AS THE CONDUCTIVE LAYER AND NOVEL TRASFER METHODOLOGIES THEREIN IN TRANSPARENT ORGANIC SOLAR CELLS

6.1 Summary.....	92
6.2 Introduction.....	93
6.3 Experimental Procedures.....	94
6.3.1 Device Fabrications.....	94

6.3.1.1 <i>Transfer of non-doped SWNT</i>	95
6.3.1.2 <i>HNO₃ doping Sandwich-transfer method</i>	96
6.3.1.3 <i>MoO_x doping Bridge-transfer method</i>	96
6.3.2 Characterisations.....	96
6.4 Results and Discussion.....	96
6.5 Conclusion.....	105

Chapter 7 – OZONE-TREATED NIOBIUM-DOPED TITANIUM OXIDE AS BOTH THE CONDUCTIVE LAYER AND CHARGE SELECTIVE LAYER IN INVERTED ORGANIC SOLAR CELLS

7.1 Summary	107
7.2 Introduction	108
7.3 Experimental Procedures.....	108
7.3.1 Device Fabrications.....	108
7.3.2 TNO Film Fabrications.....	109
7.3.3 Characterisations.....	109
7.4 Results and Discussion.....	109
7.5 Conclusion.....	119

Chapter 8 – LIGAND-FREE ZnO NANOPARTICLES AS THE CHARGE SELECTIVE LAYER THAT REQUIRES NO THERMAL ANNEALING IN INVERTED ORGANIC SOLAR CELLS

8.1 Summary.....	120
8.2 Introduction.....	121
8.3 Experimental Procedures.....	122
8.4.1 ZnO NPs Synthesis.....	122
8.4.2 Device Fabrications.....	122
8.4.3 Characterisations.....	123
8.4 Results and Discussion.....	124
8.5 Conclusion.....	134

Chapter 9 – SPUTTERED ZnO FILM AS THE CHARGE SELECTIVE LAYER IN INVERTED ORGANIC SOLAR CELLS

9.1 Summary	135
9.2 Introduction	136
9.3 Experimental Procedures.....	137
9.3.1 ZnO Sputtering.....	137
9.3.2 Device Fabrications.....	138

9.3.3 Characterisations.....	138
9.4 Results and Discussion.....	138
9.5 Conclusion.....	143

Chapter 10 – SURFACE MODIFICATION OF THE CHARGE CONDUCTIVE AND SELECTIVE LAYERS USING ANTHRACENE DERIVATIVES IN INVERTED ORGANIC SOLAR CELLS

10.1 Summary.....	144
10.2 Introduction.....	145
10.3 Experimental Procedures.....	146
10.3.1 Device Fabrications.....	146
10.3.2 Characterisations.....	147
10.4 Results and Discussion.....	147
10.5 Conclusion.....	157

Chapter 11 – SURFACE MODIFICATION OF THE CHARGE SELECTIVE LAYER USING CATECHOL DERIVATIVES IN INVERTED ORGANIC SOLAR CELLS

11.1 Summary.....	158
11.2 Introduction.....	159
11.3 Experimental Procedures.....	160
11.4 Results and Discussion.....	161
11.5 Conclusion.....	163

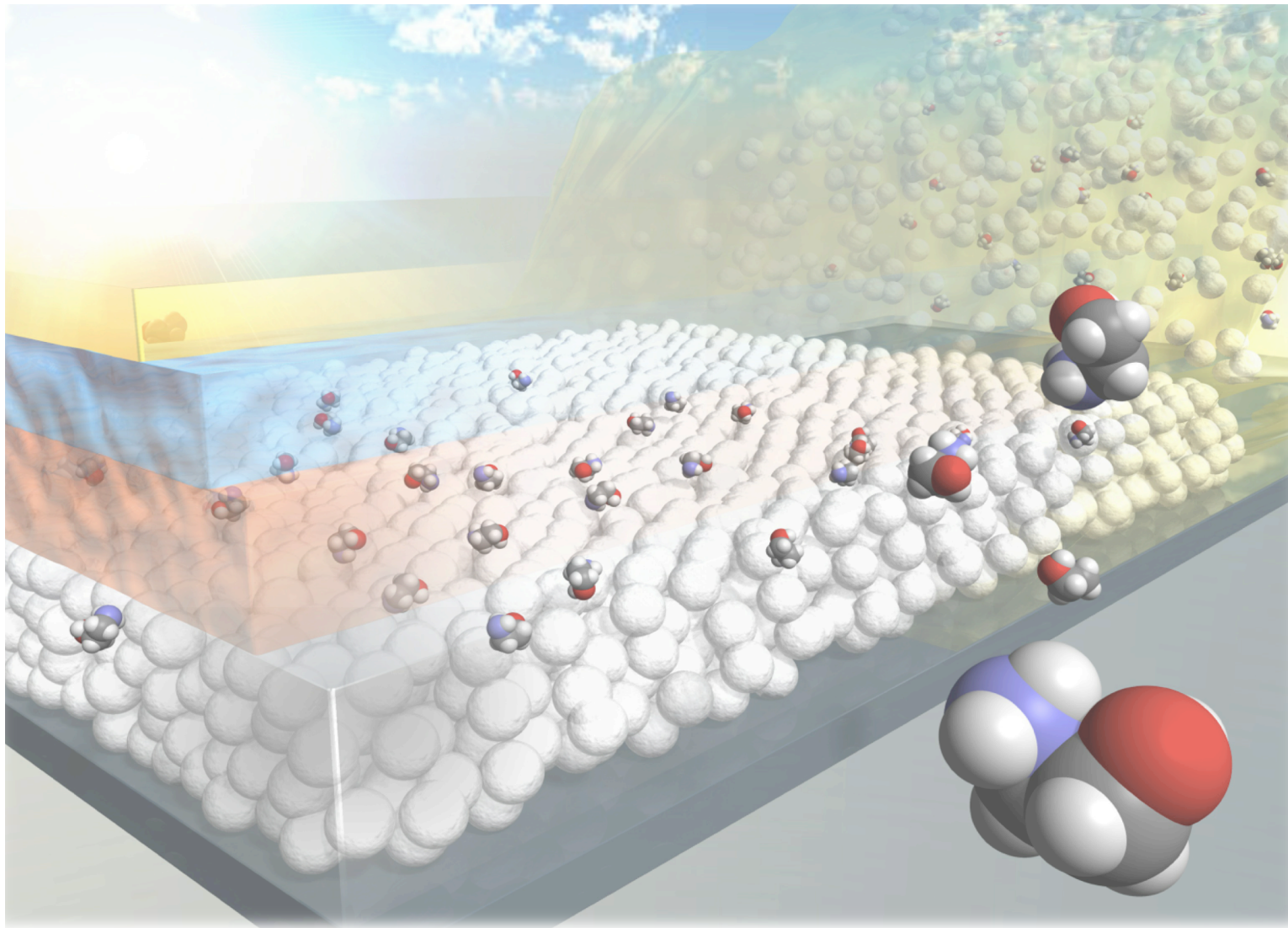
Chapter 12 – CHEMICAL VAPOUR DEPOSITED MoS₂ ON CARBON NANOTUBE FLAKES AS THE CHARGE SELECTIVE LAYER AND THAT ENABLES INTERCALATION WITH P3HT IN BULK HETEROJUNCTION ORGANIC SOLAR CELLS

12.1 Summary.....	164
12.2 Introduction.....	165
12.3 Experimental Procedures.....	166
12.3.1 Deposition of Multilayered MoS ₂ Nanoflakes on CNT Bundle.....	166
12.3.2 P3HT and MoS ₂ CNT Active Layer Preparation.....	167
12.3.3 Device Fabrications.....	167
12.3.4 Characterisations.....	167
12.4 Results and Discussion.....	168
12.5 Conclusion.....	172

Chapter 13 – VERTICAL PHASE SEPARATION AND INTERFACE CONTROL USING PHOTOACTIVE LAYER SPINCOATING INITIATION TIME IN ORGANIC SOLAR CELLS

13.1 Summary.....	173
13.2 Introduction.....	174
13.3 Experimental Procedures.....	174
13.3.1 Device Fabrications.....	174
13.3.2 Characterisations.....	175
13.4 Results and Discussion.....	175
13.5 Conclusion.....	186

Chapter 14 – OUTLOOK AND REFERENCES



CHAPTER 1

INTRODUCTION TO THESIS

1.0 Background

1.0.1 Inspiration

1.0.1.1 Energy crisis

Over the past century, human population has grown exponentially and relied on fossil fuels as the primary source of energy.^[2,3] Such inordinate dependence on fossil fuels has engendered constant threats and damage to the humanity that the

energy crisis has become a problem of all concerns. For a start, they emit a large volume of greenhouse gas into the atmosphere disturbing the ecological balance.^[4] This is due to over-utilisation of fuels to meet the ever-expanding demands to drive the industry and facilitate everyday requirements. Moreover, the gloomy fact that it is a finite source of energy that eventually run-out in near future has come close to toppling the economical balance as well.^[5,6]

The solution to this problem is to use fossil fuels in conjunction with other ecological energy sources under the term, 'Energy mix'. Renewable energies such as solar, tidal, geothermal, biofuels, and wind provide appealing alternatives to conventional energy sources.^[7-11] These are supplying approximately 14% of the total world energy demand at this stage. This percentage is due to increase with nations now setting in motion of energy revolution based on environmental and political interests.^[11-16] Therefore, reducing the reliance on fossil fuels and replacing them with renewable energy sources more and more are essential for reducing the damage imposed on the environment and providing future generations a habitable planet.

Yet, none of those alternative energy sources has what it takes to be a total solution. They have their own gritty foibles that limit their usages. To name a few, nuclear power relies on uranium, which is finite. Also it has severe consequences associated with it, highlighted by the disasters at Chernobyl, Three Mile Island, and Fukushima nuclear power plant. Wind- and hydro-powers are limited to certain locations, not to mention expensive set-up costs. In this regards, solar energy is by far the most prominent candidate among the listed energy sources.^[18,19] It is so abundant that the sun provides one-year-worth of energy humanity consumes, which is 4.6×10^{20} J, in mere one hour.^[20] Fossil fuels garnered in Earth amount to 3 trillion barrels, which equal to 1.7×10^{22} J of energy, but the Sun can supply this in just 1.5 days. By covering 0.16% of Earth's landmass with 10% efficient solar cells, it can offer 20 TW of energy which is about twice the world's current fossil fuel consumption and nuclear fission reactors combined.^[18] It is no surprise that nature has taken advantage of this in the form of photosynthesis for the past three billion years.^[21]

1.0.1.2 Solar cells

Inorganic solar cells including silicon solar cells, CIGS (copper indium gallium (di)selenide), dye-sensitized solar cells initiated the photovoltaic research. Especially, silicon solar cells are dominant in the photovoltaic industry today, because of their high power conversion efficiency (PCE). Nevertheless, expensive material cost of silicon is still a big hurdle in commercialisation, and on top of that, heavy weight and inflexibility limit their wide acceptance. Their potential for alternative applications is deemed dismal for the time being.^[22] In the wake of the latest technologies such as smart phones and IoT (internet of things), versatility has become the chief driving force that expedites the paradigm shifts from the conventional performance-oriented technology to versatility-oriented technology. Taking flexibility for instance, foldable and wearable concepts are replacing rigid and inflexible devices in present-day electronic market.

Likewise, in academia, the limelight has veered its way to organic material-based solar cells.^[23] What silicon solar cells lack in terms of versatility, organic solar cells (OSCs) make up for with flexibility and low-cost that conventional solar cells cannot parallel. OSCs utilise the conductive organic compounds as electron donors and electron rich fullerene derivatives as electron acceptors.^[24,25] Owing to their high absorption coefficient, low-cost, and mechanical flexibility, OSCs have become the epicentre of the solar cell research. Nevertheless, despite laudable achievements in recent years, OSCs are still faced with certain limitations: one of the examples includes the fixed light absorption range of organic compounds, along with restricted hole mobility and intrinsic instability.^[26] Above all, the maximum PCEs of around 10% are still lagging behind the conventional solar cells with PCEs of around 20%.

Recently, perovskite solar cells (PSCs), which harness hybridisation of organic and inorganic compounds, came into its own by complementing the efficiency that OSCs lack while retaining their versatility. This is enabled by taking advantage of an intrinsically long exciton dissociation length and high mobility of inorganic molecules, at the same time exploiting solution processability and abundance unique to OSCs. Although, there had been sceptical voices, it is an accepted fact in the academic field of solar cells now that PSC technology has more potential than meets the eye.

1.0.2 Agenda and Layout of this Thesis

1.0.2.1 Agenda

The main objective of this thesis is amplifying the abovementioned key features of OSCs and PSCs. They are efficiency, flexibility, facility, and stability (Figure 1). PCE is an ever so important issue shared by all of the photovoltaic devices and requires no emphasis. Flexibility, facility, and stability fall into the same category of versatility. To elaborate one by one, the core of flexibility is in the low-temperature process. Active materials used in OSCs and PSCs already qualify for flexibility. Nonetheless, it is the flexible substrates that cannot withstand the high temperature processes inflicted before the active layer deposition. Tackling this problem is one of the goals this thesis endeavour to achieve. Facility can be referred to as easiness of fabrication process or low-cost process. This can be accomplished by either reducing fabrication steps or using cheaper materials. Stability is another aspect that is forced to be reckoned with, for it is the only critical shortcoming of OSCs and PSCs.

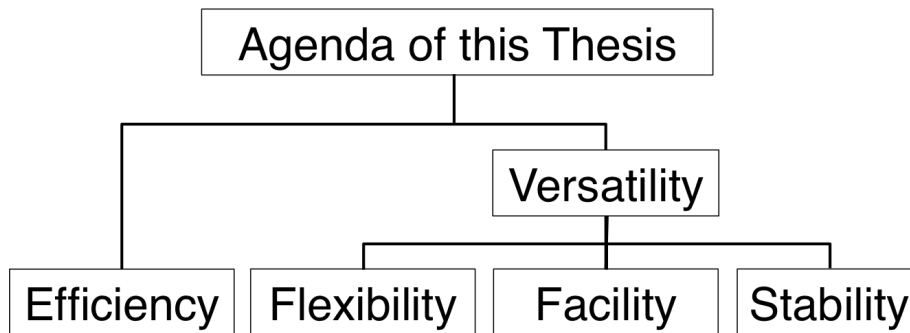


Figure 1. Agenda of this thesis in a flow chart.

Solar cells in general are composed in the same way (Figure 2). There are an active layer, a charge selective layer, and a charge conductive layer. The active layer absorbs light and generates excitons; the choice of active materials determines the solar cell type. If organic compounds are used, it will be an OSC. If organic-inorganic perovskite materials are used, it will be a PSC. The charge selective layers are placed above and below the active layer to filter out any unwanted charges followed by the conductive layers, which extract filtered charges. The charge selective and conductive layers are the two common essential layers in all types of solar cells.

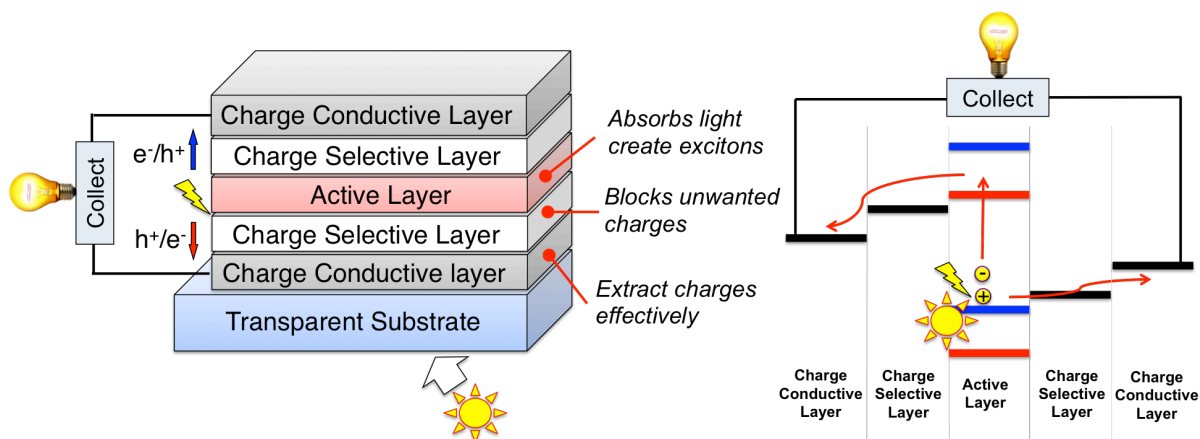


Figure 2. Graphical illustrations briefly explaining how solar cell works.

So far, the majority of the solar cell researches have been mostly focused on active layer improvements and structural alteration in microscopic and macroscopic levels, respectively. In this thesis, however, I focus on interfaces of the charge selective/conductive layers. This includes introduction of novel materials and modification of conventional materials to understand and improve the interface, which extends to overall performance of the solar cell device. Studying the charge conductive/selective interfaces of both OSCs and PSCs allows exploration of traits common to both systems, and exclusive to each system.

1.0.2.2 Layout

This dissertation is divided into three parts: introduction, experimental, and results and discussion. Chapter 1 deals with a broad overview on OSC and PSC. Chapter 2 comprises of experimental procedures used in this work. Both Chapter 1 and 2 deal with contents that are common to the projects in this thesis to minimise redundancy. Building an efficient solar cell via interface study involves a holistic consideration of morphology, material selections, and interface engineering. I endeavoured to go over each and every layer from the charge conductive layers to the active layer interface. From Chapter 3 to Chapter 13, each chapter corresponds to each research project. A schematic illustration displaying which chapter deals with whereabouts in solar cell device is given in Figure 3.

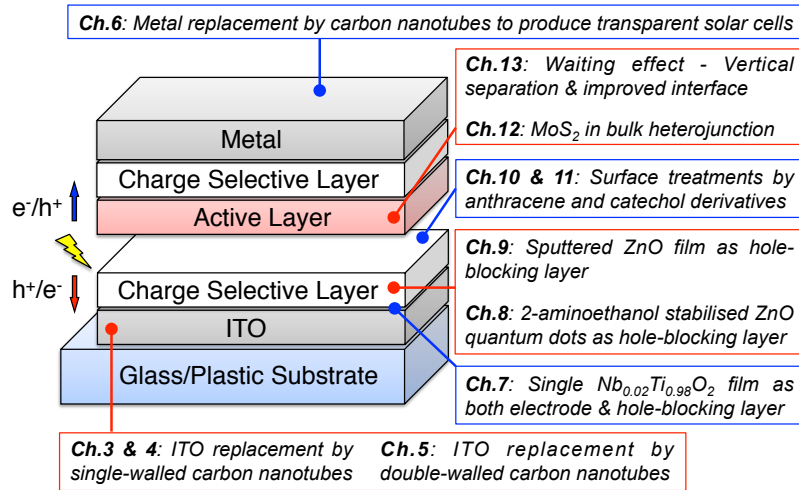


Figure 3. A schematic illustration of chapters in this thesis and their research themes.

Interface research of solar cells is a convergent study of diverse fields, so the scope is comprehensive. It extends from material chemistry (organic-inorganic chemistry) to electrochemistry (physical chemistry). As a work of interdisciplinary, this PhD course has been carried out under supervision of two professors: Professor Tetsuya Hasegawa from Solid State Chemistry Laboratory and Professor Matsuo from Photoelectric Conversion Laboratory. Professor Hasegawa possesses accumulated knowledge and know-hows in inorganic thin films and analytical techniques. Meanwhile, Professor Matsuo has dedicated a long time in the field of photovoltaics. This work is a collaborative research of the two strong laboratories. Projects were conducted in an almost simultaneous manner to meet the initially set target of covering all the interfaces involved in a solar cell (Figure 4).

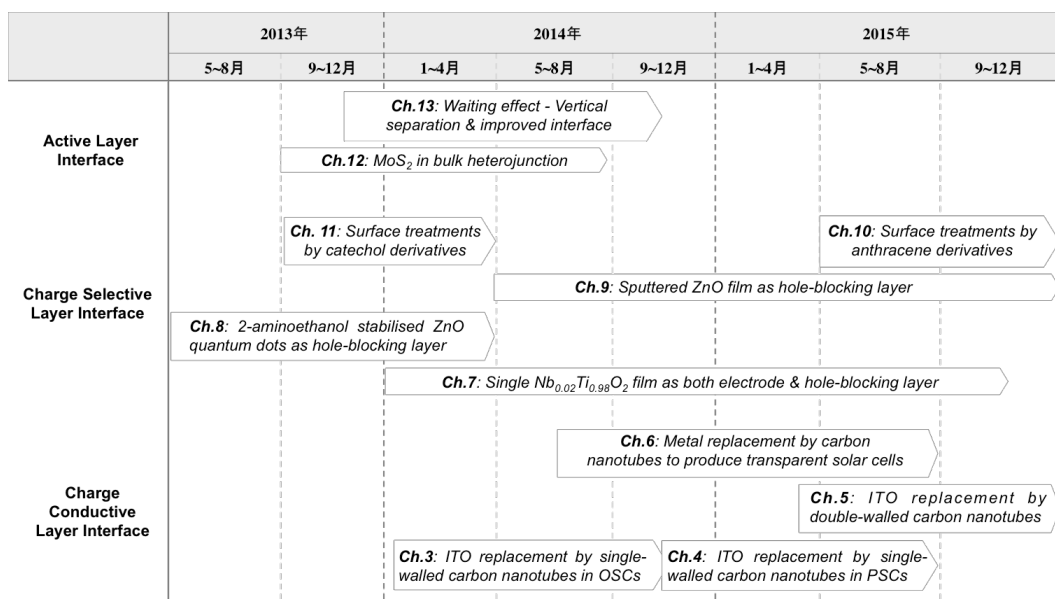


Figure 4. A timeline and chronological project assignments in this PhD period.

1.1 Organic Solar Cell

1.1.1 History and Overview

With a prototype introduced in 1986 by W. Tang, OSCs have continued its development as new generation photovoltaic device.^[27] Alternating C–C and C=C bonds of organic semiconductors give rise to either electron or hole conductive properties through electron delocalization along the conjugated backbone.^[28] These materials are different from inorganic semiconductors in a way that tightly bonded excitons (electron–hole pairs) are present owing to low dielectric constant, ϵ_r of around 2 to 4.^[29] A large binding energy of the Frenkel exciton, which is between 0.3 and 1 eV hampers exciton dissociation by an electrical field. On the other hand, weak intermolecular van de Waals forces enable large-area and low-cost solution processability.

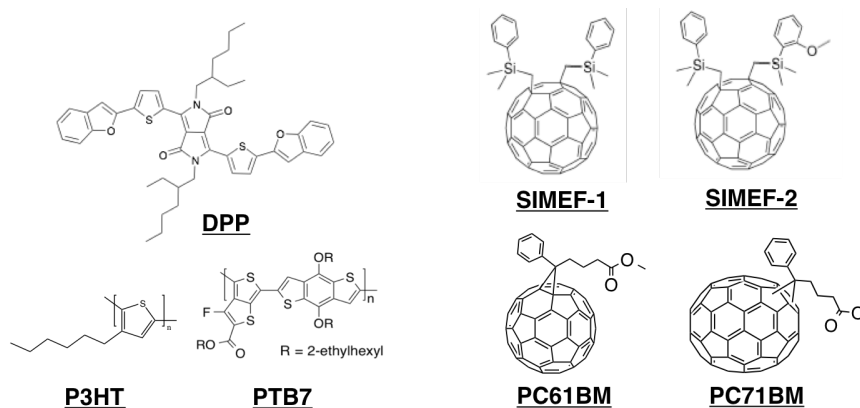


Figure 1. Examples of organic electron donors (left) and fullerene electron acceptors (right).

These organic photoactive materials can be bifurcated into small molecules and polymers that are quite different in terms of their synthesis, purification, and characteristics. Small molecule-based solar cells have recently gained momentum, but their stability and crystallinity still remain as bottlenecks.^[24] Polymer solar cells are in favour because of their higher stability and reliability, and chemical tunability over small molecules.^[25] So delving into polymer solar cells more, the energy difference between the lowest unoccupied molecular orbital (LUMO) of the polymer donors and highest occupied molecular orbital (HOMO) of the fullerene acceptors provides the driving force for the dissociation of Frenkel excitons. The separated holes and

electrons are then collected at the anode and cathode, respectively. C_{60} derivatives for example, [6,6]-phenyl- C_{61} -butyric acid methyl ester (PCBM) are standard n-type acceptors with their strong electronegativity and high electron mobility (Figure 1).^[30] Their photo-induced electron transfer process of around 50–100 fs between conjugated polymers and fullerene derivatives was demonstrated by Heeger et al. and Yoshino et al independently in the early 1990s.^[31,32] This served as a solid foundation for OSC technology with the first demonstration of planar heterojunction solar cell reported in 1993 (Figure 2).^[33] The planar junction concept still had certain limitations. Above all, its small surface area between the donor–acceptor interfaces meant the carrier lifetime had to be long to ensure that the electrons and holes to reach their electrodes. This problem has been addressed by development of a bulk heterojunction system, in which donor and acceptor materials are mixed thoroughly. Hiramoto *et al.* introduced this concept for the first time by co-evaporation of donor and acceptor species under high-vacuum conditions.^[34] In 1995, prof. Heeger and prof. Friend realised the first efficient bulk heterojunction OSCs by using polymer-fullerene and polymer-polymer blends, respectively.^[35,36] Since then, the PCEs of OSCs had soared like sky is the limit. During the progress, there was another powerful and significant discovery, which was the morphology of the active layer. To be more precise, the donor and acceptor phase separation governed charge transport channels for extracting electrons and holes.^[37,38] Appositely aggregated domains of photoactive materials enhance the charge extraction which is patently observable from the short-circuit current density (J_{SC}) value or better still the external quantum efficiency (EQE). There are two perspectives of looking at the separation: one is parochial and the other is vertical, both of which I will discuss in the coming section.

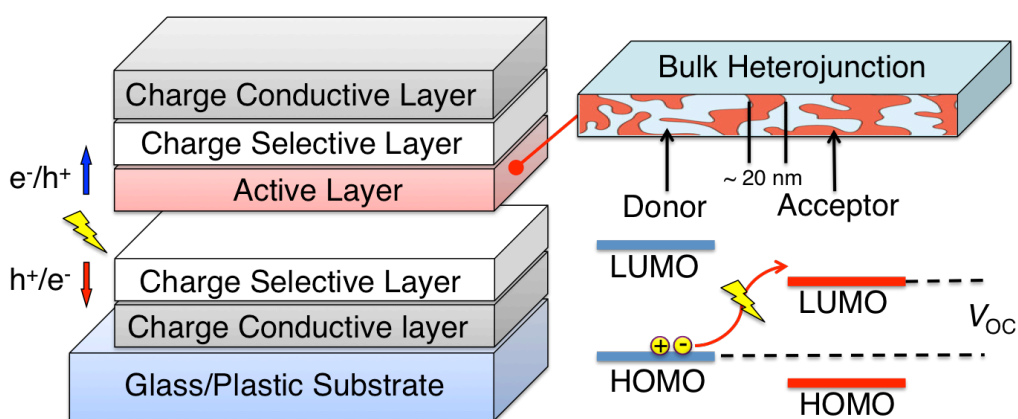


Figure 2. An illustration of a bulk heterojunction OSC and inside the active layer.

1.1.2 Photoactive Material Developments

Chemistry of materials is one of the key elements that governs the performance of OSCs. There are several factors that have direct impact on synthesis of photoactive materials: Tailoring the band gap to achieve high J_{SC} and open-circuit voltage (V_{OC}); enhancing molecular planarity to attain higher carrier mobility, processability, and stability; side-chain tuning to increase fill factor (FF),^[39,40] improving intermolecular interactions, molecular chain packing, and crystallinity all come to play a big part in driving up the efficiency. In the next paragraph, I briefly go over some of the exemplary photoactive materials developed from the nascence of OSCs chronologically.

Starting from one of the earliest polymers that was used in OSCs, poly [2-methoxy-5-(2'-ethylhexyloxy)-*p*-phenylene vinylene] (MEH-PPV)^[36] was developed by Wudl *et al.* along with PC₆₁BM^[30]. In 1995, Yu *et al.* blended MEH-PPV with C₆₀ to produce OSCs with a high PCE for the first time.^[36] Follow-up researches boosted PCEs to more than 3%.^[41,42] Meanwhile, in order to confront the low hole mobility of MEH-PPV, poly(3-hexylthiophene) (P3HT) was developed.^[43,44] P3HT possessed wider light absorption range too. Today, the P3HT and PC₆₁BM combination is regarded to be the archetypal photoactive layer.^[37,38] In recent years, higher performing polymers have been developed. One of these includes poly [2,6-(4,4-bis-(2-ethylhexyl)-4*H*-cyclopenta [2,1-*b*;3,4-*b'*] dithiophene)-alt-4,7-(2,1,3-benzothiadiazole)] (PCPDTBT), a low-band gap polymer whose absorption extends to 900 nm. Though, OSCs made from this polymer had shown an initial PCE of around 3%, by incorporating alkanedithiol additives, its PCE improved to around 5.5%.^[45,46] Another low band gap polymer, poly [*N*-9'-hepta-decanyl-2,7-carbazole-alt-5,5-(4',7'-di-2-thienyl-2',1',3'-benzothiadiazole)] (PCDTBT), which started with a PCE of 3.6%,^[47] and later increased to 6.1% with the aid of TiO_x as an optical spacer.^[48] Then another example of high performing polymer called PTB1 was discovered which was made up of thieno[3,4-*b*]-thiophene (TT) and benzodithiophene (BDT) alternating units.^[49,50] Further optimisations were followed and these kick-started what is now commonly used PTB7.^[40,51-56]

As the development of the photoactive donors have panned out, acceptors have made some significant improvements too.^[57] To begin with, it was discovered

that J_{SC} could be increased by roughly 10% if C_{70} derivatives, which absorb more light, could be used instead of C_{60} derivatives. V_{OC} could also be improved when fullerene derivatives were chemically modified to have a high lying LUMO level. Well-known examples are SIMEF derivatives and C_{60} indene bisadduct. Adding electron-rich adducts to fullerene shifted LUMO level up. Yet, the compatibility with donors and high material cost remains a challenge even to this day.

1.1.3 Photoactive Materials and Interface

As mentioned in ‘1.1.2 Photoactive Material Developments’, morphology of photoactive layer is imperative in OSCs. Since the discovery in 2005, thermal annealing^[43] and solvent annealing^[37] have been the mandatory process for controlling the morphology.^[38] Other approaches including solvent selection^[58,59] and additives addition that are readily used as well.

1.1.3.1 Vertical phase separation

Electron donor and acceptor species in a photoactive bulk heterojunction layer, such as P3HT:PCBM blends will favour the inverted structure due to the surface energy difference between PCBM and P3HT (Figure 3).^[60,61] Researchers observed a vertical concentration gradient and Near-edge X-ray absorption fine structure spectroscopy studies by DeLongchamp have shown that the P3HT:PCBM blends ETL induces more P3HT on the top and more PCBM at the bottom. Therefore, the resulting structure will benefit from better charge flow at the interfaces between ETL, photoactive layer, and HTL.^[62] Researchers have so far been exploiting tendency of P3HT to crystallize for controlling the alignment of conjugated polymer chains^[63,64] through myriad ways. These are namely post-annealing treatments,^[65,66] appropriate solvent choice,^[58,67] slow drying of spin-coated films,^[37,68,69] melting of bilayers, and etc.^[70] However, those methodologies take long time and sometimes are difficult to perform.

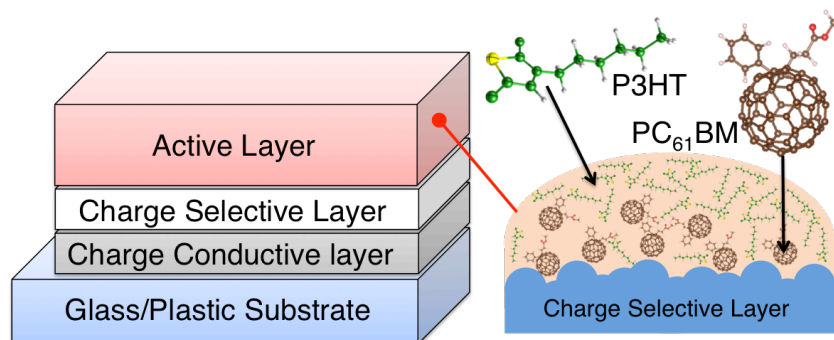


Figure 3. An illustration of vertical phase separation of active layer in OSCs.

1.1.3.2 Interface of the photoactive layer

Also there is a significant hitch in inverted type OSCs and it is called ‘light-soaking effect’. Under general circumstances, a current-density versus voltage ($J-V$) curve of solar cells should be ‘J-shaped’ and can be rationalised through the diode equation; however, an inflection point appears causing the curve to be ‘S-shaped’. A such characteristic is also called ‘kink’ and this results in decreasing FF and PCE.^[71–73] This is observed only in the light curve.^[73] This can be overcome by exposing the cells to a combination of illumination and temperature.^[74] A certain period of UV activation on ETL metal oxides restrains the ‘S-curve’ and increases PCE.^[75,76] This is because electrons on valence band of the metal oxide get excited to fill up any trap sites created and increase the electron number on conduction band, which enhance the transfer rate. However, during the process, OSCs are imposed with several problems: a long UV exposure time can damage and reduce the performance and it limits the use of any substrate with low UV transmission.^[77] The origin of the ‘S-curve’ is still not understood clearly, but we know, it can be attributed to the limited donor–acceptor electron transfer rate of intermolecular charge hopping which is largely caused by electron traps at the interface and morphology of domains in the photoactive layer.^[78–83] Since those traps are induced by surface-adsorbed oxygen, PCE of air-processed inverted OSCs imperatively lags behind the anaerobically fabricated normal type OSCs. In order to fully exploit the inverted OSCs’ air processability, it is crucial that the interfaces are free of oxygen adsorption.

1.2 Perovskite Solar Cell

1.2.1 History and Overview

1.2.1.1 History

OSCs have unique advantages that silicon solar cells do not possess. Yet, their PCEs have not come close to even paralleling the silicon-based devices. Thus, new photovoltaic that has a promising PCE while retaining flexibility and low-cost merits of OSCs was called for. Recently, there has been a boom in scientific community with emergence of a new generation solar cells made up of organic–inorganic halide perovskites.^[84]

PSCs initially bloomed from dye-sensitised solar cells. In 2006, Miyasaka and colleagues reported dye-sensitized cells using $\text{CH}_3\text{NH}_3\text{PbBr}_3$ and $\text{CH}_3\text{NH}_3\text{PbI}_3$ on nano-porous TiO_2 for the first time to produce PCEs of 2.2% and 3.8%, respectively.^[85] An organic electrolyte containing lithium halide was used as a HTL. A follow-up was done by Park and his colleagues in which they achieved a PCE of 6.5% in 2011, by utilising hemispheric perovskite nanoparticles with a diameter of 2.5 nm.^[86] This was a momentous breakthrough in PSC history as the performance of the perovskite nanoparticles superseded what was then the standard, N719 dye sensitiser. To tackle the problem of the electrolyte damaging the perovskite, spiro-MeOTAD was employed.^[87–89] Spiro-MeOTAD not only improved the stability, but it also boosted a PCE to 9.7%. Almost simultaneously Snaith and his colleagues reported a successful exploitation of spiro-MeOTAD along with other advancements including the use of the mixed-halide $\text{CH}_3\text{NH}_3\text{PbI}_{3-x}\text{Cl}_x$, which demonstrated better stability and carrier mobility than its pure iodide equivalent.^[90] They also replaced conducting nanoporous TiO_2 by a non-conducting Al_2O_3 network, which improved the V_{OC} , boosting the reported PCE to 10.9%. This revealed that perovskites could function not only as the active material, but also as the charge transporter within the cell. A great leap to 12.0% came from the collaboration between Seok, Gratzel, and their members by employing a perovskite capping layer overlying the scaffold and poly-triarylamine as the HTL.^[91] The performance was improved further to 12.3% using $\text{CH}_3\text{NH}_3\text{PbI}_3$.

$x\text{Br}_x$ in which, low Br composition (<10%) gave high initial PCEs owing to a lower band gap, but higher Br composition (>20%) proved to offer better stability.^[91] This was related to structural transition of perovskites from tetragonal to pseudo-cubic arising from a higher t factor due to the smaller ionic radius of Br.^[92] Further progress was reported in May 2013, by Gratzel's group with an efficiency above 15% achieved by morphological improvement through TiO_2 scaffolding and two-step iodide deposition, which improved the morphology.^[93] 15.4% was recorded by Snaith's group by thermal deposition of $\text{CH}_3\text{NH}_3\text{PbI}_{3-x}\text{Cl}_x$ in planar cells without scaffolding.^[94,95] Subsequently, an efficiency of 15.6% was reported for a structure where graphene has been used with Al_2O_3 scaffolding.^[95] An improvement soon followed with an efficiency of 15.9% by combining small TiO_2 nanoparticles and a titanium diisopropoxide bis(acetylacetonate) binder.^[96] More recently, Im and his colleagues developed inverted $\text{CH}_3\text{NH}_3\text{PbI}_3$ planar hybrid solar cells with an efficiency of 18.1% without significant J - V hysteresis with respect to the forward and reverse scan directions by forming a pinhole-free dense perovskite layer via a single-step spin-coating of a solubility controlled perovskite solution.^[97] This marked PCEs of both normal and inverted type PSCs levelling out with silicon solar cells in terms of efficiency and they have continued to surge from this on out until this day.

1.2.1.2 Overview

Since Miyasaka reported a prototype perovskite-based dye-sensitized solar cell, there has been a remarkable advancement and now the PCEs reach around 20%.^[85,98,99] Its high PCE arises from a long exciton diffusion length of around 100 nm to 1 μm , high absorption coefficient and carrier mobility, and a suitable band gap of around 1.55 eV offer a new pathway over OSCs.^[88,91,94,100] One negative aspect of PSCs is that the major constituent is lead, which is renowned to be extremely toxic and environmentally detrimental. Also, they undergo rapid degradation on exposure to oxygen or water.

Lead halide perovskite can be written as ABO_3 where O is an anion, and A and B are cations in which A is bigger than B. Their crystallographic structure and stability can be demonstrated by a combination of a tolerance factor, t and an octahedral factor, μ .^[101] t is the ratio of the distance A-O to the distance B-O in an idealized solid-sphere model, $t = (R_A + R_O) / \{\sqrt{2}(R_B + R_O)\}$, where R_A , R_B , and R_O are

the ionic radii of the corresponding ions. μ is defined as the ratio R_B/R_O . For halide perovskites ($O = X, F, Cl, Br, I$) in general, to should be between 0.81 and 1.11 and μ should be between 0.44 and 0.90. If t is in the narrower range 0.89–1.0, the structure will be cubic. With lower t values, they will form less symmetric tetragonal or orthorhombic structure.^[102] The larger cation, A is normally methylammonium (CH_3NH_3^+) with $R_{\text{MA}} = 0.18 \text{ nm}$,^[103] while ethylammonium ($\text{CH}_3\text{CH}_2\text{NH}_3^+$) ($R_{\text{EA}} = 0.23 \text{ nm}$)^[104] and formamidinium ($\text{NH}_2\text{CH}=\text{NH}_2^+$) (R_{FA} is estimated to lie in the range 0.19–0.22 nm)^[105,106] have been reported to be also compatible. The anion, X is a halogen, generally iodine ($R_{\text{I}} = 0.220 \text{ nm}$), although other halogens such as Br and Cl can also be used ($R_{\text{Br}} = 0.196 \text{ nm}$ and $R_{\text{Cl}} = 0.181 \text{ nm}$). Cation, B is immutably Pb ($R_{\text{Pb}} = 0.119 \text{ nm}$) for other metals like Sn ($R_{\text{Sn}} = 0.110 \text{ nm}$) manifested much lower stability.^[107] This is because Sn is more easily oxidised to SnI_4 than Pb. Summing up the above components give us the standard methylammonium lead trihalide with a formula, $\text{CH}_3\text{NH}_3\text{PbX}_3$. One last important thing to note is that regardless of the crystalline constraints, the perovskite transmute to a cubic phase upon application of high temperature (Figure 4).

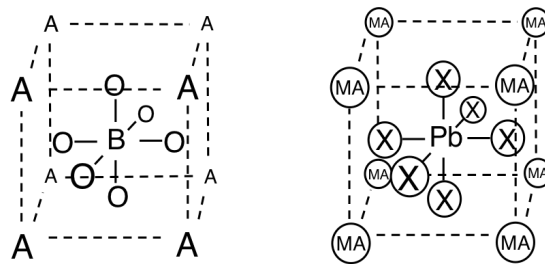


Figure 4. Cubic crystal structures of perovskite, ABO_3 (left); and lead halide perovskite, $\text{CH}_3\text{NH}_3\text{PbX}_3$ (right)

1.2.2 Photoactive Materials and Interface

Superiority of PSCs is centred around the perovskite photoactive layer ($\text{CH}_3\text{NH}_3\text{PbI}_3$) with appropriate band gap (1.55 eV), high absorption coefficient, long hole–electron diffusion length, and excellent carrier transport.^[85,87,91,99,108–110] Further chemical modifications are possible by substituting with other halides (Br or Cl) or replacing the methylammonium organic species with various other constituents (ethylammonium, formamidium etc.) to control band gaps, crystalline phase transitions, and hole–electron diffusion lengths.^[111–113] Many researchers are working on modifications of perovskite layer in order to top the current lead halide perovskite.

1.3 Photovoltaic Parameters

The device performance of a photovoltaic cell is characterised by J_{SC} , V_{OC} , and FF. Product of these three parameters leads to PCE (η_e):

$$\eta_e = J_{SC} \times V_{OC} \times FF \quad (1)$$

J_{SC} is short-circuit current (I_{SC}) divided by active area. Any improvement that influences one of those three parameters will lead to an increase in solar cell efficiency.

The current (I) in an equivalent circuit of a photovoltaic cell can be described by the following equation:^[114,115]

$$I = I_0 \times \left[\exp\left(e \frac{U - IR_S}{nkT}\right) - 1 \right] + \frac{U - IR_S}{R_{SH}} - I_{PH} \quad (2)$$

where I_0 is the dark current, e is the electron charge, n is the diode ideality factor, U is the applied voltage, R_S is the series resistance, R_{SH} is the shunt resistance, and I_{PH} is the photocurrent. Thus, to obtain high short-circuit current, I_{SC} ($U = 0$ V), solar cell devices must have small R_S and large R_{SH} . The FF can be written as:

$$FF = \frac{V_{MPP} \times I_{MPP}}{V_{OC} \times I_{SC}} \quad (3)$$

where MPP denotes the maximum power point. Thus, large FF needs that the photocurrent rise sharply as U approaches V_{OC} (i.e., to acquire the maximum of $V_{MPP} \times I_{MPP}$). This optimum condition can only be met without photocurrent loss from recombination. Therefore, FF is limited by the carrier drift length (L_d)

$$L_d = \mu\tau E \quad (4)$$

where μ is the carrier mobility, τ is the carrier recombination lifetime, and E is the electric field. L_d is pivotal in avoiding recombination.^[116,117] Accordingly, high mobility and appropriate active layer thickness is required for efficient charge extraction.

In OSCs J_{SC} can be improved by using narrow band gap photoactive materials

(<1.8 eV) for a broader coverage of the solar spectrum.^[118-120] Methods for achieving this include designing the quinoid structure, polymer chain planarity,^[121,122] and tuning the effective conjugation length which controls electron delocalization over the polymer backbone OSC applications.^[123,124] According to molecular orbital perturbation theory, electron delocalization leads to the hybridization of molecular orbitals, resulting in electron redistribution among the interacting orbitals. This provides two new hybridized orbitals, a higher HOMO level and a lower LUMO level — resulting in a narrower band gap. Other parameters, such as carrier mobility, intermolecular interaction and molecular chain packing can also improve J_{SC} .^[125,126] Excitons are free carriers excited from incident photons absorbed by the photoactive materials. Amount of excitons created over absorbed photons can be measured and this is called the external quantum efficiency (EQE). EQE is calculated using Incident photon to current efficiency (explained in 2.2.1.2) data and UV-vis absorption (explained in 2.2.2.1) of the photoactive layer. Improving EQE also increases J_{SC} .

V_{OC} is directly associated with the energy difference between the LUMO level of the acceptor and the HOMO level of the donor, thereby providing the chief driving force for charge separation. V_{OC} can be expressed by the empirical equation $V_{OC} = e^{-1} \times (|E_{HOMO}^{donor}| - |E_{LUMO}^{acceptor}| - 0.3 \text{ eV})$, where e is the elementary charge, E is the energy level, and 0.3 eV is an empirical value for efficient charge separation.^[127] In OSCs, a donor with a lower HOMO level will give a higher V_{OC} .

FF is currently the least understood photovoltaic parameter. The FF is the ratio of the maximum power to the product of J_{SC} and V_{OC} . It is affected by charge carrier mobility, interface recombination, series and shunt resistances, miscibility between the donor and acceptor and etc.^[128] However, obtaining a clear understanding and the ability to modulate the FF remains an enigma.

Knowledge of the link between these parameters has been immensely improved over the past decade. Still, the factors that affect each parameter are not straightforward and intertwined with each other. Consequently, in a practical approach, all factors should be taken into consideration and no sole affirmative explanation is possible.

1.4 Charge Selective Layers and the Interface

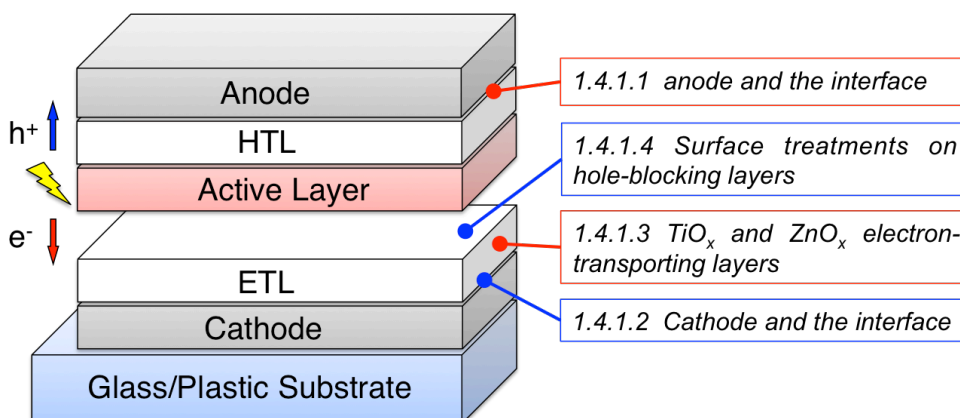


Figure 5. A schematic diagram of an inverted OSC and their charge selective interfaces

1.4.1 Charge Selective Layers in Organic Solar Cells

Pertaining to the charge selective layers, they have multiple functions in solar cells.^[61] Firstly, they reduce the energy barrier between the photoactive layer and the electrode, thus forming an Ohmic contact for effective charge extraction. Secondly, they can form selective contacts for a single type of carrier, allowing only desired charges to pass through. Lastly, optical field modulation and protection are also known to be essential functions that charge selective layers can offer.

1.4.1.1 Anode and the interface

ITO (Indium tin oxide), which has a high work function of around 4.8 eV is traditionally used as the transparent and conductive substrate for OSC fabrications. A p-type interface layer of PEDOT:PSS (work function of around 5.0 eV) is applied on ITO to form an Ohmic contact with the photoactive layer and filling up pinholes on the ITO surface. The acidic nature of PEDOT:PSS, however, undermines device's stability. As a solution to this, various transition metal oxides such as V_2O_5 , MoO_3 , WO_3 and NiO_x have been proposed to replace PEDOT:PSS.^[129–132]

1.4.1.2 Cathode and the interface

For the cathode on the other hand, metals with low-work-functions such as calcium, barium, and magnesium are used to at the interface. Many researchers have introduced inorganic compounds to replace such reactive metals. For example, Tang

et al. and Brabec *et al.* introduced n-type interface layer, LiF and demonstrated that LiF/Al can perform comparable to Ca/Al electrode.^[133] Jönsson *et al.* reported that Al decomposes LiF, thus causing subsequent lithium doping of the organic material to lower the contact's work function.^[134] Applying a thicker layer of LiF creates a dipole layer that lowers the work function too.^[135] Other fluorides such as CsF have displayed analogous results.^[136] Yang *et al.* demonstrated an inverted OSC using ITO and Al which are traditionally used in normal-type OSCs by exploiting Cs₂CO₃ next to ITO and V₂O₅ next to Al.^[137] Thus, even device architectures are determined by the charge selective interfacial layers.

1.4.1.3 TiO_x and ZnO_x electron-transporting layers

Solution-processed interface layers are preferred over vacuum processes such as thermal evaporation and sputtering owing to the low-cost merit. In this regards, n-type inorganic metal oxides such as titanium oxide (TiO_x) and zinc oxide (ZnO_x) have been widely used as the ETLs.^[138,139] Low-temperature (150 °C) process of amorphous TiO_x has been effective as both a ETL and an optical spacer, which enhances absorption by modulating the optical field. TiO_x optical spacer has been shown to enhance photocurrent and EQE by around 40% for a P3HT:PCBM system and nearly a 100% enhancement in internal quantum efficiency for a PCDTBT:PCBM system.^[140] It was also reported that by incorporating Cs₂CO₃ into nanocrystalline TiO_x the Cs-doping can lower the TiO_x work function or improve device performance.^[141]

1.4.1.4 Surface treatments on electron-transporting layers

Surface modifiers with permanent dipole moments can improve polymer-electrode interfaces. Self-assembled monolayers with electron-withdrawing or electron-donating groups can increased or decreased work function of a material, respectively. Numerous researchers have demonstrated improvement in OSC efficiencies via a surface treatment on ZnO^[142] and other n-type interface materials such as conjugated poly-electrolyte,^[143,144] on the TT-BDT copolymer.^[145]

1.4.2 Charge Selective Layers in Perovskite Solar Cells

HTL and ETL are vital components that give rise to advanced progress in PSCs. The standard fluorine-doped tin oxide (FTO)/TiO₂ layers were replaced by ITO/ZnO-nanoparticle layer and gave a PCE of 15.7% on glass.^[146] Use of ZnO meant that low-temperature fabrication was possible. Inorganic HTLs such as CuI^[147] also showed descent efficiencies, as did some organics compounds, particularly, PC₆₁BM as an ETL and P3HT as a HTM.^[148–150] As the spotlight shifted from performance of PSCs to flexible applications, low processing temperatures of less than 150 °C drew the attention. To avoid the typical compact TiO₂ which requires temperatures around 500 °C, graphene nano-flakes were mixed in the normally compact TiO₂ layer (0.6% graphene/TiO₂ by weight) to produce an efficiency of 15.6% for a structure that includes all optional layers and Al₂O₃ scaffolding.^[151] A PCE of 15.9% has also been achieved by combining small TiO₂ nanoparticles with a titanium diisopropoxide bis(acetylacetonate) binder.^[96]

1.5 Charge Conductive Layers and the Interface

Mechanical flexibility is said to be an advantage of OSCs. However, as long as there are inflexible metal oxides and metals being used as the charge conductive layers, they can be bendable, but never totally flexible. Among them, ITO is at the heart of this problem. A relatively high thickness with brittle property of ITO limits the device flexibility.^[152,153] Indium's limited availability is also a hot potato in the industry and even in politics. As a result, the price has been increasing dramatically since year 2000. In the field of OSCs, there has been a continuous effort to replace this ITO.^[154–156] Suitable candidates are known to be silver nanowires^[157–159], graphene^[160–162], carbon nanotubes^[163–167], and etc.

1.5.1 Alternatives to Indium Tin Oxide

There have been great advancements for each component of photovoltaic

devices to date, namely charge selective layers, active layers, metal top-electrodes. Yet, ITO has continuously been used in spite of high cost that manufactures are keen to avoid. The other major downside of ITO is its brittle nature that cannot withstand flexible movement without breaking. Other number of drawbacks such as vulnerability against high temperature and finite natural abundance of indium cannot be underestimated either. Avoiding these limitations by employing alternative electrode materials has therefore been the subject of intense research for many years.^[157,168] The difficulty has been the finding of an alternative electrode that is not only robust and low-cost, but also combines high optical transparency with high electrical conductivity.^[154–156] There has been an attempt in which silver embedded ITO is used to render low resistivity of around $30 \Omega \text{ sq}^{-1}$ on a PET substrate, but it is still not flexible enough and costly.^[159] Unlike ITO, fluorine-doped tin oxide^[169,170] can withstand a temperature above $300 \text{ }^\circ\text{C}$ without undermining the performance.^[171] Nevertheless, its transmittance and conductivity are lower than those of ITO. Aluminum-doped zinc oxide (AZO) is another viable option, yet ITO outperforms AZO in terms of stability to moisture which is pivotal in devices.^[172–174]

1.5.2 Single-walled Carbon Nanotubes

Carbon nanotubes (CNT) and graphene have emerged as materials for next-generation electrodes in OSCs, offering a possible alternative to ITO.^[175] Among those, single-walled CNTs (SWCNTs or SWNTs) have advantages in terms of stretchability, ease of synthesis, and suitability for direct roll-to-roll deposition onto substrates, which translate into lower costs.^[164] Thus, SWNTs as transparent conductive films in photovoltaics have been the subject of active research. SWNTs are structurally the simplest class of carbon nanotubes and their architecture can be described as an entangled single-layered graphene rolled in a cylindrical shape with typical diameters in the range of $0.4\text{--}3.0 \text{ nm}$ (Figure 6).^[176] Following the independent discoveries by Iijima in early 1990s, research of its synthesis and properties accelerated greatly.^[177] Recently, the high quality, free-standing, and purely single-walled carbon nanotubes, which are directly transferrable by aerosol chemical vapour deposition, have been developed. This technique can produce a SWNT film with the transparency of over 90% and the resistance of around $85 \Omega \text{ sq}^{-1}$. Its synthetic process

is better than the other conventional methods, which suffer from resource-consuming liquid dispersion and purification steps ending up with dense SWNT networks.^[178–180] The success of SWNT application in photovoltaics depends on two things: the effectiveness of doping in a manner that the dopant does not undermine the device performance and overcoming the intrinsic hydrophobicity of SWNTs for uniform film fabrication.^[181,182]

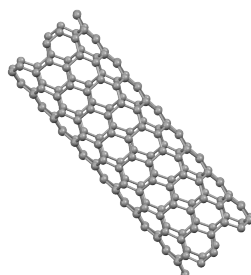


Figure 6. A 3D image of single-walled carbon nanotube.

1.6 Purpose of each chapter

Chapter	Purpose and aim
3	1. Application of single-walled carbon nanotube as an electrode to replace ITO 2. Using MoO _x layer to function as both dopant and charge selective layer 3. Thus, producing flexible yet high performing ITO-free organic solar cells
4	1. Application of single-walled carbon nanotube as an electrode to replace ITO 2. Discovering why MoO _x layer does not work for perovskite solar cells 3. Introducing diluted nitric acid doping and PEDOT:PSS modification methods
5	1. Application of double-walled carbon nanotube as an electrode to replace ITO 2. Compare the mechanical and electronic properties of double-walled and single-walled nanotubes as the potential electrodes
6	1. Application of single-walled carbon nanotube as an electrode to replace metal 2. Produce novel methods of doping carbon nanotubes that are laminated from top 3. Thus, producing transparent window-like and metal-free organic solar cells
7	1. Application of niobium-doped titanium oxide as an electrode to replace ITO 2. Application of ozone-treated niobium-doped titanium oxide as both electrode and charge selective layer in inverted organic solar cells
8	1. Develop a new way of forming ZnO films without applying high temperature annealing 2. Introduce amino-2-ethanol as stabilisers for the ZnO nanoparticles
9	1. Develop a way to produce sputtered ZnO films that are as efficiency as the sol-gel ZnO
10	1. Modify the surface of metal oxide charge selective layers by anthracene compounds 2. Enhance the efficiency of organic solar cells by reinforcing charge selective function
11	1. Modify the surface of metal oxide charge selective layers by catechol compounds 2. Enhance the efficiency of solar cells by drawing fullerene acceptors to the surface
12	1. Introduce MoS ₂ as electron acceptors in organic solar cells by using carbon nanotube
13	1. Induce vertical separation and better contact in active layer via new technique.

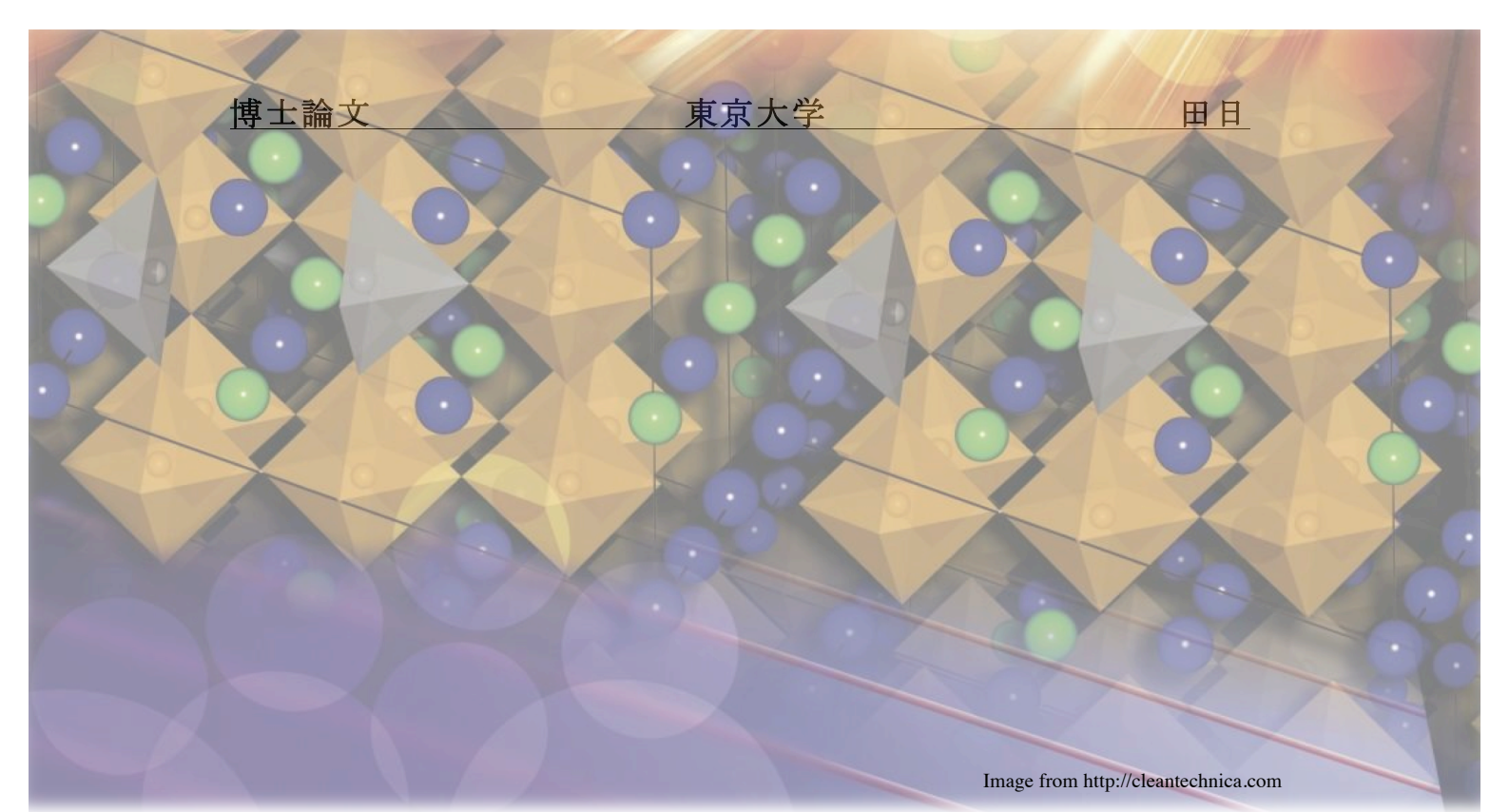


Image from <http://cleantechnica.com>

CHAPTER 2

EXPERIMENTAL AND ANALYSES

General information regarding experimental procedures and characterisations are adequately explained in this chapter. Those include device fabrications of organic and perovskite solar cells, material preparations, and their analytical methods that are common in most of the chapters. As each chapter varies slightly, more niceties may have been added to each chapter separately.

2.1 Device Fabrications

Lab-scale devices were prepared on two types of ITO glass substrates unless new materials were used to replace ITO. They were either $22 \times 38 \text{ mm}^2$ substrate with a sheet resistance of $6 \Omega \text{ sq.}^{-1}$ (Kuramoto Co., Ltd.) etched by Zn and 1 M HCl or $15 \times 15 \text{ mm}^2$ substrate with the same resistance. All substrates were sonicated in cleaning surfactant (Semi Clean, M-Lo), water, acetone and 2-isopropanol for 15 min each. They were then dried in the oven at $70 \text{ }^\circ\text{C}$ followed by exposure to UV/O₃ for 30 min in order to remove any remaining organic impurities.

2.1.1 Organic Solar Cell Fabrications

There are two main device architectures (Figure 1). The main difference is direction of the charge flow. In other words, whether ITO is employed as the anode (normally referred to as the conventional architecture) or the cathode (inverted architecture).

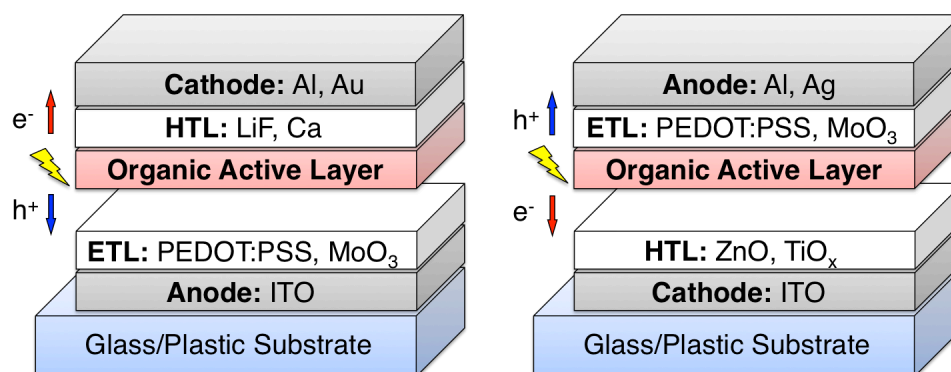


Figure 1. Illustrations of a normal type OSC (left) and an inverted type OSC (right).

2.1.1.1 Organic solar cell normal device architecture

Normal type is most common for lab-scale solar cell evaluations for its relatively facile and reproducible process. Here, ITO works as the anode. This is deposited on a transparent substrates, such as glass or plastic substrates. For the reference device, ITO substrates with size $15 \times 15 \text{ mm}^2$ and an active area of $3 \times 3 \text{ mm}^2$ with a sheet resistance of $6 \Omega \text{ sq.}^{-1}$ (Kuramoto Co., Ltd.) were sonicated in cleaning surfactant (Semi Clean, M-Lo), water, acetone and 2-isopropanol (IPA) for 15 minutes each. The substrates were then dried in an oven at $70 \text{ }^\circ\text{C}$. ITO substrates were exposed to UV/O₃ for 30 min in order to remove any remaining organic impurities. Either, 15 nm MoO₃ was deposited with the average rate of 0.2 \AA s^{-1} or PEDOT:PSS dispersed in water (Clevios P VP, Heraeus Precious Metals GmbH & Co.) was spin-coated at the speed of 4500 rpm for 45 s for EBL. For the PH3T:PCBM photoactive layer deposition, fast-growth method was employed. The solution was spin-coated on PEDOT:PSS (or MoO₃) layer at a speed of 2000 rpm for 90 s to give films of approximately 140 nm. Thermal annealing at $150 \text{ }^\circ\text{C}$ for 14 minutes was performed on prepared sample. For the PTB7:PC₇₁BM:DIO photoactive layer deposition. The solution of PTB7:PC₇₁BM:DIO was spin-coated at 1500 rpm for 60 s on PEDOT:PSS (or MoO₃) layer to give approximately 100 nm. No thermal annealing

was required. For the cathodes, LiF (0.7 nm) followed by aluminum (100 nm) was deposited by vacuum thermal evaporation at the rate of 0.2 \AA s^{-1} .

2.1.1.2 Organic solar cell inverted device architecture

For inverted devices, the bottom electrode can likewise be ITO on top of a transparent substrate, but here it functions as the cathode. ITO substrates with size $150 \times 150 \text{ mm}^2$ and an active area of $22 \times 38 \text{ mm}^2$ with a sheet resistance of $6 \text{ \Omega sq.}^{-1}$ (Kuramoto Co., Ltd.) were firstly etched using Zn and 1 M HCl, followed by sonicating the substrates sequentially in cleaning surfactant (Semi Clean, M-Lo), water, acetone and IPA for 15 min each. The substrates were then dried in an oven at $70 \text{ }^\circ\text{C}$. Prior to metal oxide deposition, ITO substrates were exposed to UV/ O_3 for 20 min. The TiO_2 films and ZnO sol-gel films were prepared using the method reported by Kuwabara and Heeger, respectively.^[183,184] The metal oxides were baked at $150 \text{ }^\circ\text{C}$ before depositing the photoactive layer to dry and improve conductivity. This minimises the light-soaking time of the OSC.^[75] The prepared photoactive layer solution was then spin coated on the metal oxide layers at a speed of 850 rpm for 45 s to give slow-growth films of approximately 300 nm. The films were then immediately placed in a petridish for 40 min to allow slow evaporation of the solvent. A poly (3,4-ethylenedioxythiophene) / poly (styrenesulfonate) (PEDOT:PSS) dispersion in water (CleviosPVP, Heraeus Precious Metals GmbH & Co.) containing 0.5wt% polyoxyethylene(6)tridecyl ether (Sigma Aldrich Chemical Co., Inc.) was spin coated on top of the active layer to form the HTL with a 30 nm thickness. Approximately 200 nm thick Au layer was thermally evaporated at pressure of $3 \times 10^{-3} \text{ Pa}$, with the use of a shadow mask, which defined the device active area as 1 cm^2 . All processes, except for Au deposition, were performed in air and the devices were not encapsulated. All devices were thermally annealed at $150 \text{ }^\circ\text{C}$ for 10 min.

2.1.1.3 P3HT:mix-PCBM solution preparation

For the PH3T:PCBM photoactive solution, P3HT (regioregular, Sigma Aldrich Chemical Co., Inc.) and [6,6]-phenyl C_{61} -butyric acid methyl ester and [6,6]-phenyl C_{71} -butyric acid methyl ester in a 16:3 ratio (mix-PCBM) (Frontier Carbon Co., Nanom spectra E124) solution with a donor:acceptor ratio of 5:3 and concentration of 40 mg mL^{-1} in ortho-dichlorobenzene (ODCB) (anhydrous, 99%,

Sigma Aldrich Chemical Co., Inc.) was prepared. The solution was left stirring for 2 h at 65 °C.

In the case of P3HT:PC₆₁BM, everything was the same except, [6,6]-phenyl C₆₁-butyric acid methyl ester (PC₆₁BM) (Frontier Carbon Co., Nanom spectra E123) was used in a ratio of 5:4.

2.1.1.4 PTB7:PC₇₁BM solution preparation

For the PTB7:PC₇₁BM:DIO photoactive layer deposition, PTB7 and [6,6]-phenyl C₇₁-butyric acid methyl ester (PC₇₁BM) were purchased from Luminescence Technology Corporation and used as received without further purification. A blend solution of PTB7 and PC₇₁BM was prepared in a mixed solvent of chlorobenzene (99%, CB) and 1,8-diiodooctane (DIO) at a 97:3 ratio. PTB7 (10 mg) and PC₇₁BM (15 mg) were initially dissolved in CB inside a nitrogen glovebox (0.97 mL). The solution was left stirring overnight at 60 °C. After 24 h, the corresponding amount of DIO (30 μL) was added. The new solution was stirred 1 h at 70 °C.

2.1.2 Perovskite Solar Cell Fabrications

There are also two main device architectures for PSCs. However, with PSCs ITO is employed as the cathode is referred to as the conventional architecture and ITO as the anode is the inverted architecture (Figure 2).

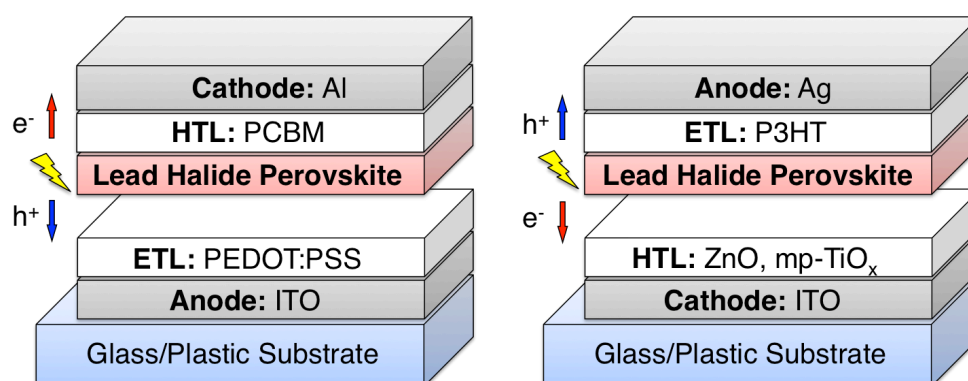


Figure 2. Illustrations of an inverted type PSC (left) and a normal type PSC (right).

2.1.2.1 Perovskite solar cell normal device architecture

A 30 nm thick dense layer of TiO₂ was then coated on the ITO substrates by spin coating of a bis (isopropoxide) bis (acetylacetonato) titanium (IV) solution (75% in 2-propanol, Sigma-Aldrich) diluted in 2-propanol (1:9, volume ratio) at 450 °C. To deposit perovskite films, the CH₃NH₃PbI₃ solution (25 μL) was first dropped onto a TiO₂. The substrate was then spun at 4500 rpm and after eight seconds anhydrous chlorobenzene (10 μL) was quickly dropped onto the centre of the substrate. This instantly changed the colour of the substrate from transparent to light brown. The hole-transporting material was deposited by spin coating at 1500 rpm for 30 s. The spin coating solution was prepared by dissolving 80 mg spiro-MeOTAD, 15 μL of a stock solution of 520 mg mL⁻¹ lithium bis(trifluoromethylsulphonyl)imide in acetonitrile and 22.5 μL 4-tert-butylpyridine in 1 mL chlorobenzene. Device fabrication was finally completed by thermal evaporation of a 70-nm- thick film of silver as the cathode. Devices were left in a desiccator overnight and tested next day. Device fabrication was carried out in a N₂-filled glove box.

2.1.2.2 Perovskite solar cell inverted device architecture

PEDOT:PSS was spin coated at 300 rpm for 3 s and then 4500 rpm for 60 s on ITO. In the case of MoO₃, 15nm thickness was thermally deposited under vacuum. CH₃NH₃PbI₃ solution (25 μL) was first dropped onto a PEDOT:PSS or MoO₃. The substrate was then spun at 4500 rpm and after eight seconds anhydrous chlorobenzene (10 μL) was quickly dropped onto the centre of the substrate. This instantly changed the colour of the substrate from transparent to light brown. The electron-transporting material was deposited by spin coating at 1500 rpm for 30 s. The spin coating solution was prepared by dissolving 20 mg of PC₆₁BM in 1000 μL chlorobenzene. Device fabrication was finally completed by thermal evaporation of a 70 nm thick film of aluminum as the cathode. Device fabrication was carried out in a N₂-filled glove box.

2.1.2.3 Perovskite solution preparation

One-step solution method was used for all of my perovskite fabrications. The synthesised CH₃NH₃I (0.172 g) was mixed with PbI₂ (0.500 g) in anhydrous N,N-dimethylformamide (1.07 mL) by stirring at 60°C overnight to produce clear CH₃NH₃PbI₃ solution with a concentration of 45 wt%.

2.1.3 SWNT Preparations

2.1.3.1 Aerosol SWNT

The randomly oriented SWNT networks with high purity and a long nanotube bundle length can be synthesised by the aerosol CVD method.^[185,186] The floating catalyst aerosol CVD was carried out in a scaled-up reaction tube with the diameter of 150 mm. The catalyst precursor was vaporised by passing ambient temperature CO through a cartridge filled with ferrocene powder. To obtain stable growth of SWNTs, a controlled amount of CO₂ was added together with the carbon source (CO). SWNTs were directly collected downstream of the reactor by filtering the flow through a nitrocellulose or silver membrane filter (Millipore Corp., USA; HAWP, 0.45 µm pore diameter). The flow containing ferrocene vapour was then introduced into the high-temperature zone of a ceramic tube reactor through a water-cooled probe and mixed with additional CO. Ferrocene vapour was thermally decomposed in the gas phase in the aerosol CVD reactor at the temperature of 880 °C. The CO gas was supplied at 4 L min⁻¹ and decomposed on the iron nanoparticles, resulting in growth of SWNTs. The as-synthesised SWNTs were collected by passing the flow through microporous filters at the downstream of the reactor, while the transparency and sheet resistance was controlled by varying the collection time. The collected SWNT networks were transferred to wide variety of substrates through the dry press-transfer process. The FC-CVD synthesised and dry deposited SWNT networks had high purity. Furthermore, as the process requires no sonication based dispersion steps the resulting SWNT network consisted of exceptionally long SWNTs.

2.1.3.1 SWNT electrode

For the SWNT device, bare glass substrates (Kuramoto Co., Ltd.) were purchased and cleaned by the same method as the ITO substrates. Prior to SWNT transfer, the substrates were exposed to UV/O₃ for 30 min. For the flexible device, Toyobo ltd. polyethylene terephthalate (A4300-38 µm) were used. The films were cleaned by ethanol and clean gauze.

SWNT films were transferred onto the substrates by laminating from the top.

A drop of ethanol was used to ensure firm adhesion of SWNT. Then the substrates were transferred to a N₂ filled glove box for further fabrication.

2.2 Characterisations

Characterisations are pivotal this thesis. Here, the different methods that have been used are listed:

2.2.1 Device Characterisations

2.2.1.1 Current-voltage characterisation

Current–voltage (J – V) characteristics were measured using a software-controlled source meter (Keithley 2400) under dark conditions and 1 sun AM 1.5 G simulated sunlight irradiation (100 mW cm⁻²) using a solar simulator (EMS-35AAA, Ushio Spax Inc.), which was calibrated using a silicon diode (BS-520BK, Bunkokeiki).

2.2.1.2 Incident photon to current efficiency (IPCE)

A homebuilt system was used to record the IPCE consisting of a 150 W Oriol xenon lamp, connected to a Spectral Products Cm110 monochromator to scan the Uv-vis spectrum. A Keithley 2400 digital source meter was used to record the current at each specific wavelength, and a Gentec Solo2 power monitor probed the power of the incident light.

2.2.1.3 Space-charge limited current (SCLC)

The structure of the electron-only device was Al/target layer/ETL/Al. The mobility was determined by fitting the dark current to a model of a single-carrier SCLC, which is described by the equation: $J = \frac{9}{8} \epsilon_0 \epsilon_r \mu \frac{V^2}{L^3}$, where J is the current density, μ is the mobility, ϵ_0 is the permittivity of free space, ϵ_r is the relative permittivity of the material, L is the thickness of the active layer, and V is the effective voltage. The experimental dark current density J of both P3HT:PCBM and

P3HT:mix-PCBM was measured under an applied voltage swept from 0 to -5 V.^[188,189]

2.2.1.4 Impedance measurement

Solartron SI1287 Electrochemical Interface and Solartron 1255B Frequency Response Analyser were used for the Impedance measurement.

2.2.2 Material Characterisations

2.2.2.1 UV-vis absorption

UV-vis measurements were carried out on a Shimadzu UV-1700PC spectrophotometer equipped with a photomultiplier detector, double beam optics, and D₂ and W light source. In the case of UV-Vis-NIR measurements, they were carried out on a Lambda 1050 PerkinElmer spectrophotometer equipped with a PMT, InGaAs and PbS detectors system, double beam optics, double monochromator and D₂ and W light sources.

2.2.2.2 Photoluminescence

Films and solutions were probed using an Aminco-Bowman Series 2 Luminescence spectrofluorimeter equipped with a high voltage PMT detector and continuum Xe light source.

2.2.2.3 Atomic force microscopy (AFM)

The surface composition and topography can be studied by AFM, where phase and height images can be recorded. The phase image can display differences in the surface composition whereas the height image provides information about the topography. In addition, the surface roughness can be measured. An oscillating cantilever is used to image the sample and depending on the interaction between the tip of the cantilever and the different regions of the sample, the strength of oscillations varies. The resolution limit depends on the size of the cantilever tip, which normally has a diameter of several tenths of nanometres.

AFM topography images were recorded using a Bruker Multi- mode atomic force microscope operating in tapping mode. Silicon AFM probes were used that had a nominal frequency of 70 kHz.

Surface roughness was measured either by root mean squared (r.m.s.) roughness: r.m.s. roughness is the root mean square average of the profile height deviations from the mean line, recorded within the evaluation length.

$$r. m. s. = \left[\left(\frac{1}{L} \right) \int_0^L Z(x)^2 dx \right]^{1/2} \quad r. m. s. = [(Z_1^2 + Z_2^2 + \dots + Z_N^2)/N]^{1/2}$$

or average roughness (Ra): Ra is the arithmetic average of the absolute values of the profile height deviations from the mean line, recorded within the evaluation length. Simply put, Ra is the average of a set of individual measurements of a surfaces peaks and valleys.

$$Ra = \left(\frac{1}{L} \right) \int_0^L |Z(x)| dx \quad Ra = (|Z_1| + |Z_2| + \dots + |Z_N|)/N$$

Ra and r.m.s. are both representations of surface roughness. Each value uses the same individual height measurements of the surfaces peaks and valleys, but uses the measurements in a different formula. The formulas are shown below. One can infer from examination of the formulas, that a single large peak or flaw within the microscopic surface texture will effect the r.m.s. value more than the Ra value.^[190]

2.2.2.4 Scanning electron microscopy (SEM)

In SEM, an electron beam is used to image the sample, which makes it possible to achieve a higher resolution compared to an optical microscope. The electrons are scattered by the surface of the sample and subsequently collected with different types of detectors, providing different information about the surface. A SEM micrograph can be recorded by either using backscattered or secondary electrons. To be able to analyse the sample without additional preparation the analysed sample has to be either conducting or semi-conducting, since charges induced by the electron beam have to be transported away from the area that is analysed. Non-conductive samples can be covered by a thin metal layer, allowing imaging of those samples. SEM measurement was carried out on S-4800 (Hitachi)

2.2.2.5 *Transmission electron microscopy (TEM)*

TEM image the sample with transmitted electrons, which implies that the sample has to be very thin. The incident electrons will be scattered when passing through a sample: To what extent the electrons will be scattered depends on the density of the different materials. This gives rise to darker and brighter domains in the image. In addition, electron diffraction patterns can be recorded when analysing a sample with TEM. TEM observation used a focused ion beam (FIB)-SEM-Ar triple beam system. The sample was observed using a Cs-corrected transmission electron microscope (Titan Cubed G2 60-300, FEI COMPANY) operated at 300 kV.

2.2.2.6 *X-ray photoelectron spectroscopy (XPS)*

XPS measurements were carried out on two different equipment: either JEOL XPS (JPS-9010 MC) using a Mg-K α X-ray source or PerkinElmer XPS (5400MC) using monochromatic Al K α radiation. Their energy offset were both calibrated using the C 1s peak of graphite (284.8 eV) as a reference. The XPS resolution was estimated to be ~ 1 eV

2.2.2.7 *X-ray powder diffraction (XRD)*

Out-of-plane X-ray diffraction was carried out on a Rigaku Smartlab diffractometer using Cu-K α radiation operating with a power of 9 kW (45 kV, 200 mA). The diffraction pattern of each sample was recorded between an angular 2θ of 2 and 14° at 0.5° increments, the durations of which were 3 sec.

2.2.2.8 *Photoelectron yield spectroscopy (PYS) and Kelvin probe*

Valence band information and Fermi levels were measured by Riken Keiki PYS-A AC-2 and kelvin probe S spectroscopy in air (ESA), respectively. They were calibrated by Au before the measurement.

2.2.2.9 *Raman spectroscopy*

Raman microscope with a $\times 50$ lens and 5×10^{-6} % of 200 mW power (Renishaw InVia with 532 nm excitation).

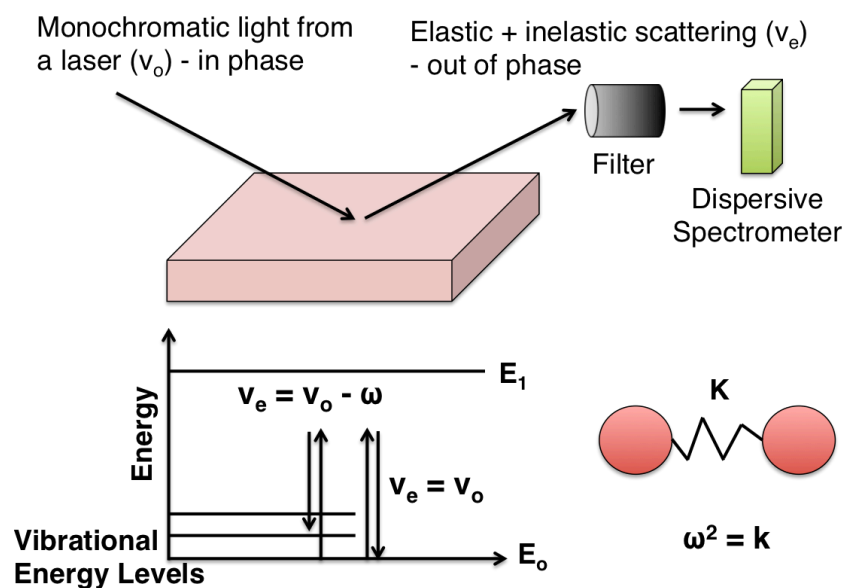


Figure 3. Illustration of Raman spectrometer.

2.2.2.10 Auger electron microscope (AES)

Elemental analysis was done by AES JEOL JAMP-9500F.

2.2.2.11 Water contact angle test

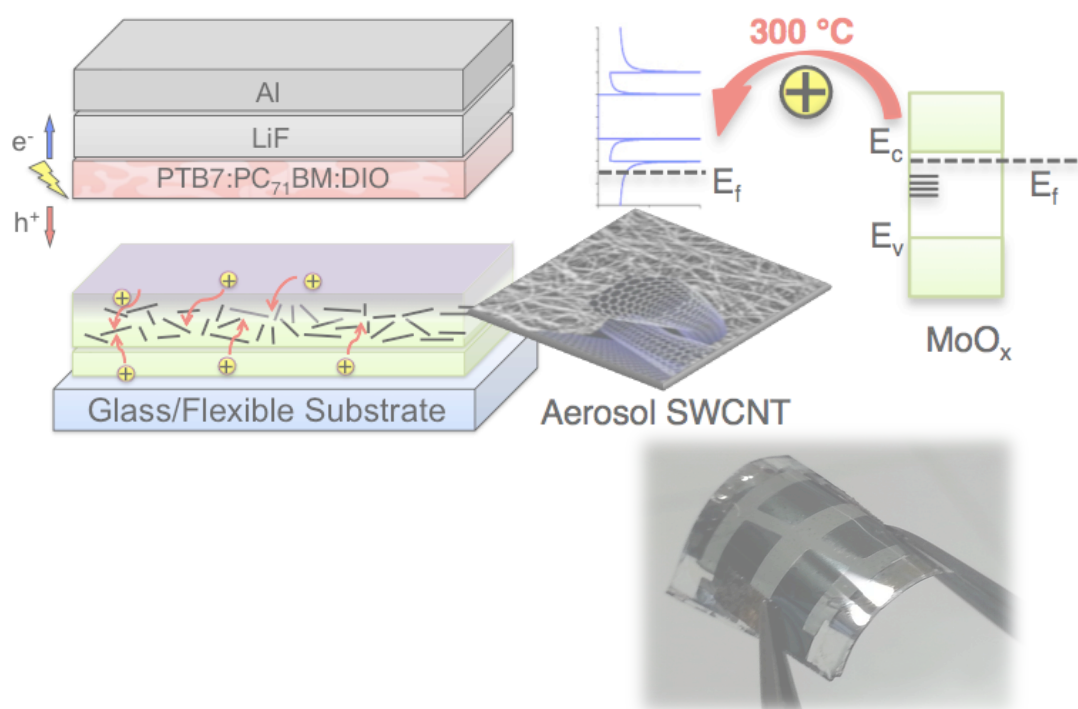
Contact angle measurements were collected on a FAMAS (Kyowa Products) where 3 μL droplets were applied to the surface and left equilibrating for 5 s before measuring the contact angle. A minimum of 10 droplets was measured for each samples.

2.2.2.12 Profilometer

Thickness of a film was measured with a Dektak 6M stylus profilometer.

2.2.2.13 Four-probe measurement

Four-probe SR4-S with SH-100 was used.



CHAPTER 3

SINGLE-WALLED CARBON NANOTUBES AS THE CONDUCTIVE LAYER IN FLEXIBLE ORGANIC SOLAR CELLS

3.1 Summary

OSCs have been regarded as a promising electrical energy source. Transparent and conductive carbon nanotube film offers an alternative to commonly used ITO in photovoltaics with superior flexibility. This chapter reports carbon nanotube-based indium-free OSCs and their flexible application. Direct- and dry-deposited CNT film doped with MoO_x functioned as an electron-blocking transparent electrode, and its performance was enhanced further by overcoating with PEDOT:PSS. The SWCNT OSC in this work showed a PCE of 6.04%. This value is 83% of the leading ITO-based device performance (7.48%). Flexible application showed 3.91% efficiency and was capable of withstanding a severe cyclic flex test.

3.2 Introduction

The objective of this chapter is to develop the best methodology for ITO-free SWCNT-utilised efficient OSC fabrication. First, a CNT electrode was prepared by direct and dry deposition of SWCNTs grown by the floating catalyst i.e., aerosol chemical vapour deposition technique.^[187] Compared with other solution-based processes,^[179,180] my process used no surfactant and induced less defects. Moreover, electrical performance of the films produced by this method was higher than that of other CNT films including flexible ITO. Second, MoO₃ doping, which was originally proposed by Bao et al.,^[191] was employed and optimised for other reported dopants that are unstable in air, chemicals, thermal stress, and humidity.^[192] Third, for the photoactive layer, the low band gap polymer, PTB7^[193] was used for its high performance among organic photoactive materials. In addition, PTB7 does not require thermal annealing. This enabled us to use flexible substrates.^[194] The present SWCNT OSCs showed a PCE of 6.04% with the PTB7:PC₇₁BM photoactive layer. In addition, flexible OSCs on polyimide (PI) and polyethylene terephthalate (PET) films gave PCEs of 3.43% and 3.91%, respectively. I anticipate that the methodology presented here will help pave the way toward carbon-based flexible solar cells.

3.3 Experimental Procedures

3.3.1 Device Fabrications

Please refer to ‘2.1.1.1 Organic solar cell normal device architecture’, 2.1.1.3 P3HT:mix-PCBM solution preparation’, 2.1.1.4 PTB7:PC₇₁BM solution preparation’, and ‘2.1.3 SWNT Preparations’.

MoO₃, functioning as both an HTL and dopant, was deposited under vacuum via a thermal evaporator. 15 nm MoO₃ was deposited with the average rate of 0.2 Å s⁻¹. It was annealed at 300 °C for 3 h in N₂. PEDOT:PSS dispersed in water (Clevios P VP, Heraeus Precious Metals GmbH & Co.) was spin-coated on top of the MoO_x to assist the electron-blocking ability by and filling up the pin holes formed from high temperature annealing.

For the cathodes, LiF (0.7 nm) followed by aluminum (100 nm) was deposited by vacuum thermal evaporation. Other metals (100 nm) were also deposited in this way at the rate of 0.2 \AA s^{-1} .

For the flexible devices, Low Colour Polyimide film – 25 μm thickness from Industrial Summit Technology (IST) Ltd. and Toyobo Ltd. polyethylene terephthalate (A4300-38 μm) were used. The films were cleaned by ethanol and clean gauze.

3.3.2 Characterisations

Please refer to ‘2.2.1.1 Current-voltage characterisation’, ‘2.2.2.1 UV-vis absorption’, ‘2.2.2.3 Atomic force microscopy (AFM)’, ‘2.2.2.4 Scanning electron microscopy (SEM)’, ‘2.2.2.8 Photoelectron yield spectroscopy (PYS) and Kevin probe’, ‘2.2.2.8 Photoelectron yield spectroscopy (PYS) and Kevin probe’, ‘2.2.2.9 Raman spectroscopy’, and ‘2.2.2.13 Four-probe measurement’.

For the bending test of flexible devices, J – V measurements were recorded after 10 compressive flexing cycles (radius of curvature: 5 mm).

3.4 Results and Discussion

I first investigated thickness dependence of the SWCNT films on photovoltaic property of SWCNT-OSCs by varying the deposition time of the SWCNT production. I obtained three thicknesses that gave 65%, 80%, and 90% transparency at 550 nm.^[195] AFM images showed that all the SWCNT films have similar root-mean-square roughness of 8 to 10 nm (Figure 1).

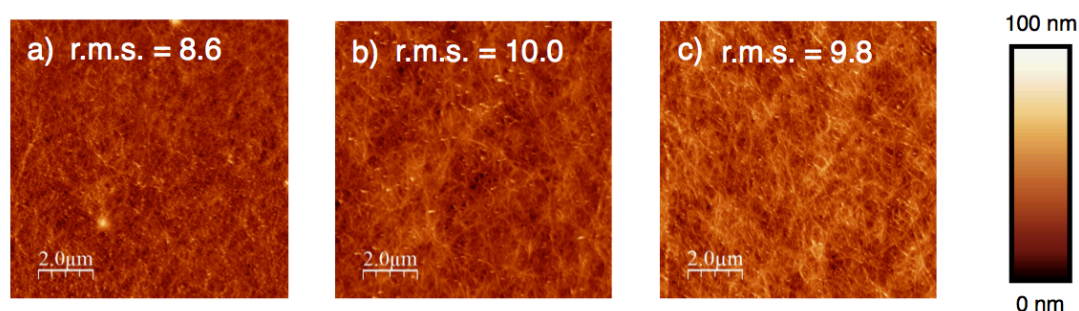


Figure 1. AFM images and r.m.s. roughness values of SWCNTs with different thicknesses a) 90% transparent SWCNT, b) 80% transparent SWCNT, c) 65% transparent SWCNT

For the device fabrication, I used P3HT as a donor because it is a benchmark material in the field of OSCs, and most CNT OSCs reported to date have also used this material.^[192] Therefore, valid comparisons could be made. Using this material, OSCs were fabricated on SWCNT films with different thicknesses (transparency). Fast growth method^[196] was adopted for high performance without solvent annealing. MoO₃ was used here as an HTL, and it was not subjected to thermal annealing. Three devices with various thicknesses of SWCNT films showed similar PCEs of under 1% (Table 1). The similarity of the PCEs is due to the trade-off between J_{SC} and FF, which are closely related to the transparency and the conductivity, respectively. The overall performances were poor and doping was called for.

MoO₃ was subjected to thermal annealing on SWCNT for the doping. In previous work, bottom MoO₃ under spray-coated CNTs was thermally annealed at 450–500 °C for more than 3 h in Ar.^[191] However, in this work, I annealed MoO₃ on top of the aerosol SWCNT films at 300 °C for 3 h in N₂, considering the use of flexible PI substrates, which have a glass transition temperature (T_g) of 320 °C. Utilising this thermally driven hole doping from MoO₃ to SWCNT, the device gave a PCE of 1.91%, which is nearly twice the improvement from the non-annealed device (Figure 2a; Table 2: devices A and B).

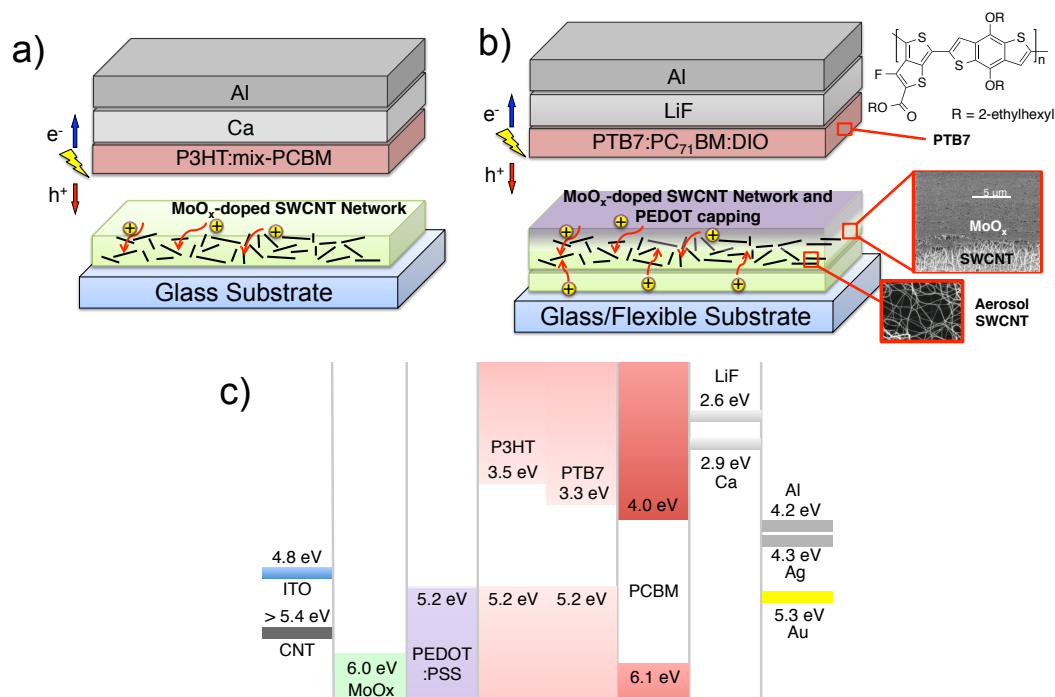


Figure 2. SWCNT OSC configurations of (a) P3HT-based cells (glass/ SWCNT /MoO_x/ P3HT:mix-PCBM/LiF/Al) and (b) the most optimised device that gave high efficiency (glass or flexible substrate/ MoO_x/SWCNT/MoO_x/PEDOT:PSS/PTB7:PC₇₁BM/LiF/Al). (c) Energy band alignment diagram of SWCNT OSCs.

Corresponding $J-V$ curves are shown in Figure 3. Both increase in J_{SC} and decrease in R_s were observed, and these are indications of improved transmittance and conductivity of SWCNTs. High R_{SH} even after the thermal annealing indicates that thermally annealed MoO_3 can still function as an HTL.

Table 1. Aerosol SWCNTs with different transparencies with non-annealed MoO_3 have been fabricated in a P3HT:PCBM system to compare its influence on the overall efficiency as OSC electrodes without doping effect.

Anode	V_{OC} (V)	J_{SC} (mA/cm ²)	FF	R_s (Ω cm ²)	R_{SH} (Ω cm ²)	PCE _{best} (%)
ITO/ MoO_3	0.60	9.42	0.50	23.5	1.56×10^4	2.83
90%-SWNT/ MoO_3	0.59	4.74	0.33	1480	2.23×10^3	0.92
80%-SWNT/ MoO_3	0.54	4.54	0.39	201	7.66×10^3	0.95
65%-SWNT/ MoO_3	0.52	3.30	0.54	198	2.42×10^4	0.93

Table 2. Photovoltaic performance parameter table for the structural optimisation of P3HT system OSCs with various layers.

Device	Anode	V_{oc} (V)	J_{sc} (mAcm ⁻²)	FF	R_s (Ω cm ²)	R_{SH} (Ω cm ²)	PCE _{best} (%)
A	90%-SWCNT/ MoO_3	0.59	4.74	0.33	1480	2.23×10^3	0.92
B	*90%-SWCNT/* MoO_x	0.60	7.47	0.43	239	2.05×10^4	1.91
C	* MoO_x /*90%-SWCNT/ MoO_3	0.45	0.36	0.38	310	7.82×10^4	0.06
D	*90%-SWCNT/* MoO_x / MoO_3	0.55	3.10	0.42	301	1.46×10^4	0.72
E	* MoO_x /*90%-SWCNT/PEDOT:PSS	0.58	8.44	0.48	163	3.43×10^4	2.35
F	*90%-SWCNT/* MoO_x /PEDOT:PSS	0.59	8.99	0.44	128	1.70×10^4	2.34
G	* MoO_x /*90%-SWCNT/* MoO_x /PEDOT:PSS	0.59	8.84	0.46	116	7.05×10^3	2.43

^a MoO_3 and MoO_x represent as-deposited MoO_3 and thermal annealed one for doping, respectively. 90%-, 80%-, and 65%-SWCNT denotes 90%, 80%, and 65% transparent SWCNT films.

I further investigated the doping effect. Doping was visually confirmed by colour change of MoO_3 from transparent green to deep blue (Figure 4). It is caused by oxygen deficiency, which induces electron traps that increase absorbance in the deep-blue wavelengths region.^[197] MoO_3 was changed to MoO_x , where x is less than 3. UV-vis spectra show MoO_3 thermally doped SWCNT films having higher transmittance compared with the pristine SWCNT films (Figure 5a and 5b). Furthermore, thin 90%- and 80%-SWCNT films displayed an absorption curve with

higher transparency at 400–500 nm but less transparency at long-wavelength region due to the absorption by MoO_x (Figures 4 and 5b). Thus, I hypothesise that P3HT, which absorbs shorter wavelengths of light, is compatible with the 90% transparent SWCNT electrode, while PTB7, which absorbs longer wavelengths of light, is more compatible with the 65% transparent SWCNT electrode.

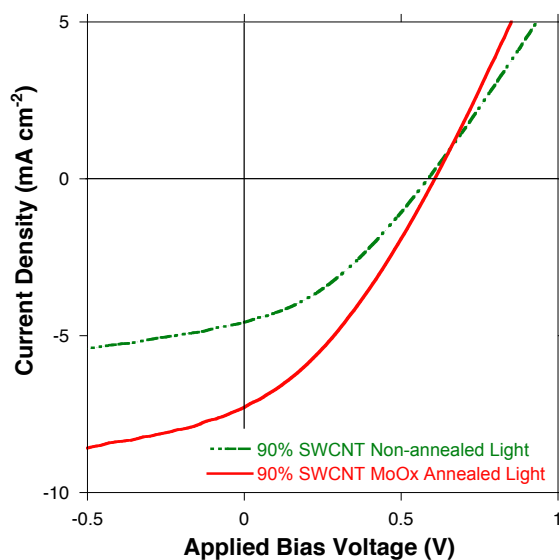


Figure 3. *J-V* curves of the non-annealed device A (dashed green line) and the MoO_x annealed device B (solid red line) under 1 sun AM1.5G.

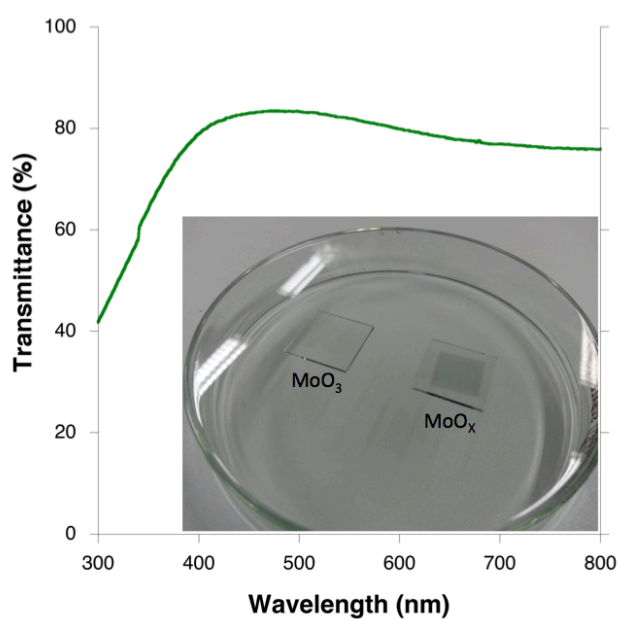


Figure 4. UV-Vis spectrum of an annealed MoO_x film on glass. Substrate spectrum has been subtracted from the MoO_x /glass substrate spectrum.

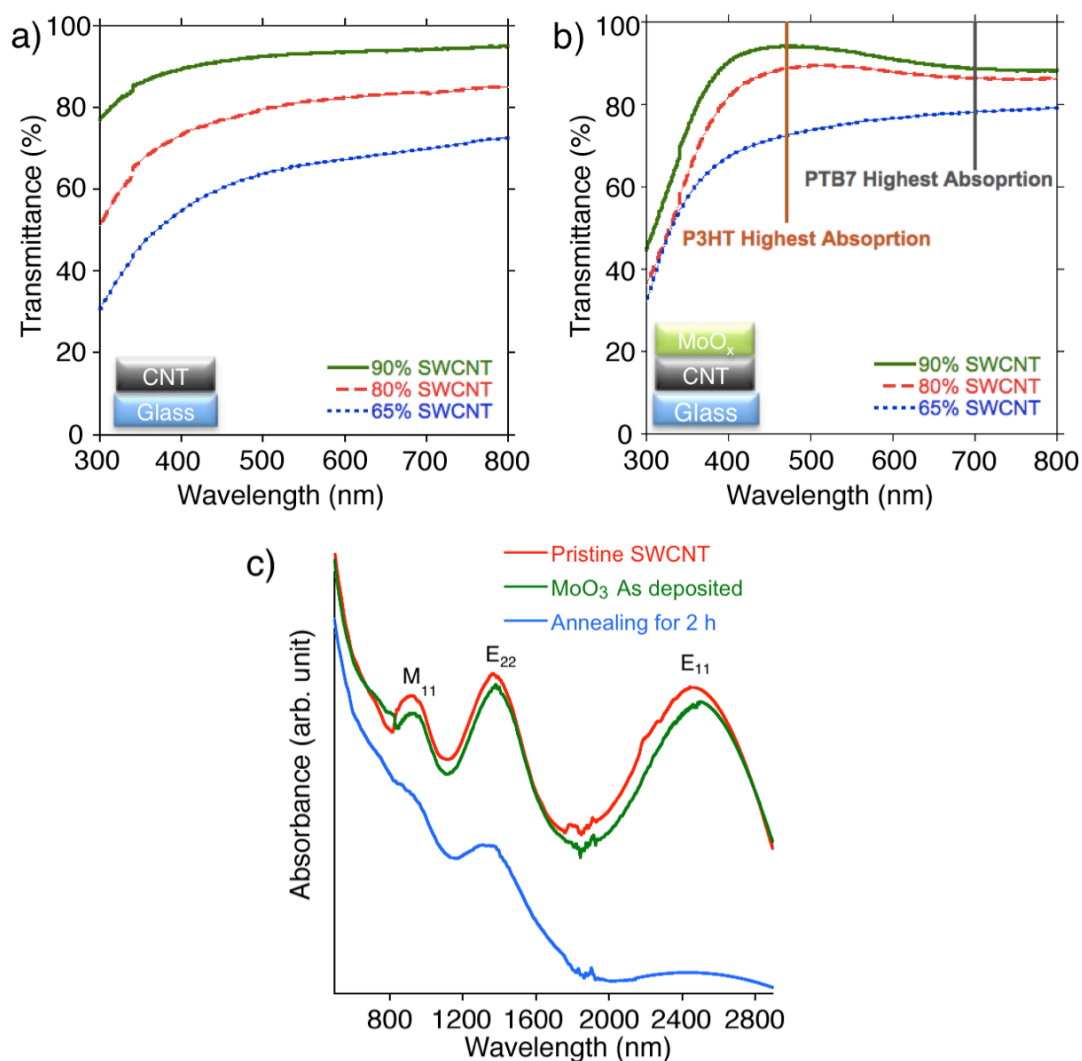


Figure 5. Optical property of SWCNT films with different thicknesses. (a) UV–vis transmittance for pristine SWCNTs films. (b) UV–vis transmittance for SWCNT films after depositing MoO₃ and thermally annealing at 300 °C for 2 h in N₂ with indications of the highest absorption wavelength of P3HT and PTB7. (c) Absorbance in infrared region for SWCNT film pristine (red), with MoO₃ on top (green), and after annealing for 2 h (blue).

Doping effect was further confirmed by absorption spectra of SWCNT films on quartz substrates (Figure 5c). Clear peaks for transitions of E₁₁, E₂₂, and M₁₁ in SWCNT indicate the high quality of aerosol CVD synthesis. Those peaks were slightly suppressed when MoO₃ was deposited on SWCNT, and almost completely suppressed when it is followed by 2 h of thermal annealing as an indication of successful doping. In addition, decrease in resistivity of the SWCNT films after thermal doping provided further evidence of doping (Table 3).

Table 3. Four-probe measurement sheet resistance (R_{Sheet}) of the SWCNTs with different transparencies on MoO₃ before and after the thermal doping. MoO₃ was measured as a control.

	MoO ₃ only	R_{Sheet} of 65%- SWNT on MoO ₃	R_{Sheet} of 80%- SWNT on MoO ₃	R_{Sheet} of 90%- SWNT on MoO ₃
Pristine	~1 MΩ/sq.	83.89 Ω/sq.	205.08 Ω/sq.	326.05 Ω/sq.
After thermal annealing	~1 MΩ/sq.	28.49 Ω/sq.	73.97 Ω/sq.	101.55 Ω/sq.

Work functions were measured by photoelectron yield spectroscopy. I found that the thermal doping narrowed the gap between the Fermi levels of SWCNT and MoO₃. Pristine SWCNT films on glass exhibited a work function of 4.86 eV. After thermal annealing with MoO₃, its work function increased to 5.4 eV (Figure 2c). The work function of MoO₃ is reported to be 5.4 eV. The PCE of doped SWCNT-based device was still lower than the ITO-based device. Thus, I analysed the morphology of MoO_x on SWCNT. The SEM images indicated that there are pinholes created on MoO_x film after the annealing (Figure 6d and 6e); the AFM r.m.s. roughness value of 9.7 increased to 23.1 (Figure 6a and 6b). To find a solution to this, I tested various configurations involving additional MoO₃ and PEDOT:PSS. Use of extra MoO₃ on MoO_x decreased J_{SC} (Table 2: devices C and D), which is attributable to a mismatch in energy levels, whereas when PEDOT:PSS was overcoated on MoO_x, both V_{OC} and J_{SC} were enhanced (Table 2: device E, Figure 7). I ascribe this to the hydrophilic nature of hydroxyl groups on MoO_x and the solution coating method, which allows PEDOT:PSS to fill up the pinholes more effectively. Besides, the acidic PEDOT:PSS can also function as a weak additional dopant (Figure 6c and 6f).^[198] With the optimised configuration, a PCE of 2.34% was achieved (Table 2: device G, Figure 2b). Moreover, applying sandwich doping of MoO_x above and below SWCNT film enhanced the performance even further, giving a PCE of 2.43% (Table 4). This value is 86% of the corresponding ITO-based OSC efficiency (2.83%; Table 4; Figure 8a).

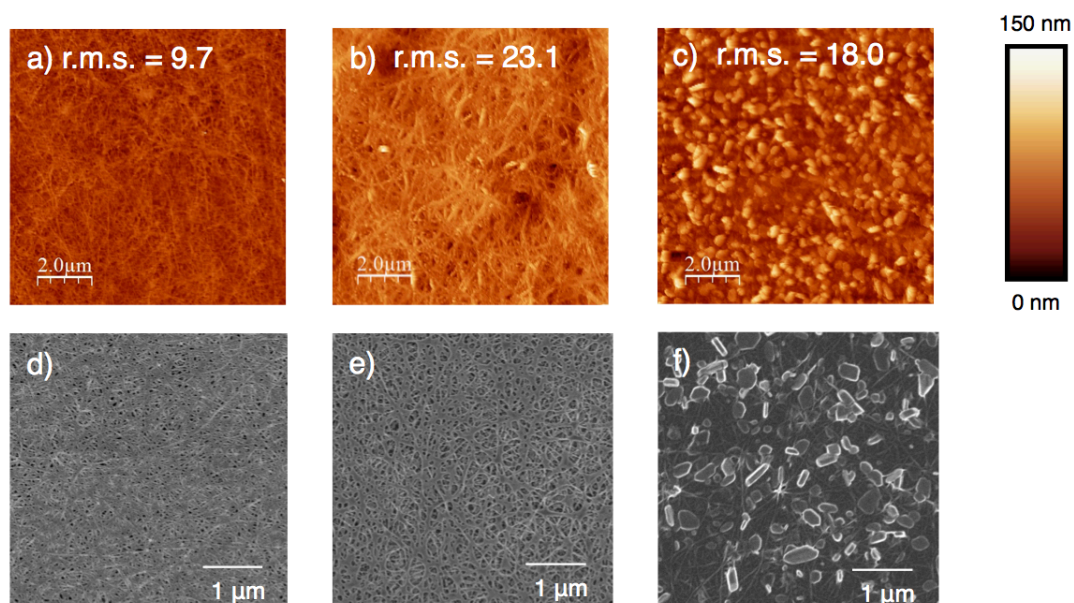


Figure 6. AFM images with r.m.s. roughness values and SEM images of SWCNTs with a) and d) MoO_3 on SWCNT, b) and e) thermally annealed MoO_x on SWCNT, c) and f) PEDOT:PSS soaked thermally annealed MoO_x on SWCNT.

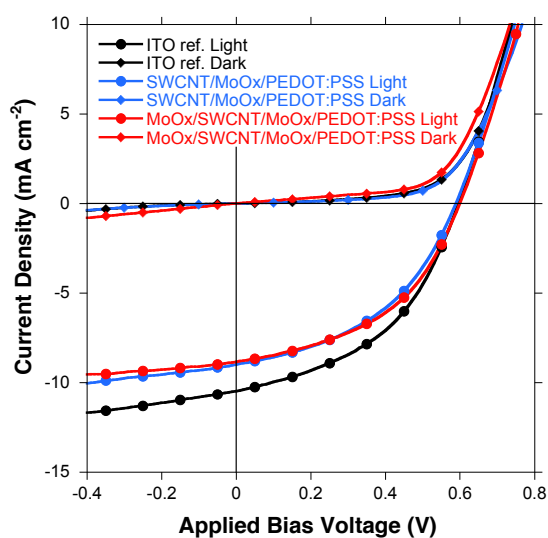


Figure 7. J - V curves of the ITO reference device (black lines) and the device J (blue lines) and device K (red lines) under 1 sun AM1.5G (circle) and dark (diamond) each.

Table 4. Photovoltaic performance for the optimised SWCNT-MoO_x OSCs.^a

Substrate	Anode	Donor	V _{oc} (V)	J _{sc} (mAcm ⁻²)	FF	R _s (Ωcm ²)	R _{sh} (Ωcm ²)	PCE _{best} (%)
Glass	ITO/MoO ₃	P3HT	0.60	9.42	0.50	23.5	1.56 x 10 ⁴	2.83
Glass	MoO _x /90%-SWCNT/MoO ₃ /PEDOT:PSS		0.59	8.84	0.46	116	7.05 x 10 ³	2.43
Glass	ITO/MoO ₃		0.74	15.5	0.64	31.1	1.18 x 10 ⁷	7.31
Glass	MoO _x /65%-SWCNT/MoO ₃ /PEDOT:PSS	PTB7	0.72	13.7	0.61	51.6	1.22 x 10 ⁴	6.04
PI	MoO _x /65%-SWCNT/MoO ₃ /PEDOT:PSS	PTB7	0.69	11.3	0.44	454	1.15 x 10 ⁵	3.43
PI	After 10-time cyclic flex test		0.70	11.1	0.27	588	3.85 x 10 ⁴	2.10
Glass	65%-SWCNT/MoO ₃ /PEDOT:PSS		0.70	12.7	0.58	94.5	4.00 x 10 ⁴	5.27
PET	65%-SWCNT/MoO ₃ /PEDOT:PSS	PTB7	0.69	12.6	0.45	160	2.06 x 10 ³	3.91
PET	After 10-time cyclic flex test		0.69	12.3	0.45	222	2.83 x 10 ³	3.82

^a MoO₃ and MoO_x represent as-deposited MoO₃ and thermal annealed, respectively. 90%-, 80%-, and 65%-SWCNT denotes 90%, 80%, and 65% transparent SWCNT films

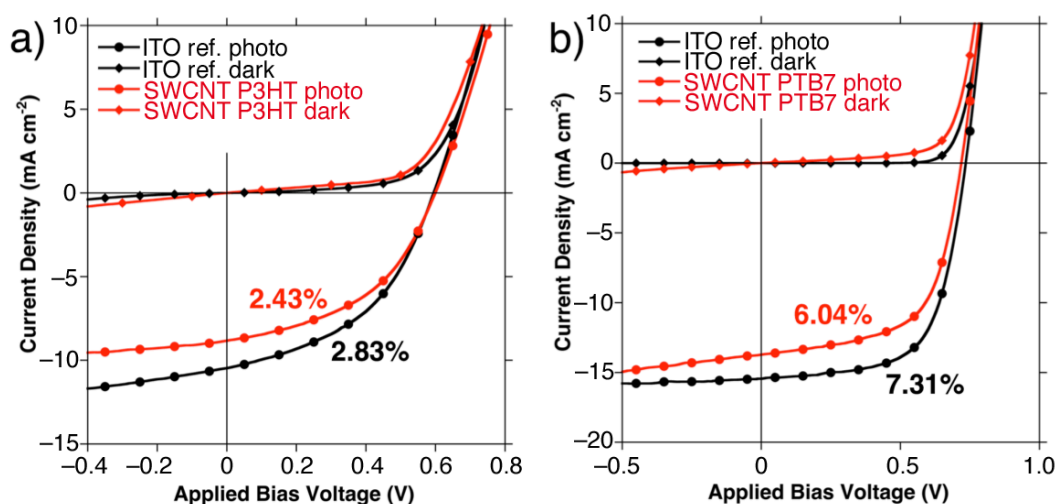


Figure 8. J - V curves of the two optimised SWCNT OSCs (red lines) in comparison with reference ITO-based OSCs under light and dark conditions. (a) P3HT:mix-PBM-based devices; (b) PTB7:PC₇₁BM-based devices.

Another unique phenomenon of SWCNT-based OSCs is that it was not compatible with Ca/Al cathode unlike its ITO counterpart (Table 5).^[199] This is because Ca causes non-spontaneous electron extraction as Eo et al. have demonstrated.^[200] Although LiF possesses the work function of 2.6 eV, which seems not compatible with the energy levels of Al and PCBM, it is extremely thin (0.7 nm). Thus, it can act as a protective layer without interfering energetically.

Table 5. Table where various cathodes are applied in a structure SWCNT/MoO_x annealed/P3HT:PCBM/cathode.^[201]

Cathode	Work function (-eV)	V_{oc} (V)	J_{sc} (mA/cm ²)	FF	PCE (%)
Ca/Al	2.9	0.61	7.28	0.33	1.47
Al	4.2	0.35	4.55	0.41	0.65
Ag	4.3	0.50	3.97	0.37	0.74
Au	5.3	0.46	1.52	0.49	0.35
LiF/Al	2.6	0.60	7.47	0.43	1.91

Next, I tested the low band gap polymer PTB7 for the first time in CNT OSCs. The OSC device with the 65% transparent SWCNT film gave a PCE of 6.04%, which is a record-high result (Figures 2b and 3b; Table 4; see also Figures 9 and 10). This is 83% of the ITO-based device efficiency (7.48%; Table 4). This result reveals that the

low band gap polymer system is also compatible with existing SWCNT-based electrodes.

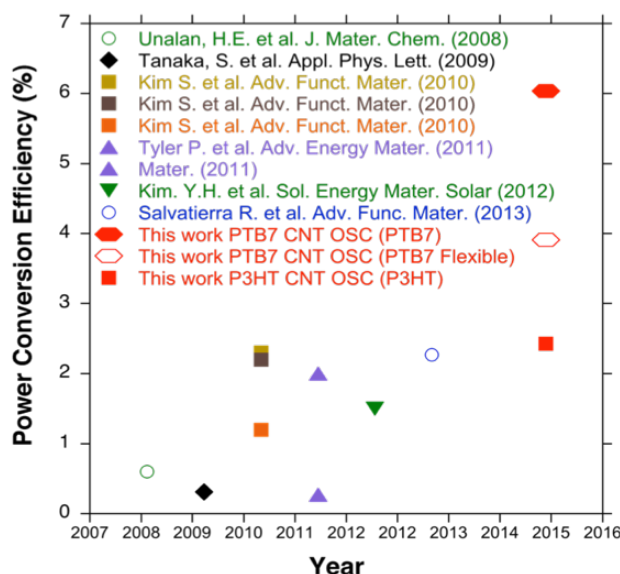


Figure 9. Reported PCEs of CNT OSCs on glass (closed symbols) and on flexible substrate (open symbols).

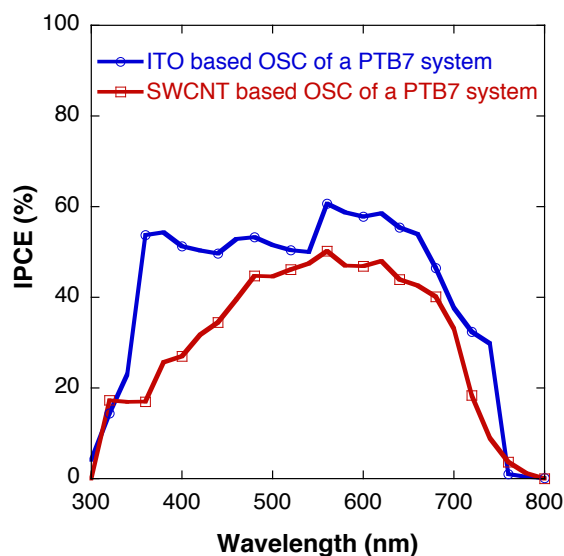


Figure 10. IPCE of an ITO-based OSC and a SWCNT-based OSC using PTB7 system.

Finally, flexible application was accomplished using both PI and PET as substrates. PI's high T_g enabled thermal annealing of MoO_3 , but PET with T_g of 80°C could not be annealed. Initially, the flexible OSCs gave PCEs of 3.78% (PI) and 3.91% (PET) (Table 4). I ascribe the low performance in both the flexible devices to the damage on MoO_3 during fabrication by looking at the decrease in R_s . Additionally, the PI device's low J_{sc} was limited by the intrinsically low transparency of the film

(Figure 11). The PET-based device to which thermal annealing was not applied gave a higher PCE than that of the PI-based device. After subjecting the devices to 10 flexing cycles (radius of curvature: 5 mm), the PET-based flexible OSC retained its performance, while the PI-based flexible OSC significantly decreased the performance (Figure 12; Table 4). This points toward the fact that PI-based device is strongly affected by the high temperature annealing.

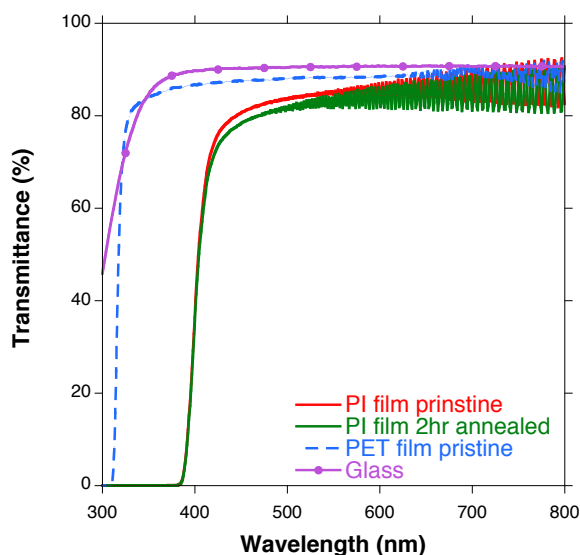


Figure 11. Transmittance data of PI, thermally annealed PI, PET, and bare glass.

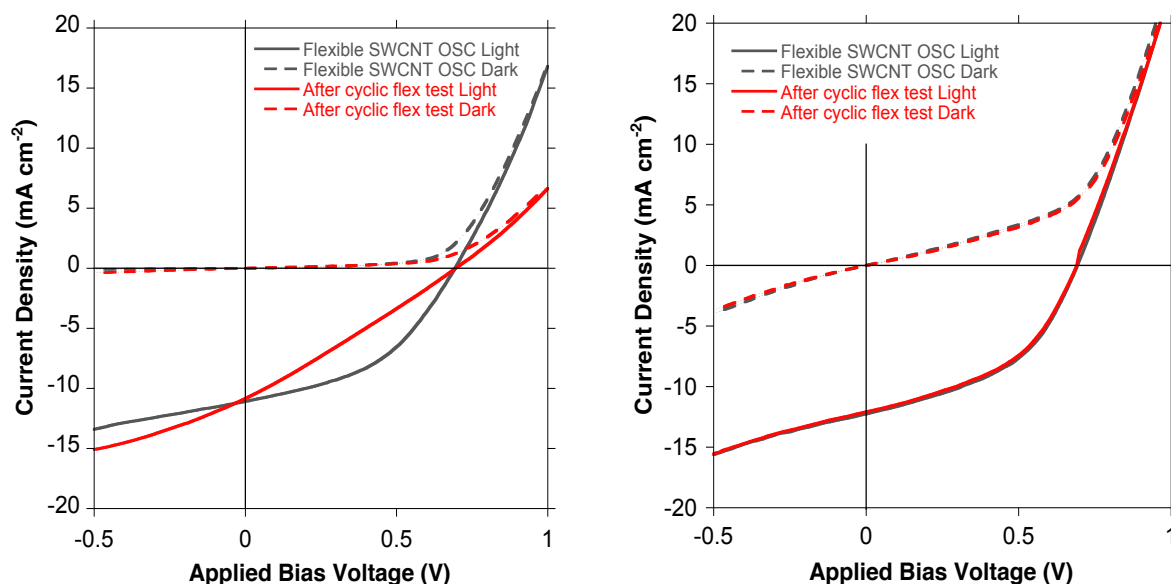


Figure 12 a). *J-V* curves of flexible OSC on PI before and after the cyclic flex test (left) and on PET before and after the cyclic flex test (right).

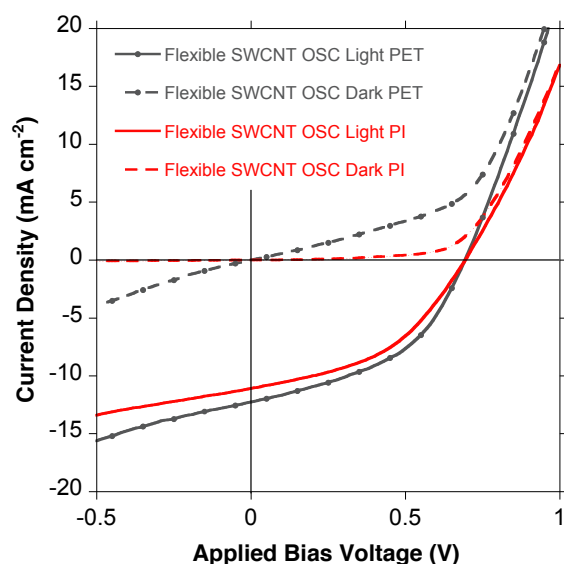
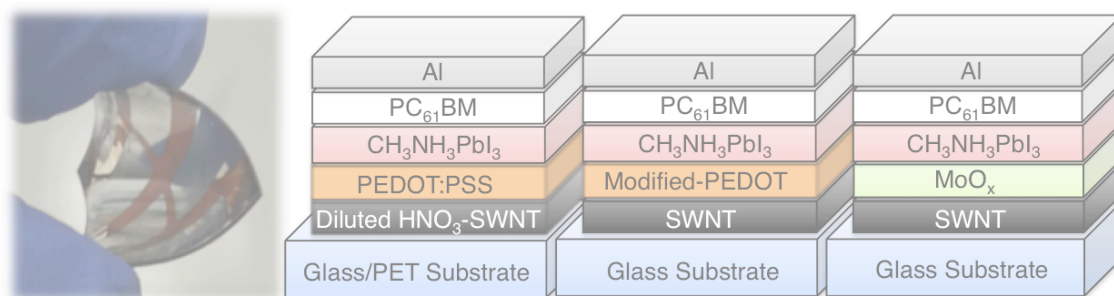


Figure 12 b). *J-V* curve comparisons of the flexible OSCs on both PI and PET.

3.5 Conclusion

In conclusion, this work showed a way for efficient and flexible CNT-based OSCs with application of direct and dry deposited SWCNT film in OSCs and demonstrated the dual functionality of thermally annealed MoO_x on SWCNTs as both transparent electrode and HTL. Thus, the MoO_x/SWCNT worked as an electron-blocking transparent electrode. The PTB7 system was applied in CNT OSCs and produced a high PCE as well as successfully exhibiting flexible application. Taken together, this findings demonstrate that ITO-free flexible SWCNT OSCs can be fabricated with high efficiency through a remarkably facile and stable process. I anticipate that these results will be useful in the further development of flexible carbon-based solar cells as well as other related organic electronics.



CHAPTER 4

SINGLE-WALLED CARBON NANOTUBES AS THE CONDUCTIVE LAYER IN FLEXIBLE PLANAR HETEROJUNCTION PEROVSKITE SOLAR CELLS

4.1 Summary

In this chapter, I fabricated indium-free PSCs using direct- and dry-transferred aerosol SWNTs. I investigated diverse methodologies to solve SWNTs' hydrophobicity and doping issues in PSC devices. These include changing wettability of PEDOT:PSS, MoO₃ thermal doping, and HNO₃(aq) doping with various dilutions from 15 to 70 v/v% to minimise its instability and toxic nature. I discovered that IPA modified PEDOT:PSS works better than surfactant modified PEDOT:PSS as an HTL on SWNTs in PSCs due to superior wettability, whereas MoO₃ was not compatible owing to energy level mismatching. Diluted HNO₃ (35 v/v%)-doped SWNT-based device produced the highest PCE of 6.32% amongst SWNT-based PSCs, which is 70% of an ITO-based device (9.05%). Its flexible application showed a PCE of 5.38% on PET substrate.

4.2 Introduction

So far, SWNT electrode for organic SCs have been reported in a great amount^[164,192,202-212] and the PCE has been reported to reach as high as 83% to that of ITO counterpart.^[183] Yet, analogue applications in PSCs have not been reported to date. SWNT electrode application was limited only to a metal electrode replacement.^[213] Besides, other flexible PSCs reported utilise flexible ITO, which suffers from many shortcomings such as low conductivity and crack-damage when bent too much.^[153]

Here, I report SWNT-based indium-free PSCs and flexible application along with investigations of different charge selective layers and doping methods that overcome the issues of doping and hydrophobicity of SWNTs. A planar heterojunction structure was used in this study, and it is comprised of PEDOT:PSS as an EBL, followed by a lead perovskite layer ($\text{CH}_3\text{NH}_3\text{PbI}_3$), [6,6]- phenyl C61-butyric acid methyl ester (PC_{61}BM), and an aluminum metal electrode. This was coined by Snaith as “inverted cell architecture”.^[149] Although mesoporous (mp) TiO_2 -based PSCs exhibit a higher PCE, the formation of mp- TiO_2 layer requires a thermal process over 450 °C. Because flexible substrates are vulnerable to high temperature, the inverted planar heterojunction PSC, which requires annealing temperatures of lower than 100 °C, was regarded more promising for this flexible applications.^[214-216] Furthermore, this structure demonstrates better stability under ultraviolet light^[217] and almost no hysteresis with sweep directions in measurement because of the exclusion of mp- TiO_2 .^[218,219] One-step method, which is widely established, was employed in this work as I focused on achieving reliable investigation prior to a record-breaking PCE.^[220]

4.3 Experimental Procedures

4.3.1 Device Fabrications

Please refer to ‘2.1.2 Perovskite solar cell fabrications’ and ‘2.1.3 SWNT Preparations’

For MoO_x thermal doping, please refer to ‘3.3.1 Device Fabrications’. For HNO₃ doping, HNO₃(aq) solution was dropped on a SWNT film followed by drying at 80 °C for 10 min.

Surfactant-PEDOT:PSS was produced by adding 0.5 wt% of polyoxyethylene(6) tridecyl ether (Sigma Aldrich Chemical Co., Inc.) in PEDOT:PSS dispersion in water. IPA-PEDOT:PSS was produced by diluting PEDOT:PSS in IPA at 3:1(v/v) ratio. Modified PEDOT:PSS was spin-coated at the same condition as the normal PEDOT:PSS.

4.3.2 Characterisations

Please refer to ‘2.2.1.1 Current-voltage characterisation’, ‘2.2.1.4 Impedance measurement’, ‘2.2.2.1 UV-vis absorption’, ‘2.2.2.3 Atomic force microscopy (AFM)’, ‘2.2.2.4 Scanning electron microscopy (SEM)’, ‘2.2.2.8 Photoelectron yield spectroscopy (PYS) and Kelvin probe’, ‘2.2.2.9 Raman spectroscopy’ and ‘2.2.2.13 Four-probe measurement’. For the flex cyclic test, please refer to Chapter 3.

4.4 Results and Discussion

One of the challenges for SWNT electrode-based solar cells has been doping the carbon nanotubes while having a desirable EBL function. PEDOT:PSS with acidic nature functions as both the EBL and dopant.^[198] However, hydrophilic PEDOT:PSS cannot be applied directly onto hydrophobic SWNTs. As a solution to this problem, I selected two approaches: diluting PEDOT:PSS in IPA solvent by 1:3 (v/v) ratio^[162] or adding a small amount (0.5 wt %) of surfactant, polyoxyethylene(6) tridecyl ether to the PEDOT:PSS solution.^[221] These two are already well-established methods in the application of graphene and inverted organic SCs, respectively. These modifications change PEDOT:PSS property from hydrophilic to hydrophobic. In the case of planar graphene sheet, modified PEDOT:PSS cannot form a complete coverage, and deposition of additional MoO₃ is mandatory.^[222] But, in the case of carbon nanotube, both IPA-modified PEDOT:PSS (IPA-PEDOT:PSS) and surfactant-modified PEDOT:PSS (surfactant-PEDOT:PSS) thoroughly overcoated the individual tubes as

evidenced by SEM images (Figure 1b and c). Knowing that the SWNT films do not have shunt pathways, planar heterojunction PSCs were fabricated without an additional MoO₃ layer. During the fabrication, specifically when spin-coating the perovskite layer, it was interesting to observe formation of discontinuous large crystals in the perovskite layer on the surfactant-PEDOT:PSS-coated SWNTs (Figure 2). The cross-sectional SEM revealed a bad uniformity of the perovskite layer. Those unwanted crystals could be avoided by shortening the CB rinsing time from the usual 10 to 6 s. From AFM images and their Ra values, it is visible that the surfactant-PEDOT:PSS-coated SWNTs had rougher morphology than the IPA-PEDOT:PSS-coated SWNTs (Figure 1f and g). The perovskite layers formed on top of those films showed even bigger difference (Figure 1j and k). Both AFM images of the modified-PEDOT:PSS-based perovskite showed bigger crystal size and rougher surface than the reference perovskite layer (Figure 1j, k, and i).

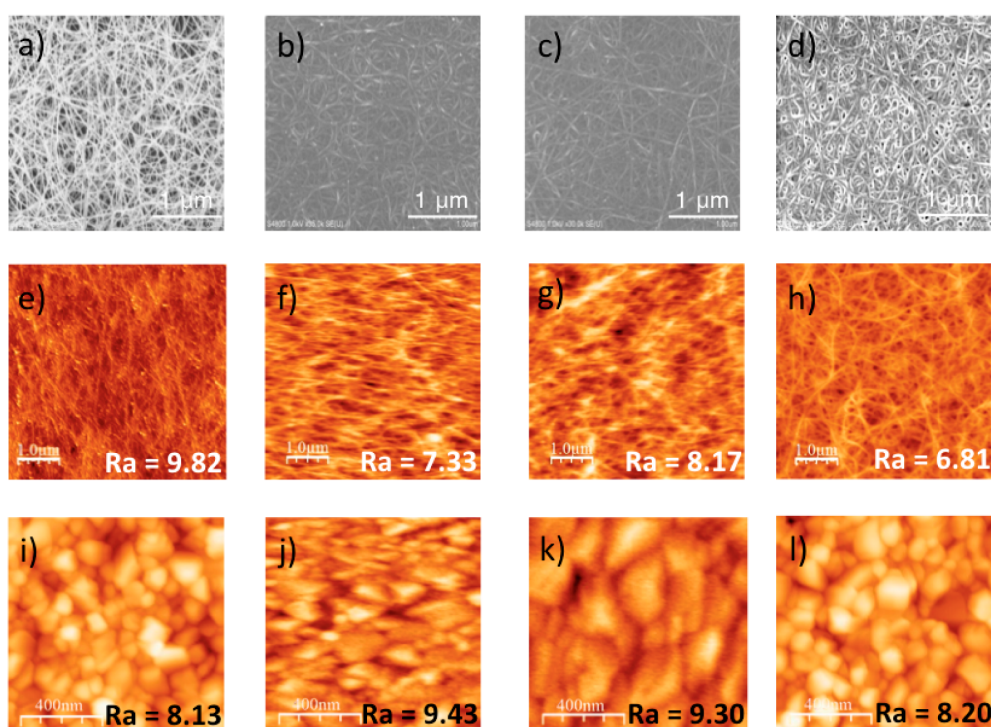


Figure 1. SEM images of (a) SWNTs, (b) IPA-PEDOT:PSS on SWNTs, (c) surfactant-PEDOT:PSS on SWNTs, (d) PEDOT:PSS on HNO₃-doped SWNTs; AFM images and r.m.s. roughness values of (e) SWNTs, (f) IPA-PEDOT:PSS on SWNTs, (g) surfactant-PEDOT:PSS on SWNTs, (h) PEDOT:PSS on HNO₃-doped SWNTs, (i) perovskite layer on PEDOT:PSS on ITO, (j) perovskite layer on IPA-PEDOT:PSS on SWNTs, (k) perovskite layer on Surfactant-PEDOT:PSS on SWNTs, and (l) perovskite layer on PEDOT:PSS on HNO₃-doped SWNTs.

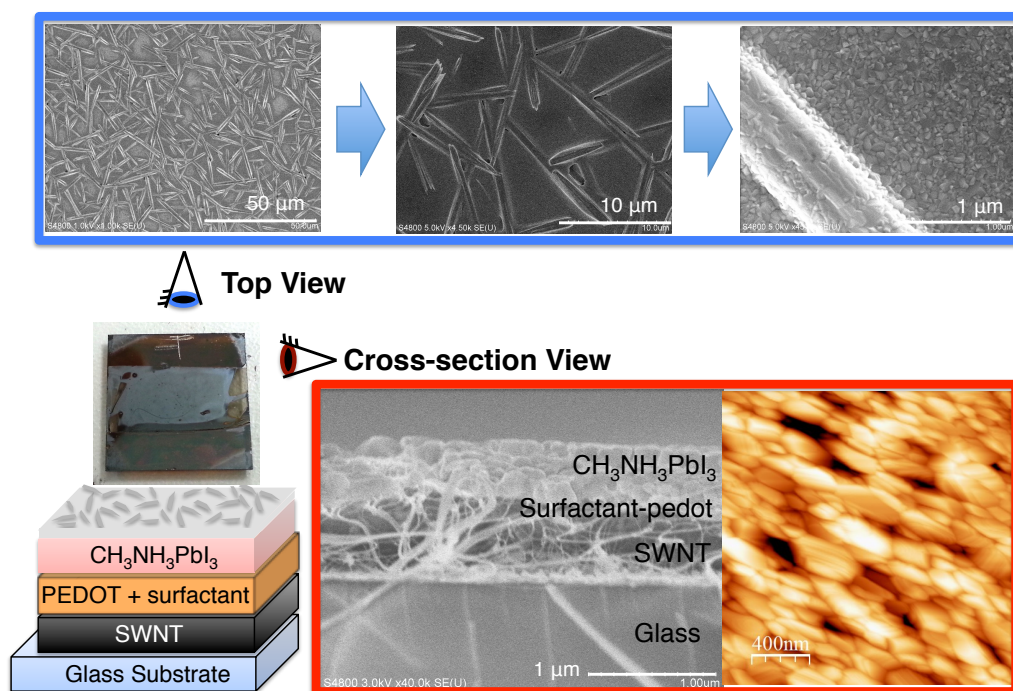


Figure 2. Top view and cross-sectional view of the Perovskite film on top of the surfactant-PEDOT:PSS-coated SWNTs without shortening the CB rinsing time. The top view SEM images show magnification identifying the large aggregated crystals forming while the cross-sectional SEM shows a dissection of the aggregated perovskite layer.

Table 1. Photovoltaic performance table for SWNT-based PSCs using modified PEDOT:PSS and a range of SWNTs with different HNO₃ concentrations^a

No	electrode	EBL	V_{OC} (V)	J_{SC} (mA cm ⁻²)	FF	R_S (Ω)	R_{SH} (Ω)	PCE_{AVR} (%)	PCE_{REC} (%)
1	ITO	PEDOT:PSS	0.83	16.3	0.64	25.8	5.2×10^5	8.71 ± 0.39	9.05
2	SWNT	IPA-PEDOT:PSS	0.77	11.1	0.50	53.7	2.7×10^3	4.01 ± 0.14	4.27
3	SWNT	surfactant-PEDOT:PSS	0.61	11.8	0.38	40.9	1.2×10^3	1.85 ± 0.59	2.71
4	70 v/v% HNO ₃ -SWNT	PEDOT:PSS	0.77	14.4	0.55	79.2	5.7×10^3	5.96 ± 0.34	6.09
5	50 v/v% HNO ₃ -SWNT		0.76	14.5	0.52	86.0	2.5×10^3	5.82 ± 0.46	5.84
6	35 v/v% HNO ₃ -SWNT		0.79	14.9	0.54	94.1	4.8×10^3	5.70 ± 0.60	6.32
7	15 v/v% HNO ₃ -SWNT		0.77	13.6	0.39	122	1.8×10^3	3.80 ± 0.48	3.88

^aCorresponding $J-V$ curves are shown in Figure 3. Average PCEs (PCE_{AVR}) with error ranges and record PCEs (PCE_{REC}) are included when all the devices were fabricated in the same condition for valid comparisons.

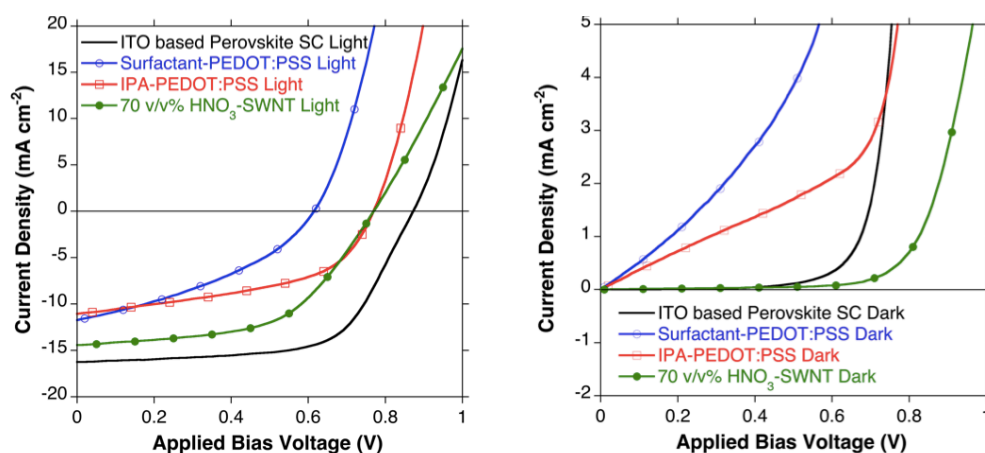


Figure 3a. J - V curves of the ITO-based PSC, the modified PEDOT:PSS-based PSCs, and the nitric acid-treated SWNT-based PSC in light (left) and dark (right).

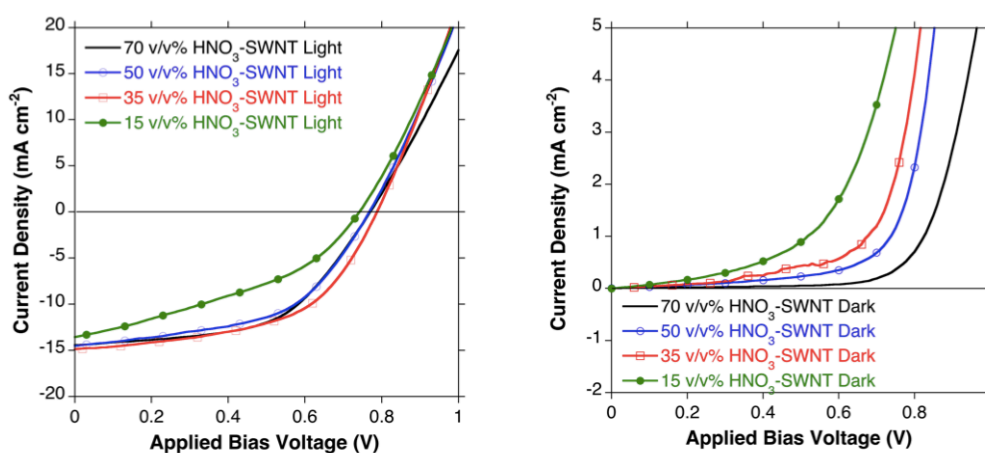


Figure 3b. J - V curves of the PSCs using nitric acid-treated SWNTs with different concentrations in light (left) and dark (right).

According to Table 1, the IPA-PEDOT:PSS-applied SWNT- based PSC performed better than the surfactant-PEDOT:PSS-applied SWNT-based PSC. (Device 2 and Device 3, respectively.) The J_{SC} values were similar, but the V_{OC} and the FF in the IPA-PEDOT:PSS-based device were higher than the surfactant-PEDOT:PSS-based device. Similar J_{SC} meant that their exciton dissociation and extraction were fine. But lower V_{OC} and R_{SH} indicated that the PEDOT:PSS coverage was the problem. Figure 4 shows observation of the IPA- PEDOT:PSS and the surfactant-PEDOT:PSS as cast, and water contact angle test results. The IPA-PEDOT:PSS on SWNTs showed a complete coverage on the substrate (Figure 4a), yet the surfactant-PEDOT:PSS barely soaked SWNTs and could not expand to the glass part (Figure 4b). Compared to the IPA-PEDOT:PSS solution, the surfactant-PEDOT:PSS solution was less hydrophilic.

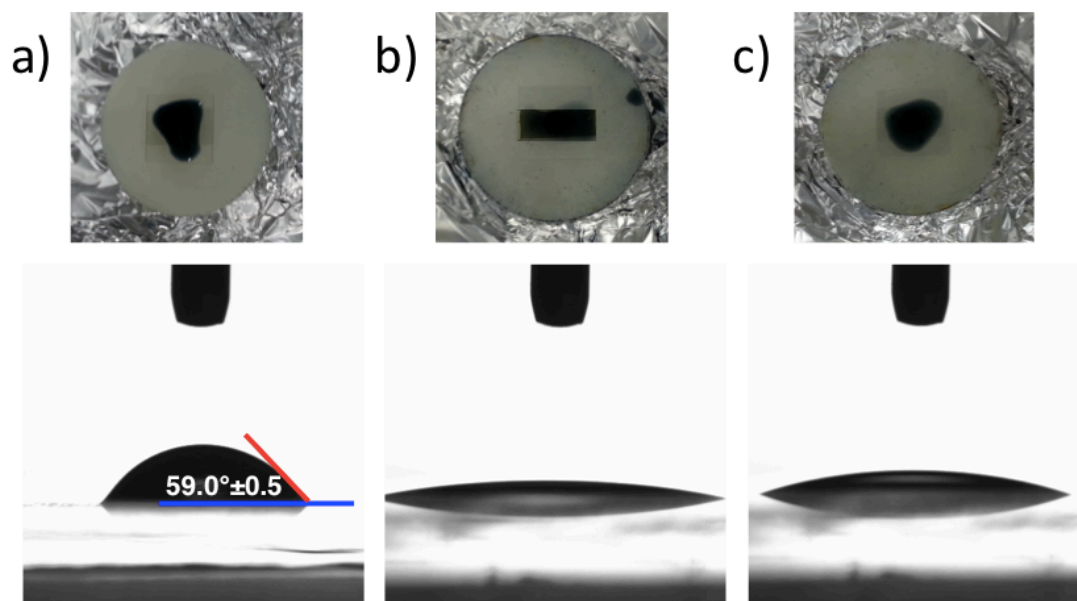


Figure 4. As cast wettability images (above) and water contact angle test on a) IPA-PEDOT:PSS on SWNT film on glass, b) surfactant-PEDOT:PSS on SWNT film on glass, and c) PEDOT:PSS on nitric acid 70 v/v%-treated SWNT film on glass.

As it has been proposed that the lower performance of PSCs arises from pinhole formation and incomplete coverage of the perovskite layer,^[223–225] inconsistently dewetted PEDOT:PSS surface will aggravate perovskite crystals because of perovskite layer's thermodynamic instability as predicted from the energetic standpoint.^[226] CB reduces the solubility of $\text{CH}_3\text{NH}_3\text{PbI}_3$ by removing the first solvent, thereby promoting fast nucleation and growth of the crystals. Therefore, the CB rinsing time had to be shortened for the surfactant-PEDOT:PSS applied SWNTs to avoid the crystal aggregations. Nevertheless, shortening the rinsing time induced premature crystallisation, which undercut the device performance. This explains why the surfactant-PEDOT:PSS-applied SWNT-based device performed badly, whereas the surfactant-PEDOT:PSS-applied on ITO, which has flatter morphology than SWNTs, gave a higher PCE (Table 2).

Table 2. Photovoltaic table of a nitric acid-doped thicker SWNT-based PSC.

Electrode	EBL	V_{oc} (V)	J_{sc} (mA cm^{-2})	FF	R_s (Ω)	R_{sh} (Ω)	PCE (%)
70 v/v% HNO_3 -SWNT	Surfactant- PEDOT:PSS	0.56	11.5	0.37	100	2.9×10^3	2.37
ITO		0.89	14.9	0.61	98	6.5×10^3	8.03
Thicker SWNT doped by 70 v/v% HNO_3	PEDOT:PSS	0.87	10.5	0.61	95	7.13×10^3	5.62

Using a four-point probe measurement, resistivity of various SWNTs was measured (Table 3). The IPA-PEDOT:PSS on SWNTs displayed higher R_{sheet} than the surfactant-PEDOT:PSS on SWNTs. This is due to a relatively large amount of IPA-PEDOT:PSS dilution, which is 1:3 in volume to volume ratio. Its influence is reflected from the higher R_s value of Device 2 (Table 1). This denotes that possible remnants of the surfactant in surfactant-PEDOT:PSS do not hinder the mobility of SWNTs greatly if they ever do. Nevertheless, overall, the IPA-PEDOT:PSS on SWNT films is more compatible in PSCs than the surfactant-PEDOT:PSS on SWNT films because of its favoured wettability.

Table 3. Conductivity of ITO/PEDOT:PSS, SWNT/modified-PEDOT:PSS, SWNT/surfactant-PEDOT:PSS, and SWNTs doped with different HNO_3 concentrations measured by four-point probe measurement.

Electrode	EBL	$R_{\text{sheet}} (\Omega \text{ sq.}^{-1})$
ITO	PEDOT:PSS	9.8
SWNT	IPA-PEDOT:PSS	208.2
SWNT	surfactant-PEDOT:PSS	109.6
70 v/v% HNO_3 -SWNT		23.7
50 v/v% HNO_3 -SWNT	PEDOT:PSS	28.3
35 v/v% HNO_3 -SWNT		25.6
15 v/v% HNO_3 -SWNT		38.6

The compatibility of SWNTs with PEDOT:PSS can be improved by doping SWNTs with HNO_3 , which changes SWNTs' property from hydrophobic to hydrophilic. This also entails strong doping effect due to the strongly acidic nature of HNO_3 . Nitric acid doping serves as the most effective dopant to date. However, it is toxic and highly reactive.^[227] Therefore, HNO_3 was diluted to the extent that its lethal effect was minimised, whereas its doping effective was still retained. It was reported that the greater the acid concentration, the greater the doping effect, but too highly concentrated acid can damage SWNTs.^[228,229] Accordingly, I investigated the relationship between the acid concentrations and the device performance.

HNO_3 doping on SWNT films was achieved by applying one drop of $\text{HNO}_3(\text{aq})$ and drying at 80 °C for 10 min. HNO_3 doping made SWNTs hydrophilic enough to allow formation of a fine layer of unmodified PEDOT:PSS on top (Figure

1d). The AFM images and Ra roughness values reveals uniform PEDOT:PSS-soaked SWNTs compared to the modified PEDOT:PSS-soaked SWNTs (Figure 1f, g, and h). Indeed, high V_{OC} and R_{SH} values of Device 4 (Table 1) tell us that there is no shunt pathway created between the perovskite layer and the SWNT electrode. These values are higher than those of the devices fabricated using the modified PEDOT:PSS-soaked SWNT electrodes.^[130,230] The perovskite films also showed nice morphology as good as the reference (Figure 1i and l). I attribute this to the uniformity of the electrode as well as the use of unmodified PEDOT:PSS.

Device performances of the HNO_3 -doped SWNT-based PSCs with different HNO_3 concentrations were compared (Table 1, Devices 4–7). I could observe that all of the HNO_3 -doped SWNT-based PSCs showed much higher PCEs than those of the modified PEDOT:PSS-based SWNTs. The high performance can be attributed to the improved J_{SC} , which is due to enhanced transmittance of SWNT films by the acid doping. It must be mentioned that strong 70 v/v% HNO_3 did not destroy nor undermine the device performance (Device 4). In addition, there was no stark difference among average PCEs between acid concentrations, except for 15 v/v% in which the PCE dropped to 3.88% (Device 7).

UV–vis spectroscopy and Raman spectroscopy were carried out to confirm and compare the transparency and the doping effect. Figure 5a shows spectra of HNO_3 -doped SWNTs having subdued Van Hove peaks (M_{11} , E_{22} , E_{11}), which is an indication of successful doping. The transmittance spectrum of the SWNTs doped by HNO_3 (15 v/v%) was lower than the spectra of the other samples doped by HNO_3 with higher concentrations. This shows that the 15 v/v% HNO_3 possesses weaker doping effect than the rest. Raman spectra (Figure 5b) followed the same trend: all of the HNO_3 -doped SWNTs, except 15 v/v%-concentrated sample exhibited the G-band shifts. Yet, the HNO_3 (15 v/v%)-doped SWNT film's doping effect was stronger than that of the SWNT film treated by IPA-PEDOT:PSS which showed a slightly higher transmittance than the untreated SWNT film in the UV-vis spectra while showing no shift in Raman spectra. Conductivity measurement also revealed higher resistivity of HNO_3 (15 v/v%)-doped SWNT film (Table 3). It can be concluded that HNO_3 (35 v/v%) is the optimum concentration for the doping application in SWNT-based PSCs.

Another fascinating point about HNO_3 -doped SWNTs in PSCs is that R_s values were rather high considering their low R_{sheet} in Device 4 to 7 (Table 1). This phenomenon was not observed in OSCs.^[192] Therefore, I employed a thicker SWNT film (65% transmittance at 550 nm wavelength) and fabricated a device expecting lower R_s , because thicker SWNT films possess lower resistance intrinsically. However, the HNO_3 -doped thicker SWNT-based PSC did not improve R_s (Table 2). To find out the reason behind this, impedance measurement was carried out. Spectra at 0 mV in dark condition are shown in Figure 5c. The data reveal that HNO_3 -doped SWNT-based PSCs possesses much higher electrical boundaries than the IPA-PEDOT:PSS-treated SWNTs, despite low R_{sheet} in both thinner and thicker SWNT films. The Fermi levels of SWNTs measured by Kelvin probe force microscopy indicated that HNO_3 -doped SWNT films' Fermi levels were around 5.4 eV or higher for all of the HNO_3 concentrations, whereas pure SWNT films' Fermi levels sat around at 5.0 eV.^[231] It can be concluded that the HNO_3 -doped SWNT films provide relatively less driving force for the hole injection from the perovskite layer and this causes higher R_s . Indeed, if I compare the energy band diagrams of SWNT-based PSCs and OSCs, I can understand that the OSCs are energetically more favoured (Figure 6).

MoO_3 as an EBL has been commonly used in place of PEDOT:PSS in OSCs. In fact, MoO_3 is preferred over acidic PEDOT:PSS.^[232] However, the same usage has not been witnessed in the field of PSCs. It can be presumed that this is due to its incompatibility in PSCs, but no clear account has been given so far. Because it was reported that thermally annealing MoO_3 could dope SWNTs in a safe and effective manner, I was compelled to study its compatibility in SWNT-based PSCs.^[191]

Table 4 shows diverse configurations of PSCs using MoO_3 . It reveals that MoO_3 -applied PSCs performed poorly on both ITO (Table 1: Device A) and SWNT film (Table 1: Device B). When PEDOT:PSS and MoO_3 combinations were used in the hope of improving the interface morphology, the photovoltaic parameters did not improve (Table 4). Moreover, I thermally annealed MoO_3 above or below SWNTs in order to dope SWNTs. This process reduced oxygen stoichiometry of MoO_3 to MoO_x where x is a number between 2 and 3. The PCEs improved only little (Table 4: Device C).

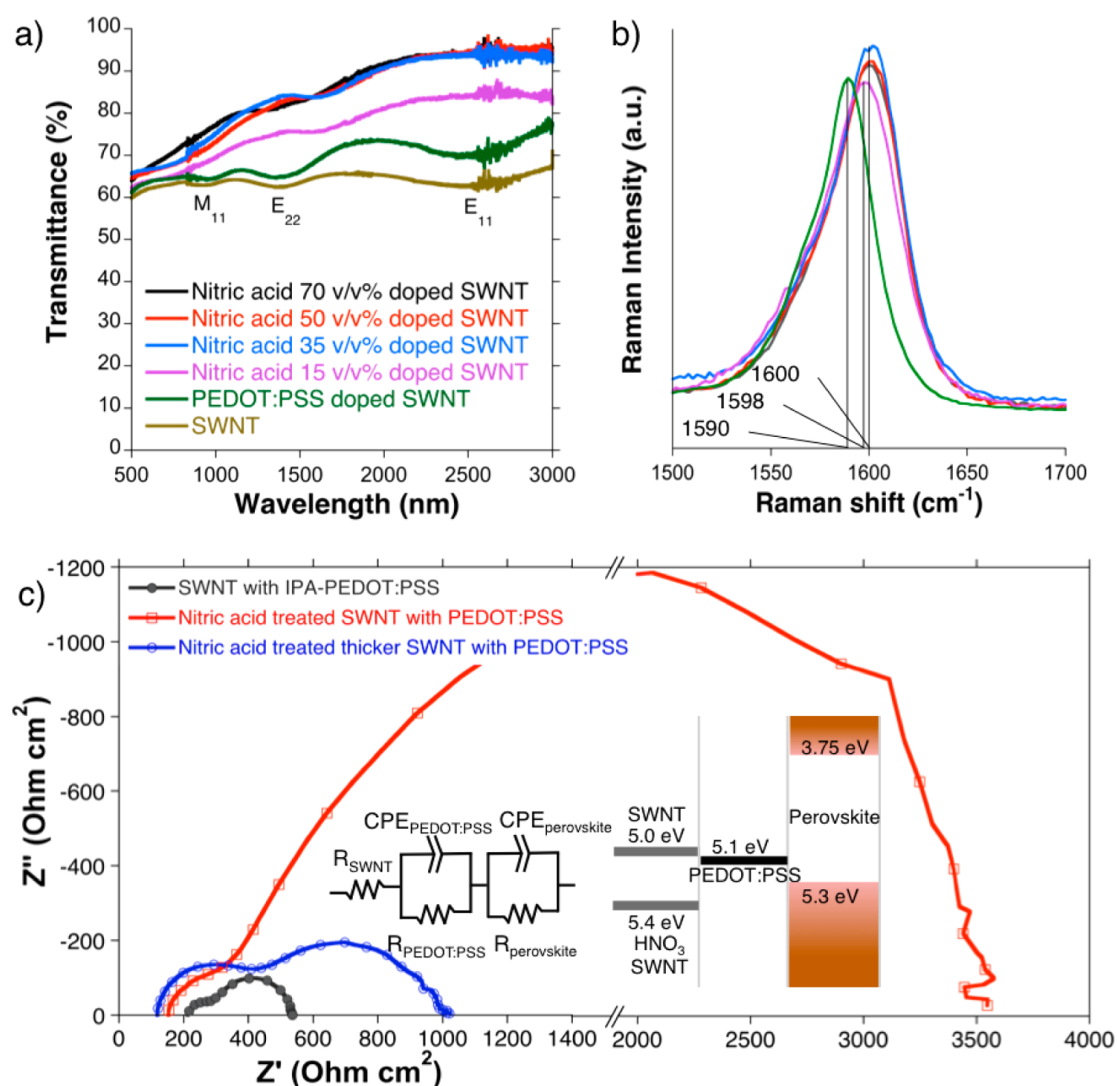


Figure 5. Transmittance, (a) and Raman shift values, (b) of HNO₃-doped SWNT films with different acid concentrations, an IPA-PEDOT:PSS-soaked SWNT film and an untreated SWNT film using UV-vis spectroscopy and Raman spectroscopy, respectively. Both spectra share the same legend. (c) Nyquist plot of PSCs with IPA-PEDOT:PSS-applied SWNT film, HNO₃-doped (treated) SWNT film, and HNO₃-doped (treated) thicker SWNT film measured at 0 mV applied bias under dark condition; the equivalent circuit and the band diagram are shown in the inset.

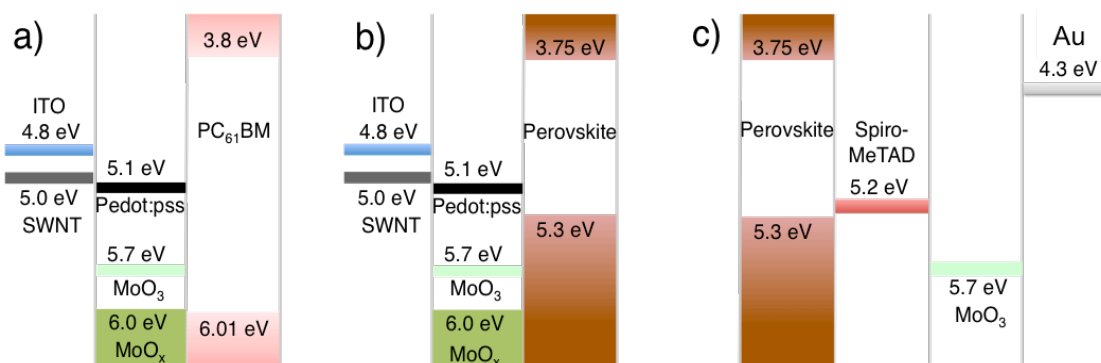


Figure 6. The energy band diagrams of a) OSCs, b) inverted type PSCs, and normal type PSCs.

Table 4. Photovoltaic performance table for inverted planar heterojunction SWNT-based PSCs and normal planar heterojunction ITO-based PSCs using MoO₃ and MoO_x layers in various structural configurations^a

Device	Electrode material	V _{oc} (V)	J _{sc} (mA cm ⁻²)	FF	PCE (%)
Anode					
A	ITO	0.79	5.17	0.53	2.19
	ITO/MoO ₃	0.46	0.64	0.42	0.12
B	SWNT/MoO ₃	0.37	0.51	0.28	0.05
C	SWNT/MoO _x /PEDOT:PSS	0.58	13.0	0.42	2.09
	SWNT/MoO ₃ /PEDOT:PSS	0.06	1.79	0.25	0.03
	SWNT/IPA-PEDOT:PSS/MoO ₃	0.07	0.77	0.25	0.02
	MoO _x /SWNT/PEDOT:PSS	0.35	10.5	0.36	1.30
Cathode					
D	spiro-MeOTAD/Ag	0.96	21.0	0.68	13.7
E	spiro-MeOTAD/MoO ₃ /Ag	0.56	11.5	0.37	2.22
F	MoO ₃ /Ag	0.48	2.01	0.32	0.30

^aCorresponding *J*-*V* curves are shown in Figure 7.

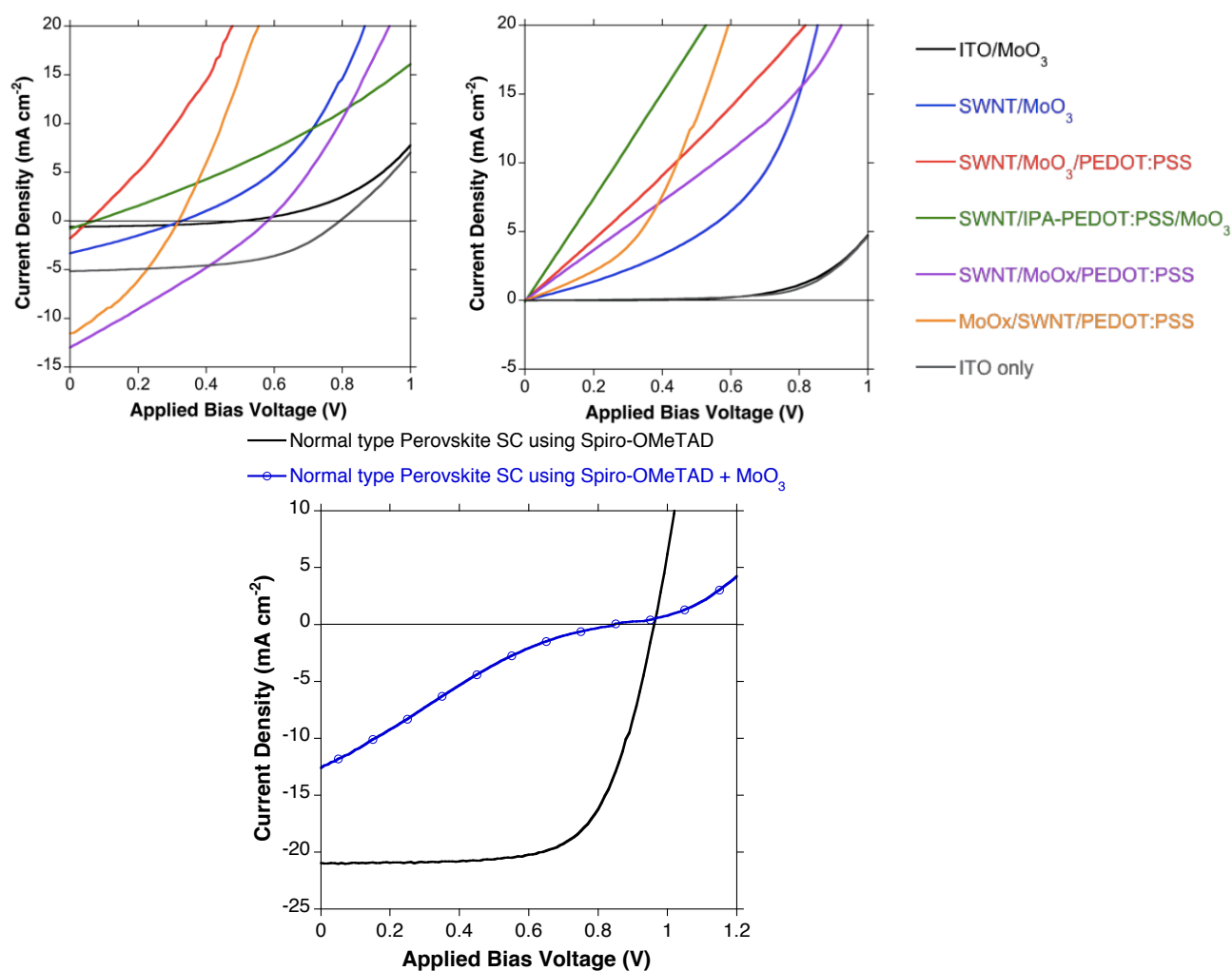


Figure 7. *J*-*V* curves of the PSCs with various configurations involving MoO₃ (above). *J*-*V* curves of the normal type PSCs with and without MoO₃ (below).

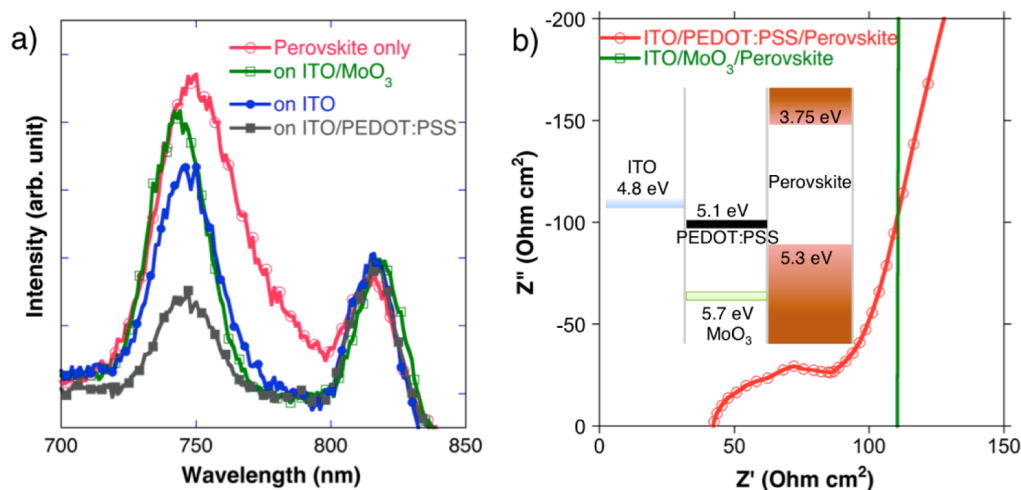


Figure 8. (a) Photoluminescence spectra of a perovskite layer only, a perovskite film on a MoO₃ film on an ITO glass, a perovskite film on an ITO glass, and a perovskite film on a PEDOT:PSS film on an ITO glass. (b) Nyquist plot of PSCs with a PEDOT:PSS film on an ITO glass and a MoO₃ film on an ITO glass measured at 0 mV applied bias under dark condition; the band diagram is shown in the inset.

As the quality of the perovskite layers were visually fine during the fabrication, energy mismatching was suspected to be the root of this incompatibility. Photoluminescence spectroscopy and impedance measurement were carried out to investigate this. Photoluminescence quenching is a well-established method demonstrating a charge extraction ability of EBL in contact with perovskite.^[149] Figure 8a shows that photoluminescence of halide methylammonium lead perovskite was reduced strongly when it was next to PEDOT:PSS, but not when it was next to neither ITO nor MoO₃.^[90] According to Figure 8b, the electronic boundary between perovskite and MoO₃ was too big that it made a complete vertical line. The Fermi level of MoO₃ was measured using photoelectron yield spectroscopy. It indicated that MoO₃ had the Fermi level of around 5.7 eV. Thermal annealing dropped this value to 7.0 eV. As the valence band of perovskite is around 5.3 eV, there was energy level mismatch with MoO₃. On the contrary, PEDOT:PSS had the Fermi level at around 5.1 eV. Therefore, the hole transfer was not hindered between perovskite and PEDOT:PSS. In the case of organic acceptors like PC₆₁BM, its HOMO (6.01 eV) lies much lower than the valence band of the perovskite. Although PC₆₁BM is an electron conductor not a hole conductor, I suspect its HOMO is key in understanding energetic compatibility of MoO₃ in OSC system.^[233,234]

In spite of this incompatibility of MoO₃ in inverted-type PSCs, there are some reports on MoO₃ being utilised as an EBL in normal-type PSCs.^[235,236] In order to

verify this, I fabricated normal-type planar heterojunction PSCs using MoO₃. Device D in Table 3 (glass/ITO/TiO₂/perovskite/spiro-MeTAD/Ag) showed a typical performance of a normal-type PSC using spiro-MeOTAD. When MoO₃ was inserted next to spiro-MeOTAD, it decreased PCE greatly. When only MoO₃ was used as an EBL, its performance was even worse. These results support my assertion that the MoO₃ is not compatible in either architecture.

The best performing configuration from this study was chosen and PSCs were fabricated on flexible polyethylene terephthalate (PET) substrate with HNO₃ (35 v/v%)-doped SWNTs as an electrode. A cyclic flex test with a curvature of 10 mm was imposed to check the resilience (Table 4). A PCE of 5.38% with V_{OC} of 0.81 V, J_{SC} of 11.8 mA cm⁻², and FF of 0.56 under AM1.5 100 mW cm⁻² illumination was achieved. After the severe flex cyclic test, the performance dropped a little (4.60%), but it retained its diode character well enough. Pictures and a cross-sectional SEM image are shown Figure 10.

Table 4. Photovoltaic performance of a flexible SWNT-based PSC and after 10 mm curvature cyclic flex was applied. Corresponding J - V curves are shown in Figure 9.

Type	V_{OC} (V)	J_{SC} (mA cm ⁻²)	FF	R_s (Ω)	R_{SH} (Ω)	PCE (%)
Flexible	0.81	11.8	0.56	105	6.05×10^3	5.38
After cyclic flex test	0.79	11.5	0.50	135	4.22×10^3	4.60

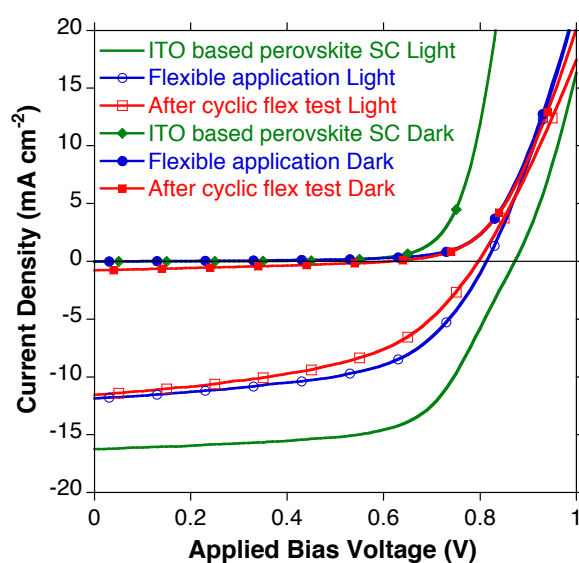


Figure 9. J - V curves of the ITO-based PSC and a HNO₃ (35 v/v%)-doped SWNT-based flexible PSC, before and after the cyclic flex test.

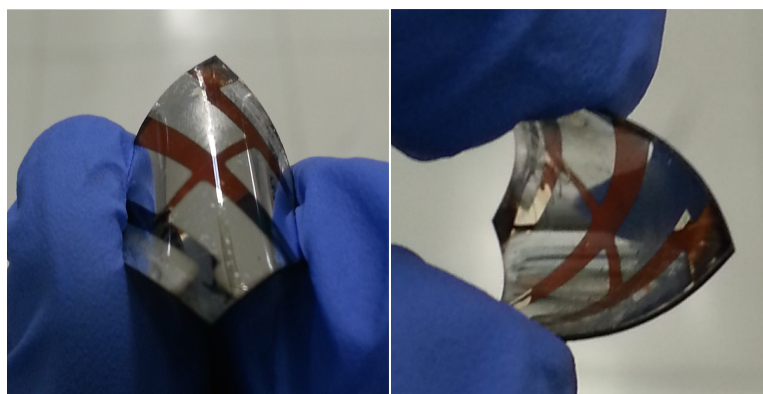


Figure 10a. Pictures of a HNO_3 (35 v/v%)-doped SWNT-based flexible PSCs.

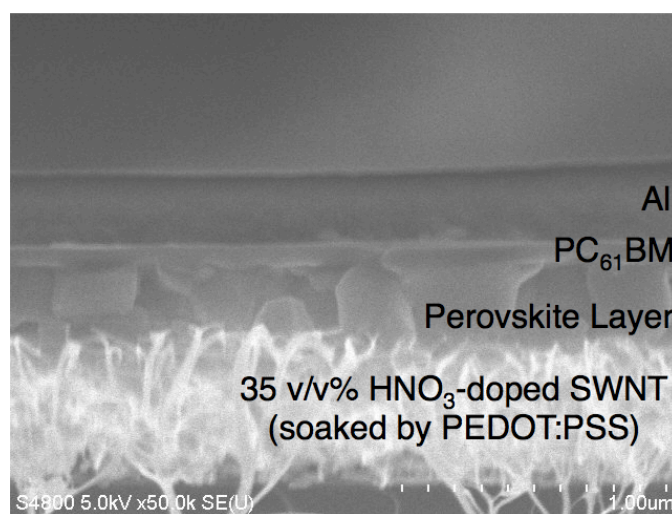


Figure 10b. A cross-sectional SEM image of a HNO_3 (35 v/v%)-doped SWNT-based flexible PSC.

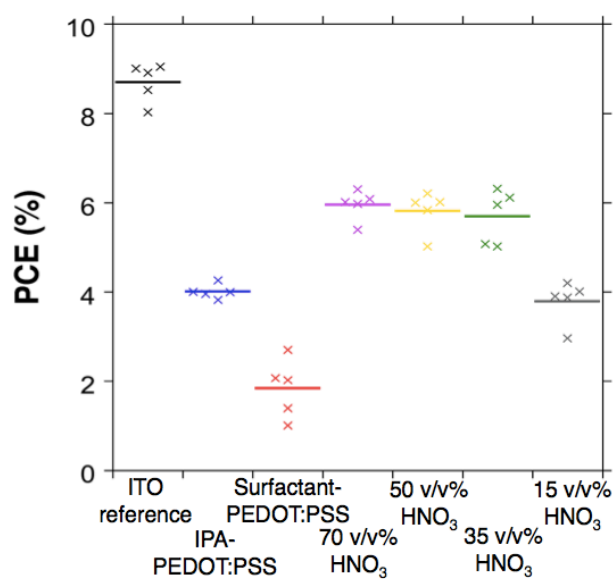


Figure 11. A statistical analysis graph illustrating reproducibility of the PSCs in this work. Crosses represent each device performance and bars represent averages.

4.5 Conclusion

In conclusion, the three mainstream approaches to SWNT application in PSCs had been viewed. Their compatibility, effectiveness, and mechanism had been studied to understand the uniqueness of PSCs. Modified PEDOT:PSS worked fairly well, but the PCEs were limited. Application of MoO_x on the other hand was not compatible in PSCs, much to my surprise. HNO_3 -doped SWNTs were the best performing even in its diluted form, up to 35 v/v %, yet its mobility was marginally hindered by the energy level difference between highly lying perovskite valence band and strongly p-doped SWNT electrode's Fermi level. Using this approach, I achieved a flexible ITO-free planar heterojunction PSC device with a PCE of 5.38%, which is 60% of ITO reference device (9.05%). As non-ITO and SWNT-based PSCs, I anticipate this work can initiate and contribute to the development of ITO-free PSC research. I believe these findings will provide better understanding of CNT applications as transparent conductive electrodes in ITO-free PSCs.

CHAPTER 5

DOUBLE-WALLED CARBON NANOTUBES AS THE CONDUCTIVE LAYER IN FLEXIBLE ORGANIC SOLAR CELLS

5.1 Summary

In this chapter, we introduce solution-processed DWNT-based OSCs. DWNT films possess similar electric properties to SWNT films, but stronger chemical resistance against acids. Thus, HNO_3 doping can be applied without damaging inner tubes which leads to higher electric properties than SWNT films after acid doping. Ultimately solution-processed DWNT-based OSCs perform as good as SWNT-based OSCs when HNO_3 doping was applied, with advantages of being solution-processed. A PCE of 2.68% was achieved from HNO_3 -doped DWNT-based OSCs when ITO-based reference devices show a PCE of 2.95%. As all the other carbon-based electrodes including SWNT and graphene utilise CVD transfer methodology, which are costly and difficult to cover a large area, our solution-deposited DWNT film can bring a breakthrough in the research field of indium-free flexible photovoltaics.

5.2 Introduction

Until now, carbon-based electrodes in solar cells have been reported in great numbers. Presently, SWNTs and graphene are the primarily used electrodes.^[164,182,183,192,202–213,237–244] But both of the electrodes are CVD-processed. One of the major drawback with the CVD technique is that high defects are unavoidable due to the lack of sufficient thermal energy for annealing carbon-based electrodes arising from relatively low growth temperature.^[245] This and high-vacuum process combined limit large-surface deposition and raise the cost of process.

CNTs can be classified chiefly into three: SWNTs, double-walled carbon nanotubes (DWNTs), and multi-walled carbon nanotubes (MWNTs). They differ in the arrangement of their graphene cylinders. MWNTs are multiple SWNTs of varying diameters arranged concentrically within one another with the distance of layers in graphite. DWNTs are just MWNTs with two layers. Despite MWNTs being much more stable than SWNTs in terms of lifetime and resistance to oxidation,^[246–248] the reason that DWNTs have been rarely used for the electrode applications can be ascribed to more difficult CVD process and slightly lagging optoelectrical properties.^[249–253] More specifically, for a variety of CVD processes of DWNTs such as arc-discharge,^[253–255] C₆₀-peapods,^[256] catalytic pyrolysis,^[252,257–260] and zeolite-supported CVD,^[261–263] higher temperatures than SWNT syntheses are required. Also, as the syntheses of thick outer tubes having diameters larger than 2.0 nm are necessary, electrical conductivity and transparency are not as good as those of SWNTs.^[264]

In this work, we synthesized solution-processed DWNT films with inner and outer diameters of 0.9 nm and 1.7 nm, respectively, and demonstrated their superior advantages over SWNTs in OSC applications. This solution-processed DWNT films could yield large area coverage with exceedingly low-cost. Moreover, DWNT films showed better physical and chemical properties than SWNT films as reported.^[248,265,266] Particularly, acid doping on the surface of DWNT films yielded a change in chemical property while maintaining the inner tube intact. DWNT electrode-utilised and SWNT electrode-utilised OSCs were fabricated each with different doping methods, more specifically MoO_x-thermal doping^[191] and nitric acid doping. Whilst the SWNT-based

devices performed better than those of DWNT when MoO_x-thermal doping was used, the DWNT-based devices performed similar to those of SWNT when nitric acid-doping was applied. This is due to the fact that nitric acid doping modified only the outer wall of DWNTs and inner walls are kept defect-free. In addition, DWNT films produced by our method showed smoother surface which was reflected by high V_{oc} photovoltaic parameter and low roughness from AFM. This means that application of DWNT films in PSCs may result in higher performance than SWNT-based PSCs as the perovskite layer in PSCs is sensitive to the morphology of the substrates being coated onto.

5.3 Experimental Procedures

5.3.1 Device Fabrications

Please refer to 2.1.1.1 Organic solar cell normal device architecture ‘2.1.1.3 P3HT:mix-PCBM solution preparation’ and ‘2.1.3 SWNT Preparations’

The fabrication method of solution-processed DWNT cannot be disclosed at this stage due to confidentiality.

For MoO_x thermal doping, please refer to ‘3.3.1 Device Fabrications’. For HNO₃ doping, HNO₃(aq) solution was dropped on a SWNT film followed by drying at 80 °C for 10 min.

5.3.2 Characterisations

Please refer to ‘2.2.1.1 Current-voltage characterisation’, ‘2.2.2.1 UV-vis absorption’, ‘2.2.2.3 Atomic force microscopy (AFM)’, ‘2.2.2.4 Scanning electron microscopy (SEM)’, ‘2.2.2.8 Photoelectron yield spectroscopy (PYS) and Kelvin probe’, ‘2.2.2.9 Raman spectroscopy’ and ‘2.2.2.13 Four-probe measurement’.

5.4 Results and Discussion

Both conductivity and transmittance of the CNT films significantly affects the device performance. Therefore, to make a valid comparison, it is imperative that I used CNT films with similar transmittance. UV-vis spectra of DWNT and SWNT films, which are approximately 80% transparent at 550 nm, are shown in Figure 1. Despite DWNT film having low transparency in the near-UV region, both DWNT and SWNT films show the same transparency in the visible wavelengths, validating the comparison.

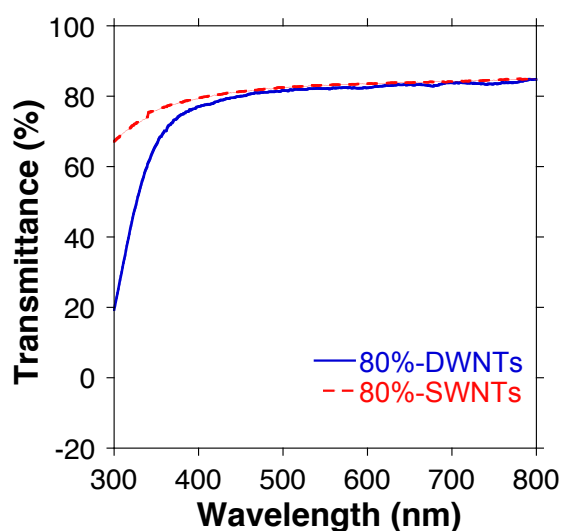


Figure 1. UV-vis spectra of 80%-transparent DWNT and SWNT films

Table 2. Photovoltaic parameters of ITO-, SWNT-, and DWNT-based OSCs under 1 sun (AM1.5G illumination, 100 mW cm⁻²).

Device	V_{oc} (V)	J_{sc} (mA cm ⁻²)	FF	R_s (Ω)	R_{sh} (Ω)	PCE (%)
ITO/PEDOT:PSS/P3HT:PCBM/LiF/Al	0.60	8.44	0.58	20	3.2×10^3	2.95
SWNTs/MoO _x /PEDOT:PSS/P3HT:PCBM/LiF/Al	0.59	7.56	0.54	120	3.6×10^6	2.38
DWNTs/MoO _x /PEDOT:PSS/P3HT:PCBM/LiF/Al	0.61	7.51	0.49	200	1.3×10^7	2.26
SWNTs/HNO ₃ /PEDOT:PSS/P3HT:PCBM/LiF/Al	0.59	7.65	0.58	20	9.4×10^5	2.66
DWNTs/HNO ₃ /PEDOT:PSS/P3HT:PCBM/LiF/Al	0.60	7.76	0.57	10	4.5×10^4	2.68

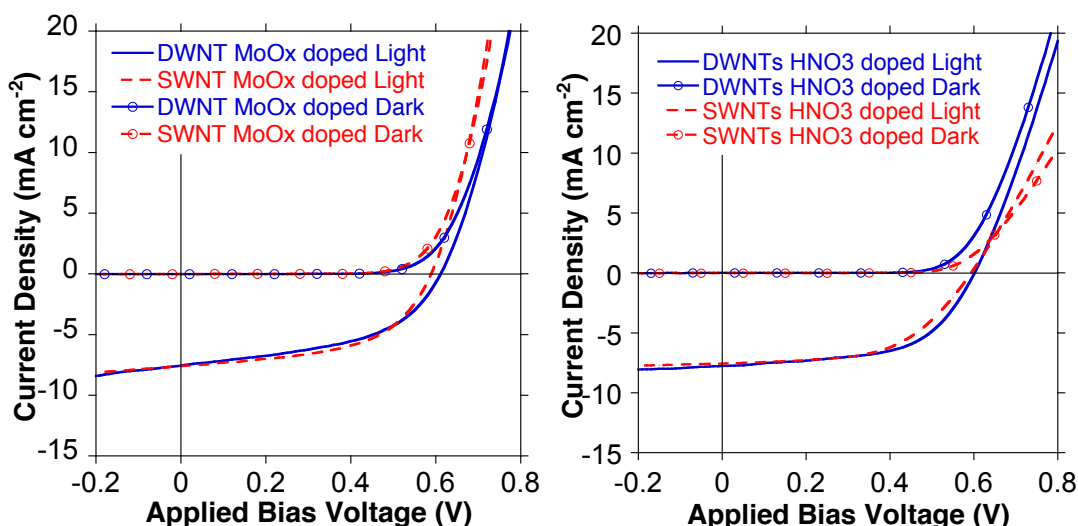


Figure 2. J - V curves of SWNT- and DWNT-based MoO_x thermally doped OSCs (left) and SWNT- and DWNT-based HNO_3 -doped OSCs (right) under 1 sun and in dark.

P3HT:PCBM-based OSCs using DWNT and SWNT films were fabricated using MoO_x thermal doping and HNO_3 acid doping. Table 1 shows the photovoltaic parameters of those devices. It is interesting that the SWNT-based OSCs showed higher performance than the MWNT-based OSCs when MoO_x -thermal doping was applied, whereas, the MWNT-based OSCs performed similar to the SWNT-based OSCs when HNO_3 doping was applied. According to photovoltaic table 1 and J - V curves in Figure 2, the main driving factor for such result were improvements in FF and R_s values. The R_s of the DWNT-based devices with MoO_x doping was higher than that of the SWNT counterparts, which led to low FF. But with HNO_3 doping, the DWNT-based devices showed lower R_s and a FF value similar to that of the SWNT-based devices. In addition, V_{OC} of the DWNT-based devices was higher than that of the SWNT-based devices in all cases.

To investigate the electric property of the CNTs under doping, four-probe measurement was carried out (Table 2). While non-doped and MoO_x thermally doped DWNT films displayed higher R_{Sheet} than SWNT films, HNO_3 -doped DWNT films showed lower R_{Sheet} than SWNT films. This explains why DWNT-based OSCs performed as good as SWNT-based OSCs under HNO_3 doping. This phenomenon is related to unique electric and chemical properties of DWNT films.^[267] Non-doped DWNT films have higher resistance than SWNT films, because with the same transparency, DWNT films are speculated to have a fewer number of nanotubes than SWNT films. But when HNO_3 is applied, unlike ITO, CNT films can stay robust

changing their electronic properties only.^[229] More precisely, covalent functionalisation of HNO₃ breaks C=C double bonds on CNTs creating more holes, thus improving their hole conductivity.^[227] One of the fortes of DWNT films is functionalising the outer walls while retaining the mechanical and electronic properties of the inner nanotubes.^[268] This means DWNT films can stay intact when SWNT films suffer from defect sites hindering charge transfer. This is not seen in MoO_x doping, because MoO_x doping does not involving chemical functionalisation but redox reaction.

Table 2. Four-probe measurements of DWNT and SWNT films with non-doped, MoO_x thermally doped, and HNO₃-doped.

Sample	$R_{\text{Sheet}} (\Omega)$	$R_{\text{Sheet after MoO}_x \text{ doping}} (\Omega)$	$R_{\text{Sheet after HNO}_3 \text{ doping}} (\Omega)$
80%-transparent DWNT film	189	113	72
80%-transparent SWNT film	154	107	82

To further examine chemical propriety of the CNTs, their Fermi levels were checked using PYS. Before doping SWNT films had a slightly higher Fermi level, but after HNO₃ doping, the Fermi levels of SWNT and DWNT films were the same.^[248] This demonstrates that in terms of chemical property, DWNT films show the same property as SWNT films after HNO₃ doping. This corroborates the fact that outer nanotubes of DWNTs were modified the same way SWNTs were modified.

Table 3. PYS measurements of DWNT and SWNT films with non-doped and HNO₃-doped.

Sample	Fermi level (-eV)	Fermi level after HNO ₃ doping (-eV)
80%-transparent DWNT film	5.10	5.40
80%-transparent SWNT film	5.00	5.40

AFM was used to examine the morphology. According to the AFM images and r.m.s. roughness values in Figure 3, the DWNT films showed much lower roughness with a r.m.s. roughness value of 6 while the SWNT films showed a r.m.s. roughness value of 10. This can be attributed to solution deposition of DWNTs which overcoats the substrate's rough surface and the gravity pulling the solution flat, as opposed to aerosol CVD deposition of SWNTs which grows the film in the absence

of gravity influence. I conjecture that such favourable morphology of DWNT films is the reason for the enhanced V_{OC} . Since substrate morphology is critical in PSC fabrications, we can expect a better outcome from the DWNT film application in PSCs. This will be conducted in due course.

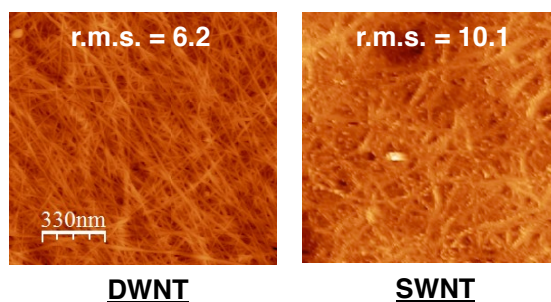
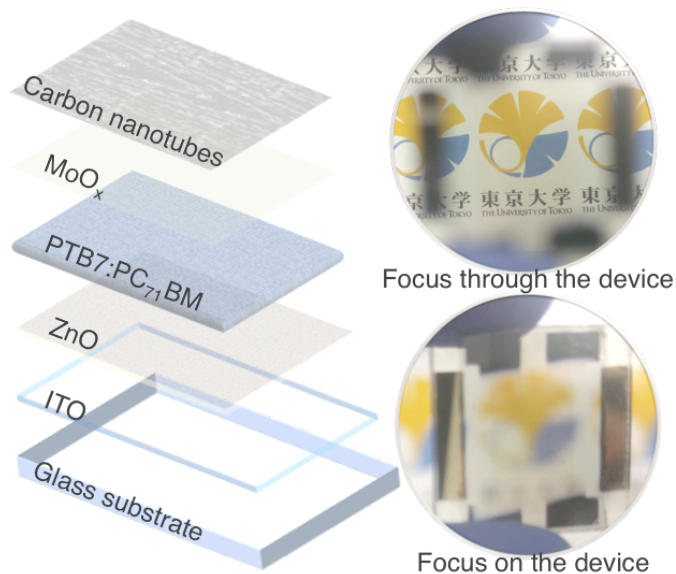


Figure 3. AFM images of DWNT and SWNT films with r.m.s. roughness values.

Advantages of DWNTs are not limited to their chemical stability. For example, with narrower inner tube diameters, DWNTs may offer intriguing quantum effects which can be exploited in nano-electronics.^[248] In addition, DWNTs have shown to facilitate hole-transporting effect in P3HT-DWNT composite films.^[269–277] High built-in voltage arising from the interaction between P3HT and DWNTs can be explored more. I plan to delve into these aspects as well as the flexible application in near future.^[278]

5.5 Conclusion

We have introduced solution-processed DWNT film and demonstrated its application in OSCs by making a comparison with SWNT-based OSCs. DWNT-based OSCs performed slightly worse than SWNT counterparts with MoO_x doping, whereas they performed on par with the SWNT-based OSCs when HNO_3 doping was applied. This was ascribed to increase in FF arising from defect-free nature of DWNTs against strong acids. While outer tubes of DWNTs undergo chemical change, inner tubes stayed intact without defects, maintaining its mobility. DWNT films also showed better morphology than SWNT films as well, exhibiting its potential as an electrode in PSCs. Their other advantages such as quantum effects and interaction with P3HT will be researched in depth as a follow-up work in due time.



CHAPTER 6

SINGLE-WALLED CARBON NANOTUBES AS THE CONDUCTIVE LAYER AND NOVEL TRAFER METHODOLOGIES THEREIN IN TRANSPARENT ORGANIC SOLAR CELLS

6.1 Summary

Here expensive top metal electrode was replaced by highly performing and easy-to-transfer aerosol-synthesised carbon nanotubes to produce transparent OSCs for window applications. Moreover, the carbon nanotubes were doped by two new methodologies presented in this work: HNO₃ doping ‘Sandwich transfer’ and MoO_x thermal doping ‘Bridge transfer’. While both doping methods enhanced the performance of the carbon nanotubes, thus photovoltaic performance in device, HNO₃ doping Sandwich method with 4.1% power conversion efficiency was marginally more effective than the Bridge transfer with a power conversion efficiency of 3.4%. Applying much thinner carbon nanotube with 90% transparency decreased the efficiency little, yet still retained to 3.7%. Compared with the efficiency of the non-transparent metal-based solar cells (7.8%), it showed more than 50% efficiency while being fully transparent. This research will open the door to top electrode application of carbon-based electrodes and we can anticipate its adaptation in both academia and industry.

6.2 Introduction

In addition to the pursuit of high efficiency, OSCs have also been intensively studied for their potential in making advances for broader applications.^[279,280] On the same note, future OSCs are regarded to be greener technology that serves various functions such as wearable, surface conforming, window application and etc. Prerequisites to these include use of metal-free, mechanically resilient, and translucence materials, while retaining a high PCE. The first step towards this achievement is replacing metal electrode, which is expensive and blindingly glare (Figure 1). Previously, many attempts have been made in demonstrating transparent and flexible solar cells such as building-integrated photovoltaics and solar chargers for portable electronics using metallic grids, nanowire networks, metal oxides, or conducting polymers.^[281–293] Yet, transparent conductors often result in low visible light transparency, low PCEs, or low flexibility, because no suitable transparent and conductive material was adopted in device design and fabrication.



Figure 1. A real window application of transparent OSCs (right) and the highlighted problem of sunlight glare from use of reflective (left) Ag even when thin metal electrodes were used.

SWNT films as an electrode replacing ITO in photovoltaics has been reported in great numbers.^[237,294] However, a SWNT film working as a top-electrode has been rarely reported because of the challenging nature of SWNT lamination from above.^[213] There was one recent success in the work presented by Li et al.^[213] Their SWNT films were used as the top-electrode in PSCs. However, their SWNT films

could not be doped, because doping laminated SWNT electrode is extremely difficult without damaging the device.

Here I report SWNT-based metal-free and window-like transparent OSCs where SWNT films have been doped by two mainstream dopants, HNO_3 and MoO_3 which I named ‘Sandwich transfer’ and ‘Bridge transfer’, respectively. The HNO_3 -doped, and MoO_3 -doped 60% transparent SWNT-laminated OSCs showed PCEs of 4.1% and 3.4%, respectively. Applying 90% transparent SWNT films, which rendered tinted-window visual, resulted in PCEs of 3.7% and 3.1% for HNO_3 -doped and MoO_3 -doped, respectively, while the reference ITO-based OSC showed a PCE of 7.8%. Hence, I introduce window-applicable transparent OSCs by means of safely doping direct- and dry-lamination of SWNT films for the top electrode, bypassing the expensive and energy-consuming metal deposition process. The double-sided light response feature of these transparent yet highly efficient solar cells offers advantages in many applications. I expect the methodologies presented here will open the way to the future of multifunctional OSCs.

6.3 Experimental Procedures

6.3.1 Device Fabrications

Please refer to ‘2.1.1.2 Organic solar cell inverted device architecture’, ‘2.1.1.4 PTB7:PC₇₁BM solution preparation’, and ‘2.1.3.1 Aerosol SWNT’. For the SWNT-based devices, only up to MoO_3 deposition was carried out. To improve the contact between the solar simulator and SWNT, Ag (100 nm) pattern was deposited only at the contact where wires of the solar simulator will be clipped.

6.3.1.1 *Transfer of non-doped SWNT*

SWNT films were transferred onto MoO_3 by laminating from the top. A drop of poly(3,4-ethylenedioxythiophene)/poly(styrenesulfonate) (PEDOT:PSS) was applied and spin-coating at 4500 rpm for 60 s to assist lamination.

6.3.1.2 *HNO_3 doping Sandwich-transfer method*

SWNT films were transferred on bare glass substrates. HNO_3 (70% in water) was applied drop-wise and dried at 80°C to dope the SWNT films. The HNO_3 -doped SWNT substrates were transferred onto MoO_3 and Ag patterned device ($\text{MoO}_3/\text{PTB7:PC}_{71}\text{BM:DIO/ZnO/ITO}$) like a sandwich and UV-resin was applied at the edges only in order to hold the two substrates and encapsulate.

6.3.1.3 MoO_x doping Bridge-transfer method

A special holder for SWNT films was prepared and SWNT films were transferred onto the holder so that the films hang like a bridge. 15 nm MoO_3 was thermally deposited on the bridged SWNT films followed by thermal annealing at 300°C for 3 h anaerobically to induce MoO_x doping. The bridged SWNT films were transferred carefully on to the Ag patterned photoactive layer. A drop of PEDOT:PSS was applied and spin-coating at 4500 rpm for 60 s to assist lamination. Since MoO_x can function as the HTL, MoO_3 step was omitted for this method only. In other words, SWNT/ MoO_x was laminated on PTB7:PC₇₁BM:DIO/ZnO/ITO rather than $\text{MoO}_3/\text{PTB7:PC}_{71}\text{BM:DIO/ZnO/ITO}$.

6.3.2 Characterisations

Please refer to ‘2.2.1.1 Current-voltage characterisation’, ‘2.2.1.4 Impedance measurement’, ‘2.2.1.2 Incident photon to current efficiency (IPCE)’ ‘2.2.2.1 UV-vis absorption’, ‘2.2.2.2 Photoluminescence’, ‘2.2.2.3 Atomic force microscopy (AFM)’, ‘2.2.2.4 Scanning electron microscopy (SEM)’.

6.4 Results and Discussion

The randomly oriented SWNT networks with high purity and long nanotube bundle length were synthesised by the aerosol CVD method.^[186,187] The floating catalyst aerosol CVD was carried out in a scaled-up reaction tube with the diameter of 150 mm. The dry deposited SWNT networks had high purity as evidenced by clear Van Hove peaks in UV-vis spectroscopy and relatively low defect derived D band intensity in Raman spectroscopy.^[206] Furthermore, as the process required no sonication-based dispersion step, the resulting SWNT network consisted of

exceptionally long SWNTs. Facile transferability is another advantage of the Aerosol SWNT films. Once deposited from the aerosol, the CNTs showed strong tube-to-tube interaction and assembled into a freestanding thin film. The SWNT films were easily peeled off from a nitrocellulose film by a pair of tweezers and transferred onto other substrates for device fabrication.

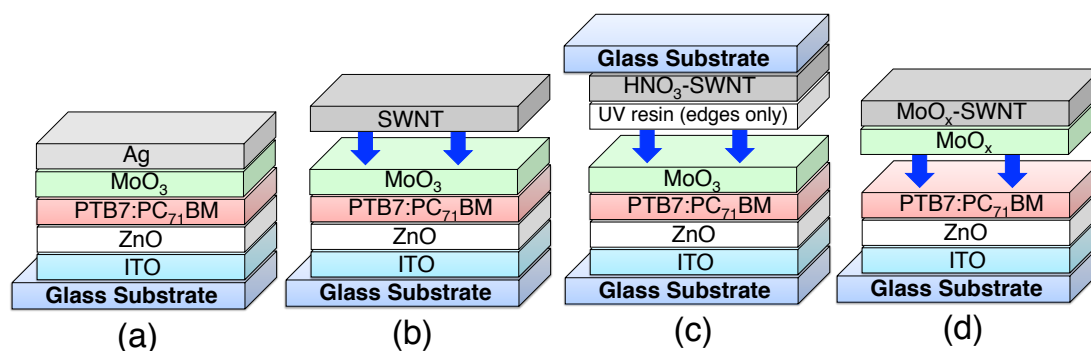


Figure 2. Illustrations of architecture of (a) a conventional inverted OSC, (b) a SWNT-based transparent OSC, (c) a HNO₃-doped SWNT-based transparent OSC, and (d) a MoO_x-doped SWNT-based transparent OSC.

The structures of SWNT-based transparent OSCs are shown in Figure 2. Figure 2a shows the conventional inverted OSC structure where Ag was used as an anode. This entails expensive metal deposition cost and leads to a non-transparent device. Figure 2b represents the same structure, except that Ag has been replaced by low-cost and highly transparent aerosol SWNT. Here, light can be shone either from ITO or SWNT sides, or both sides to generate photo-induced power. Thus, it can be called window-like transparent OSCs. The conductivity and the transparency of SWNT must be enhanced by doping in order to produce efficiency solar cells. Figure 2c and 2d demonstrate HNO₃-doped, and MoO_x-doped SWNT-applied window-like transparent OSCs, respectively. Due to the difficult nature of doping, two very different methodologies were employed and resulted in different architectures as illustrated. This will be discussed in detail later in this work. It is worth noting that a mixture of the low band gap polymer, PTB7 and the acceptor, PC₇₁BM with an additive, DIO has been used as the photoactive layer for all the devices on account of their high efficiency.

Photoluminescence quenching can demonstrate the charge extraction ability.^[149] A PTB7-based organic photoactive layer was deposited on a glass substrate

and a SWNT film was laminated from top. As shown in Figure 3, the spectrum of the organic photoactive layer was suppressed significantly when the SWNT film sat on top of it. This indicates effective charge extraction and successful lamination.

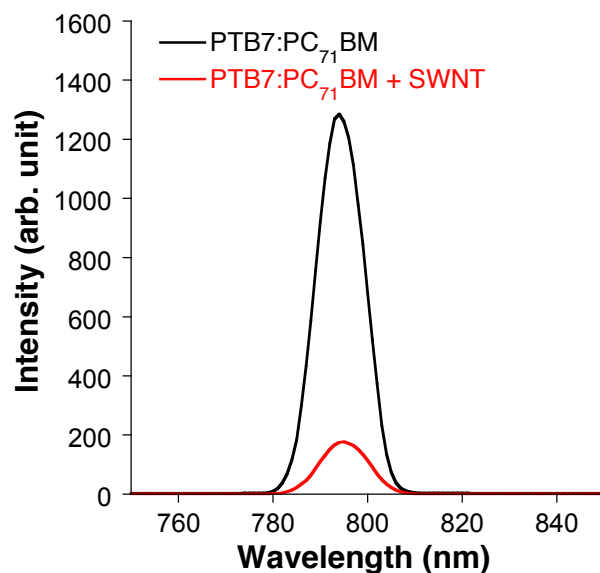


Figure 3. Photoluminescence spectrum of PTB7:PC₇₁BM active layer is subdued when SWNT film is over-coated on the very same active layer.

Table 1. Photovoltaic Performance for the SWNT-based transparent inverted OSCs under 1 sun, AM1.5G illumination (100 mW cm⁻²)

Device	Light direction	Anode	Dopant	V_{oc} (V)	J_{sc} (mA cm ⁻²)	FF	R_s (Ω cm ²)	R_{sh} (Ω cm ²)	PCE_{best} (%)
A	from ITO	Ag	None	0.73	16.0	0.65	16	6.4×10^4	7.8
B	from SWNT	SWNT T=90%		0.58	4.8	0.32	470	4.6×10^5	0.9
C	from ITO			0.66	6.5	0.40	320	8.9×10^4	1.8
D	with reflector			0.66	8.6	0.39	280	5.8×10^4	2.2
E	from ITO	SWNT	HNO ₃	0.69	9.5	0.56	70	1.5×10^4	3.7
F		T=90%	MoO _x	0.62	8.8	0.56	100	1.8×10^5	3.1
G		SWNT	HNO ₃	0.70	9.0	0.65	53	1.6×10^7	4.1
H		T=60%	MoO _x	0.68	8.2	0.60	61	8.4×10^5	3.4

Footnote: T = transmittance

First, OSCs using 90% transparent SWNT films were fabricated. Then, PCEs were measured with light shining from the SWNT side, the ITO side, and the ITO side with a mirror reflecting from behind. According to Table 1, different PCEs were

obtained depending on which direction light was coming from (Table 1: Devices B and C). When light was shone from the ITO side, a PCE of 2% was obtained which was approximately twice higher than the PCE when light was shone from the SWNT side (0.9%). These values are substantially low in comparison with the non-transparent conventional reference, Device A (7.8%). This is because the SWNT films were not doped. The UV-vis spectra (Figure 4a) revealed that ITO possessed higher transparency than 90% transparent SWNT. The difference got bigger when I included the whole device: the photoactive layer, ZnO, and MoO₃. As well as the intrinsic transmittance of the layers, the internal surface reflection between layers might also have augmented this difference. In other words, light shining on the ITO side is optically more favoured for the solar cell performance. This results in a higher PCE for Device B than that of Device C, for a larger number of photon is converted into higher J_{SC} for Device B. IPCE was measured to confirm this. As expected, when light was shone from the ITO side, more charges were extracted (Figure 4b).

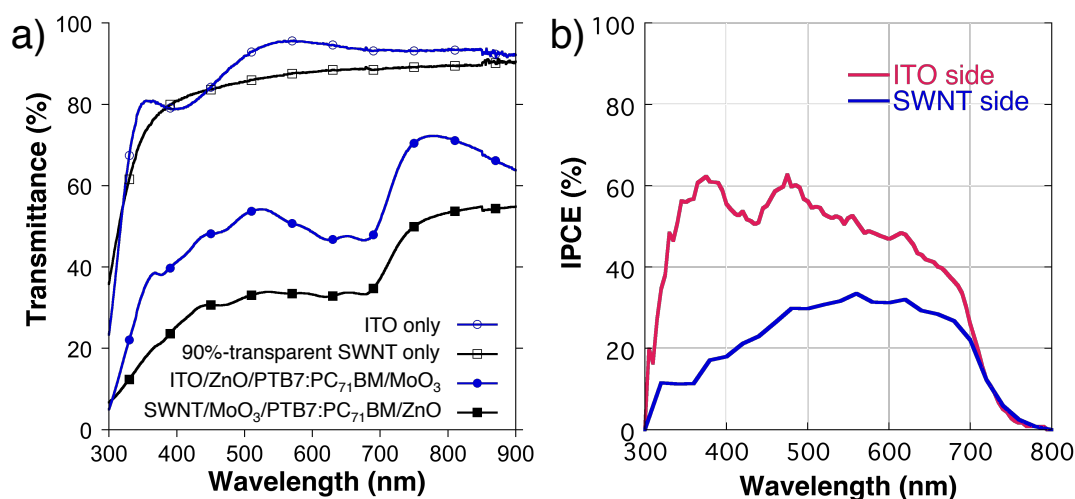


Figure 4. a) UV-vis transmittance measurement spectra of glass/ITO, glass/90%-SWNT, glass/ITO/ZnO/PTB7:PC₇₁BM/MoO₃, and glass/90%-SWNT/MoO₃/PTB7:PC₇₁BM/ZnO. b) IPCE measurement spectra of transparent OSCs when light is shone from ITO side and when light is shone from SWNT side.

Regarding the photovoltaic parameters in Table 1, Device B showed not only high J_{SC} but also higher V_{OC} and higher FF than those of Device C. This is a typical characteristic of solar cells that can be described by the Shockley equation. In principle, it is related to logarithmic scaling of V_{OC} with the light intensity.^[295] Therefore, Device C with higher J_{SC} will exhibit higher V_{OC} . Concerning FF, equation (1) shows that FF is affected by V_{OC} too.^[296] This is especially so with real solar cell

devices which show a non-ideal diode behaviour. Thus, low J_{SC} can induce low V_{OC} and FF.

$$FF = \frac{V_{OC} - \ln(V_{OC} + 0.72)}{V_{OC} + 1} \quad (1)$$

The value of shunt resistance (R_{SH}) is especially important in transparent OSCs because there is not enough light intensity. With low light intensity, both the bias point and the current of the solar cell devices will decrease. This causes the equivalent resistance of the solar cell devices to approach R_{SH} .^[297] If the equivalent and shunt resistances are similar, the fraction of the total current flowing through the R_{SH} will increase and this may lead to recombination of charges. So it is crucial that we have a device system with a high enough R_{SH} value to avoid recombination can happen which will undercut device performance. From the J - V curves shown in Figure 5a and 5b, We can see that 90% transparent SWNT applied OSCs possess sufficiently high R_{SH} regardless of the light direction. Therefore, it confirms that no recombination is taking place.

In the conventional OSCs' case, metal electrodes can act as a rear reflector to direct unabsorbed light back to the photoactive layer. This provides a higher photocurrent especially in the wavelength region shorter than 700 nm. However, for the transparent OSCs, because the no light can be reflected back and the active material is not thick enough to absorb all of the sunlight, much light going through unabsorbed. When a silver reflector (mirror) was introduced at the opposite side of the light source, the J_{SC} increased from 6.5 mA cm⁻² to 8.6 mA cm⁻² (Table 1: Device D; Figure 5d). However, despite the enhanced light intensity, V_{OC} and FF did not improve any further. This reveals that the maximum V_{OC} obtained from use of pristine 90% transparent SWNT is limited to around 0.66. I suspect this could be due to imperfect interface contact between SWNT and MoO₃.^[298,299] In general, V_{OC} is controlled by difference between HOMO of a donor and LUMO of an acceptor; what is more, the HOMO and LUMO are affected by the interfacial layers' Fermi levels and electrodes' work functions.^[300] Therefore, in my belief, poor contact between SWNT and MoO₃ was the limiting factor for the V_{OC} . The overall PCE improvement was only 0.4%. This concludes that the double-sided light response feature of the

transparent OSCs leads to sufficient photon excitations that the application of a reflector at the cost of losing window-like transparency is not necessary.

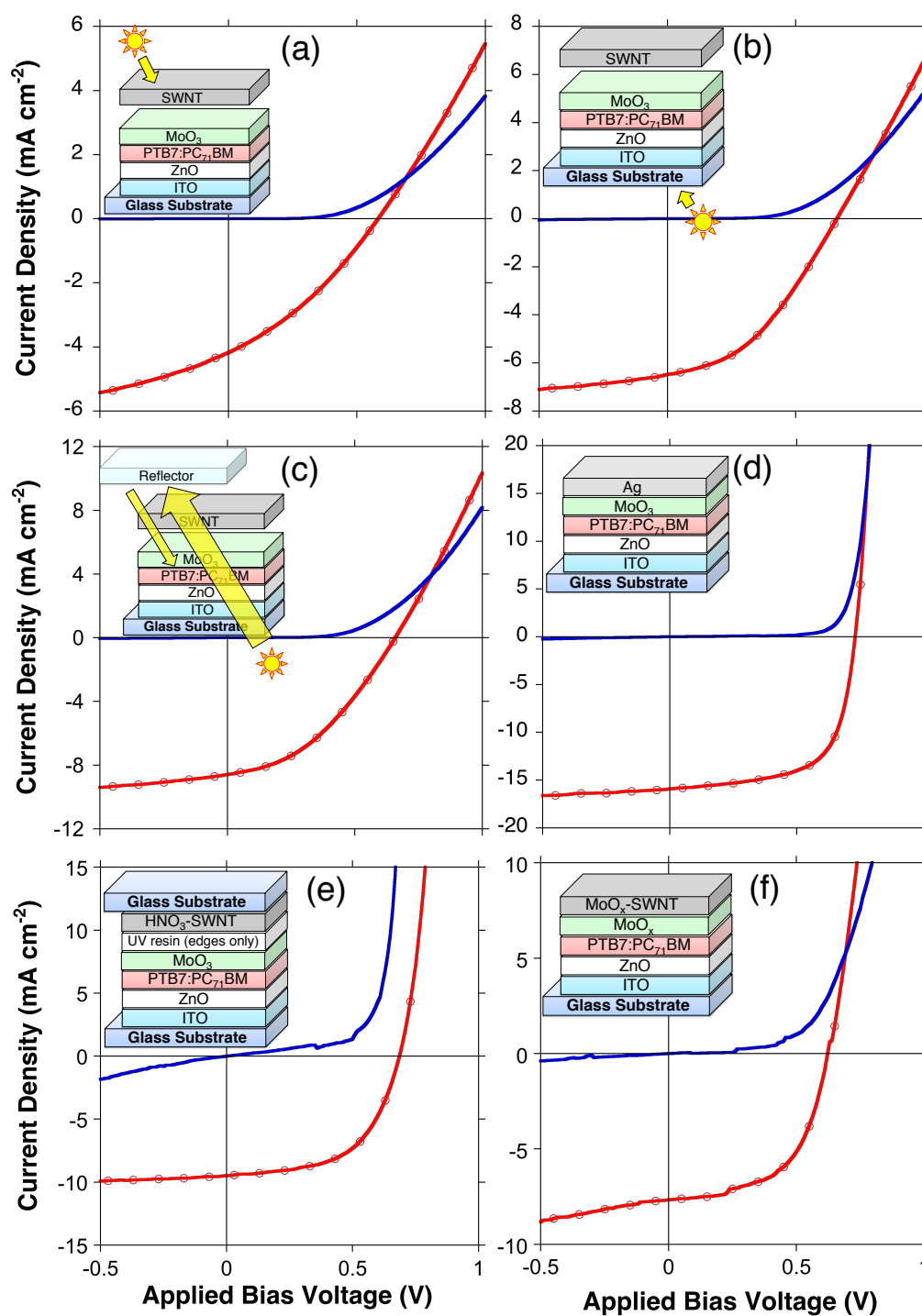


Figure 5. J - V curves under 1 sun (red dotted) and in dark (blue plane) of (a) a SWNT-based transparent OSC with light from the SWNT side, (b) a SWNT-based transparent OSC with light from the ITO side, (c) a SWNT-based transparent OSC with light from the ITO side and a reflector, and (d) a conventional inverted OSC.

Though transparent OSCs have been demonstrated, SWNT should be doped to improve its conductivity and transmittance to boost the PCE. So far, doping SWNT, which is being laminated from top, has not been reported yet. This is owing to mechanical difficulty of the doping: unlike SWNT on a glass substrate, doping the top-laminated SWNT will damage the device underneath. Hence, in this work, I devised two methodologies of safely doping SWNT by HNO_3 and MoO_3 each.

Application of $\text{HNO}_3(\text{aq})$ acid has been reported to be one of the most effective doping methods.^[227] Nevertheless, its strong acidic nature makes it impossible to apply directly: When a drop of HNO_3 was applied on a SWNT laminated device, it percolated through the film and utterly destroyed the organic materials underneath (Figure 6). Therefore, doping had to be performed on SWNT only first. Figure 7a illustrates how the HNO_3 -doped Sandwich-transfer can be proceeded. One droplet of HNO_3 was applied to a SWNT film on a glass substrate followed by heating at 80 °C for 5 min to dry up. The SWNT film turned slightly reddish as the acid dried up and this signified successful doping. The HNO_3 -SWNT was then transferred onto a quasi-fabricated OSC interfacing a MoO_3 film like a sandwich. UV resin was applied at the edges only to reinforce the adhesion. A PCE of 3.7% was achieved with the light source positioned at the ITO side (Table 1: Device E). Enhancement in J_{SC} and reduction in R_s confirmed improvement of the transparency and the conductivity of HNO_3 -doped SWNT. Increase in V_{OC} meant that the interfacial contact improved. This I surmise is owing to pressure applied on HNO_3 -SWNT during the Sandwich-transfer.

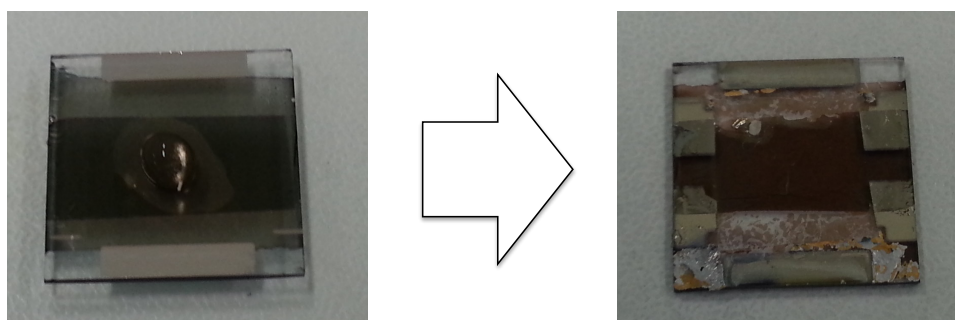


Figure 6. Application of $\text{HNO}_3(\text{aq})$ directly onto a SWNT-based transparent OSC (left) will lead to a holistic destruction of the device system (right) within 5 h.

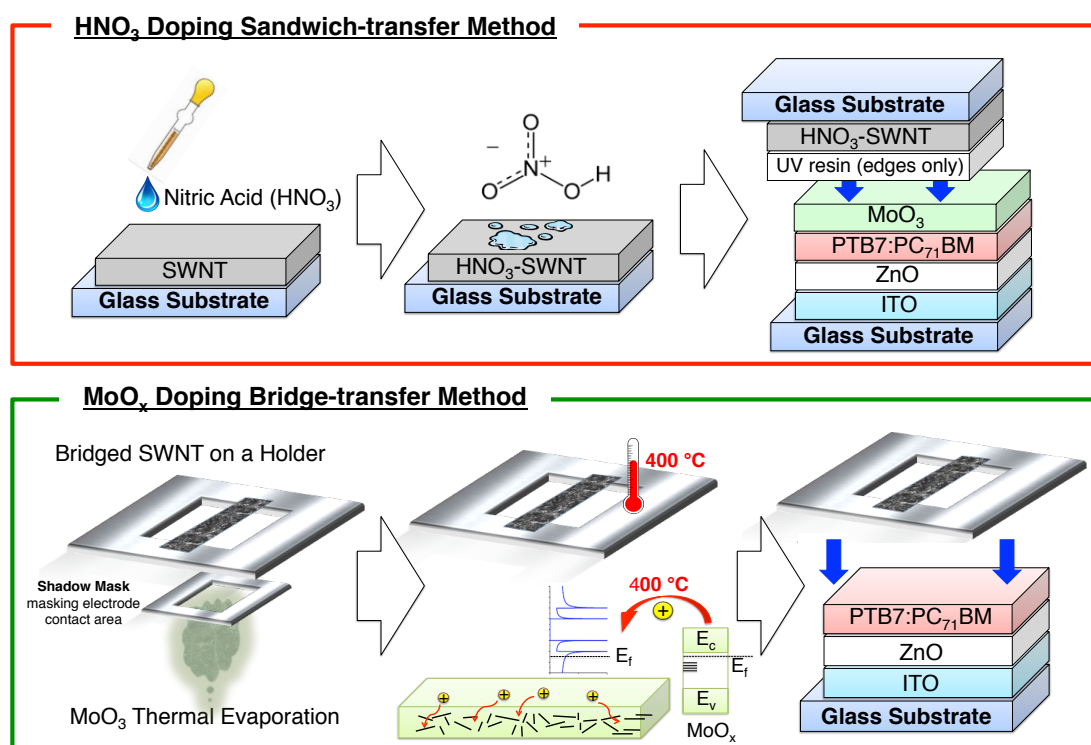


Figure 7. Graphical illustrations of (a) HNO₃ doping Sandwich-transfer process (above) and (b) MoO_x thermal doping Bridge-transfer process (below).

Thermal MoO_x doping of SWNT is known to be more stable doping than HNO₃ in spite of its marginally lower effectiveness.^[191] Its successful application in OSCs has been reported.^[183] However, again this is not applicable to the SWNT films laminated from top, because it undergoes high temperature annealing process of above 300 °C. Thus, I propose bridge-transfer methodology (Figure 7b). SWNT was transferred onto a metal holder where a SWNT film hung like a bridge (Figure 8). Then a shadow mask was placed below the SWNT film to mask the electrode contact area. MoO₃ was deposited from below through vacuum thermal evaporation. MoO₃-SWNT was then annealed at 400 °C together with the holder to boost the doping effect: MoO₃-SWNT was reduced to MoO_x-SWNT where x is between 2 and 3.^[191] MoO_x-SWNT was gently laminated using the holder onto a quasi-fabricated device where the MoO₃ film was not deposited because the MoO_x on the SWNT can function as both a dopant and ETL. A PCE of 3.1% was recorded for this device (Table 1: Device F). Lower J_{SC} and higher R_s than those of Device E were observed because MoO_x thermal doping is known to be less effective than HNO₃ doping. An important point to note in this methodology is that because the SWNT hung precariously on the metal holder, extra caution was necessary during the handling. Any small external impact or draught strong enough to crumple the SWNT created micro-wrinkles on

SWNT films, which were invisible to naked eye but only by atomic force microscopy (Figure 9). Lower V_{OC} in this device possibly came from two reasons: The first reason is the remnants of micro-wrinkles undermining the interface. Second reason is that pressure was not applied during the lamination of SWNT unlike the Sandwich-transfer method. Compared to the HNO_3 -SWNT Sandwich-transfer, this method manifested lower reproducibility due to sensitive process.

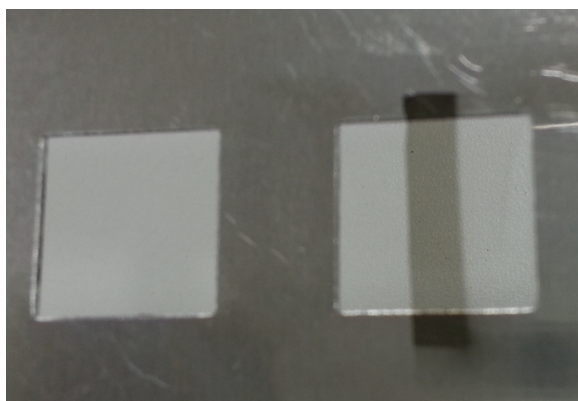


Figure 8. A picture of a SWNT film bridged on a holder

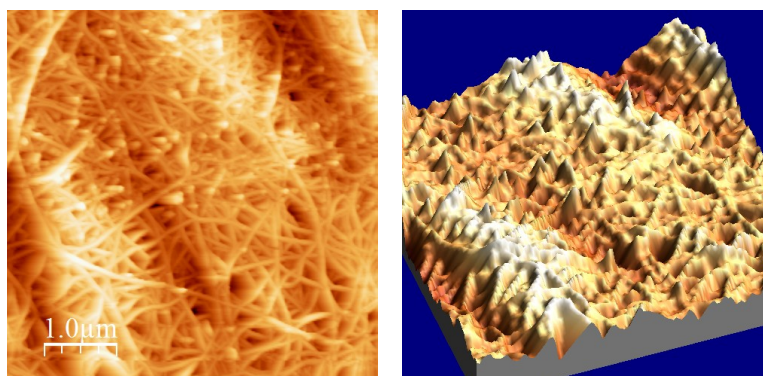


Figure 9. AFM 2D image (left) and 3D image (right) of micro wrinkles formed on bridge-transferred SWNT.

Despite high PCEs, both doping methodologies suffered from instability with J - V sweeps (Figure 3e and 3f). I ascribe this to the mechanical instability of the fabrication i.e., possible excess pressure applied on SWNT during the HNO_3 -SWNT Sandwich-transfer, and delicate nature of the MoO_x -SWNT Bridge-transfer. However, if mechanical optimisations are followed, high efficient and stability will be obtained.

Thicker SWNT films possess higher conductivity, but their transmittance is lower. By incorporating the thicker SWNT films (60% transparency at 550 nm wavelength), higher PCEs were obtained (Figure 10 and 11). HNO_3 -doped device

produced 4.1% (Table 1: Device G) and MoO_x-doped device produced 3.4% (Table 1: Device H). Arising from the higher conductivity of the 60%-SWNT films, FF was higher than that of the 90%-SWNT-based devices by around 0.1. Interestingly, V_{OC} of Device H was higher than expected. I attribute this to thicker SWNT films being less vulnerable to the micro wrinkle formation during the Bridge-transfer. Despite lower transmittance of the films, both Device G and H displayed rather high J_{SC} , because the main source of photon comes from the ITO side not the SWNT side. While it may appear obvious to employ thicker SWNT to gain higher PCEs, using them will substantially undermine the window-like visual of transparent OSCs (Figure 12). The improvement of PCE only came in the expense of window-like transparency.

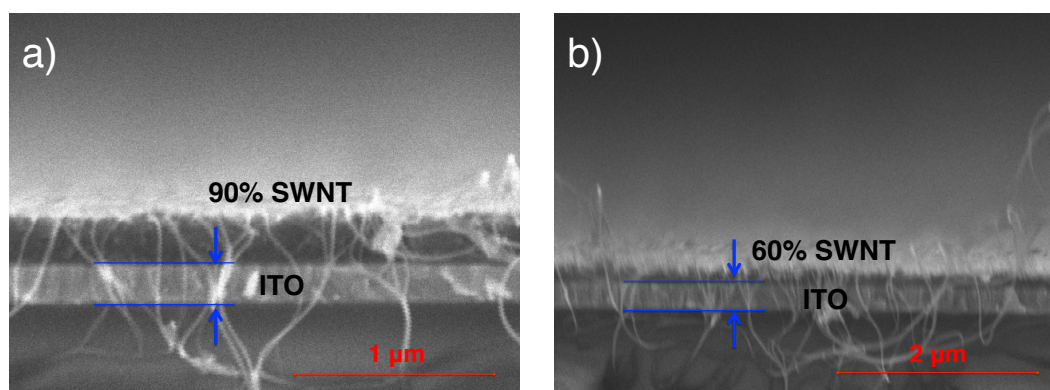


Figure 10. Cross-sectional SEM images of transparent OSC devices with a) a 90%-SWNT film and b) a 60%-SWNT film.

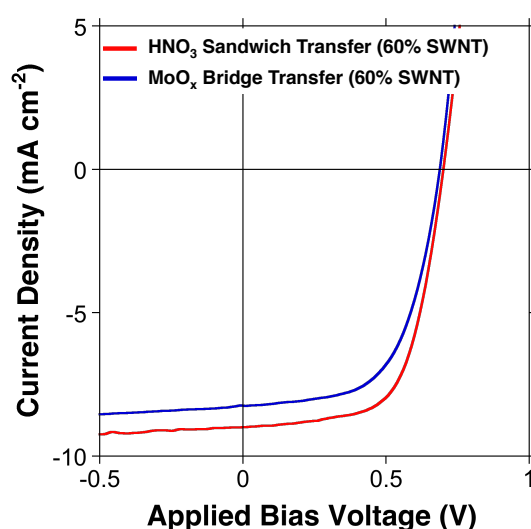


Figure 11. J - V curves of 60% transparent SWNT-based transparent OSCs when the HNO₃ Sandwich transfer method is applied (red) and the MoO_x Bridge transfer method is applied (blue)

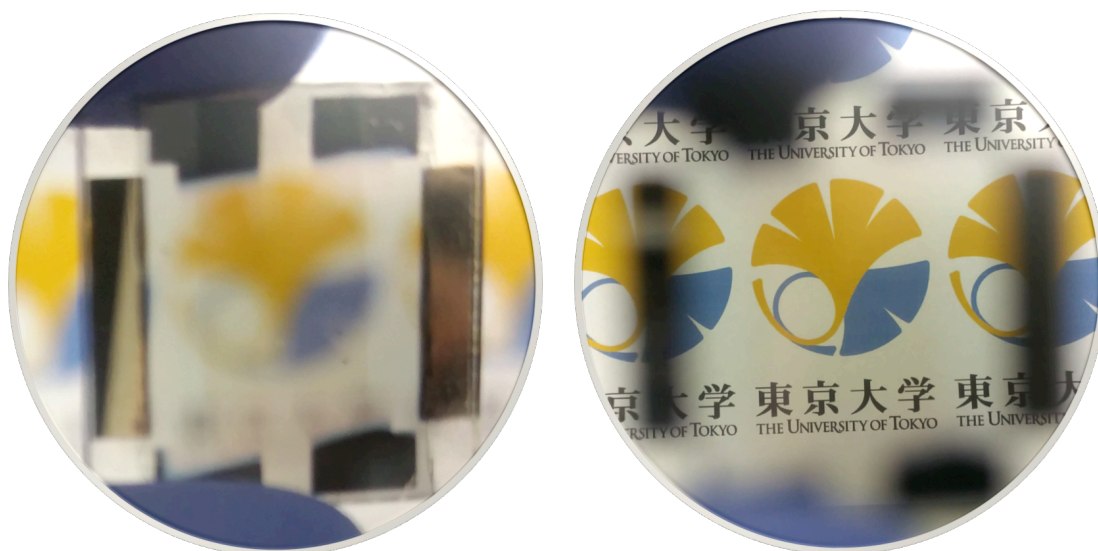


Figure 12a. Pictures of 90% transparent SWNT-based transparent OSC when focused on the device (left) and on a behind object, the University of Tokyo logo (right).

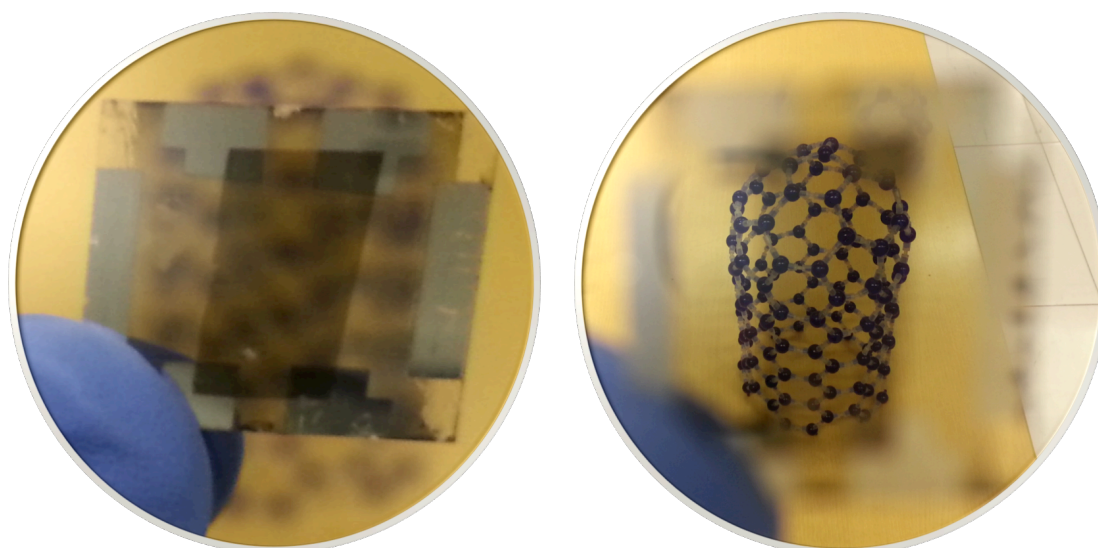
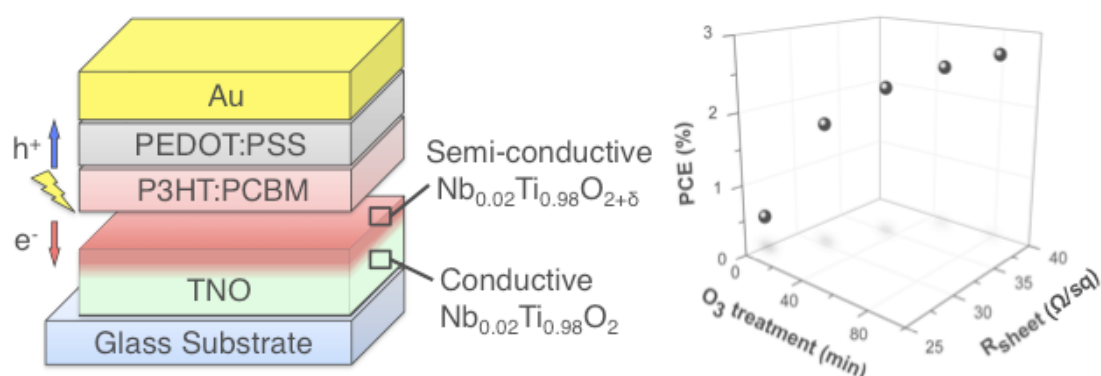


Figure 12b. Pictures of 60% transparent SWNT-based transparent OSC when focused on the device (left) and on a behind object, the SWNT plastic model (right).

6.5 Conclusion

In conclusion, non-doped SWNT (90% transmittance)-based $\text{MoO}_3/\text{PTB7}:\text{PC}_{71}\text{BM}:\text{DIO}/\text{ZnO}/\text{ITO}$ window-like transparent OSCs showed a PCE of 1.8%. Aerosol synthesised SWNT electrode, which was laminated from above as a top-electrode showed facile processability, chemical stability, electrical compatibility,

and mechanical resilience. By applying p-doping on SWNT through HNO₃ Sandwich-transfer and MoO₃ Bridge-transfer methods, both of which are unprecedented, PCEs of the transparent OSCs further improved to 3.7% and 3.1%, respectively. Obtaining an even higher PCE of 4.1% was possible at the cost of transparency by incorporating thicker SWNT films. By replacing metal electrodes, these OSCs showed advantageous properties of low-cost, window-like transparency, and glare-free visuals. This research successfully demonstrated a promising potential in window solar cell applications and flexible tandem OSCs.



CHAPTER 7

OZONE-TREATED NIOBIUM-DOPED TITANIUM OXIDE AS BOTH THE CONDUCTIVE LAYER AND CHARGE SELECTIVE LAYER IN INVERTED ORGANIC SOLAR CELLS

7.1 Summary

This chapter reports an inverted solar cell, where simple UV-ozone treatment changed non-indium electrode into integrated film of semiconductor and conductor. Niobium doped titania ($\text{Nb}_{0.02}\text{Ti}_{0.98}\text{O}_2$), which was subjected to O_3 treatment for 90 minutes, exhibited a dual-functionality of electron-transporter at the surface and electrode in the bulk. Therefore, an additional deposition process of ETL such as ZnO was not necessary for the application in inverted solar cells. The longer the O_3 treatment was applied on the film, the better the solar cell performed. While indium tin oxide-based reference device (ITO/ZnO/P3HT:PCBM/PEDOT:PSS/Au) showed an average power conversion efficiency of 2.91%, the novel device (TNO/P3HT:PCBM/PEDOT:PSS/Au) showed an average of 2.75% with higher reproducibility. This finding will render a simpler and lower-cost fabrication of indium-free inverted OSCs.

7.2 Introduction

Recently, anatase niobium doped titanium oxide (TNO), $\text{Ti}_{1-x}\text{Nb}_x\text{O}_2$ has been developed.^[301] As a transparent conductive oxide, TNO meets the requirement of 80% above transparency and possesses the resistivity of minimum $2 \times 10^{-4} \Omega\text{cm}$ in epitaxial thin film form. Also TNO has a higher dielectric constant which leads to larger effective mass in the infrared region.^[302–304] In addition, TNO can tolerate a temperature above 300 °C, which, in fact, enhances its hall mobility.^[305] Despite such advantages, the TNO application was focused mainly on dye-sensitised solar cells, and only few OSCs are reported.^[155–157,306]

In this work, TNO electrode films were prepared in a manner that both the transmittance and sheet resistance are optimal for OSC applications. For this purpose, niobium dopant stoichiometry in TNO was reduced to 2at%.^[303] Additionally, TNO was annealed at temperature over 600 °C under H_2 to optimise oxygen stoichiometry for the optimal conductivity. Moreover, UV-ozone (O_3) treatment was applied on TNO films for a certain period of time to induce surface oxidation. Intrusion of oxygen species caused Nb[IV] and Ti[III] at the TNO surface to oxidise to Nb[V] and Ti[IV], losing free electron carriers as evidenced by analyses in this work. Thus, oxidised surface ($\text{Nb}_{0.02}\text{Ti}_{0.98}\text{O}_{2+\delta}$) manifested semiconducting behaviour, which functioned as an ETL. Air-processed inverted type OSCs fabricated using O_3 -treated TNO without an ETL deposition process produced an average PCE of 2.75% with higher reproducibility, while ITO-based OSCs, where ZnO had to be deposited as the ETL, produced 2.91%. Finding of such phenomenon offered eradication of the ETL deposition process in the inverted OSC fabrication. I anticipate cost reduction, reproducibility enhancement, and a breakthrough in fabrication of the solar cell research field.

7.3 Experimental Procedures

7.3.1 Device Fabrications

Please refer to ‘2.1.1.2 Organic solar cell inverted device architecture’, and

‘2.1.1.3 P3HT:mix-PCBM solution preparation’.

7.3.2 TNO Film Fabrication

The TNO films used in this study were fabricated via crystallisation of amorphous precursor films. The as-deposited precursor TNO films were grown on unheated alkaline-free glass substrates (Corning, Eagle XG) by radio frequency (RF) magnetron sputtering. A commercially available ceramic disc of $\text{Ti}_{0.98}\text{Nb}_{0.02}\text{O}_{1.93}$ (Toshiba MFG) was used as a sputtering target. RF power applied to the target was 100 W. Sputter deposition was conducted in an Ar and O_2 gas mixture. The total gas flow rate and working pressure were 5 standard cubic cm per minute and 1 Pa, respectively. The oxygen partial pressure during deposition was 6×10^{-4} Pa. The base pressure in the sputtering chamber was 5×10^{-5} Pa. The amorphous precursor films were isothermally crystallise into polycrystalline anatase phase, and were then annealed in reducing ambient (5% H_2 + 95% Ar) at 600 °C in order to improve electrical and optical properties.

7.3.3 Characterisations

Please refer to ‘2.2.1.1 Current-voltage characterisation’, ‘2.2.1.4 Impedance measurement’, ‘2.2.2.1 UV-vis absorption’, ‘2.2.2.3 Atomic force microscopy (AFM)’, ‘2.2.2.4 Scanning electron microscopy (SEM)’, ‘2.2.2.5 Transmission electron microscopy (TEM)’, ‘2.2.2.6 X-ray photoelectron spectroscopy (XPS)’, ‘2.2.2.7 X-ray powder diffraction (XRD)’, ‘2.2.2.8 Photoelectron yield spectroscopy (PYS) and Kevin probe’, and ‘2.2.2.13 Four-probe measurement’.

7.4 Results and Discussion

First of all, OSCs were fabricated using TNO films with different thicknesses from 200 nm to 800 nm without O_3 treatment. A ZnO layer was deposited on TNO as the ETL (Figure 1b). Table 1 and Figure 2 show the photovoltaic performances of the devices and corresponding J - V curves, respectively. The device with 300-nm-thick TNO produced the highest PCE of 2.31%, which is decent considering ITO-free device. It was expected that if the films get thicker, the sheet resistance would

decrease, while the transmittance would decrease. Accordingly, both the R_s and J_{sc} decreased with an increase in thickness. This trend is also observed in the UV-vis transmittance data (Figure 3a). However, there was a reverse trend in J_{sc} between 200 nm and 300 nm. The UV-vis spectra (Figure 3b) show that 200-nm-thick TNO film possesses similar transmittance to that of the 300-nm-thick TNO film. Therefore, 300 nm was deemed to be the optimum thickness for TNO in OSCs.

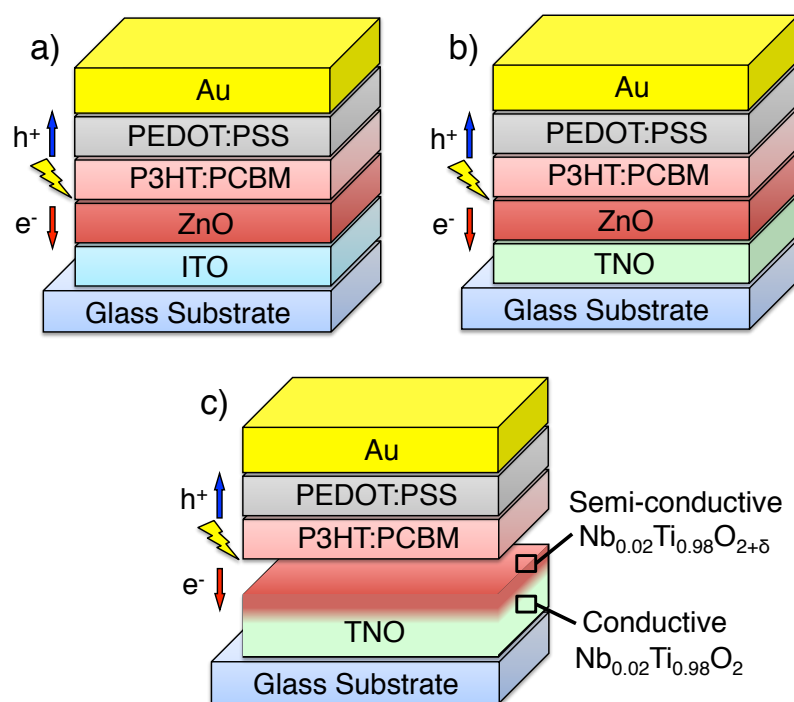


Figure 1. Graphical structure illustrations of (a) a conventional inverted OSC, (b) a TNO-based OSC with ZnO as the ETL, and (c) an O_3 -treated TNO-based OSC without ZnO.

Table 1. Photovoltaic performance (average and standard deviation error range) of OSCs using TNO with different thicknesses, and ITO as a reference device.

Electrode [thickness]	ETL	V_{oc} (V)	J_{sc} ($mA\ cm^{-2}$)	FF	R_s (Ω)	R_{sh} (Ω)	$PCE_{average}$ (%)
TNO [800 nm]	ZnO	0.60 ± 0	5.36 ± 0.06	0.56 ± 0.01	23.1	1.2×10^6	1.81 ± 0.01
TNO [600 nm]	ZnO	0.61 ± 0	6.77 ± 0.23	0.53 ± 0.00	24.7	5.4×10^5	2.15 ± 0.07
TNO [400 nm]	ZnO	0.60 ± 0	7.45 ± 0.19	0.51 ± 0.05	25.7	4.3×10^5	2.29 ± 0.28
TNO [300 nm]	ZnO	0.62 ± 0	8.51 ± 0.14	0.49 ± 0.03	27.6	1.9×10^4	2.31 ± 0.02
TNO [200 nm]	ZnO	0.62 ± 0	7.69 ± 0.38	0.29 ± 0.03	77.9	4.9×10^4	1.41 ± 0.24
ITO	ZnO	0.61 ± 0	9.72 ± 0.20	0.49 ± 0.03	5.5	2.2×10^4	2.91 ± 0.22

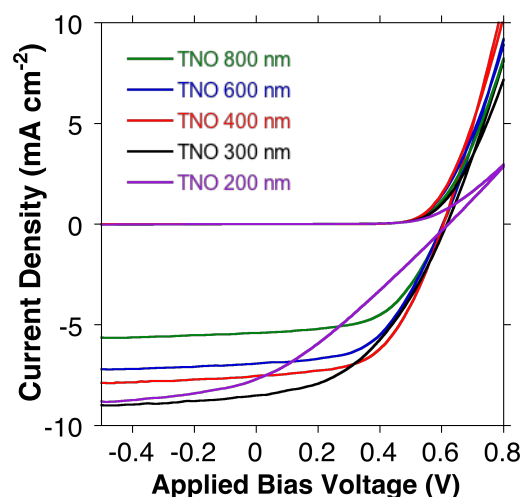


Figure 2. *J-V* curves of OSCs where TNO films with different thicknesses have been used.

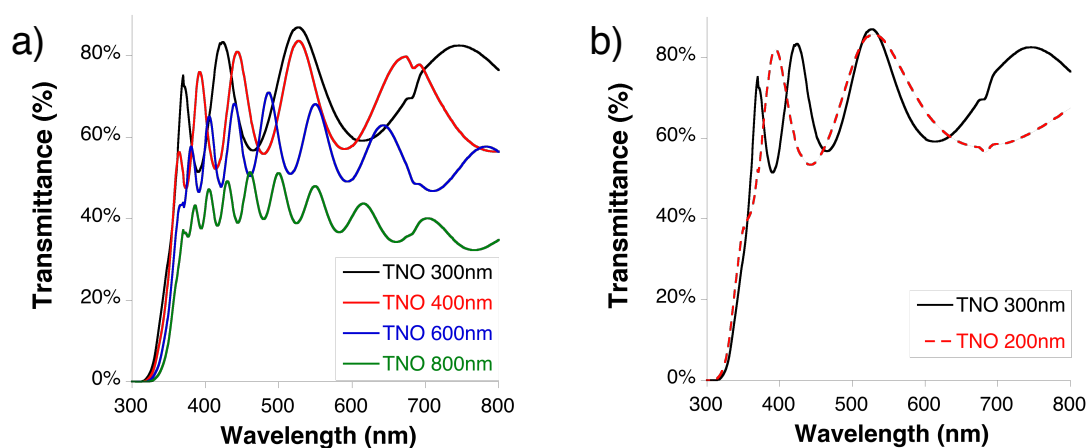


Figure 3. UV-vis transmittance spectra of TNO films with different thicknesses. (a) Thicknesses from 800 nm to 300 nm. (b) Thicknesses of 300 nm and 200 nm.

This time, O₃ treatment was imposed on 300-nm-thick TNO films from 0 to 90 minutes followed by OSC device fabrications in air without deposition of the ETL (Figure 1c, Table 2). The 90 minutes O₃-treated TNO-based device produced an average PCE of 2.75% without a deposition of ZnO. The result was as good as the ITO-based device where a ZnO layer had to be used (2.91%; Figure 1a). In addition, since the ETL deposition step was not necessary, the reproducibility was much better for the TNO-based devices (± 0.02) than the ITO-based control device (± 0.22).

Table 2. Photovoltaic performance (average and standard deviation error range) of OSCs using TNO with different O₃ treatment timespans without the ETL, and ITO-based reference device with and without the ETL.

Cathode	O ₃ treatment (min)	V _{OC} (V)	J _{SC} (mA cm ⁻²)	FF	R _S (Ωcm ²)	R _{SH} (Ωcm ²)	PCE _{average} (%)
TNO	0	0.24±0.14	6.26±0.88	0.28±0.03	23.3	720	0.45±0.35
TNO	15	0.55±0.03	6.11±0.45	0.51±0.04	14.4	1.1 x 10 ³	1.69±0.09
TNO	30	0.57±0.01	6.98±0.60	0.54±0.03	15.2	7.7 x 10 ³	2.13±0.10
TNO	60	0.59±0.01	7.59±0.17	0.56±0.02	13.5	3.7 x 10 ⁴	2.49±0.09
TNO	90	0.60±0.02	8.29±0.67	0.55±0.06	18.4	1.2 x 10 ⁵	2.75±0.02
ITO/ZnO	0	0.61±0.01	9.72±0.20	0.49±0.03	5.5	2.2 x 10 ⁴	2.91±0.22
ITO	60	0.07	5.02	0.25	10.2	12	0.09

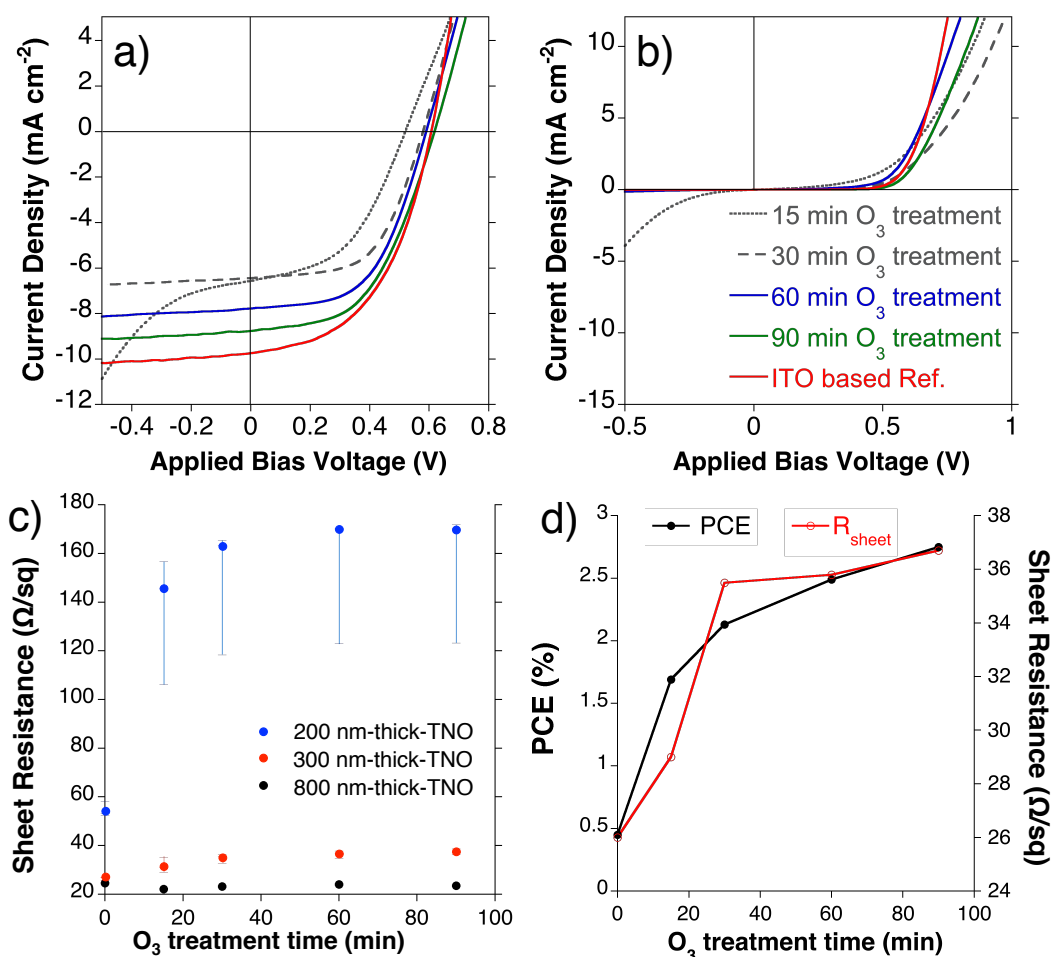


Figure 4. The *J-V* curves of the O₃-treated TNO-based OSCs and an ITO-based control device under (a) 1 sun, and (b) dark. (c) 4-Probe measurement data of TNO films with different thicknesses. Averages (blob) and ranges (line) represented according to the O₃-treatment time. (d) A double Y graph representing relationship between PCE, R_{sheet}, and O₃ treatment time.

According to Table 1, the ITO-based control device without the ETL gave a poor PCE (0.09 %) regardless of the O₃ treatment time. Therefore, the ETL deposition step was mandatory for the conventional OSCs. Whereas, for the TNO-based devices, they showed an average PCE of 0.45% even without the ETL and its performance increased with the O₃ treatment time. The photovoltaic data and corresponding *J-V* curves (Figure 4a and b) indicate that J_{SC} and R_{SH} improved dramatically with the O₃ treatment time. Since the increase in those two parameters represent an enhanced ability of charge-extraction without surface recombination,^[307,308] TNO functioned as the ETL and its effect got stronger with the O₃ treatment time. Incidentally, the V_{OC} showed the same behaviour. As it is known that V_{OC} values can serve as an indicator of an incomplete coverage of the ETL, it was clear that a long O₃ treatment ensured no shunt pathway between the photoactive layer and the TNO electrode.^[309,310] R_{sheet} of TNO films measured by four-probe measurement showed a significant increase after O₃ treatment followed by saturation with longer O₃ timespan (Figure 4c). The oxidation and reduction kinetics of niobium-based materials are known to be slow and the surface oxide diffusion is limiting.^[311] Hence, we can expect a slow oxidation in TNO surface reaching a certain limit with O₃ treatment as displayed by the R_{sheet} and PCE data (Figure 4d). Thus, a valid conjecture that O₃-treatment is creating ETL at the surface of TNO could be made.

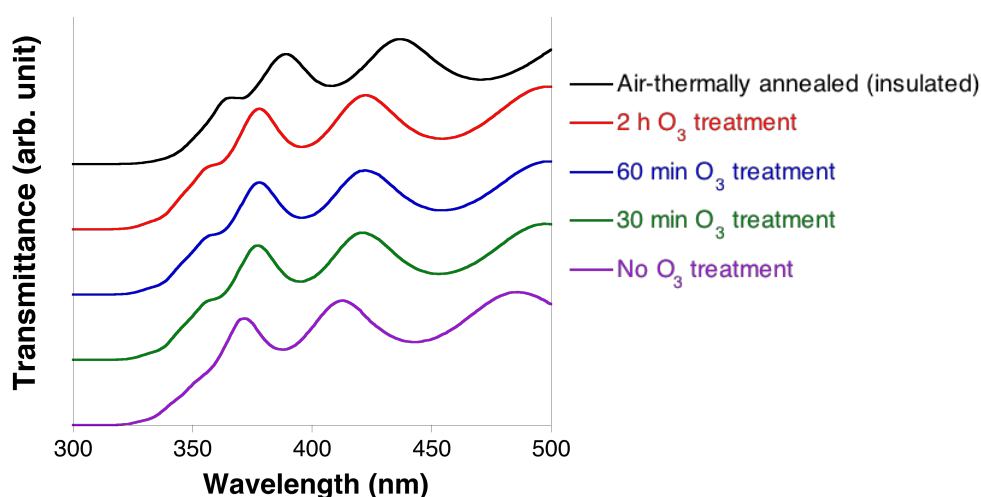


Figure 5. The UV-vis transmittance data of TNO films with no O₃ treatment, different O₃ treatment timespans, and air-thermal insulation.

UV-vis transmittance of TNO films before and after O_3 treatment with different timespans, and air-thermal annealing ($600\text{ }^\circ\text{C}$) was measured (Figure 5). The data shows that O_3 treatment increased the refractive indices (RIs) of the TNO films slightly and bigger increase was observed for the air-thermal insulated TNO films. It is reported that RI is inversely proportional to the band gap of materials.^[312–314] Therefore, it can be said that the conductive TNO film, which is a degenerate semiconductor, decreased its band gap by losing Burstein-Moss shift upon oxidation (Figure 6a). Unfortunately, difference among TNOs with different O_3 treatment timespans could not be distinguished. I speculate that this is owing to markedly thin layer of TNOs' oxidised surfaces. Figure 6b illustrates how RIs were derived from the spectra. When conductive TNO surface was oxidised by either O_3 or air-thermal annealing, fringe interference of the spectrum changed towards more maxima and minima in the pattern. The interference arises from difference in RIs between the air and a TNO film. This causes retardation of the travelling light by the film's effective RI (or thickness). Depending on wavelength of the light, constructive or destructive superposition is formed creating maxima and minima, respectively.^[315]

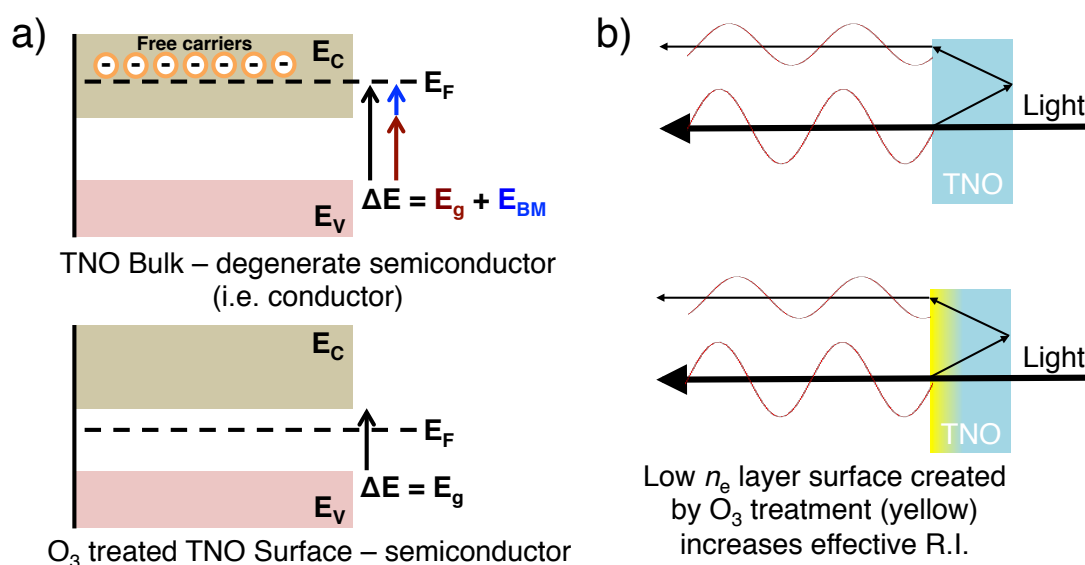


Figure 6. Graphical illustrations of (a) Burstein-Moss shift in conductive bulk TNO (above) and semiconducting surface of O_3 -treated TNO (below), and (b) the light superposition in pristine TNO (above) and O_3 -treated TNO (below).

The difference in O₃ treatment time effect on TNO was observed by XPS measurement (Figure 7). A strong Ti⁴⁺ peak at around 458.4 eV, which corresponds to Ti 2p_{3/2} core, appeared as shown in Figure 4b. The individual spectrum was magnified to observe relatively weak Ti³⁺ peaks, which indicate that a small portion of Ti atoms exist as free carrier Ti[3+] with a nominal d¹ configuration (Figure 7c–f).^[316] With an increase in the O₃ treatment time, the Ti³⁺ peak decreased and when it was air-thermally insulated, the peak was not observable in shoulder. Figure 7a show Nb 3d core XPS spectra. The two peaks indicate a mixture of typical NbO₂ and Nb₂O₅.^[317] Nb stoichiometry being too low (2%), characteristic difference between Nb⁴⁺ peak of conductive NbO₂ and Nb⁵⁺ peak of semiconducting Nb₂O₅, were not observable.^[318,319]

The valence bands and Fermi levels of TNO were measured by PYS and Kelvin probe force microscopy. I found that the conductive TNO film before the O₃ treatment had a work function of 5.0 eV. After the O₃ treatment, it possessed the Fermi level at around 5.1 eV and a valence band at 6.4 eV. The values did not change with the O₃ treatment timespan. A commonly used ETL, TiO₂ prepared by a chemical bath deposition was also measured for comparison.^[184] It possessed the Fermi level of 5.3 eV and the valence band at 6.1 eV. My measurement as well as other reports indicate lower lying valence band of TNO than TiO₂.^[320,321] This explains why TNO-based OSCs showed exceptionally higher R_{SH} , thus being better ETL.

The TNO surface was smoother than ZnO surface according to AFM (Figure 8). The roughness increased with an increase in film thickness, which is a typical behaviour of a sputtered film. Furthermore, there was no difference observed in AFM before and after O₃ treatment. Cross-sectional high resolution TEM was used on the O₃-treated TNO, but it did not show significant difference (Figure 9). X-ray diffraction data revealed that anatase phase of TNO was retained even after the O₃ treatment (Figure 10).

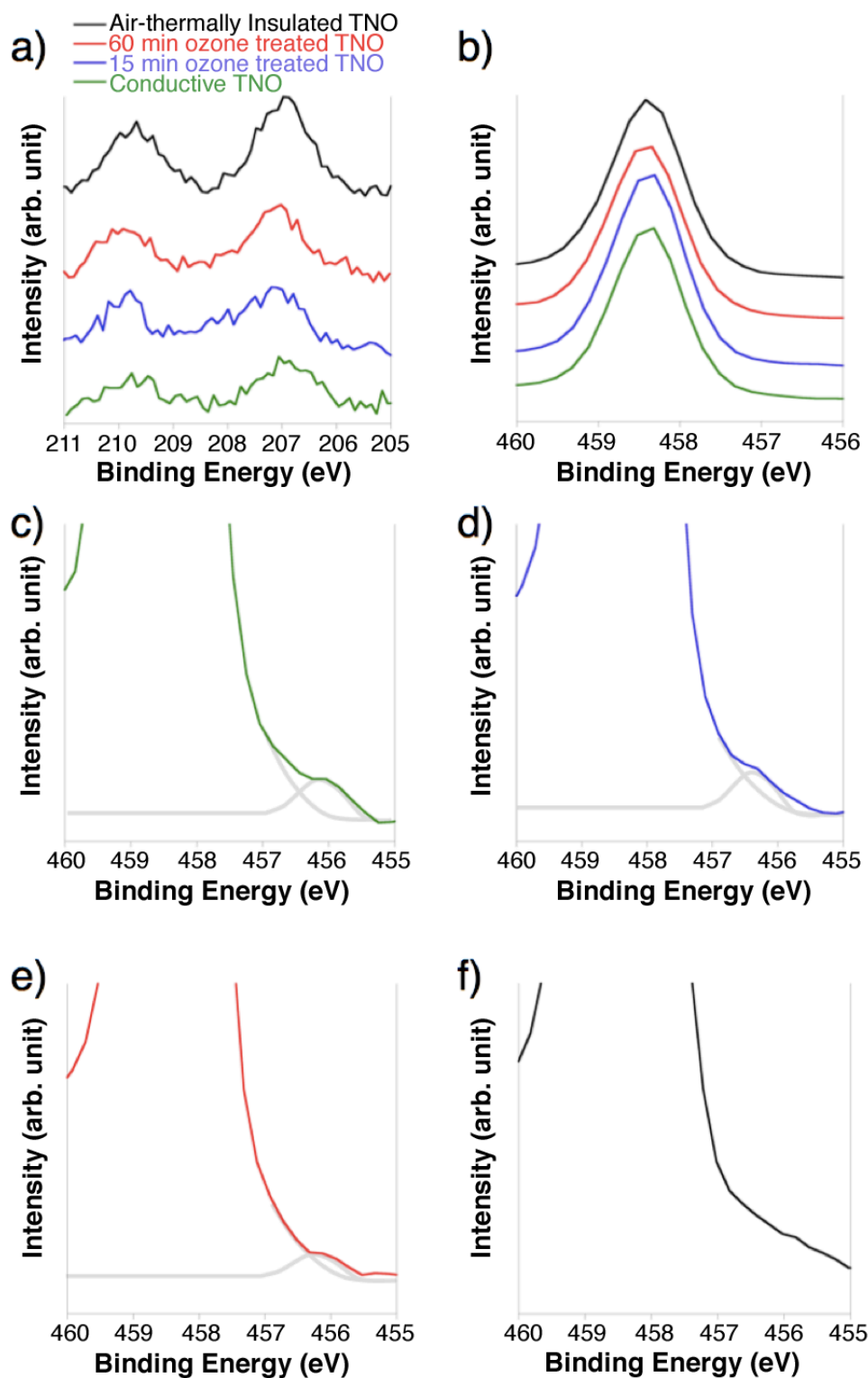


Figure 7. (a) Nb 3d core X-ray photoemission spectra and (b) Ti 2p_{3/2} core X-ray photoemission spectra of a conductive TNO, 15 minutes O₃-treated TNO, 60 minutes O₃-treated TNO, and air-thermally insulated TNO. Legends are placed in order of the spectra position. Magnified Ti 2p_{3/2} core X-ray photoemission spectrum of (c) conductive TNO, (d) 15 minutes O₃-treated TNO, (e) 60 minutes O₃-treated TNO, and (f) air-thermally insulated TNO.

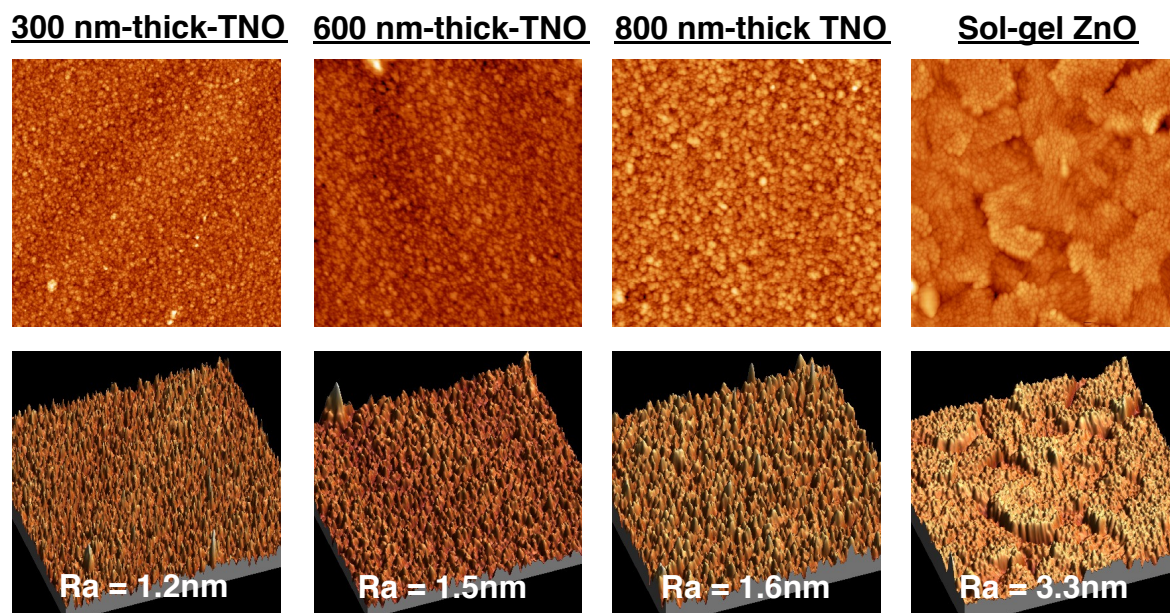


Figure 8. AFM images of TNO surface and roughness average values according to their thickness with ZnO surface as a comparison.

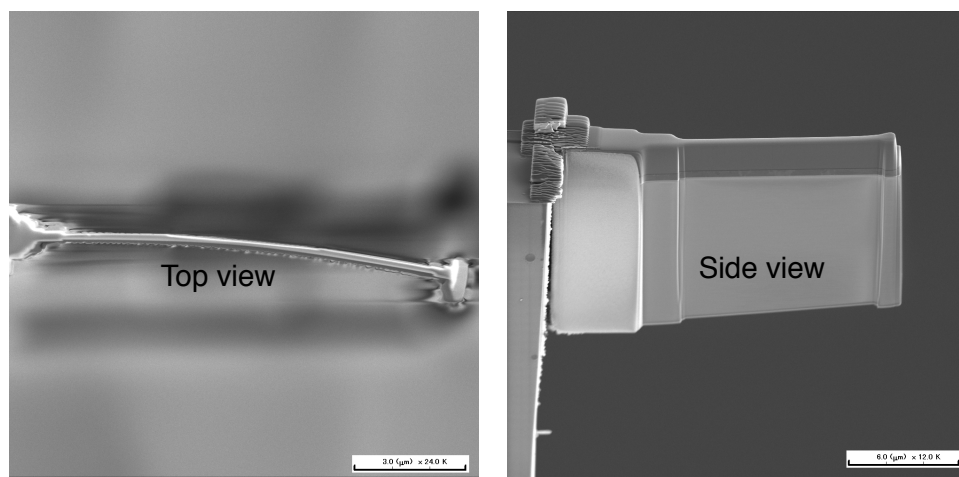
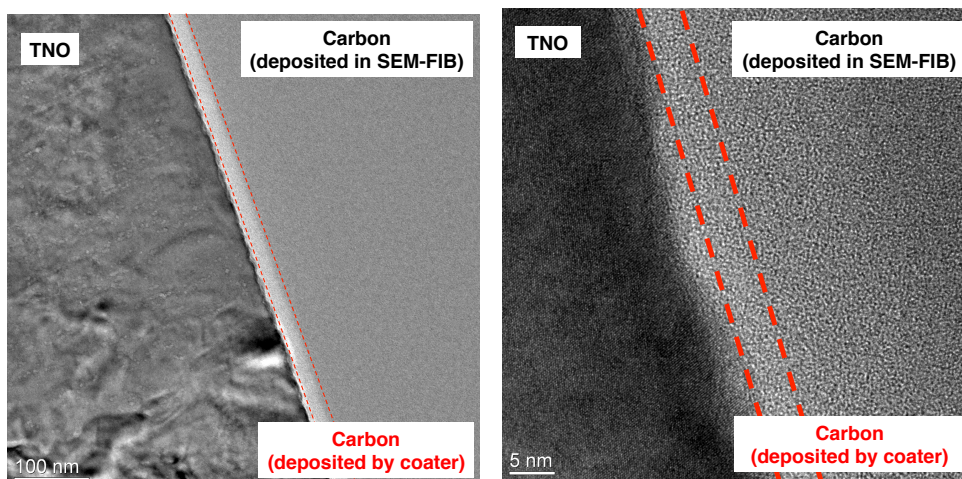


Figure 9a. HR-TEM cross-sectional images of TNO from top (left) and from side (right).

Conductive sample



O₃ Treated sample

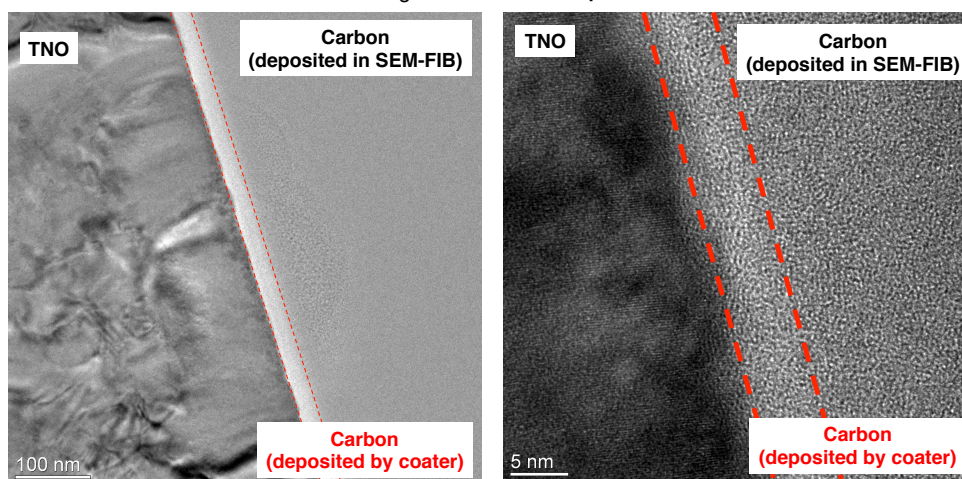


Figure 9b. HR-TEM cross-sectional images of pristine TNO (above) and O₃-treated TNO (below).

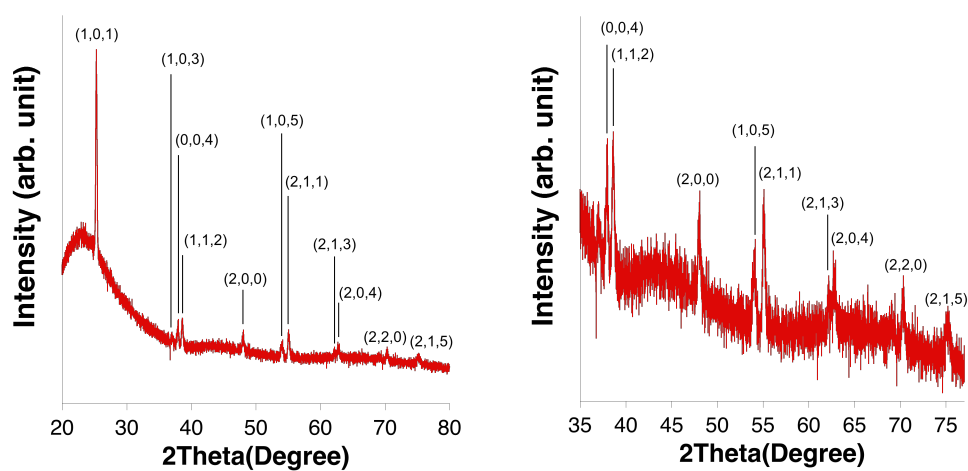
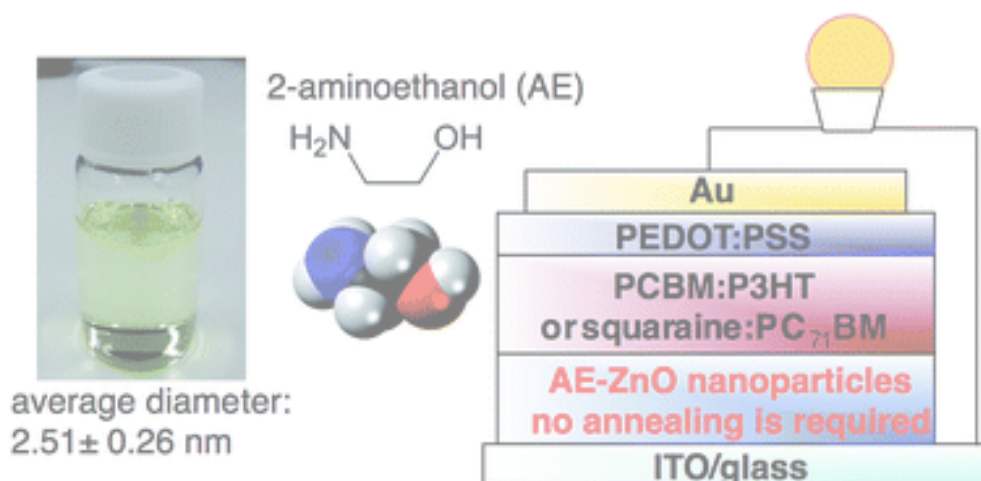


Figure 10. An XRD spectrum of TNO film after O₃-treatment denoting retained anatase phase as a standard version (left) and as a magnified version (right).

7.5 Conclusion

In conclusion, this chapter has presented the application of TNO electrode in OSCs and a simple methodology of creating semiconducting ETL surface on a conductive TNO by O₃ treatment. Utilising this, I demonstrated indium-free air-processed inverted OSCs which does not require the ETL deposition, yet achieving PCE as high as that of the conventional ITO-based devices. I am continuing this research by broadening its investigations such as adopting low-band gap polymers and PSC applications. I anticipate this finding will contribute to the development of ITO-free OSCs by pioneering a facile, low-cost, and highly reproducible new structure.



CHAPTER 8

LIGAND-FREE ZnO NANOPARTICLES AS THE CHARGE SELECTIVE LAYER THAT REQUIRES NO THERMAL ANNEALING IN INVERTED ORGANIC SOLAR CELLS

8.1 Summary

Highly stable ZnO nanoparticles (NPs) for use in OSCs have been synthesised in 2-aminoethanol, which acts as both a stabilising ligand and a solvent. The ZnO NP films do not require thermal annealing and applying them in inverted P3HT:mix-PCBM OSCs fabricated almost entirely under ambient conditions show efficiencies >3%. I find that thermally annealing the ZnO NP films does not give rise to any significant differences in device performance up to 150 °C. Annealing the films at higher temperatures leads to reduced short-circuit current densities and fill factors due to the removal of 2-aminoethanol from the NP surface, as evidenced by XPS. Furthermore, to confirm that the post-annealing of P3HT:PCBM devices at 150 °C does not affect the results, I fabricated inverted small molecule OSCs using a 2,4-bis[4-(N,N-diisobutylamino)-2,6-dihydroxyphenyl] squaraine (SQ) donor and PC₇₁BM acceptor that only requires a low-temperature thermal annealing step (70 °C). No substantial differences between annealed and non-annealed devices were observed, which demonstrates the applicability of these new ZnO NPs in flexible OSCs.

8.2 Introduction

In a normal architecture OSC, the device relies on the use of a low work function top electrode that is highly susceptible to degradation from oxygen and water, as are many of the organic materials that make up the active and interfacial layers. The final steps of device fabrication must therefore be carried out under dry anaerobic conditions and, prior to exposing the device to ambient conditions, a potentially costly encapsulation layer must be incorporated. Inverting the architecture, however, allows the use of high work function electrodes such as silver and gold, as well as air-stable metal oxide transport layers, which provide added protection to the active layer.^[185] MoO₃ is typically employed as the HTL for reducing ohmic losses between the donor's HOMO and the Au or Ag anode.^[194,322] PEDOT:PSS can also be utilised as the HTL, having the advantage of being easily deposited via spin-coating on top of the active layer.^[323] The most common electron-transport materials are ZnO and TiO₂, which offer high electron transport between the fullerene and the ITO interface.^[184,324–327] However, one common downside does exist with these materials, which is that a high temperature step is required. For most deposition methods of ZnO and TiO₂ films annealing temperatures in excess of 150 °C are generally required, which is well above the glass transition temperature of common polymeric substrates used in flexible organic electronic devices. During the preparation of this manuscript, Lu and Tao et al. reported a method for depositing ZnO films that does not require thermal annealing, using an air-sensitive ZnO NP solution.^[328] Here, I demonstrate a new and facile synthesis route for obtaining highly stable ZnO NP solutions for fabricating low-temperature ZnO films that can be applied as ETLs in OSCs. The NPs are synthesised in 2-aminoethanol and do not require any additional stabilisers or ligands, aside from the solvent molecules themselves. Furthermore, the ZnO films can be readily processed in air. Inverted OSCs were fabricated with the ZnO NP films subjected to various annealing temperatures, where the active layer was P3HT:mix-PCBM. Mix-PCBM corresponds to a mixture of PC₆₁BM (85 wt%) and PC₇₁BM (15 wt%) that is more economical and has been shown to offer higher stability and slightly higher performance than pure PC₆₁BM.^[329] XPS and AFM are employed to study the surface chemistry and topography, respectively. Inverted small molecular OSCs (SMOSCs) using the ZnO NP films are also investigated, based on a SQ donor

and a PC₇₁BM acceptor, to demonstrate the potential of this approach for fabricating low-temperature OSCs compatible with flexible substrates.

8.3 Experimental Procedures

8.4.1 ZnO NPs Synthesis

For the chemical synthesis of ZnO NPs in 2-aminoethanol the following commercially available chemicals were used without further purification: zinc(II) acetate, Zn(CH₃COO)₂ (Wako, 99%) and 2-aminoethanol, C₂H₄(OH)(NH₂) (Wako, 99%). The ZnO NPs were synthesised in a similar manner to the methodology reported by Lin et al. but using a lower b.p. solvent, 2-aminoethanol (b.p. 170 °C).^[330] Firstly, 180 mg (0.981 mol) of zinc(II) acetate Zn(CH₃COO)₂ was added to 2-aminoethanol (100 mL) and heated up to 160 °C in an oil bath and the solution was stirred and refluxed for 1 hour under isothermal treatment. The purpose of reflux was to remove any by-products such as water or acetic acid produced during the reaction. After 1 hour, the resulting solution was cooled to room temperature. The solution was then centrifuged for 30 minutes to remove precipitates. The supernatant contained well-dispersed ZnO nanoparticles with an average size of 2.5 nm, as observed from TEM. This supernatant was collected as the product and was stable for at least 6 months.

8.4.2 Device Fabrications

For the OSC fabrications, refer to 2.1.1.2 Organic solar cell inverted device architecture and 2.1.1.3 P3HT:mix-PCBM solution preparation

SQ:PC₇₁BM devices were fabricated on both ZnO NP and sol-gel films from a 20 mg mL⁻¹ CHCl₃ solution, where the SQ:PC₇₁BM weight ratio was 1 : 5. The solution was spin-coated at 3000 rpm for 60 s inside a N₂-filled glovebox and the films were then annealed at 70 °C for 10 min. Following annealing, the films were transferred, without exposure to air, to a vacuum chamber, where MoO₃ (8 nm) and Au (100 nm) were deposited by thermal evaporation. Devices were encapsulated before measuring their *J-V* curves. SQ was purchased from Sigma Aldrich and

recrystallised by the slow diffusion of MeOH in a saturated solution of SQ in chloroform, following a previously reported method.^[331] PC₇₁BM was bought from Solenne and was used as received.

8.4.3 Characterisations

Please refer to 2.2.1.1 Current-voltage characterisation, 2.2.2.1 UV-vis absorption, 2.2.2.3 Atomic force microscopy (AFM), and 2.2.2.6 X-ray photoelectron spectroscopy (XPS).

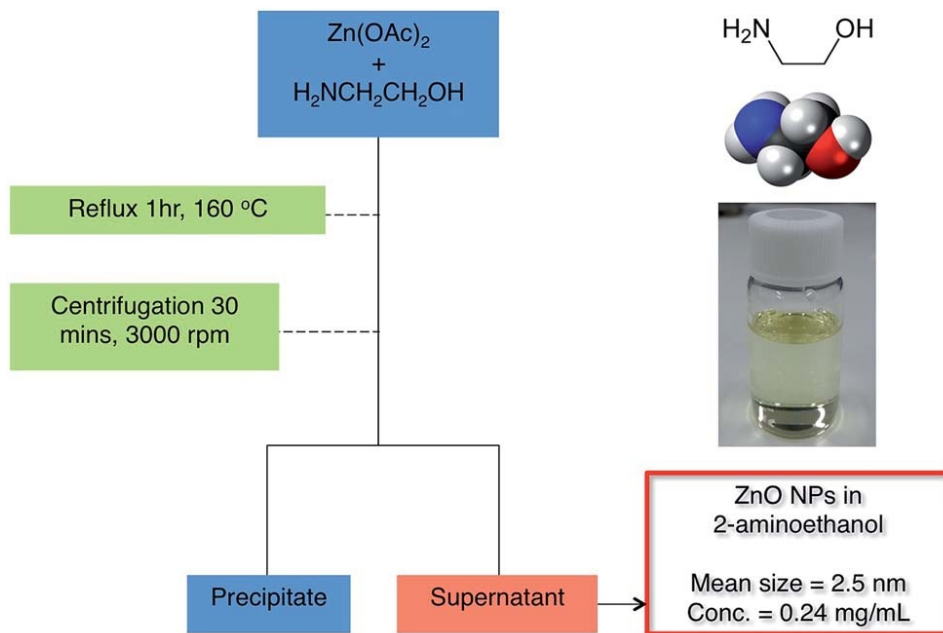
8.4 Results and Discussion

The synthesis of the ZnO NPs is similar to the method used by Lin et al.,^[330] where I replaced diethylene glycol with a shorter alkyl chained amino alcohol, 2-aminoethanol. The use of 2-aminoethanol allowed a more concentrated solution to be obtained compared with the previous method. The synthesis and isolation of the ZnO NPs is shown in Scheme 1, which consisted of heating zinc acetate (ZnOAc)₂ in 2-aminoethanol to 160 °C and refluxing for an hour. Once the solution was cooled down, it was centrifuged, which led to a precipitate that contained ZnO NPs with diameters in excess of 100 nm and a pale yellow supernatant that provided well dispersed ZnO NPs with a mean diameter of 2.5 nm as determined by transmission electron microscopy (Figure 1).

The concentration of the solution obtained was 0.24 mg mL⁻¹ and stable for at least for 6 months, which, considering that no additional stabilising ligands were required in addition to the 2-aminoethanol solvent molecules, is an interesting and important finding.

The as-obtained supernatant solution was then used in fabricating OSCs by spin-coating it on ITO patterned glass substrates. Following spin-coating, the films were then subjected to thermal annealing at temperatures ranging from room temperature (i.e. no annealing) to 210 °C. The annealing time was fixed at 1 h in each case. The transmittance of the ZnO thin films on glass/ITO substrates are shown in Figure 2 and shows a decrease in transmittance with annealing temperature. Non-

annealed ZnO NP films show the highest transmittance, with a maximum transmittance of 85.2% at 520 nm.



Scheme 1. Synthesis and separation of ZnO nanoparticles.

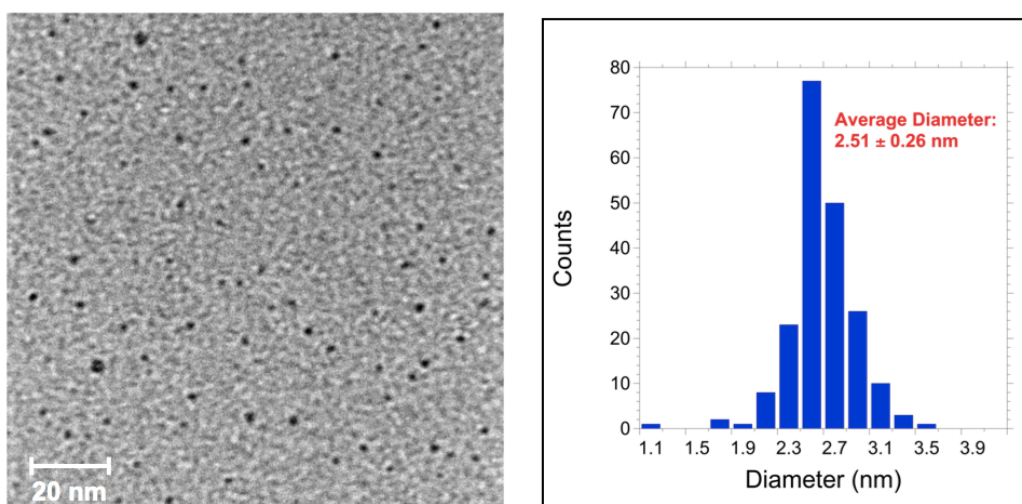


Figure 1. TEM image of ZnO NPs recorded using a JEOL, JEM-3200 electron microscope operated at 300 kV and corresponding size distribution histogram.

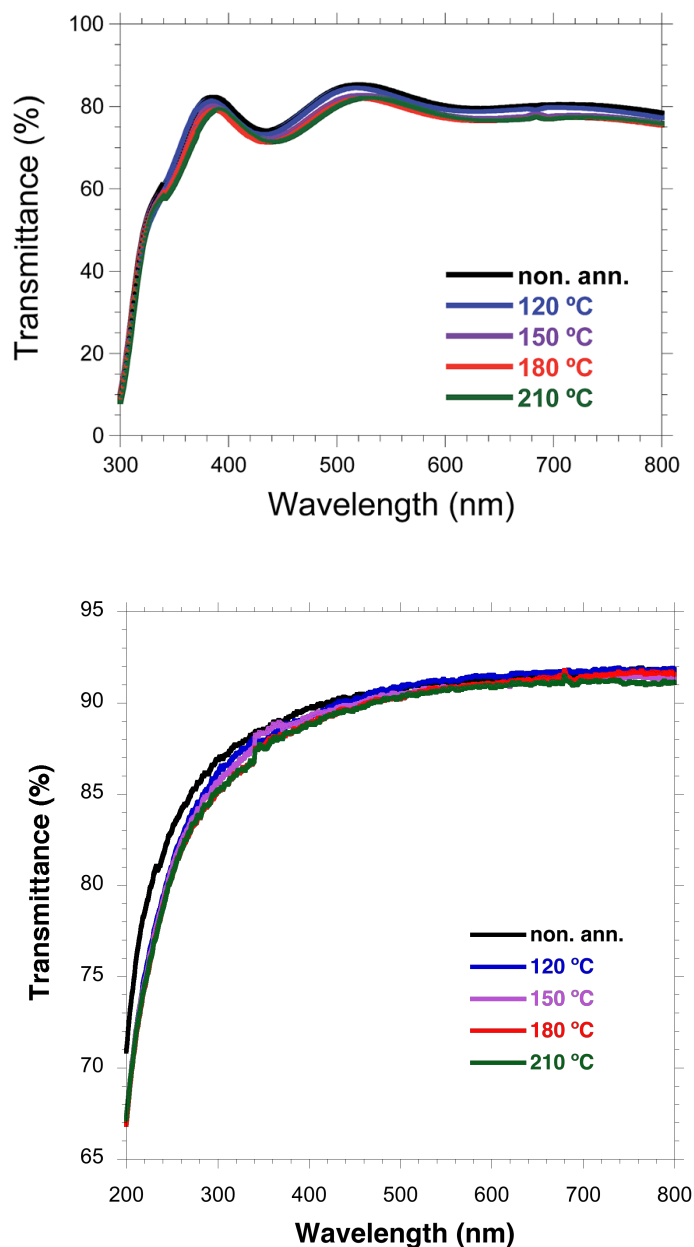


Figure 2. Transmittance spectra of ZnO NP films on glass/ITO substrates (above) on fused silica substrates (below) annealed at different temperatures.

P3HT:mix-PCBM active layers were then deposited, followed by a PEDOT:PSS HTL and Au electrode. Note that all layers, except for gold, were deposited in air. Furthermore, devices were also annealed and measured in air, without the addition of an encapsulation layer, demonstrating the good stability of these inverted devices. The J - V curves of the OSCs are shown in Figure. 3 and Table 1 summarises the key figures of merit.

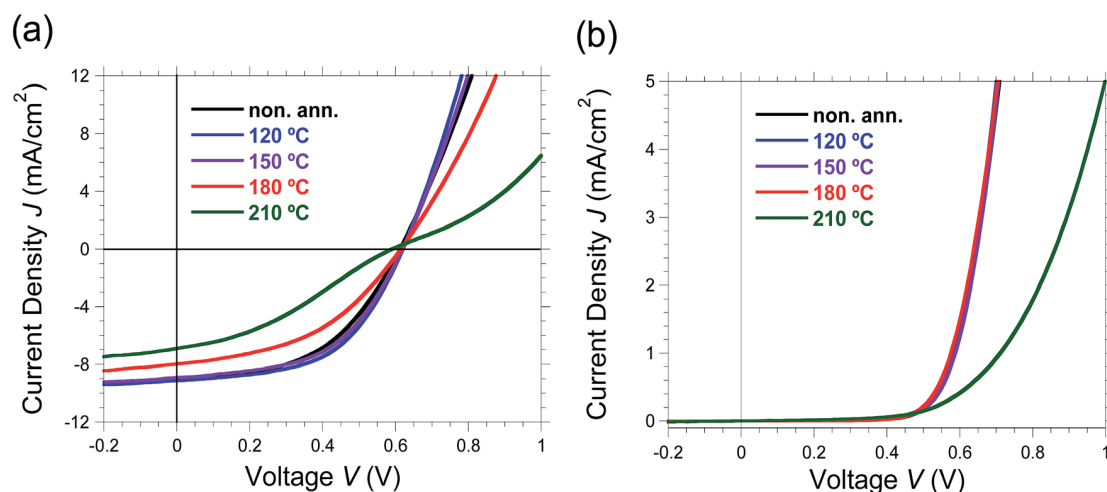


Figure 3. J - V curves for inverted P3HT:mix-PCBM devices where the ZnO NP film was subject to various annealing temperatures measured under (a) 1 sun illumination (AM 1.5 G, 100 mW cm^{-2}) and (b) dark conditions. Non-annealed (black), $120 \text{ }^{\circ}\text{C}$ (blue), $150 \text{ }^{\circ}\text{C}$ (purple), $180 \text{ }^{\circ}\text{C}$ (red) and $210 \text{ }^{\circ}\text{C}$ (green).

Table 1. J - V characteristics of P3HT:mix-PCBM devices recorded under 1 sun illumination (100 mW cm^{-2} , AM 1.5 G) and resistance values obtained from dark J - V curves

Annealing Temperature	V_{OC} (V)	J_{SC} (mA cm^{-2})	FF	η (%)	R_S (Ωcm^2)	R_{SH} (Ωcm^2)
NA	0.61	9.08	0.56	3.1	8.29	1660
$120 \text{ }^{\circ}\text{C}$	0.62	9.13	0.53	3.0	8.42	1540
$150 \text{ }^{\circ}\text{C}$	0.62	8.65	0.53	2.9	8.35	1270
$180 \text{ }^{\circ}\text{C}$	0.61	7.98	0.45	2.2	9.77	1220
$210 \text{ }^{\circ}\text{C}$	0.59	6.91	0.34	1.4	20.11	1120
$200 \text{ }^{\circ}\text{C}^a$	0.60	9.42	0.56	3.2	5.71	2230

^a Sol-gel reference devices.

Remarkably, devices processed without subjecting the ZnO layer to any thermal annealing have the highest PCE, η of 3.1% due to the higher FF compared with the annealed devices. Although, the difference between the devices with non-annealed ZnO films and the devices annealed up to $120 \text{ }^{\circ}\text{C}$ do not in fact differ considerably. There is, however, a significant difference in η when the annealing temperature exceeds $120 \text{ }^{\circ}\text{C}$, where the FF decreases with increasing temperature as does the J_{SC} , with a significant drop observed when annealing exceeds $150 \text{ }^{\circ}\text{C}$. This decrease in FF arises from an increase in R_S as well as the shunt resistance R_{SH} , with values decreasing with annealing temperature (see Table 1). S-shaped curves are observed for devices employing ZnO films annealed at $210 \text{ }^{\circ}\text{C}$, which further

decreases the FF. The origin of the S-shaped kink in the J - V curve is not entirely clear but probably arises from ZnO inducing a barrier to charge injection or extraction.^[332-334] Considering that 2-aminoethanol should have been removed from the ZnO NP surface due to the high annealing temperature (at least for the NPs on the ZnO surface), I would expect the NPs to have a high concentration of trap states that may reduce the conductivity of the ZnO film as well as act as trap-sites for free charge carriers generated in the active layer. All devices displayed a short UV-activation time, i.e. light soaking, but there was no noticeable trend between the activation time and the annealing conditions. Reference P3HT:mix-PCBM inverted devices were also fabricated for comparison using a standard sol-gel method to deposit the ZnO film (thermally annealed at 200 °C),^[185] which shows slightly higher but not significantly different performance ($\eta = 3.2\%$), demonstrating the high applicability of my ZnO NP approach in OSCs. I have fabricated devices using ZnO NPs synthesised in ethylene glycol and found that they do not perform as well as ZnO NPs in 2-aminoethanol (Table 2, Figure 4). I attribute this to the larger diameter of the ZnO NPs (4.09 nm on average) that also display a larger size deviation than the ZnO NPs in 2-aminoethanol (Figure 5).

Table 2. Device performance of ZnO NPs in ethylene glycol

Annealing Temperature	V_{oc} (V)	J_{sc} (mA cm ⁻²)	FF	η (%)	R_s (Ω cm ²)	R_{sh} (Ω cm ²)
NA	0.48	9.04	0.43	1.9	8.07	4260
150 °C	0.48	9.63	0.40	1.9	28.7	2790
210 °C	0.46	8.99	0.43	1.8	17.9	832

Investigating the effect of thermal annealing on the thin film properties of ZnO, I found that the topography, as measured by AFM on ITO/Glass substrates, did not change significantly with r.m.s. roughness values between 5 and 6 nm (Figure 6). Non-annealed films had the roughest topography and it can be seen that upon annealing at 120 °C, the roughness decreases and then increases with temperature. The changes are subtle, however, and are probably not significant enough to explain the large changes in the J - V characteristics.

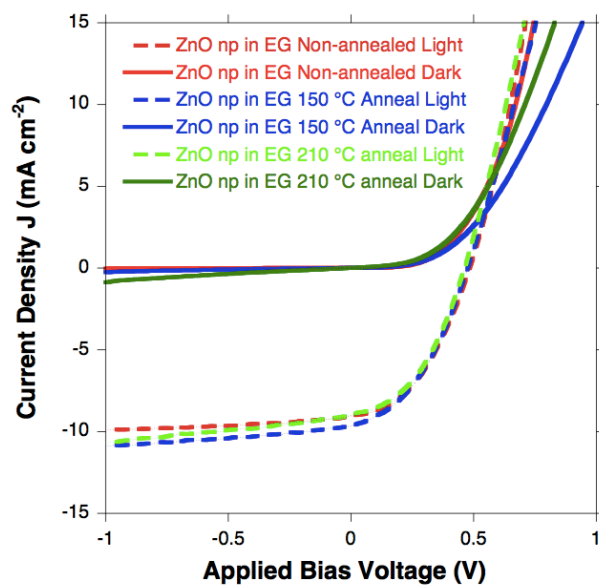


Figure 4. *J-V* curve of ZnO NPs in ethylene glycol-based OSCs

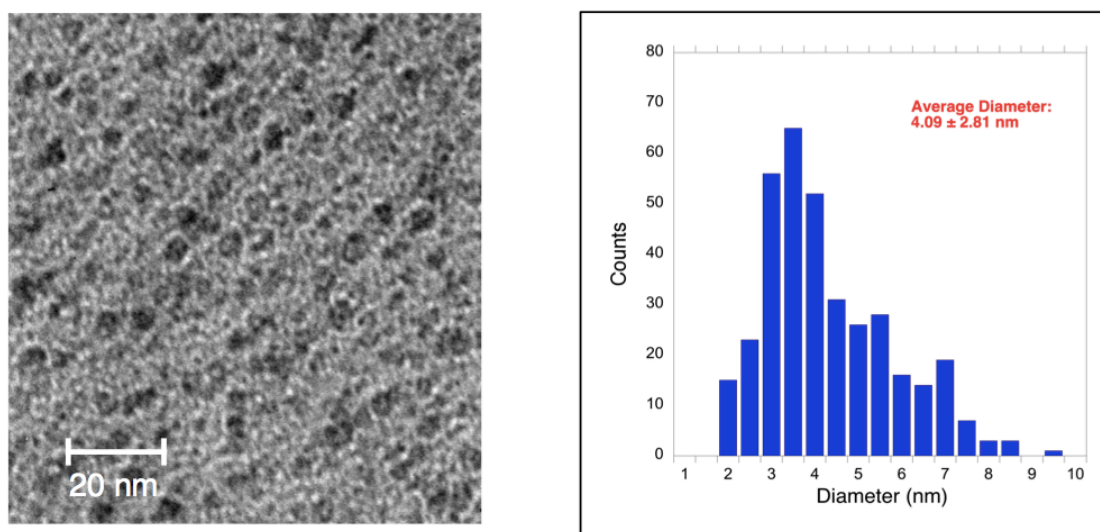


Figure 5. TEM image of ZnO NPs in ethylene glycol recorded using a JEOL, JEM-3200 electron microscope operated at 300 kV and corresponding size distribution histogram.

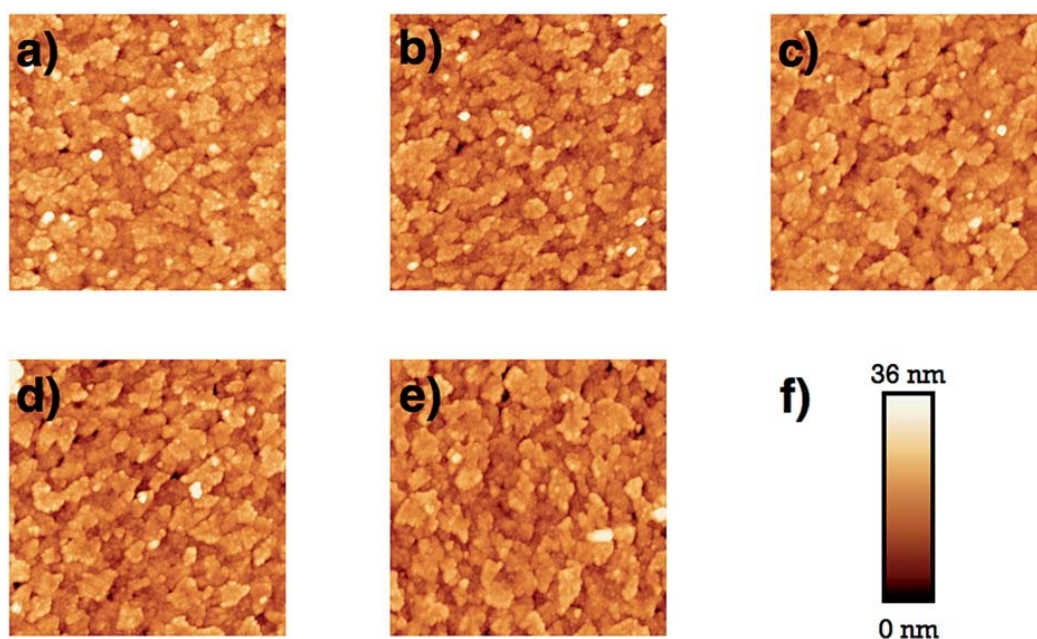


Figure 6. Atomic force microscopy topography images of ZnO NP thin films corresponding to the following annealing conditions: (a) non-annealed, (b) 120 °C, (c) 150 °C, (d) 180 °C and (e) 210 °C. The area scanned for each image was 5×5 mm and (f) the Z-scale for each image is also identical.

The surface chemistry of the ZnO films was then probed using XPS. Figure 7 shows the peaks of ZnO films corresponding to (a) Zn $2p_{3/2}$ and (b) N 1s core levels (refer to Figure 8 for the wide-scan images of each film). A positive shift in the binding energy (BE) of ~ 1 eV is observed for both Zn $2p_{3/2}$ and N 1s peaks when the films are annealed at 150 °C and above. This increase in BE for both Zn and N indicates that 2-aminoethanol is cleaved from the surface of the ZnO NPs. Furthermore, the intensity of the 2-aminoethanol peaks is seen to decrease with annealing temperature, even for the films annealed at 120 °C, which is much lower than the boiling point of 2-aminoethanol (170 °C). The ~ 1 eV increase in BE for both Zn and N does not exactly reflect the trend observed in the J - V curves above, as the device employing a ZnO film annealed at 150 °C still has relatively high efficiency even though 2-aminoethanol has been cleaved from the ZnO surface. However, when the films are annealed at temperatures above the boiling point of 2-aminoethanol we do see a significant decrease in the performance. These results suggest that the presence of 2-aminoethanol is important. Indeed, a recent study on a polar solvent treatment of rippled-ZnO films by Song and co-workers has shown that treating the metal oxide film with a solution of 2-methoxyethanol and just 1% 2-aminoethanol

enhances the electrical contact between the ZnO and the LUMO of PCBM.¹² The spectra for the O 1s core level are shown in Figure 10, which correspond to the O in ZnO. We can observe an asymmetric peak for each sample that was deconvoluted using curve fitting methods into two peaks centred at 529.7 ± 0.5 eV (O1) and 531.1 ± 0.5 eV (O2) that correspond to O^{2-} ions of the Zn–O bond for the ZnO wurtzite structure and oxygen deficient component of ZnO where O^{2-} ions correspond to the hydroxyl groups, respectively.^[335] The ratio of O1 : O2 is seen to change with annealing temperature. O1 is slightly more dominant in the non-annealed ZnO film (O1 : O2 = 55 : 45). Upon annealing at 120 °C in air, O2 is the slightly more dominant species (48 : 52). However, the percentage of O2 recorded for films heated at higher temperatures proceeds to decrease with temperature. For films annealed at 210 °C the O1 : O2 ratio is 60 : 40. It is difficult to correlate these data with the experimental J – V curves, as one would expect a decrease of hydroxyl groups to correlate with a decrease in the number of trap states and thus better performance, particularly concerning the FF. The opposite trend until 120 °C is observed, however, due to the removal of 2-aminoethanol. It could be possible that the OH group of 2-aminoethanol is also partially responsible for the peaks centred at 531 eV.

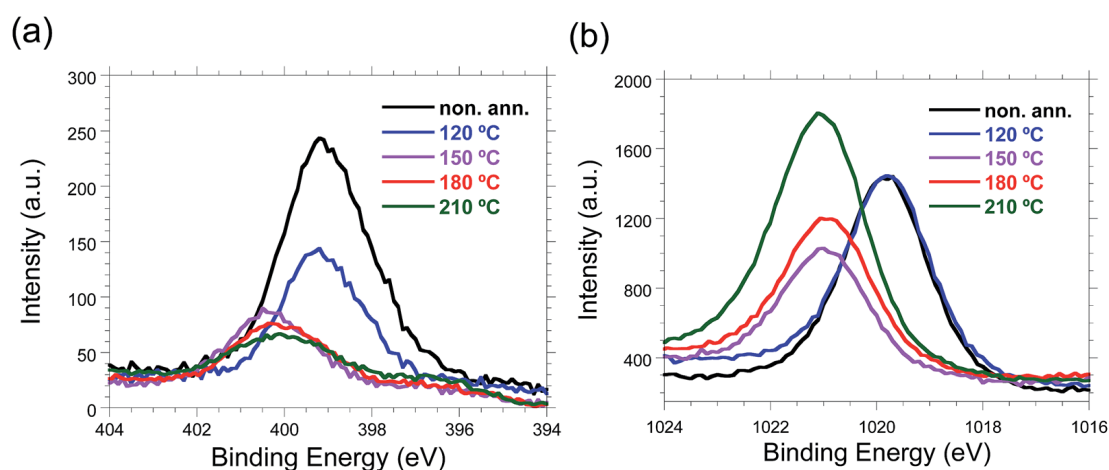
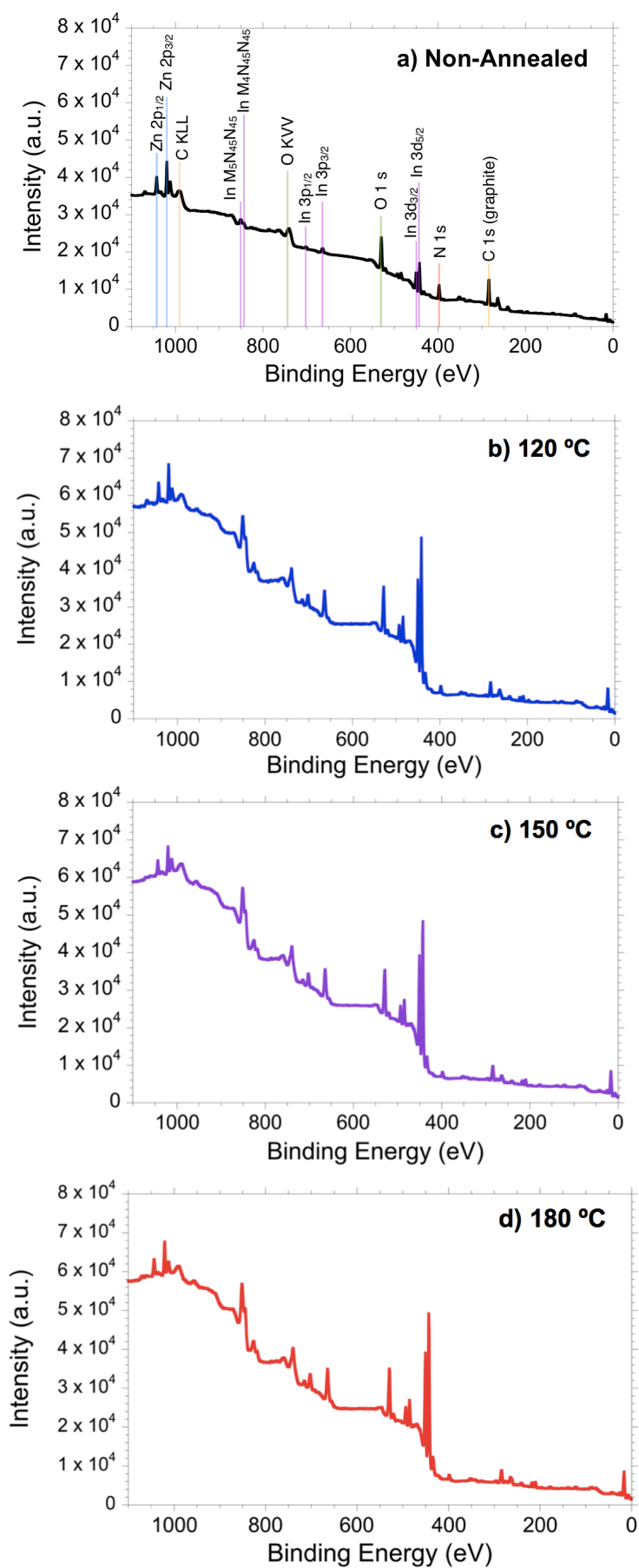


Figure 8. XPS spectra of ZnO films corresponding to (a) N 1s and (b) Zn 2p_{3/2} under the following annealing conditions: non-annealed (black), 120 °C (blue), 150 °C (purple), 180 °C (red) and 210 °C (green).



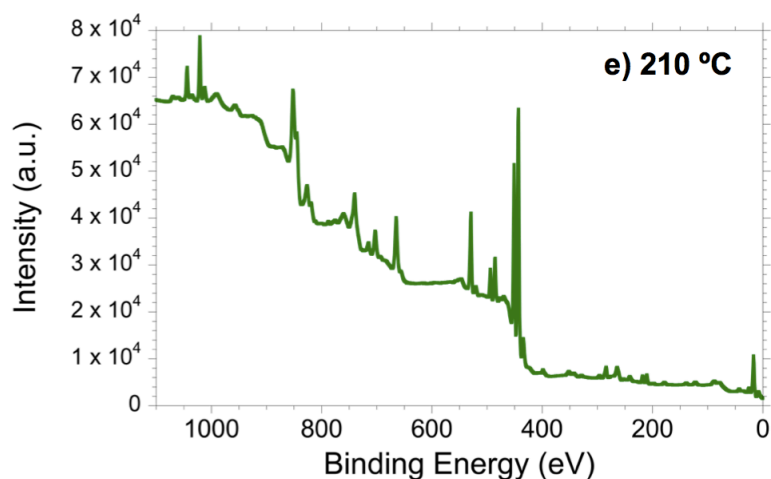


Figure 9. XPS spectra recorded between binding energies of 0 and 1100 eV.

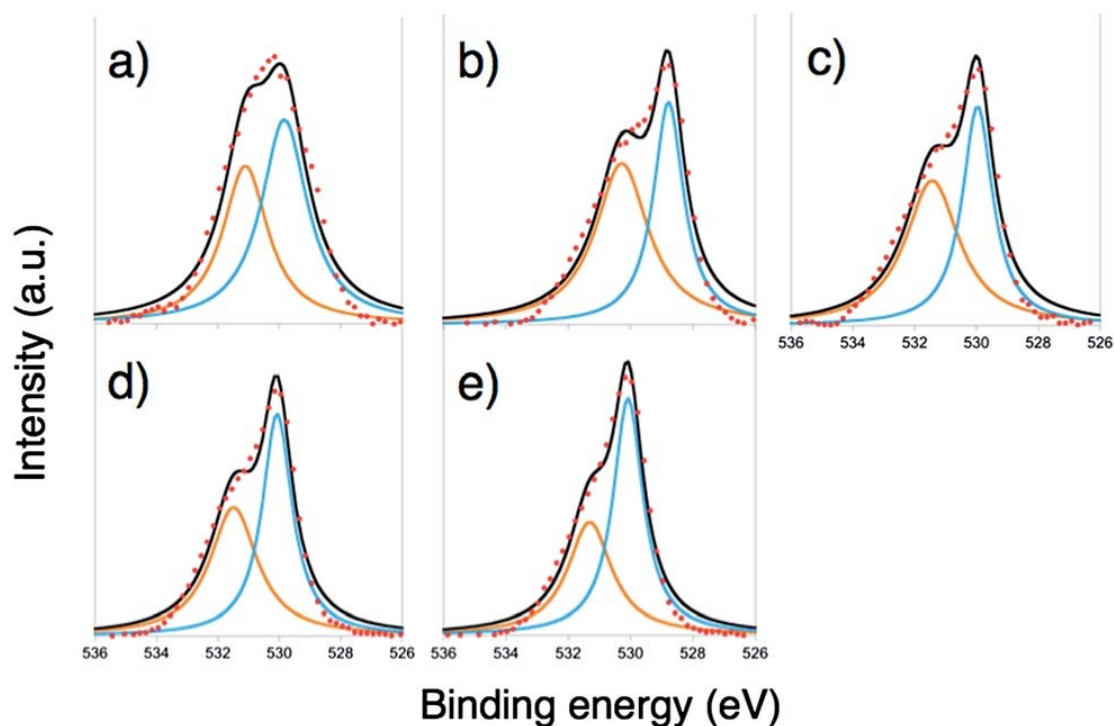


Figure 10. XPS spectra of the O 1s peaks of the ZnO films under the following annealing conditions: (a) non-annealed, (b) 120 °C, (c) 150 °C, (d) 180 °C and (e) 210 °C. The orange and blue fits correspond to the deconvoluted O^{2-} species, the former being an oxygen deficient species and the latter peak consistent with that of O^{2-} in a perfect wurtzite crystal. The raw data are represented by red circles along with best fits shown as a black line.

While a clear trend in device performance with ZnO annealing temperature is observed, it must be remembered that the device undergoes a post-annealing process at 150 °C to improve the active layer morphology, which may anneal ZnO in the process and affect the surface chemistry of the ZnO NPs. Therefore, to minimise the influence of the device annealing temperature, I fabricated inverted SMOSCs that

only require the active layer to be annealed at 70 °C based on a SQ donor, SQ^[331] and a PC₇₁BM acceptor.^[336] Active layers were prepared by spin-coating a 20 mg mL⁻¹ solution of SQ:PC₇₁BM in chloroform; the donor : acceptor ratio was 1 : 5 (see the 8.3 Experimental Procedure for a detailed description of device fabrication). Figure 11 shows the J - V curves recorded under standard 1 sun illumination conditions for devices using non-annealed ZnO NP films as well as films annealed at 120 °C and 150 °C. We can observed very little difference between the device characteristics, with PCEs of approximately 3% (see Table 3). While the FF for each device is low, it does not differ significantly to what is reported for normal-architecture SQ:PC₇₁BM devices, which generally have FFs between 40 and 45%.^[337] I expect that through optimising device fabrication, higher PCE can be achieved. However, the main focus here is simply to demonstrate that the ZnO NP films do not require high temperature thermal annealing for efficient OSCs, which is clearly evident in the J - V curves in Figure 12.

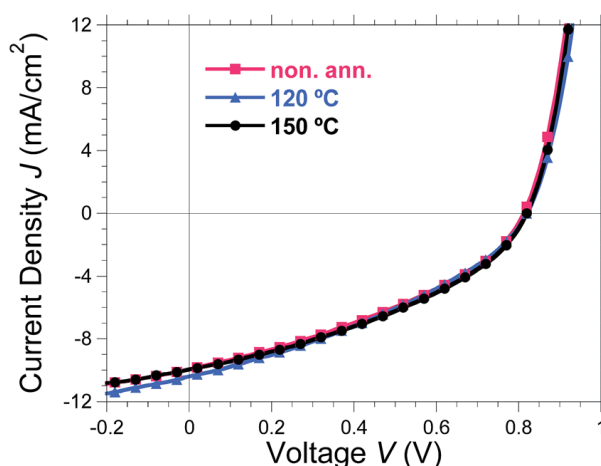


Figure 11. J - V curves under 1 sun illumination (AM 1.5 G, 100 mW cm⁻²) for inverted SQ:PC₇₁BM devices where the ZnO NP film was annealed at 120 °C (blue, triangles) and 150 °C (black, circles) as well as non-annealed (pink, squares).

Table 3. J - V characteristics of SQ:PC₇₁BM devices recorded under 1 sun illumination (100 mW cm⁻², AM 1.5 G)

Annealing Temperature	V_{oc} (V)	J_{sc} (mA cm ⁻²)	FF	η (%)
NA	0.84	9.74	0.36	3.0
150 °C	0.82	10.41	0.36	3.0
210 °C	0.82	9.96	0.38	3.1

8.5 Conclusion

I have demonstrated a new route for the synthesis of highly stable and high performance ZnO films for inverted OSCs that require no thermal annealing. Applying thermal annealing post-deposition was found to severely affect device performance for temperatures above 150 °C, due to the desorption of 2-aminoethanol from the ZnO NP surface, as evidenced by XPS. Inverted P3HT:mix-PCBM devices employing the ZnO NP films showed respectable efficiencies of ~3%, which is on par with devices utilising a conventional ZnO sol-gel derived ETL. As the P3HT:mix-PCBM devices underwent a post-deposition thermal annealing step at 150 °C, I investigated whether this affected the ZnO NP film by fabricating low-temperature SQ:PC₇₁BM devices that only required thermal annealing of 70 °C. For these small molecule OSC devices, no significant differences were observed for devices employing non-annealed ZnO films to those using ZnO films annealed at temperatures up to 150 °C. The long shelf life of the ZnO NP solution coupled with the ability to form high performance ZnO films is an important finding and I hope that this approach will find applications in not only OSCs but also in other organic and organic-inorganic electronic devices.

CHAPTER 9

SPUTTERED ZnO FILM AS THE CHARGE SELECTIVE LAYER IN INVERTED ORGANIC SOLAR CELLS

9.1 Summary

ZnO films were fabricated by sputtering under higher working pressure than usual to produce high-quality defect-free ZnO with high polycrystallinity. These films were then employed in P3HT:PCBM-based inverted OSCs to demonstrate higher performance than those of sol-gel ZnO and conventionally sputtered ZnO. OSCs with ZnO sputtered under new method produced a PCE of 3.42% ($V_{OC} = 0.62$, $J_{SC} = 9.8$, $FF = 0.56$), whilst sol-gel ZnO-based and conventionally sputtered ZnO-based OSCs produced a PCE of 3.07 % ($V_{OC} = 0.61$, $J_{SC} = 8.9$, $FF = 0.56$) and 1.49 % ($V_{OC} = 0.50$, $J_{SC} = 7.4$, $FF = 0.40$), respectively. Extremely low R_s and high FF of OSCs of the new method based-ZnO served to prove higher mobility arising from higher crystallinity along with XRD data. Although, there are still more to be done to accomplish this research project, there is no doubt that my discovery leads to high performing ZnO that has potential in flexible applications.

9.2 Introduction

ZnO forms an ohmic contact with ITO and active materials in inverted OSCs. Since the conduction-band edge of ZnO (-4.4 eV) is located between the conduction-band edge of ITO (-4.7 eV) and the LUMO energy level of acceptor molecules, such as PC₆₁BM (-3.8 eV), ZnO can facilitate efficient electron transfer.^[324,338,339] In the field of inverted OSCs, ZnO is currently the best-performing ETL over other metal oxides such as TiO_x,^[340] Cs₂CO₃, or Al₂O₃.^[341] This is due mainly to its high mobility and the fact that it does not induce light-soaking effect unlike TiO_x. Many fabrication techniques have been used to grow ZnO as cathode interfacial layer. But, the most espoused methods are wet processes by means of either sol-gel or colloidal nanoparticles.^[342–344] However, these methods require high thermal annealing at temperatures above 250 °C to produce stable and high-quality homogenous films with reproducible properties.^[345,346] This makes inverted OSCs involving ZnO ETL incompatible with flexible applications. There are several other techniques that undergoes a low temperature process to produce ZnO film, namely, plasma-enhanced chemical vapour deposition (PEC-VD),^[347] microwaves plasma chemical vapour deposition (MPCVD),^[348] atomic layer deposition (ALD),^[349] and sputtering which caught more attention lately.^[350] Sputtering not only operates at low temperature, but is also able to deposit dense, homogeneous, and reproducible ZnO films with well-defined c-axis orientation even when deposited on amorphous rigid substrates.^[351] Sputtering is also compatible with roll-to-roll processing by using high deposition rates.^[352,353]

Despite numerous merits sputtering possesses, sputtered ZnO reported so far produced low PCEs when used in OSCs.^[351,354–356] To boost their performance, high temperature annealing on ZnO has been required which defies whole point of using sputter technique. There is a two-step method reported that avoids high temperature annealing, but this technique still lacks in producing high quality film as observed by low V_{OC} .^[357]

In this chapter, I demonstrate the discovery of a high performing one-step sputtering methodology at low temperature by utilizing high working pressure (HWP) and low-oxygen ambient condition. HWP was used to facilitate high pressure which

reduces the energy of high-energy particles such as recoiled Ar and negatively charged oxygen. Moreover, low oxygen composition was used to enhance the conductivity of ZnO film. ZnO films produced by this method demonstrated much higher performance than conventional sol-gel ZnO and conventional sputtered ZnO, when used as ETLs in inverted OSCs. OSCs fabricated using HWP sputtered ZnO gave a PCE of 3.42% while those of sol-gel ZnO gave 3.07%. Such immense improvement came from high FF and increased J_{SC} . From the analyses conducted, enhancement in crystallinity in ZnO gave rise to higher mobility. There are more to be studied in respect to application of low-band gap polymer, SCLC mobility test, XPS compositional study, TEM cross-sectional investigation, and so on. Here in this chapter, I have discussed future aspects regarding diverse applications of the HWP sputtering technique also. Up to now, research has been mainly focused on efficiency, while flexible application of inverted OSCs using ZnO has hardly been discussed.^[343,358] Flexibility is something far more important pertained to progress in OSCs using semiconducting metal oxides as interfacial layers.^[359] Thus, it is imperative that I focus on diverse applications and maximise the benefit of the sputtering technique through in-depth discussion.

9.3 Experimental Procedures

9.3.1 ZnO Sputtering

ZnO thin films were deposited on ITO substrates by RF magnetron sputtering without any thermal process. An oxygen-deficient two-inch ZnO_{1-x} ceramic disk (Toshima MFG Co., Ltd.) was used as a target. The RF power applied to the target was 100 W. The thickness of ZnO layer was approximately 20 nm. The base pressure of the sputtering chamber was less than 1×10^{-5} Pa. The sputter deposition was conducted in Ar and O_2 gas mixture under a pressure of 2.6 Pa. The O_2 partial pressure was in the range of $4-6.6 \times 10^{-3}$ Pa.

For the conventionally sputtered ZnO, ZnO thin films were deposited on ITO substrates by RF magnetron sputtering without intentional substrate heating. ZnO_x target (Kojundo Chemical Laboratory Co., Ltd.) was used as a target. The RF power

applied to the target was 100 W. The thickness of ZnO layer was approximately 20 nm. The base pressure of the sputtering chamber was around 1×10^{-4} Pa. The sputter deposition was conducted in Ar and O₂ gas mixture under a pressure of 4.3 Pa. The O₂ partial pressure was in around $4.2 \cdot 10^{-2}$ Pa.

9.3.2 Device Fabrications

For the OSC fabrications, refer to 2.1.1.2 Organic solar cell inverted device architecture and 2.1.1.3 P3HT:mix-PCBM solution preparation

9.3.3 Characterisations

Please refer to 2.2.1.1 Current-voltage characterisation, 2.2.2.1 UV-vis absorption, 2.2.2.3 Atomic force microscopy (AFM), and 2.2.2.7 X-ray powder diffraction (XRD)

9.4 Results and Discussion

UV-vis spectroscopy was used to investigate sol-gel ZnO and HWP sputtered ZnO (Figure 1). While both of the samples seem to possess similar overall transmittance, we can see that HWP sputtered ZnO shows a slight shift to the right. There are two interpretations that we can derive: First is that HWP sputtered ZnO showed reduction in the light scattering. This is associated with the decrease in the grain boundary which can occur when the crystallinity of ZnO film is high.^[360] This can be corroborated by measuring reflectance of the sputtered film, in which lower reflection confirms the lower light scattering. This will be indicative of less grain boundaries. Second interpretation is enhancement in the optical band gap in the low-vacuum sputtered ZnO films. The fact that the whole spectrum including the onset shifted to the right denotes that the band gap decreased. This is related to the change of carrier concentration in ZnO film lead by the film structure and film density change.^[361] This implies an enhancement of n-doping, thus higher mobility.^[362-364] This will be further examined by finding out the Fermi level, conduction and valence bands using XPS, PYS, and Kelvin probe in near future.

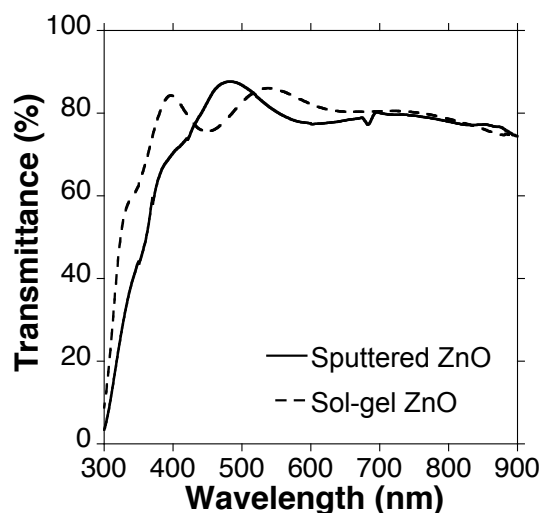


Figure 1. UV-vis spectra of sol-gel ZnO (dotted line) and low-vacuum sputtered ZnO (solid line) films on glass substrates.

XRD has been used to investigate the crystallinity of the ZnO films (Figure 2). HWP-sputtered ZnO showed a well defined (002) peak at 34.26° indicating a preferred orientation of the ZnO crystallites with the c-axis perpendicular to the glass substrate, while sol-gel ZnO showed absolutely no peaks at all. This reveals that sol-gel ZnO has amorphous layer with small crystallites size.^[360]

I have not yet measured XRD of the conventionally sputtered ZnO. Nevertheless, given the information from the literature, I am positive that conventionally sputtered ZnO will also show (002) peak, yet a calculated (002) grain size of the ZnO films will probably be bigger for the HWP-sputtered ZnO. This increase in grain size can be directly linked to the enhancement in mobility of ZnO.^[365,366] Such favourable effect can be attributed to better control of the sputtered particles in HWP atmosphere. In general, working pressure is optimised to produce dense film with high crystallinity, which belong to zone T structure in the Thornton model.^[367] Because the formation of zone T structure is assisted by the bombardment of high energy (100~1000 eV) particles such as recoiled Ar and negatively charged oxygen ions, produced films inevitably contain defects which can act as recombination centres. But, if the deposition is done under high working pressure, defects can be reduced via low energy particles arising from scattering of process gas (thermalisation). Indeed, better photocatalytic effect was observed under higher working pressure in TiO_2 also.^[368] Thus, we can expect that the possible existence of recombination centres deteriorating the performance in conventionally sputtered ZnO

films, and higher quality from HWP-sputtered ZnO which will improve hole-blocking ability, mobility of electrons, and electron collection efficiency at the interface between ZnO buffer and active layers.^[369]

From the XRD spectra, we can see that there is not only the (002) peak but also a strong (103) peak at 63.81° . This reveals that the grown ZnO films were not only wurtzite structures (JCPDS card No 36-1451), but also metallic zinc (JCPDS card No 40831) structures were simultaneously present.^[370] In general, a higher degree of polycrystallinity was observed for samples grown at the atmosphere with low oxygen composition (around 15%). Since my ZnO was fabricated at oxygen deficient condition (99% Argon and 0.01% oxygen) to enhance conductivity, we can expect strong polycrystallinity of ZnO. Moreover, from the XRD data on the right hand side of Figure 2, ZnO films grown on ITO shows one extra peak corresponding to (101) orientation, which are not observed for sol-gel ZnO on ITO. This confirms my assertion that low-vacuum sputtered ZnO possesses strong polycrystallinity. It is fascinating that we can see this only when ZnO is deposited on ITO, insinuating that its performance could have been enhanced, because it was grown on another metal oxide.

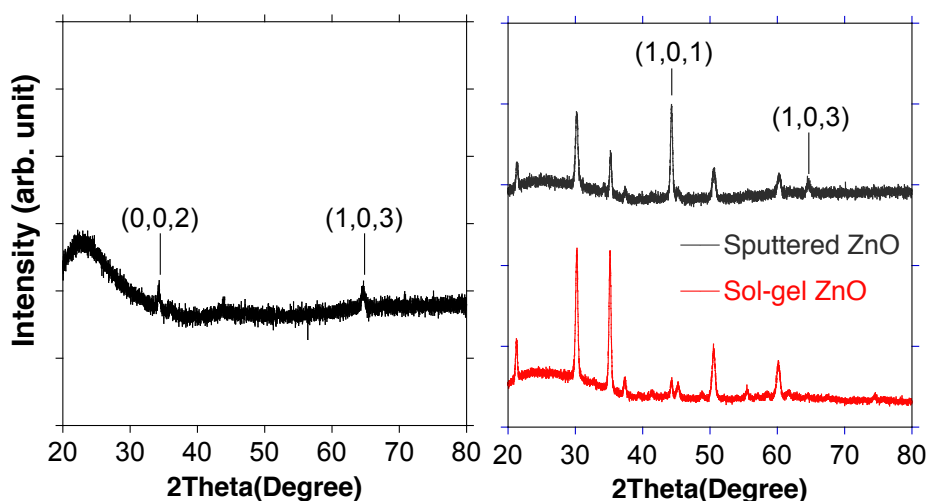


Figure 2. XRD data of sputtered ZnO film on quartz (left), and sputtered ZnO (black) and sol-gel ZnO (red) each on ITO substrates (right).

ZnO film morphology was checked using AFM (Figure 3). Since the morphology influences device performance, it can serve as an important data. From the images only, they all looked similar owing to the thin nature of ZnO layer which overcoats much rougher ITO surface. Nonetheless, there was an interesting difference

between sol-gel ZnO and sputtered ZnO. While Ra of sol-gel ZnO was lower than that of ITO, Ra of low-vacuum sputtered ZnO was similar. The reason behind this is explained in the illustration in Figure 3 below. Solution-based sol-gel ZnO welled up at the bottom of the rough surface of ITO. On the other side of the coin, ZnO sputtering grew ZnO film randomly on the ITO surface, maintaining the roughness. It has been reported that a certain degree of roughness of ETL is necessary for effective charge extraction.^[371,372] Thus, it is better to have a bit of roughness.

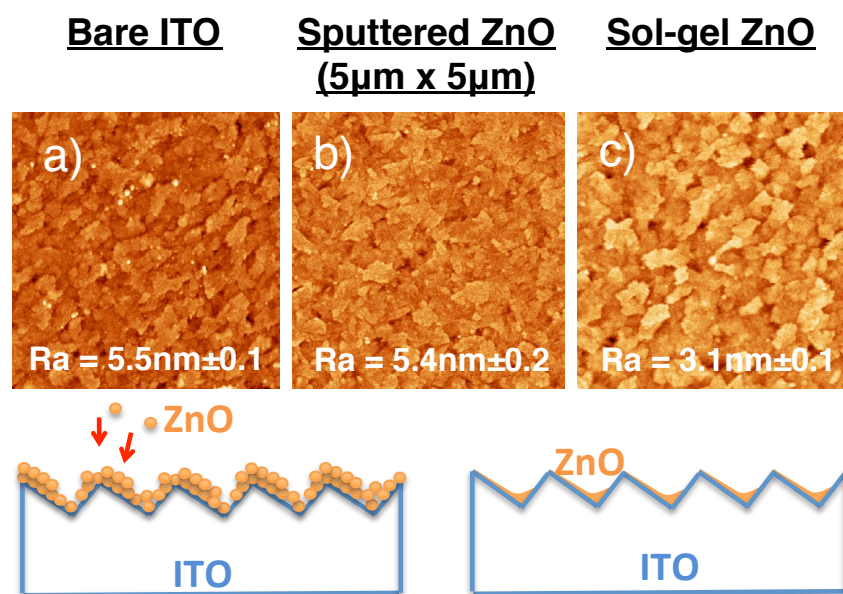


Figure 3. Above are the AFM images of a) bare ITO, b) low-vacuum sputtered ZnO and c) sol-gel ZnO both on ITO substrates. Below are the illustrations of sputtered ZnO and sol-gel ZnO samples.

According to the photovoltaic performance of solar cell devices in Table 1 and Figure 4, we can see that there is an increase of 0.45% in PCE from the sol-gel ZnO-based devices to the HWP sputtered ZnO-based devices. The escalation came from the improvement in FF which was due to high crystallinity as proven from the XRD data. What was interesting is that the HWP sputtered ZnO film-based devices showed extremely low R_s . Such low R_s corroborates high crystallinity of ZnO. This is because having high mobility enhances the movement of charge carriers in the direction of energetic bias, but since flow in the opposite direction is governed by energy gap rather than mobility, crystallinity affects R_s only. Compared with the conventionally sputtered ZnO-based devices, virtually every parameter was improved telling us that sputtering at HWP is detrimental to the quality of ZnO film in every aspect.^[345]

Table 1. Photovoltaic data of solar cell devices with sol-gel ZnO as the reference, conventional sputtered ZnO, and low-vacuum sputtered ZnO under 1 sun (AM1.5G illumination, 100 mW cm^{-2}).

ETL	V_{oc} (V)	J_{sc} (mA cm^{-2})	FF	R_s (Ω)	R_{SH} (Ω)	PCE (%)
Sol-gel ZnO	0.61	8.9	0.56	17	1.1×10^4	3.07
Conventional sputtered ZnO	0.50	7.4	0.40	20	2.0×10^3	1.49
HWP-sputtered ZnO	0.62	9.8	0.56	2	2.9×10^3	3.42

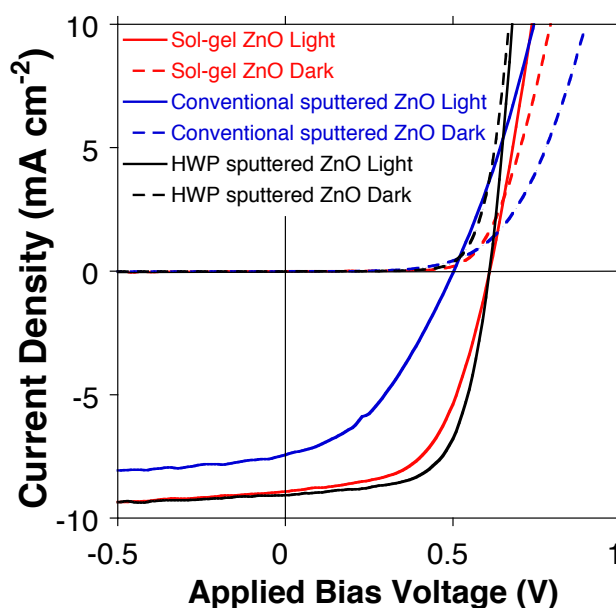


Figure 4. J - V curves solar cell devices with sol-gel ZnO as the reference, conventional sputtered ZnO, and low-vacuum sputtered ZnO under 1 sun and in dark.

Having demonstrated the feasibility of HWP-sputtered ZnO, I discuss their potential applications in this paragraph (Figure 5). Recently, different electrode materials are being introduced to OSCs as a means to broaden their application. Compatibility of these newly introduced materials hinges on numerous factors, wettability being one of them. Hydrophobic or too hydrophilic electrodes are incompatible with any kind of spin-coating-based ETL fabrications. Therefore, by adopting my methodology, OSCs application of electrodes with unfavourable surface energy can be achieved. For instance, flat ITO is known to produce marginally low R_{sheet} , yet solution cannot be spin-coated due to its extremely low surface energy. With HWP sputtering technique, I can accomplish this. What is more, while there have been many reports on flexible OSCs, they are mostly limited to normal architectures. Fabrication of inverted type OSCs involves an ETL deposition process which demands high temperature annealing. Therefore, plastic flexible substrates with low

T_g cannot be utilised. However, with my HWP ZnO sputtering, flexible electrodes such as CNT can be employed without any thermal damage to the substrate.

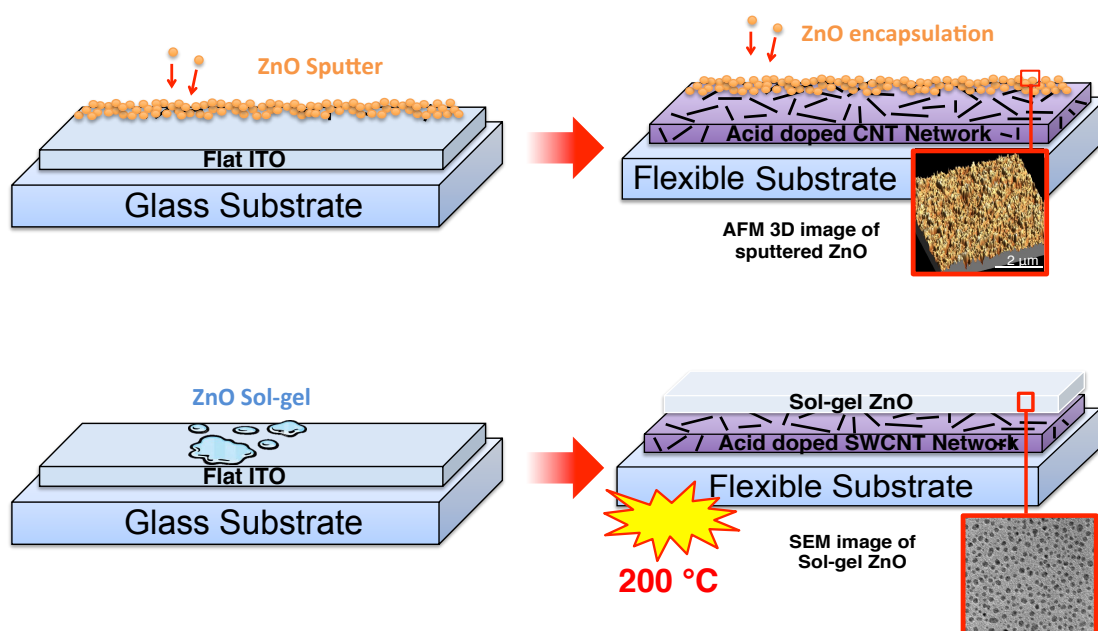


Figure 5. Examples of successful applications of sputtered ZnO sputter (above) and unviable applications of sol-gel ZnO (below).

9.5 Conclusion

I have successfully demonstrated a new sputtering methodology for the fabrication of high-performing ZnO films for inverted OSCs that require no thermal process. My method exploits HWP to reinforce high-energy ZnO sputtered particles to stabilise which improves crystallinity of ZnO as evidenced by XRD. Also it utilises low oxygen atmosphere to enhance conductivity and polycrystallinity again corroborated by XRD and the literature. Solar cell devices fabricated using HWP-sputtered ZnO shows higher FF due to higher mobility, which is reflected by the increase in PCE. Compared to both conventional sputtered ZnO and sol-gel ZnO films, they performed much better without any thermal process which means now the application can be extended to flexible and on any type of electrode. The research is still in progress and the completion will accompany a further optimised PCE with high-performing low-band gap polymers followed by demonstrations in diverse applications including those aforementioned.

CHAPTER 10

SURFACE MODIFICATION OF THE CHARGE CONDUCTIVE AND SELECTIVE LAYERS USING ANTHRACENE DERIVATIVES IN INVERTED ORGANIC SOLAR CELLS

10.1 Summary

In this work, by casting a water soluble anthracene-based V-shaped polyaromatic amphiphiles on metal oxides in OSCs, the interface between transparent metal oxide (ITO and ZnO), and photoactive organic layer has been improved. The anthracene-based organic surface modifiers re-engineered electron extraction layer by covering up the defect sites of the metal oxides with their positively charged ends to improve charge transport. Also its apposite energy level values increased the work function of ITO while acting as a hole-blocker, which allowed the thin layer of the modifier to replace ZnO. Moreover, their bent polyaromatic ends could act as fullerene catchers, forming an aligned layer of fullerene electron acceptors. They formed ohmic contact with the fullerene derivatives for photogenerated charge-carrier collection and allowed optimum photon harvest in the device. These anthracene-treated ZnO-based solar cells showed an average PCE of 3.08% while non-treated devices gave an average of 2.91%. Even for solar cells without ZnO layer, in which the anthracene derivatives were applied on ITO, they produced 2.58% efficiency. I am positive that these findings will open new avenues in understanding and tailoring the interfaces between organic semiconductors and transparent oxides for the advancement of surface modifiers and solar cell researches.

10.2 Introduction

Extensive efforts have been put into developing OSCs for their low-cost, light-weight, and potential flexibility.^[373,374] Effort to avoid the low-work-function metals have created inverted architecture of the device where oxide ETL such as ZnO^[143] have been used on ITO electrode to invert the polarity of the bulk heterojunction devices.^[343,375–377] This design not only yield high efficiencies but also prolongs the lifetime by avoiding reactive layers, thereby mitigating the encapsulation requirement.^[185,194,378,379] Among different types of ZnO, sol-gel-prepared colloidal nanoparticles, discovered by A. Heeger and his colleagues, have most widely been used for their high electron mobility and optical transparency as well as ease of synthesis.^[335] However, the major challenges in using the ZnO nanoparticle films are the inevitable near-surface defects,^[380,381] and poor spatial distribution of the nanoparticles over a large area.^[382,383] These are originated from oxygen vacancies (V(O)s) and zinc interstitials (Zn(i)) which change the degree of doping and in turn result in a change of the Fermi level position.^[384–386] Furthermore these affect carrier density, chemical potential and the chemistry with the adjacent organic layers.^[387] Hence, to realize highly efficient inverted OSCs, it is imperative that I develop low-defect and uniform ZnO films, because a significant hurdle is the extraction of charge carriers at the contact.^[388] So far, there have been numerous reports on improving the contact by means of surface treatment: Water-soluble polyfluorenes with alkylphosphonates and alkylamine salts on the side chains were found to be very effective for the elevation of V_{OC} .^[389,390] Application of carboxylic acids as a self-assembled monolayer on top of ZnO to modify the interfacial property is another example.^[143] Not only the interface of ZnO but also the interface of organic side could be improved using self-assembled cross-linked fullerene^[344,391–393] To date, poly [(9,9-bis(3-(N,N-dimethylamino)propyl)-2,7-fluorene)-alt-2,7-(9,9-dioctylfluorene)], which was originally used for light-emitting devices to enhance electron injection has demonstrated the best performance as the ETL itself replacing ZnO.^[144,394–396]

Here I present the anthracene-based amphiphile as a surface modifier that has positively charged trimethylammonium group ($-N^+(CH_3)_3$) on one end and two bent polyaromatic groups on the other end.^[397] When they overcoated ZnO, the charged ends reacted with the defect sites to alleviate the poor contact between ZnO and the

active layer interface as proven by recovery of V_{OC} loss. As organic compounds, they possessed HOMO and LUMO levels that corresponded to ETL; When they were deposited on ITO, they offered ohmic contact for collection and allowed optimum photogenerated charge-carrier harvest replacing ZnO. One distinguishing quality these anthracene derivatives possessed was that they had polyaromatic surfaces of the V-shaped amphiphiles which could effectively catch fullerenes through multiple aromatic-aromatic interactions. This induced a thin PCBM layer as a barrier for hole carrier injection as substantiated by elevations of J_{SC} and FF.

10.3 Experimental Procedures

10.3.1 Device Fabrications

For the synthesis of the anthracene-based surface modifier, the methodology in *Angew. Chem. Int. Ed.* 2013, 52, 2308 was used.

For the OSC fabrications, refer to 2.1.1.2 Organic solar cell inverted device architecture and 2.1.1.3 P3HT:mix-PCBM solution preparation

For the reference device, ITO substrates with size $15 \times 15 \text{ mm}^2$ and an active area of $3 \times 3 \text{ mm}^2$ with a sheet resistance of $6 \Omega \text{ sq.}^{-1}$ (Kuramoto Co., Ltd.) were sonicated in cleaning surfactant (Semi Clean, M-Lo), water, acetone and 2-isopropanol for 15 min each. The substrates were then dried with N_2 gun. ITO substrates were exposed to UV/ O_3 for 30 min in order to remove any remaining organic impurities. Water solutions with anthracene concentration ranging from 2.5 mg mL^{-1} to 9 mg mL^{-1} were applied on the active surface at $25 \text{ }^\circ\text{C}$ for 20 min. The water solution was covering only active area without interfering with the contacts. After 20 minutes residual solution was blown with N_2 and (in the case of ZnO treatment) rinsed with water, and then dried with N_2 gun. In the case of ITO experiment was done without rinsing.

ZnO sol-gel films were prepared using the method reported by Heeger et al.^[185] The metal oxides were baked at $200 \text{ }^\circ\text{C}$ before depositing the photoactive layer.

10.3.2 Characterisations

Please refer to 2.2.1.1 Current-voltage characterisation, 2.2.1.3 Space-charge limited current (SCLC), 2.2.2.1 UV-vis absorption, 2.2.2.3 Atomic force microscopy (AFM), 2.2.2.6 X-ray photoelectron spectroscopy (XPS), 2.2.2.7 X-ray powder diffraction (XRD), and 2.2.2.8 Photoelectron yield spectroscopy (PYS).

For the crystallography, crystals were grown slowly by evaporating a water solution at room temperature for 3 days. Further details can be found in the supporting information of the previous work (CCDC 889326).^[397]

10.4 Results and Discussion

Water is a prime solvent of nature's choice, capable of dissolving biomolecules with no harm to the environment. Whereas, the majority of electron device fabrications including solar cells rely on expensive and often harmful various organic and inorganic solvents. The anthracene derivatives (ANTHs) introduced in this work possessed high polarity and can form micelle spherical structures with core diameters of ~ 1 nm in water.^[398,399] Therefore, my approach qualified for an aqueous solution-process that was easy and fully amenable to roll-to-roll fabrication. For the surface treatment, anthracene derivative compounds were dissolved in water with different concentrations ranging from 2.5 to 9 mg mL⁻¹. Then the solution was dropped slowly on either ITO or ZnO. After 20 minutes waiting time, the film was blown with a nitrogen gun to remove the solution. For some samples, I applied water rinsing which eliminated any unreacted anthracene derivatives to induce a monolayer of ANTHs (Figure 1a). For those water rinsing was not applied, I expected thicker layers of ANTHs (Figure 1b).

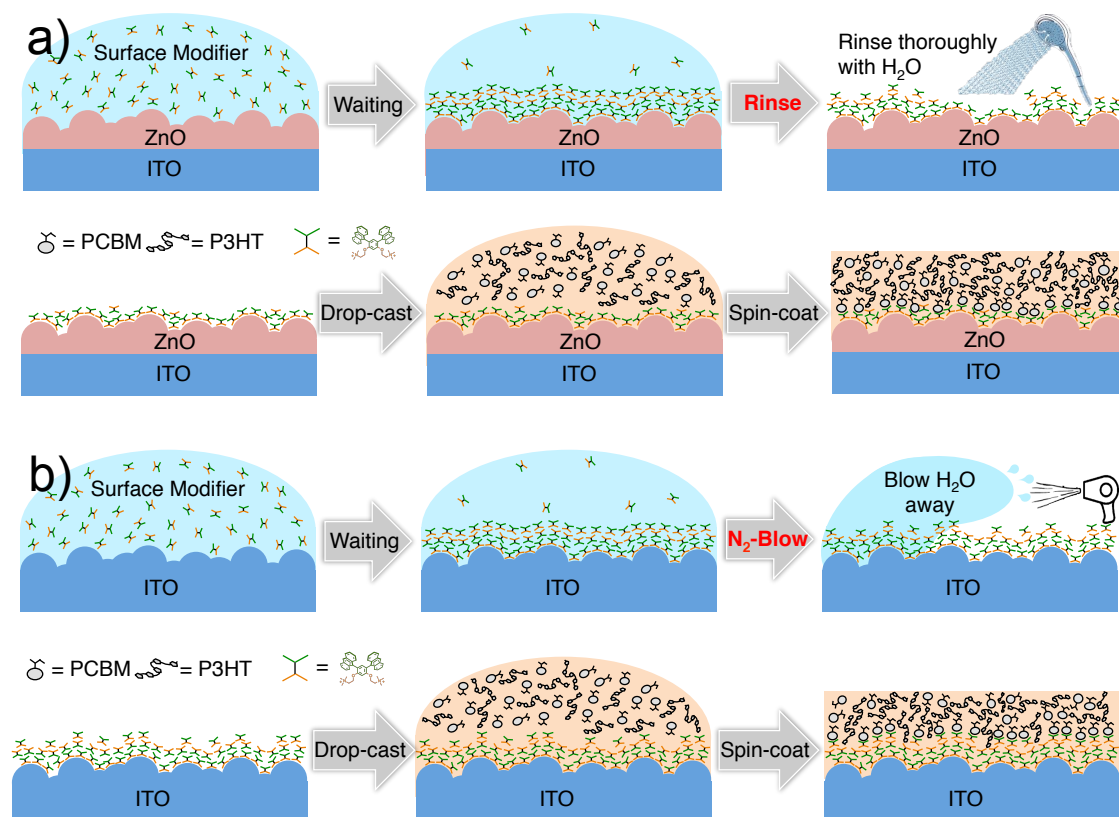


Figure 1. Illustrations of ANTH surface treatments a) with rinsing and b) without rinsing.

Inverted OSCs were fabricated using different concentrations of ANTHs on either ITO or ZnO. A mixture of P3HT and PC₆₁BM photoactive materials was used owing to their established reliability and reproducibility. PCEs of the devices are shown in Figure 2. According to the data, ANTHs applied on ZnO with rinsing performed the best regardless of the concentration. ANTHs applied on ZnO without rinse performed worse and especially with increase in their concentrations. We can conjecture that the monolayer of ANTH on ZnO induces the best performance, but when ANTHs gets thicker, they undermine the device performance. On the other hand, for ANTHs on ITO, non-rinsed ANTHs applied OSCs performed better than the rinsed ITO-based OSCs. This is because ANTHs performed as an ETL replacing ZnO. Therefore, a thicker layer was required to avoid shunt pathways between ITO and P3HT:PC₆₁BM. Yet, the concentrations from 4 to 6 mg mL⁻¹ showed the optimal results. In other words, an interlayer that is too thick leads to a high R_s , while a too-thin layer cannot provide an ohmic contact for electron extraction. Overall, rinsed ANTH-based devices showed independence of concentration, while non-rinsed ANTH-based devices showed dependence of concentration.

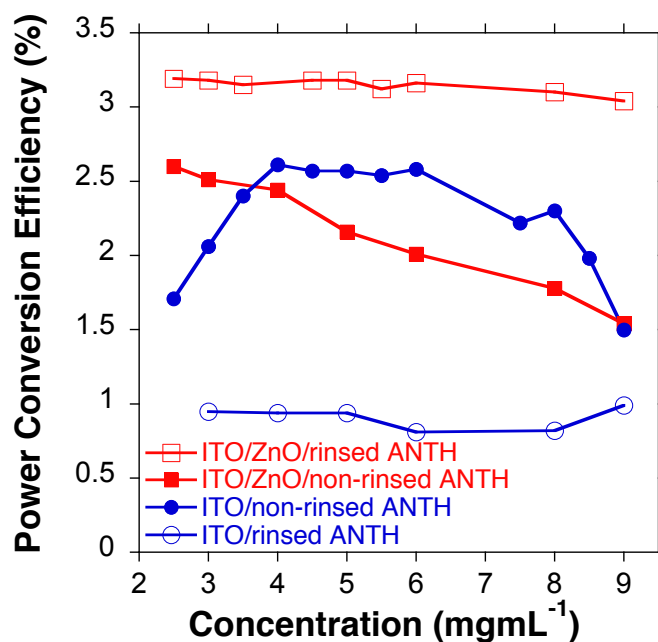


Figure 2. PCE plots of ITO/ZnO/rinsed ANTH-based device (red open squares), ITO/non-rinsed ANTH-based device (red closed squares), ITO/ZnO/non-rinsed ANTH-based device (blue closed circles), and ITO/rinsed ANTH-based device (blue open circles), according to ANTH concentrations.

Highly performed devices from each of the four conditions were selected. Corresponding photovoltaic tables are shown in Table 1 along with a reference device. The ITO/ZnO/rinsed ANTH-based devices showed an average PCE of 3.08% which is higher than that of the reference (2.91%). Higher FF was the reason for such high performance of the ANTH-applied devices, but the J_{SC} value was a little lower than that of the reference devices. Increase in both FF and R_{SH} meant that ANTHs enhanced hole-blocking effect of ZnO.^[400] Also, the fullerene catching effect of ANTHs could have induced vertical separation which entailed increase in FF.^[401] The concave polyaromatic ends of the ANTHs can effectively catch fullerenes with different sizes by multiple aromatic-aromatic interactions (Figure 3). Then those fullerenes can form an electron transfer barrier at the interface enhancing the hole-blocking ability of ANTHs even more. Nevertheless, decrease in J_{SC} is still difficult to understand. Since ANTH treatment does not decrease transmittance as evidenced by UV-vis spectroscopy in Figure 4, we can rule out the possibility of decrease in the light intensity. This leaves us with energetic hindrance in charge extraction.^[183,237,241] For the ITO/ZnO/non-rinsed ANTH-based devices, the lowest concentrations, 2.5 mg mL⁻¹ gave the highest performance, indicating that when an ETL i.e., ZnO was involved, thinner ANTH layer was preferred. The thicker it got, the more pronounced

the decrease in FF and J_{SC} were. Decrease in FF was understandable for the ANTHs are organic compounds, and organic compounds have lower carrier mobility than metal oxides;^[402,403] SCLC measurement was conducted to clarify this and a marginal decrease was observed from non-rinsed ANTH-treated ZnO compared to ZnO by calculating mobilities of electron-only devices (Figure 5). Decrease in J_{SC} was somewhat subtle, but again energetic perspective could be the reason for the phenomenon. The ITO/rinsed ANTH-based devices showed appalling performances in every parameter. Probably, after ITO has been rinsed away, there were simply not enough ANTHs to cover ITO surface fully to induce the Ohmic contact. The ITO/non-rinsed ANTH-based devices performed rather well (an average PCE of 2.58%) even in the absence of ZnO. High V_{OC} of 0.59 proved that ANTHs themselves could function as ETLs. Such behaviour is due to the increased built-in potential originating from the establishment of interfacial dipole of the ANTH layer.^[389,390,404] Compared to the reference device, FF was the same. This, I think, is on account of the combination of aforementioned intrinsic low mobility of ANTHs and more importantly disturbance in the vertical separation effect. If the ANTHs do not form a monolayer, it would form multiples layers of ANTHs. While some layers will face the photoactive layer with the polyaromatic ends to interact with the fullerene acceptors, some will face P3HT:PC₆₁BM with the trimethylammonium ends which may even interact with lone pairs on S of P3HT. Consequently, we cannot expect complete vertical phase separation effect from non-rinsed ANTHs in theory. Low J_{SC} was again witnessed which was the sole reason why the ITO/non-rinsed ANTH-devices showed lower PCE than that of the reference.

Table 1. Photovoltaic parameters of ANTHs-applied devices and a reference device under 1

Device	V_{OC} (V)	J_{SC} (mA cm ⁻²)	FF	R_S (Ω)	R_{SH} (Ω)	PCE (%)
ITO/ZnO/rinsed ANTH	0.60±0.00	8.89±0.27	0.58±0.03	3.5	4.8×10^4	3.08±0.12
ITO/ZnO/non-rinsed ANTH (2.5 mg mL ⁻¹)	0.60	8.05	0.52	5.1	3.3×10^3	2.54
ITO/rinsed ANTH	0.32±0.05	7.90±0.14	0.39±0.01	8.7	3.8×10^2	0.95±0.16
ITO/non-rinsed ANTH	0.59±0.01	8.23±0.18	0.53±0.16	8.3	4.1×10^3	2.58±0.02
Ref. ITO/ZnO	0.60±0.01	9.20±0.20	0.52±0.03	5.2	2.8×10^3	2.91±0.21

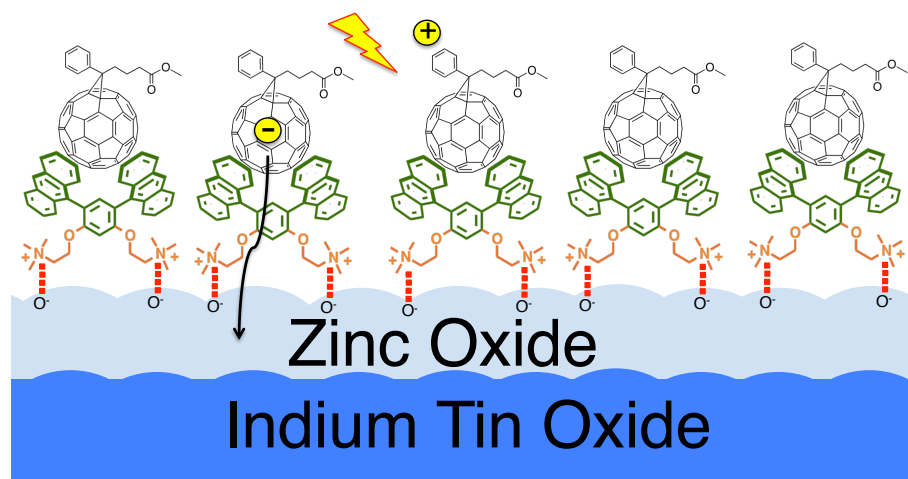


Figure 3. A graphical illustration of the ANTHs interacting with a metal oxide, ZnO and fullerene derivatives, PC₆₁BM.

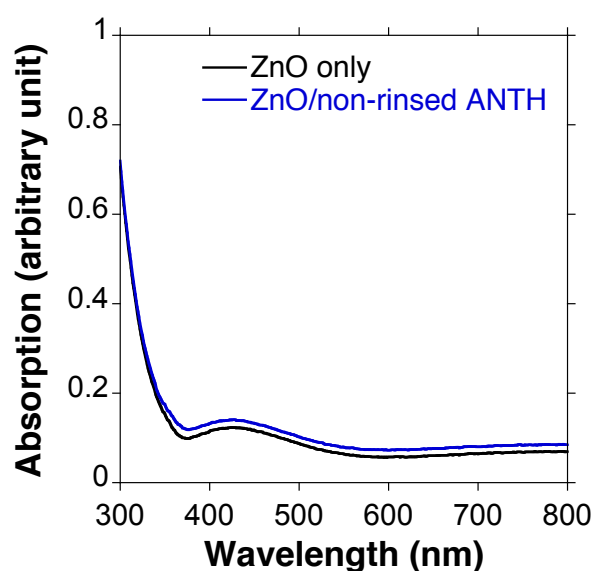


Figure 4. UV-vis spectra of a ZnO film and an ANTHs-treated ZnO film on glass.

To investigate the energetics of the ANTHs, I have run the Gaussian calculation to find out their energy level information. It is important to know that efficient electron injection and hole-blocking effect can be obtained by decreasing the work function of ITO effectively and having a deep HOMO level, respectively.^[194] By looking at HOMO-LUMO values in Figure 6, we can see that the ANTHs possess deep-lying HOMO value which induces a good hole-blocking quality. Whereas, the LUMO level of 2.25 eV seems rather low. It is certainly low enough to decrease the ITO work function, but this alludes an energy mismatching with the LUMO level of PC₆₁BM photoactive layer, which is 3.8 eV.

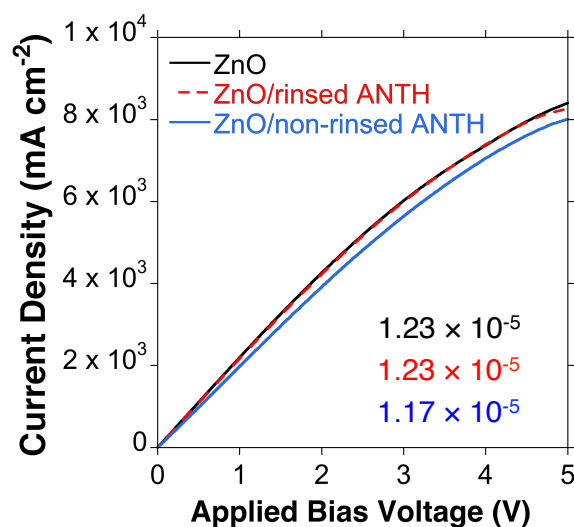


Figure 5. *J-V* curves of the electron-only devices for SCLC measurement and electron mobilities (μ) given as an inset with the unit ($\text{cm}^2 \text{V}^{-1} \text{S}^{-1}$).

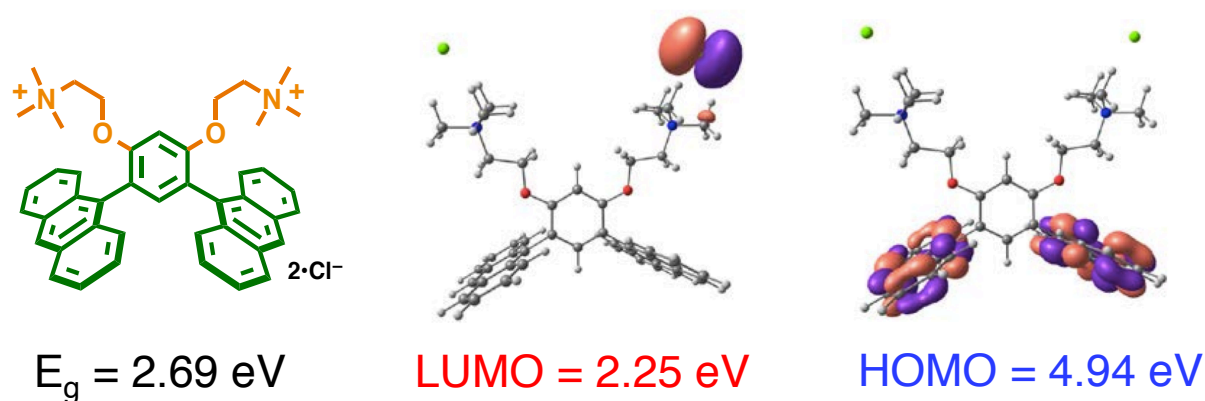


Figure 6. A chemical structure of the anthracene surface modifier with a measured band gap (left), and Gaussian calculations of LUMO (middle) and HOMO (right) with energy levels as absolute values.

Energy levels of ITO and ZnO were measured before and after the ANTHs treatment by Kelvin probe and PYS. Using PYS, I could find out about the work function of ITO and valence band (or HOMO) of semi-conductive ZnO and ANTHs. From Figure 7a, we can see that ITO possessed the work function of around 4.7 eV, but after the ANTHs were applied, the energy level value increased to around 5.7 eV (Figure 7b). This value did not change after water rinsing, indicating that chemical adsorption had occurred between the ANTHs and the ITO surface (Figure 7c). This 5.7 eV value was similar to the valence level observed from ZnO (5.5 eV) in Figure 7d. This denotes that the ANTHs have a good hole-blocking property. Application of

the ANTHs on ZnO did not change the HOMO level. This confirms the deeply lying HOMO level of the ANTHs matching the valence level of ZnO.

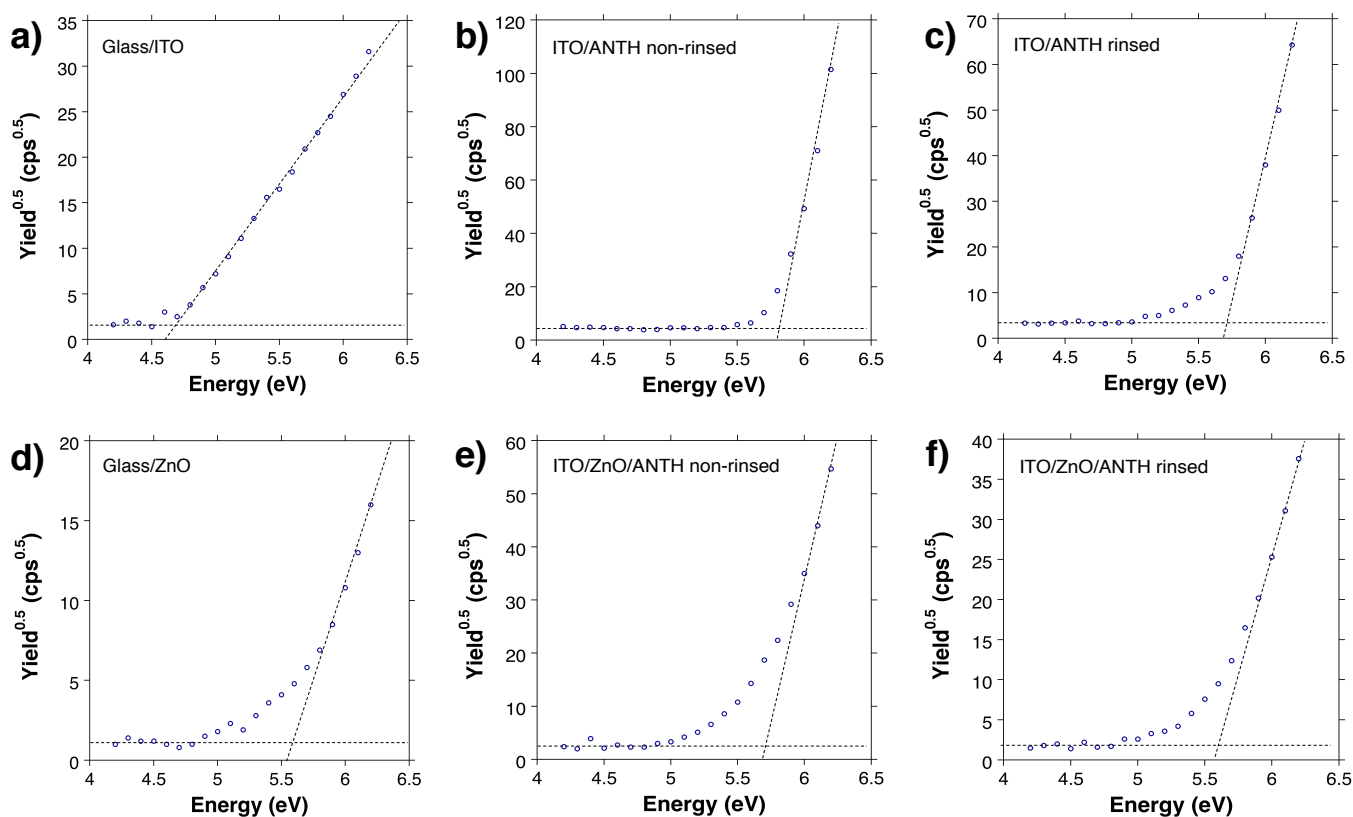


Figure 7. PYS data of a) ITO, b) water-rinsed and c) non-rinsed anthracene ANTH-applied ITO; d) ZnO, e) water-rinsed and c) non-rinsed ANTH-applied ZnO.

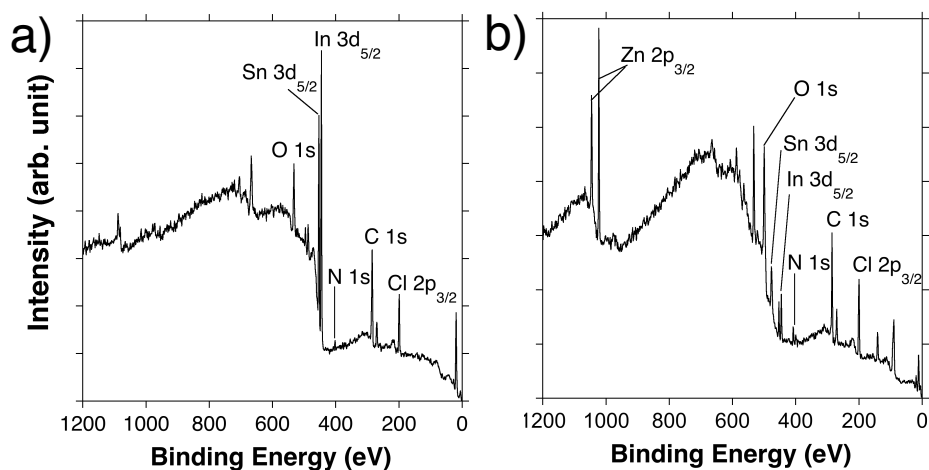


Figure 8. XPS spectra of a) ITO/non-rinsed ANTH and b) ITO/ZnO/rinsed ANTH.

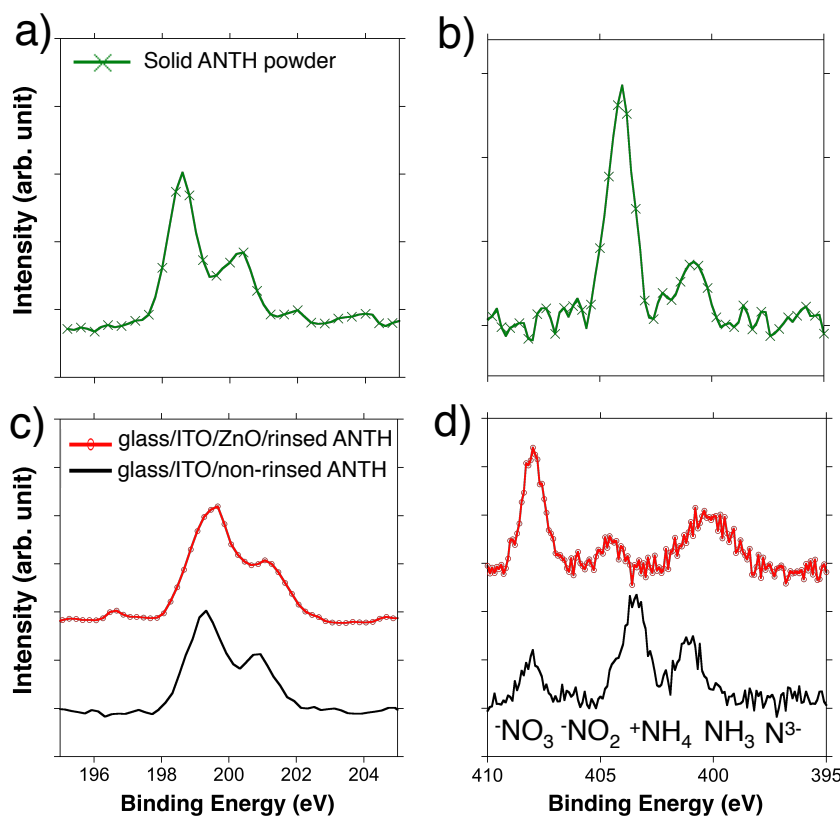


Figure 9. XPS spectra of solid ANTHs for a) Cl 2p core and b) N 1s core; and both of rinsed ANTHs on ZnO and non-rinsed ANTHs on ITO c) Cl 2p core, and d) N 1s core.

The interaction between ANTHs and metal oxides was studied by XPS. The whole range spectra are shown in Figure 8. Chlorine 2p peaks were present in all spectra (Figure 9a and 9c). This means that Cl^- stays even after the surface treatment and water rinsing. But there were interesting differences in nitrogen N 1s peaks. Solid ANTH powder possessed two peaks: one on the left corresponding to nitrogen in trimethylammonium group and one on the right corresponding to the same nitrogen affected by the organic matrix surrounding it (Figure 9b). The left peak decreased a little and a new peak appeared further to the left, corresponding to more negative nitrogen i.e. nitrate (Figure 9d). This peak became even stronger after water rinsing, meanwhile the trimethylammonium peak decreased to reveal that any non-interacting ANTHs. I believe this is an indication of ANTHs interaction with metal oxide. Although the microscopic origin of the mechanism is uncertain at this point, it is plain that the orientation of the molecules with a permanent dipole is the major reason for the energy level alignment.^[395,405] The positively charged trimethylammonium side of the molecules is speculated to have reacted with the defect sites in oxygen making the polyaromatic groups facing away from the metal oxides.

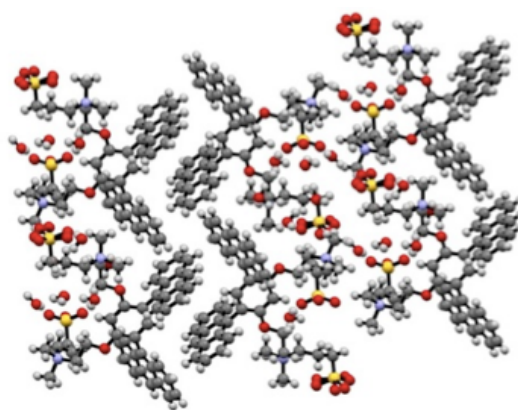


Figure 10. Crystallography of ANTHs where trimethylammonium ends are to the left and bent polyaromatic groups are facing to the right. The crystal was grown slowly by evaporating a water solution at room temperature for 3 days. Further details can be found in the supporting information of our previous work (CCDC 889326).^[397]

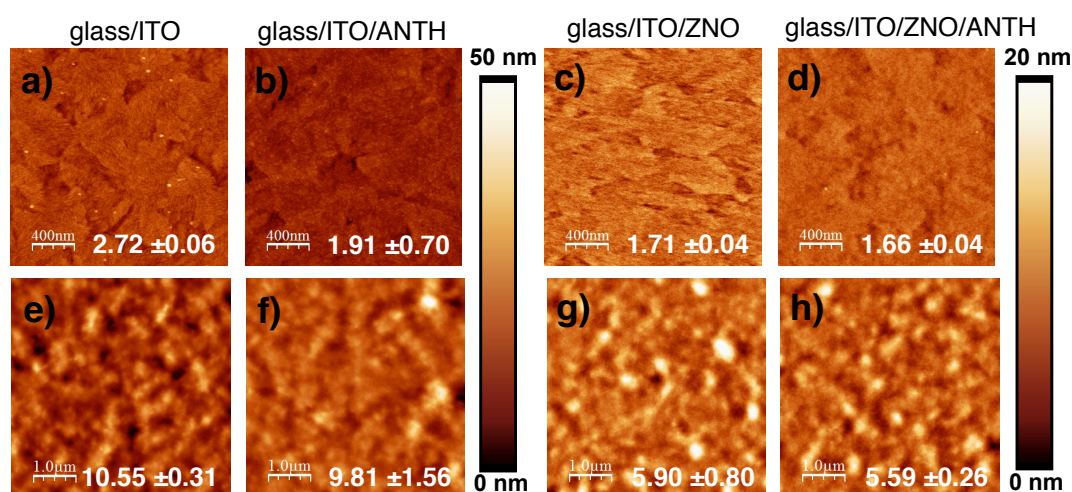


Figure 11. AFM images and r.m.s. roughness values of a) glass/ITO, b) glass/ITO/non-rinsed ANTH, c) glass/ITO/ZnO, d) glass/ITO/ZnO/rinsed ANTH, e) glass/ITO/P3HT:PCBM, f) glass/ITO/non-rinsed ANTH/P3HT:PCBM, g) glass/ITO/ZnO/P3HT:PCBM, and h) glass/ITO/ZnO/rinsed ANTH/P3HT:PCBM.

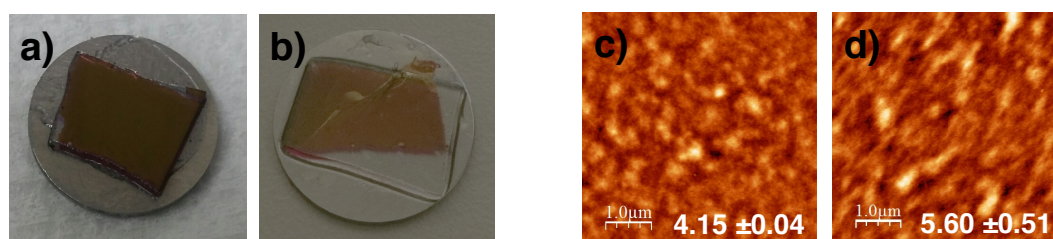


Figure 12. Pictures after OT treatment for a) glass/ITO/ZnO/P3HT:PCBM and b) glass/ITO/ZnO/rinsed ANTH/P3HT:PCBM. AFM images and r.m.s. roughness values after OT treatment for c) glass/ITO/ZnO/P3HT:PCBM and d) glass/ITO/ZnO/rinsed ANTH/P3HT:PCBM.

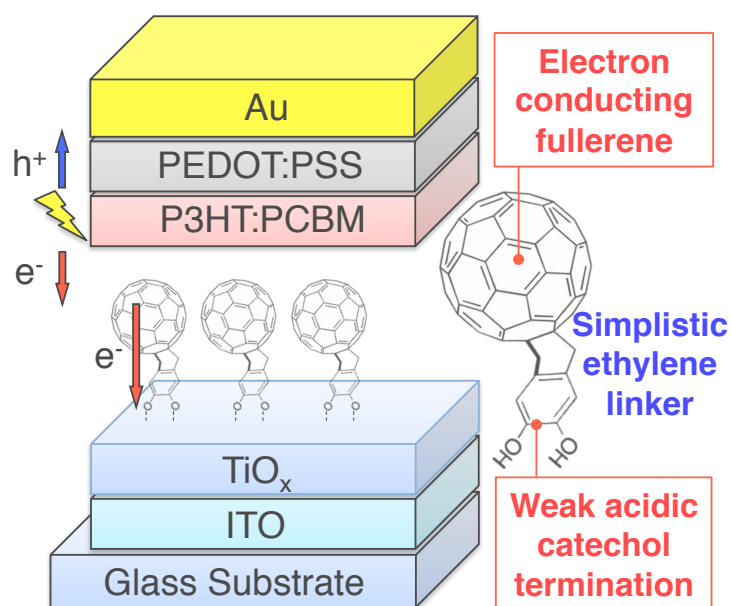
The formation of an interfacial dipole layer and orientation of multiple layers can be checked by crystallography and small-angle X-ray diffraction (XRD). As for

the XRD, it is currently under measurement and will be added in due course. According to the crystallography in Figure 10, multilayers of ANTHs were stacked in a way that their orientation alternates. This meant that when ANTHs were not rinsed, there was half a chance that the polyaromatic ends might face upwards. This explains why increase in FF was not observed in non-rinsed ANTH-treated devices as opposed to rinsed ANTH-treated devices, because they could not induce vertical separation as much.

AFM was used to delve into the ANTH's interaction with the metal oxide and its fullerene catching ability. For both ITO and ZnO, r.m.s. roughness values decreased slightly after the ANTH treatment (Figure 11 a – d). This denoted that ANTH surface treatment had an effect of improving morphology by filling up pinholes in metal oxide surfaces. To my surprise, the same thing happened on P3HT:PCBM active layers. The ANTH treatment seems to have an effect on morphology of the active layers too (Figure 11 e – h). But overall the decrease in roughness were not too big to signify deterioration of the interface.^[38,369] 1,8-octanedithiol (OT) is known to selectively dissolve PCBM and be used in detecting vertical phase separation.^[196,406] Therefore, I applied OT on the active layers to see if there are any interesting changes. When OT was applied to glass/ITO/ZnO/rinsed ANTH, it peeled off the film (Figure 12a and b). This was because OT dissolved a fullerene layer at the bottom of the active layer proving the ability of ANTHs catching fullerene derivatives in a photoactive layer. This also happened with glass/ITO/non-rinsed ANTH telling us that even non-rinsed ANTH manifests some degree of fullerene-catching ability. According to Figure 12c and d, OT treatment resulted in slightly different morphologies to ANTH-treated and non-treated P3HT:PCBM layers. However, the change was not clear as to what is expected from vertical phase separation.^[63] Thus, the vertical phase separation effect either does not exist or is too weak to detect.

10.5 Conclusion

In conclusion, I have successfully demonstrated the V-shaped amphiphile organic compound as a water-soluble surfactant in inverted OSCs. The surface modifier called ANTH in this manuscript can improve the metal oxides either ITO or ZnO by reacting on the defect sites and filling up the pin-holes. ANTH possesses deep lying HOMO level as evidenced by our PYS and the Gaussian calculations, which can function as ETL replacing ZnO when treated on ITO. ANTH also has a special fullerene catching ability as seen by AFM. It induces an interlayer of charge transporting fullerene derivatives from the photoactive layer, which leads to enhancement in FF. The performance devices with varied PFN thickness and rinsing conditions. The most optimized ANTH-treated OSCs without ZnO gave an average PCE of 2.58% while the surface treatment on ZnO gave 3.08%. I am confident that this finding will open new avenues to tailoring and understanding interfaces between organic semiconductors and transparent oxides.



CHAPTER 11

SURFACE MODIFICATION OF THE CHARGE SELECTIVE LAYER USING CATECHOL DERIVATIVES IN INVERTED ORGANIC SOLAR CELLS

11.1 Summary

[60] Fullerene catechol self-assembled monolayers were prepared and applied to inverted OSCs by an immersion method and their energy conversion properties were measured. Due to the introduction of fullerene groups, hole-blocking ability of the electron-transporting metal oxide improved as shown by fill factor enhancement. Fullerene catechol-treated TiO_x-used device gave PCE of 2.81% with fill factor of 0.56 while non-treated device gave 2.46% PCE with fill factor of 0.49. The overall improvement in solar cell efficiency was 13% compared to the reference device.

11.2 Introduction

The physical and chemical phenomena at the interface between metal oxide surface and organic semiconductor is of fundamental relevance for organic electronic applications. A new generation of thin-film OSCs relies on a rationally designed electrode/organic active layer interfacial electronic structure in facilitating efficient charge extraction. In this regards, inverted OSCs can take advantage of the vertical phase separation and concentration gradient in the active layer.^[63,196] Fullerene acceptors being near the ETL has been known to strengthen the charge-carrier transport in the inverted architecture. Thus, technology that can bring fullerenes on the metal oxide can establish the first principles of precise control over the vertical separation.

Self-assembled monolayers (SAMs) with fullerene attached are good motifs for such prospect.^[407] The coating of inorganic substrates such as metal oxides or metals with SAMs can alter the work function and the surface energy of the electrodes.^[408] There has been a variety of SAMs with fullerene reported to date.^[409–413] Among those SAMs, catechol-terminated SAMs have attracted the limelight for their weak diprotic acid nature which can form bidentate bonding with metal oxide while minimising the damage unlike carboxylic acid- or phosphonic acid-terminated modifiers.^[414–416] Recently, Jen et al. have published a number of catechol-terminated SAMs where fulleropyrrolidine has been as a linker.^[344,417–419] Although they have demonstrated improvements in OSC performance, fulleropyrrolidine containing nitrogen atom is not regarded to be fully inert.

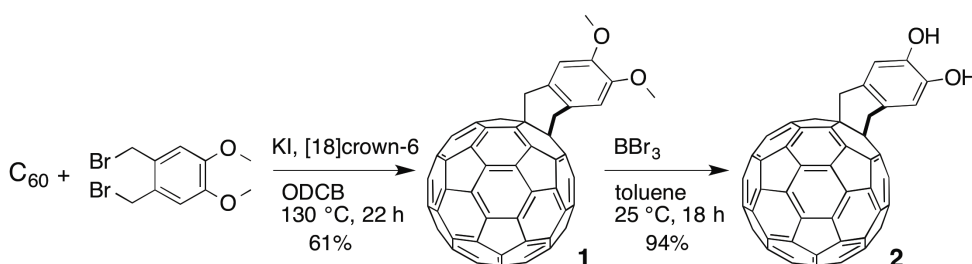
Here I have utilised a simpler SAM that is composed of a catechol end and a fullerene end, which are linked by the simplest methylene linker functioning as effective charge-carrier harvesters. Catechol being a weak acid, it can bind to TiO_x strongly.^[417,420–424] Fullerene has high electron mobility and low hole mobility. Therefore, a monolayer of fullerene can function as an additional hole-blocker. With their tendency to attract other fullerene molecules by π - π interactions, they may even induce the vertical separation effect as evidenced by enhancement in fill factor (FF) in my study.^[401] I fabricated an inverted OSC using a mixture of P3HT and PC₆₁BM in a structural configuration of glass/ITO/ TiO_x -catechol

C₆₀/P3HT:PC₆₁BM/PEDOT:PSS/Au. The SAM-treated device gave 2.81% while non-treated device sample gave 2.46% where enhancement of FF was the main reason for the improvement.

11.3 Experimental Procedures

Catechol C₆₀, compound **2**, was synthesised (Scheme 1) through addition of *ortho*-xylylene to C₆₀ according to previously reported synthetic method.^[425] C₆₀ (387 mg, 0.537 mmol), 1,2- bis(bromomethyl)-4,5-dimethoxybenzene (174 mg, 0.537 mmol), and [18]crown-6 (1.14 g, 4.29 mmol) with KI (200 mg, 0.6 mmol) in 1,2-dichlorobenzene (120 mL) were refluxed at 130 °C for 22 h. The reaction mixture was cooled and collected after evaporation of the solvent. After hexane was added to the concentrated solution, brown precipitate was collected by filtration. The crude was purified by silica gel chromatography with CS₂/toluene as eluent. Monoadduct **1** (291 mg, 0.329 mmol, 61%) and diadduct (25 mg, 0.024 mmol) were attained.

Compound **1** (571 mg, 0.645 mmol), 40 mL of BBr₃ solution (1.0 M in CH₂Cl₂) and toluene (250 mL) were placed in a flask. The solution was heated up from 0 °C to 25 °C gradually. The reaction was quenched by water after stirring for 18 h. The crude was extracted using ethyl acetate, and purified by silica gel chromatography with toluene as eluent. A brown solid **2** (519 mg, 0.604 mmol, 94%) was obtained.



Scheme 1. Synthesis of Catechol C₆₀

C₆₀-SAMs with the catechol termination could be absorbed onto the surface of TiO_x by a simple immersion process. On UV-O₃ treated ITO/glass substrates, TiO_x films were fabricated using the chemical bath method.^[184] Then TiO_x on ITO substrate

was immersed in the solution of catechol C_{60} , **2** with a concentration of 2 mg mL^{-1} in ODCB for 2 h, where electrode contact areas were masked by tapes. After the immersion, the surface-treated TiO_x films were washed with ODCB to remove any unabsorbed SAM and dried under N_2 flow. A faint yellow tint on the film and increased surface tension signified successful surface treatment (Figure 1). P3HT:PC₆₁BM solution in ODCB with a donor to acceptor ratio of 5:4 and a concentration of 2 mg mL^{-1} was spin-coated at an rpm of 750 for 45 s. Then it was kept in a Petridish for slow evaporation. A PEDOT:PSS dispersion in water (CleviosPVP, Heraeus Precious Metals GmbH & Co.) containing 0.5wt% polyoxyethylene(6)tridecyl ether (Sigma Aldrich Chemical Co., Inc.) was spin coated on top of the active layer to form the HTL with a 30 nm thickness. Approximately 200 nm thick Au layer was thermally evaporated at pressure of $3 \times 10^{-3} \text{ Pa}$, with the use of a shadow mask, which defined the device active area as 1 cm^2 . All processes, except for Au deposition, were performed in air and the devices were not encapsulated. All devices were thermally annealed at $150 \text{ }^\circ\text{C}$ for 10 min.

11.4 Results and Discussion

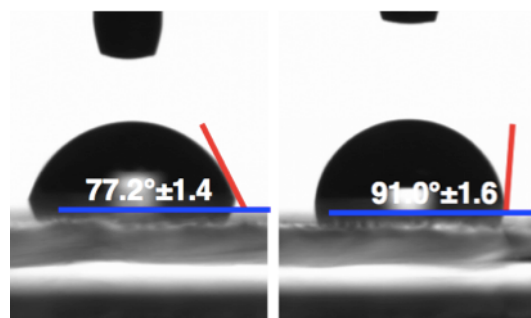


Figure 1. Water contact angle test on TiO_x before and after the catechol C_{60} treatment.

Table 1. Photovoltaic table of catechol C_{60} -applied and reference devices under 1 sun (AM1.5G illumination, 100 mW cm^{-2}).

Device	V_{oc} (V)	J_{sc} (mA cm^{-2})	FF	R_s (Ω)	R_{sh} (Ω)	PCE (%)
TiO_x	0.60	8.32	0.49	11	2.7×10^3	2.46
TiO_x -catechol C_{60}	0.60	8.40	0.56	6	1.6×10^5	2.81

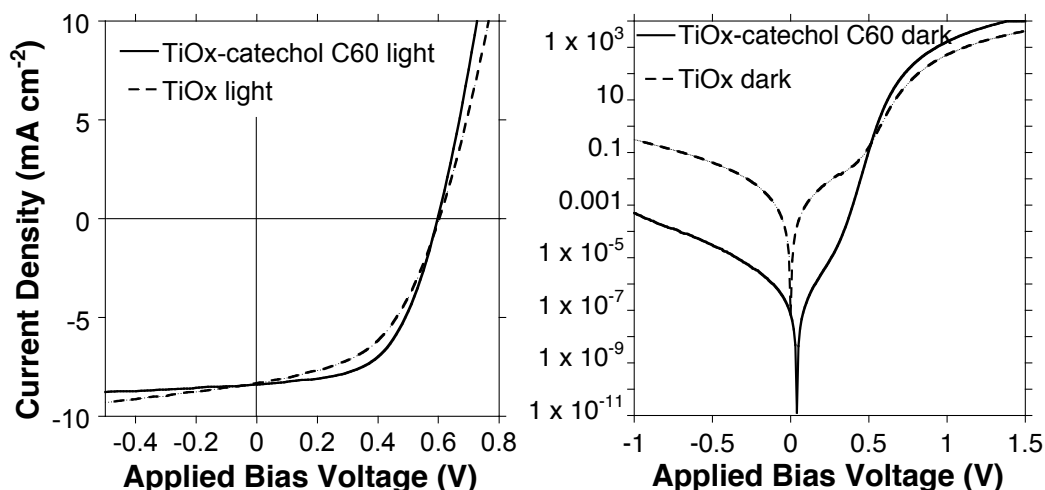


Figure 2. J - V curves of the TiO_x film-catechol C_{60} -based and TiO_x -based devices under 1 sun (left) and in dark (right)

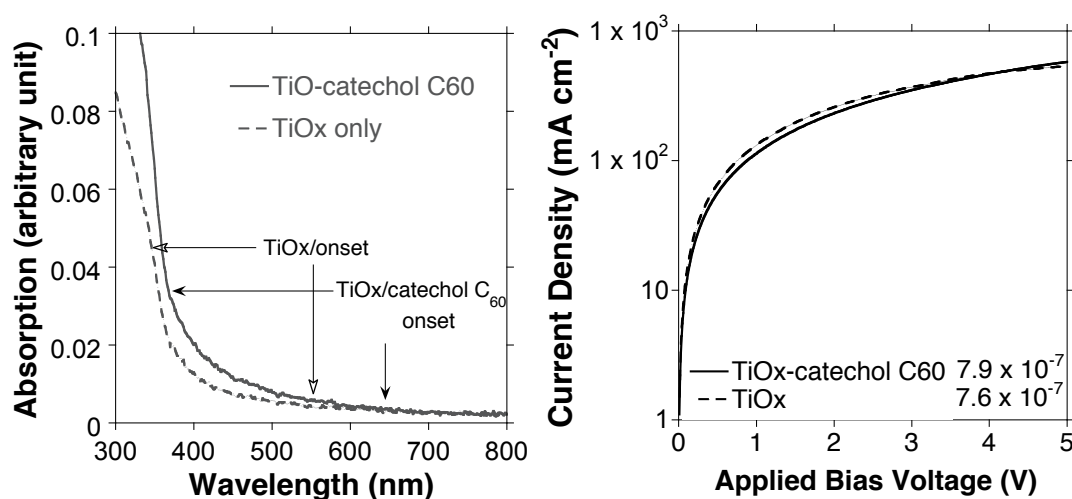


Figure 3. UV-vis absorption spectra (left) of a TiO_x film-catechol C_{60} and a TiO_x film both on glass; and J - V curves (right) of the electron-only devices for SCLC measurement and electron mobilities (μ) given in the inset with the unit ($\text{cm}^2 \text{V}^{-1} \text{S}^{-1}$).

J - V characteristics of the fabricated OSCs were measured using a software-controlled source meter (Keithley 2400) under dark conditions and 1 Sun AM 1.5 G simulated sunlight irradiation (100 mW cm^{-2}) using a solar simulator (EMS-35AAA, Ushio Spax Inc.), which was calibrated using a silicon diode (BS-520BK, Bunkokeiki). According to the photovoltaic parameters in Table 1, catechol C_{60} treatment greatly improved FF thereby increasing the PCE by 13% to 2.81%. Sharp increase in R_{SH} indicates that hole-blocking function of ETL was improved by fullerenes attached to the SAMs. This can be more clearly seen from the J - V curves in Figure 2. By looking at the J - V curves under 1 sun, that the catechol C_{60} -treated device shows more rectangular shape, indicative of higher FF. Also from the dark

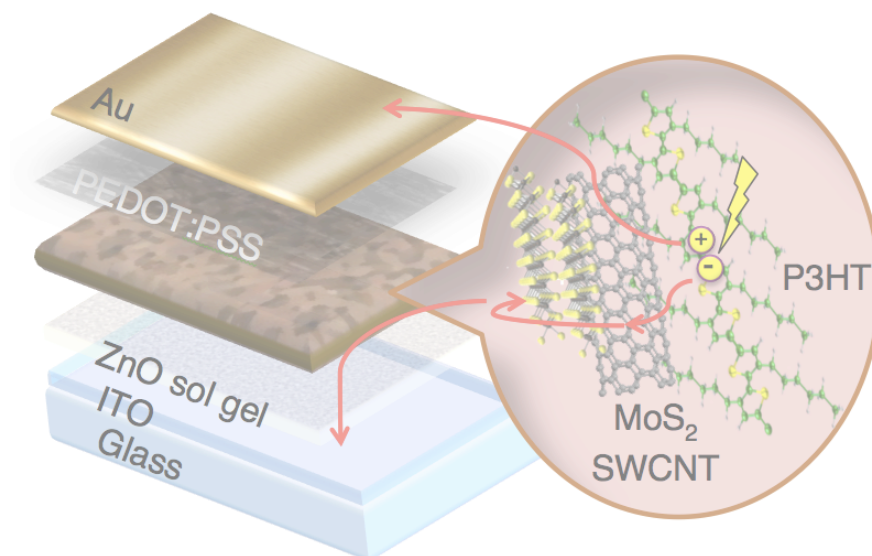
curves, it is clear that the catechol C_{60} -treated device shows higher R_{SH} while the R_S being the same as the reference device.

UV-vis absorption spectroscopy was measured on TiO_x and TiO_x -catechol C_{60} both on glass (Figure 3 left). TiO_x -catechol C_{60} showed an earlier onset at around 650 nm, revealing that catechol C_{60} treatment decreased the band gap of the TiO_x . This is an indication of either interfacial dipole or enhancement of n-doping.^[362–364] One way or another, benefiting the OSC performance.

I measured electron mobility (μ) across the films by applying single-carrier space charge limited current (SCLC) on the electron-only devices: ITO/ TiO_x /Al and ITO/ TiO_x -catechol C_{60} /Al. The results are shown in Figure 3. Catechol C_{60} treatment showed a marginally higher electron mobility. Although the difference was too small, we can at least conclude the surface treatment did not hinder the electron transfer.

11.5 Conclusion

In conclusion, surface modifier, catechol C_{60} was synthesized and applied to improve the efficiency of inverted solar cells. The fullerene-terminated surface modifier, 2 could attach to the TiO_x surface by a simple immersion process. The effect was immediate as demonstrated by the improvements in FF and PCE by 13% compared to the reference device. The methodology and analyses presented in this work are useful in designing of efficient metal oxide-based photovoltaic devices.



CHAPTER 12

CHEMICAL VAPOUR DEPOSITED MoS₂ ON CARBON NANOTUBE FLAKES AS THE CHARGE SELECTIVE LAYER AND THAT ENABLES INTERCALATION WITH P3HT IN BULK HETEROJUNCTION ORGANIC SOLAR CELLS

12.1 Summary

This chapter demonstrates the deposition of multilayered MoS₂ on a low-cost metallic-semiconducting carbon nanotube via chemical vapour deposition, and the use of this material as electron acceptor species forming a bulk heterojunction with P3HT in inverted-type organic photovoltaics. This is an uplifting discovery, in which MoS₂ has been used as an electron acceptor in spite of its innate immiscibility with organic compounds. This is possible because I utilised carbon nanotube's nature to intercalate with P3HT through π - π interaction. The successful binding of MoS₂ onto carbon nanotube bundles and its optoelectronic effect as a photovoltaic device is lucidly analysed through various techniques in this chapter. The effect was ultimately evidenced by a power conversion efficiency of 0.46%, which proved MoS₂ with many advantages could also be used as a photoactive layer.

12.2 Introduction

Research in organic–inorganic hybrid solar cells continues to rise in recent years.^[426] It is well known that organic acceptors have drawbacks in low stability and mobility, whereas inorganic materials have advantages in both stability and charge carrier mobility. Furthermore, by controlling its size, a wide range of band gap configuration can be achieved. Among the inorganic materials, layered n-type semiconductors have widely been studied for photovoltaic applications.^[427–431] Such crystalline semiconductors have wave functions as loosely bound valence electrons overlapping each other to form a global conduction band. Carriers can freely travel through the extended states.^[432] However, in organic materials, the charge carriers tend to be localised in potential wells consisting of single molecules or conjugated molecular segments. Carriers hop between these energy states through vibrations of host and adjacent molecules. These hoppings are less efficient than propagating through an extended conduction band, which causes organic materials to have a lower carrier mobility.^[402,433] As a layered n-type semiconductor, transition metal dichalcogenides have recently been drawing attention. With a formula MX_2 , where M is a transition metal element from group VI (Mo and W), strong in-plane bonding and weak out-of-plane interactions allow us to control its two-dimensional layer thickness.^[434] Amid a variety of constituent elements, I grew MoS_2 multilayered nanoflakes for its apt workfunction value of 4.8 eV which is very close to the Fermi level of CNTs and we know that since their Fermi levels are similar, there is no doping effect^[435,436] MoS_2 with its quality of being easily grafted onto CNTs using CVD makes it an outstanding candidate for this enables intercalation with other organic materials like P3HT.^[437–440] Moreover MoS_2 has no charge traps due to the absence of dangling bonds on its surface, and has easily tunable optical band gap by controlling the layer number. Also, MoS_2 multilayer has a higher mobility of 50–200 $\text{cm}^2 \text{V}^{-1} \text{s}^{-1}$ than its monolayer counterpart with a mobility of 1–8 $\text{cm}^2 \text{V}^{-1} \text{s}^{-1}$.^[440–449] Despite such advantages, multilayered MoS_2 has not been reported as photoactive materials in BHJ systems. There are mainly two reasons: one is that in the case of MoS_2 , there is no interaction between MoS_2 and P3HT. With such immiscibility, BHJ is not possible. In a BHJ, electron donor and acceptor should be thoroughly mixed for efficient exciton separations to occur. The device performance is heavily dependent

on the degree of dispersion and the interfacial area. Second reason is that the multilayered MoS₂ is more difficult to produce than the single-layered compound due to difficulties in thickness control.^[437,440] Therefore, I showed in this chapter, a novel methodology of introducing MoS₂ multilayer into an OSC BHJ system through an atmospheric CVD using MoO₃ and S as sources, and unsorted SWCNTs on a metal chip as a substrate.^[438,439] The unpurified semiconducting-and-metallic mixed SWCNTs are inexpensive materials that can assist the intercalation of MoS₂ with P3HT. P3HT can provide isolation between the CNTs, thus minimising the direct electronic coupling between the optically active semiconducting nanotubes and the metallic nanotubes present in the mixture (at approximately 30 wt%) that may quench the photo-generated excitons.^[450] Using the MoS₂CNT, I fabricated an inverted type OSC rather than a normal structure for its high stability, air-processability, and its facile process.^[194] I obtained a PCE of 0.46%, while a costly and highly pure semiconducting SWCNT and P3HT based OSC has given PCE of 0.72%.^[451] This is an encouraging result for I have achieved a PCE as good as the expensive semiconducting SWCNT based device using the unpurified SWCNTs.

12.3 Experimental Procedures

12.3.1 Deposition of Multilayered MoS₂ Nanoflakes on CNT Bundle

Multilayered MoS₂ nanoflakes were deposited on CNT (Hipco) bundles by a CVD (Figure 1). S powder (99.5%, Kanto Chemical) was placed in a quartz tube, MoO₃ powder (99.5%, Kanto Chemicals) was placed on an alumina boat in Zone 1 and Zone 2. One spatula spoonful of CNTs (0.3 mg) on a SiO₂/Si substrate (SiO₂: 1 × 1 cm², 285 nm thick) was placed on a boat in Zone 3. The vapours of S and MoO₃ were introduced through N₂ flows (99.99%) labeled as Flow 1 and Flow 2. Firstly, Flow 1 was introduced at the rate of 850 sccm and the temperature of Zone 2 and Zone 3 were increased to 650 °C (r.t. to 450 °C in 3 h and 30 min, and then 450 °C to 650 °C in 30 min) and 850 °C (r.t. to 700 °C in 3 h and 30 min, and then 700 °C to 850 °C in 30 min) each. Then, 3 h 20 min after the Flow 1 was introduced, the temperature of Zone 1 was increased to 250 °C in 10 min. After the temperatures of Zone 2 and Zone 3 reached 650 °C and 850 °C, N₂ Flow 2 was introduced at the rate

of 360 sccm. 4 h later, Flow 2 was immediately turned off and the temperature of all zone were cooled to r.t. with Flow 1 maintained at the rate of 50 sccm. Product formed on a SiO₂ substrate was put into a vial containing ethanol, which separated my product from the substrate. The substrate and ethanol were later removed.

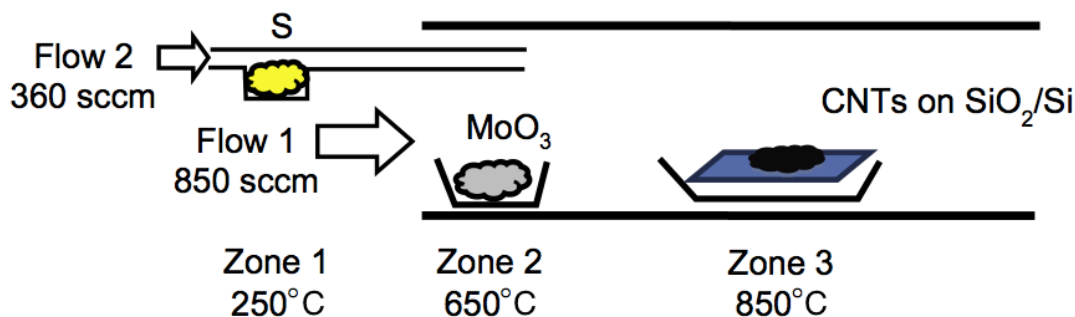


Figure 1. Illustration of the CVD for the multilayered MoS₂ nanoflakes.

12.3.2 P3HT and MoS₂CNT Active Layer Preparation

P3HT:MoS₂CNT devices were fabricated in the following manner. P3HT 20mg mL⁻¹ in ODCB, and MoS₂CNTs flakes dissolved in ODCB in concentration of 5 mg mL⁻¹ were prepared. In case aggregation of CNT was visible, I sonicated MoS₂CNT for less than 10 min before mixing P3HT. The composition of the active layer was produced by mixing together the two solutions in different proportion under stirring to achieve a solution of P3HT/MoS₂CNT with MoS₂CNT having a concentration of 3 wt%. The resulting solution, containing P3HT/MoS₂CNT nanofilaments, showed aggregation after 1 h. Therefore, I advise using the solution directly in fabrication.

12.3.3 Device Fabrications

For device fabrications, please refer to ‘2.1.1.2 Organic solar cell inverted device architecture’, and ‘2.1.1.3 P3HT:mix-PCBM solution preparation’.

12.3.4 Characterisations

For characterisations, please refer to ‘2.2.1.1 Current-voltage characterisation’, ‘2.2.2.1 UV-vis absorption’, ‘2.2.2.2 Photoluminescence’, ‘2.2.2.5 Transmission electron microscopy (TEM)’, ‘2.2.2.9 Raman spectroscopy’, and ‘2.2.2.10 Auger electron microscope (AES)’.

12.4 Results and Discussion

Firstly, for the multilayer generation and the control of layer number, I used two separate furnaces which introduce S and MoO₃ at different rates and temperatures (Figure 1).^[437,439,440,449] Barring having a higher mobility, multi-layered MoS₂ is known to have an indirect band gap of 1.2 eV, which I think is more favourable than its monolayer counterpart in terms of its energy band alignment.^[452] With decrease in crystal thickness, the band gap widens and reaches 1.8 eV for the monolayer which has a direct energy gap.^[453] Through this method, I have deposited multi-layered MoS₂ on the bundles of CNT. Successful deposition is shown by TEM (Figure 2). For CNT, the difference is clear and we can observe MoS₂ flakes from the after-deposition image (Figure 2a and 2b).

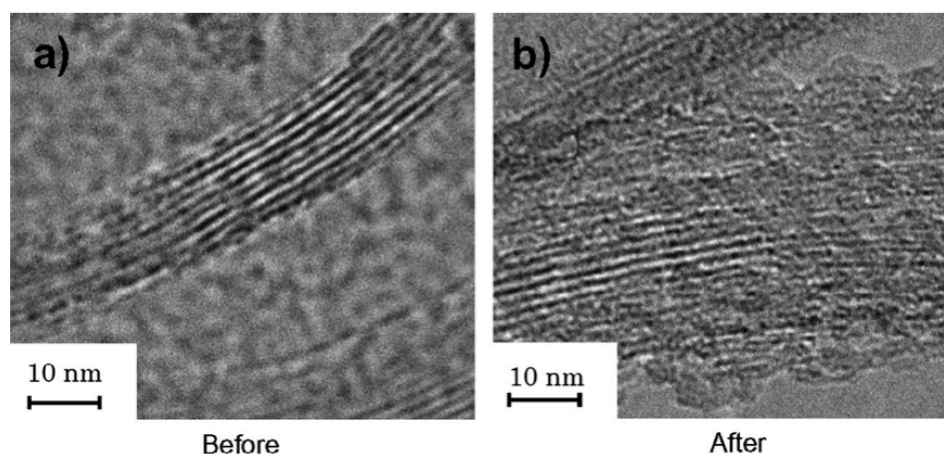


Figure 2. Deposition of MoS₂ on CNT before (a) and after (b).

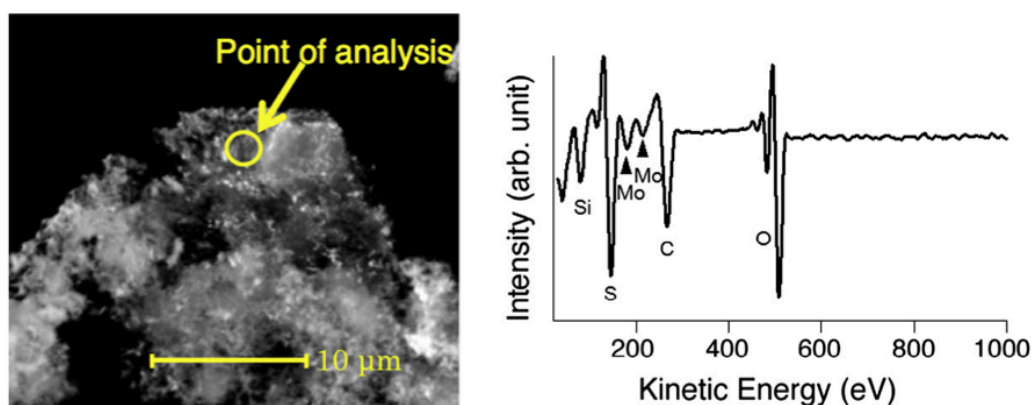


Figure 3. AES of a MoS₂ flake on a CNT bundle.

In order to identify the deposition of MoS₂ on CNT, the surface of MoS₂ flakes on CNT bundles was analysed by AES (Figure 3). Element compositions from the AES spectrum confirm the existence of MoS₂.

To consolidate the formation of multilayer, Raman spectroscopy was carried out to analyse the thickness. Figure 4 shows raman peaks of MoS₂ on CNT between 100 cm⁻¹ and 600 cm⁻¹ of raman shift. CNT's radial breathing mode (RBM) appeared at around 190 cm⁻¹ indicating the CNT bundles. The MoS₂ sheet deposited exhibits two Raman characteristic bands at 385.8 cm⁻¹ and 403.8 cm⁻¹ with the full-width-half-maximum values of 7.787 cm⁻¹ and 8.370 cm⁻¹, corresponding to the out-of-plane A_{1g} and in-plane E_{2g}¹ modes each. Note that the peak A_{1g} and E_{2g}¹ frequency difference between A_{1g} and E_{2g}¹ modes (D) can be used to identify the layer number of MoS₂. The value of D, 0.583 cm⁻¹ reveals that the multilayer of MoS₂ has been successfully deposited.^[454]

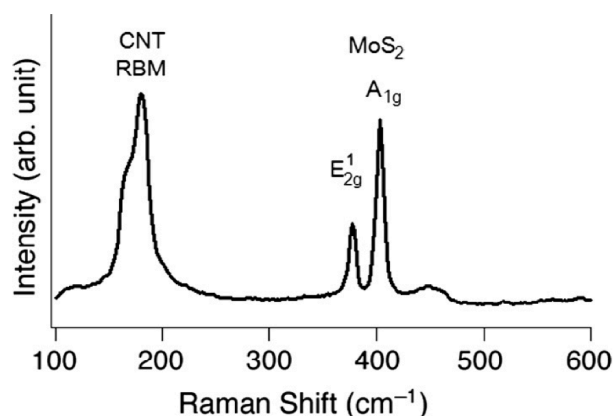


Figure 4. Raman spectrum of multilayered MoS₂ on CNT bundles.

Next, I fabricated an OSC device using MoS₂ on CNT as electron acceptor and charge transporting material, respectively. 3 wt% of MoS₂CNT flakes in ODCB is thoroughly mixed in a P3HT solution before spin coating it on a ZnO film at 850 rpm for 45 s. Interaction between P3HT and MoS₂CNT has been evidenced by the UV-vis spectroscopy (Figure 5). Figure 5a shows a typical P3HT spectrum. Figure 5b shows a spectrum where enhancements in shoulders at 450 nm⁻¹, 580 nm⁻¹, and 650 nm⁻¹ confirm the existence of MoS₂.^[455] In addition, the strong absorption peak at 610 nm and broadening of the spectrum indicates a high degree of structural order in the active layer in support of π - π interactions between CNT and P3HT^[456] (Figure 6).

Nonetheless, I am still not sure of the reason why we cannot observe SWCNT peaks around 1000 nm^{-1} . I suspect two reasons here: one is that the intensity of SWCNT peaks is intrinsically much weaker than MoS_2 absorption and the amount of SWCNT I used in here is too little for the detection. Second reason is that the SWCNT purchased from Hipco typically does not show absorption peaks around 1000 nm , which could be due to the broad range of SWCNT diameters and impure nature of the product.^[457,458]

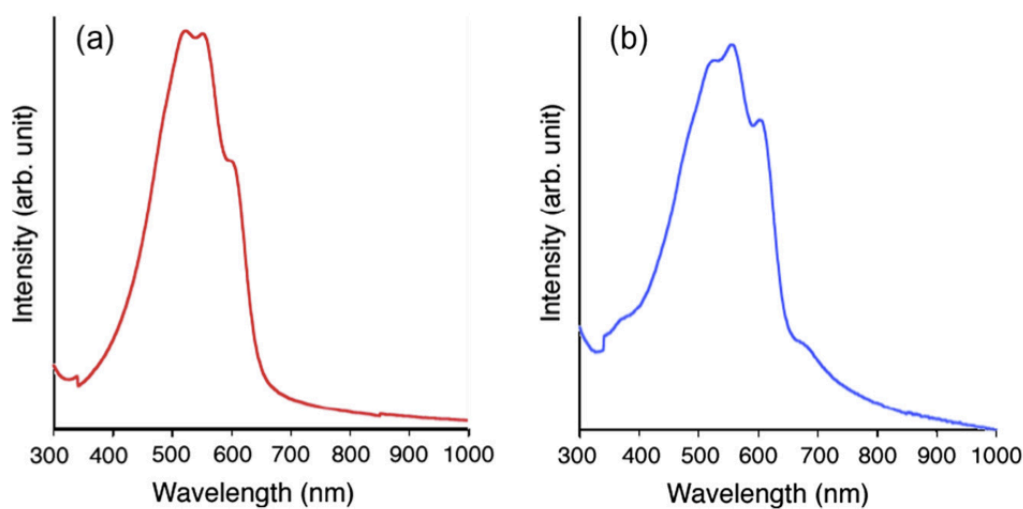


Figure 5. UV-Vis spectra of (a) P3HT film and (b) P3HT mixed with MoS_2CNT (3 wt%).

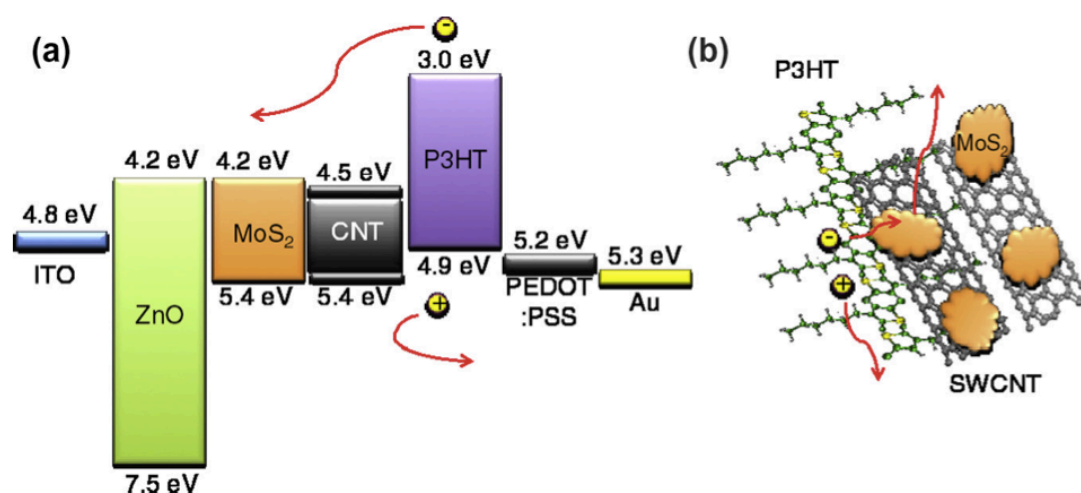


Figure 6. (a) Energy band alignment of a P3HT: MoS_2CNT solar cell where CNT is semiconducting-and-metallic mixed (Metallic CNT exhibits workfunction of 4.5–5.0 eV). (b) graphical illustration of P3HT: MoS_2CNT photoactive layer.

To assess the impact of the MoS_2 as an electron acceptor, I performed photoluminescence measurement on both $\text{MoS}_2\text{CNT}/\text{P3HT}$ solution and film. The excitation wavelength is 400 nm as derived from the UV-vis spectrum. For the

solution samples, we cannot observe anything. It could be the ODCB solvent used hindering the measurement and interaction between the two species or the concentration of the solution was not adequate. However, for the film samples where MoS₂CNT and P3HT have been mixed in different ratios show photoluminescence quenching specifically, from the sample, where 2.8 wt% of MoS₂CNT to P3HT, has been used. The quenching is further enhanced with the increase in MoS₂-CNT composition to 3 wt%. Using higher concentration of MoS₂CNT does not quench the PL spectrum completely but rather reverts back to non-quenched spectrum. This suggests that the presence of MoS₂CNT induces the dissociation of excitons generated in the polymer and 3 wt% is the most optimised concentration (Figure 7).

Finally, I show the device performance. The PCE, μ of MoS₂CNT and P3HT mixture device is measured to be 0.46%, while both the reference samples of pristine SWCNT without MoS₂ deposition and P3HT alone devices give $\mu = 0\%$ and $\mu = 0\%$ each (Figure 8, Table 1). Significant increase in V_{OC} , J_{SC} , and R_{SH} shows that MoS₂CNT functions as an electron acceptor. However, rise in R_S and limited FF suggest that many undermining factors like a random orientation of MoS₂CNT, small coverage of MoS₂ nanoflakes on CNT, purity of the SWCNT, and thickness of the SWCNT may have hampered the device potential. I also attribute to MoS₂CNT coverage and CNT's surface to volume ratio for the limited performance.

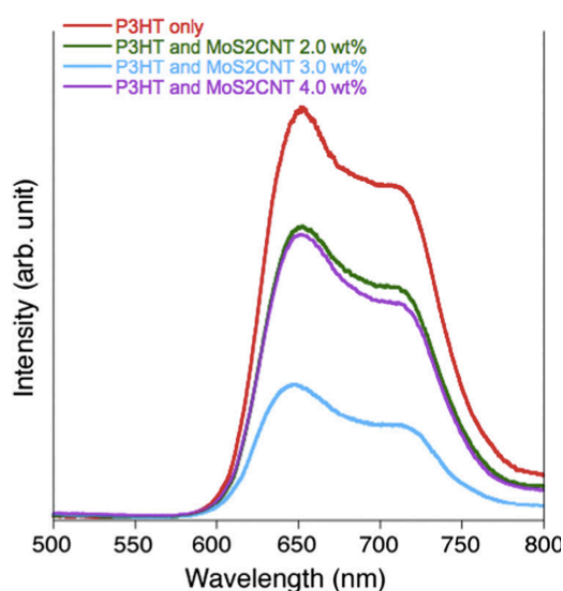


Figure 7. Photoluminescence data of the active layer with increase in MoS₂CNT concentration.

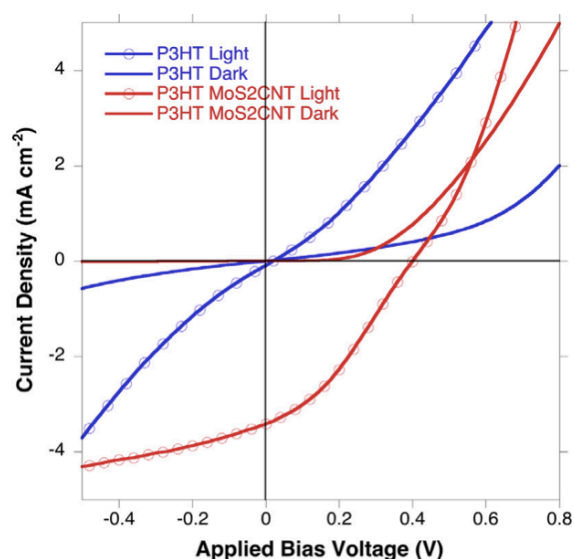


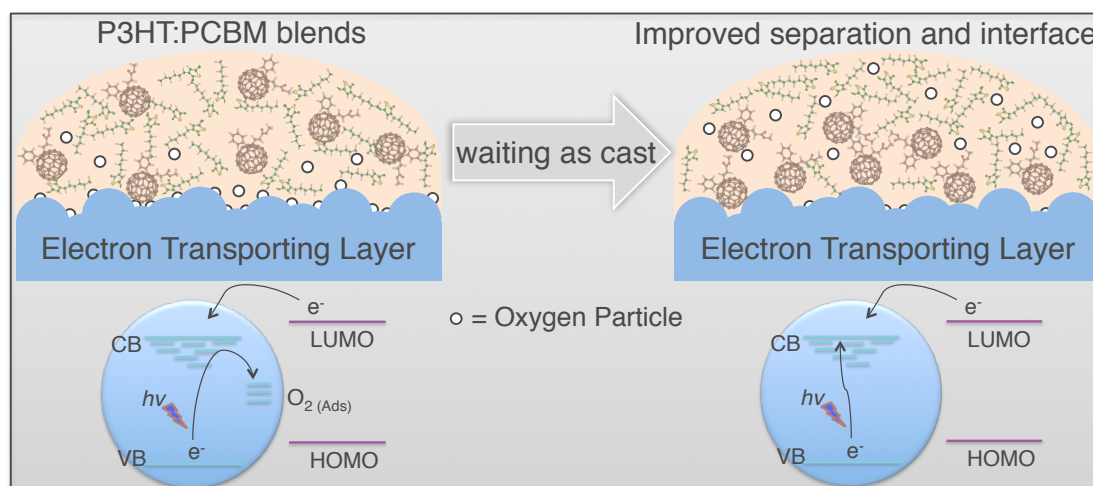
Figure 8. J - V curves of the P3HT only solar cell and P3HT:MoS₂CNT solar cell.

Table 1. Photovoltaic parameters of P3HT device, P3HT:CNT device, and P3HT:MoS₂CNT device.

Active layer	V_{OC} (V)	J_{SC} (mA cm ⁻²)	FF	η (%)	R_s (Ω cm ²)	R_{SH} (Ω cm ²)
P3HT (ref.)	0.19	0.09	0.29	0.01	15.5	15.3
P3HT/CNT	0.12	0.04	0.25	0.00	187	1540
P3HT/MoS ₂ CNT	0.40	3.42	0.33	0.46	43.6	3770

12.5 Conclusion

I have demonstrated an OSC where MoS₂ forms a BHJ and function as electron acceptor species by depositing multilayer on unpurified SWCNT bundles. Despite many advantages of multi-layered MoS₂, application in OSC had been limited due to its immiscibility with P3HT. My inverted OSC employing the MoS₂CNT:P3HT leads to the efficiency of 0.46%, which is respectable considering the fact that the expensive purely semiconducting SWCNT:P3HT inverted OSC has given 0.72%. I hope this finding can provide guidance to other researchers working on the next-generation MoS₂-based photovoltaic device.



CHAPTER 13

VERTICAL PHASE SEPARATION AND INTERFACE CONTROL USING PHOTOACTIVE LAYER SPINCOATING INITIATION TIME IN ORGANIC SOLAR CELLS

13.1 Summary

Here in this work, I report a new methodology of controlling spin coating initiation time that improves the contact at the interfaces of ETL by removing oxygen and impurities, and inducing a more favourable vertical phase separation of the photoactive layer, at the same time. In effect, this facile method reduces light-soaking time, and increases J_{sc} and FF. Accordingly, a PCE of 3.54%, which is 12% higher than the reference with 3.15%, is achieved and this result is comparable to that of anaerobically fabricated normal type OSCs. Reduced UV activation time of 3 min is achieved, which is 17 min shorter than 20 min from the reference. The mechanism behind these improvements has been studied through diverse analytical techniques and discussed in this work. This phenomenon is displayed in other ETL, ZnO, and other organic material, methano indene fullerene (MIF) as long as low volatile solvents such as ODCB are used.

13.2 Introduction

Inverted type OSCs have been regarded more promising over normal type, owing to a favourable vertical phase separation and air-processability. Many techniques, such as thermal or solvent annealing, slow growth method, melting bilayers etc. have been employed to improve the morphology of photoactive layer, which is one of the advantages of inverted type OSCs. As a result, the device performance is greatly enhanced which is also reflected in the J - V curve. However, some of the methods presented above are difficult and costly to perform. In addition, inverted OSCs still employ certain metal oxide ETL, which impose UV activation time due to light-soaking effect. Here I show a facile method that can control the vertical phase separation as well as minimise the light-soaking effect. By leaving the photoactive solution with a low volatile solvent in air before spin coating, conductive polymers (donor) and fullerene derivatives (acceptor) were separated vertically in a way that their charge extraction is enhanced. Besides, oxygen and impurities at the contact on ETL were removed by leaving the solution for a certain period. Mechanisms of these improvements were evidenced by various analytical techniques and empirical tests using different materials in different environments. I anticipate this finding can expedite the OSC research and its usage in all air-processed inverted OSCs.

13.3 Experimental Procedures

13.3.1 Device Fabrications

For device fabrications, please refer to ‘2.1.1.2 Organic solar cell inverted device architecture’, and ‘2.1.1.3 P3HT:mix-PCBM solution preparation’. The metal oxides were baked at 150 °C before depositing the photoactive layer to dry and improve conductivity. This minimised the light-soaking time of the OSC.^[75]

For P3HT:MIF photoactive layer deposition, P3HT (regioregular, Sigma Aldrich Chemical Co., Inc.) and MIF (Synthesised) solution with a donor:acceptor ratio of 1:1 and concentration of 50 mg mL⁻¹ in ODCB (anhydrous, 99%, Sigma

Aldrich Chemical Co., Inc.) was prepared.^[459] The solution was left stirring for 2 h at 65 °C.

13.3.2 Characterisations

For characterisations, please refer to ‘2.2.1.1 Current-voltage characterisation’, ‘2.2.1.2 Incident photon to current efficiency (IPCE)’, ‘2.2.2.1 UV-vis absorption’, ‘2.2.2.3 Atomic force microscopy (AFM)’, ‘2.2.2.6 X-ray photoelectron spectroscopy (XPS)’, ‘2.2.2.11 Water contact angle test’, and ‘2.2.2.12 Profilometer’.

13.4 Results and Discussion

I fabricated inverted OSCs using the P3HT:PCBM with different waiting times before spin coating. Reference device with immediate spin coating, 5 min waiting time, 10 min waiting time, and 20 min waiting time were employed. Table 1 shows photovoltaic performance of the devices. PCE is the highest when 10 min waiting time is applied due to the enhancement of J_{SC} and FF – it should be noted that the most optimal waiting time varied in every experiment but the best time was between 5 min and 10 min in all experiments. While J_{SC} increases continuously with the waiting time, FF increases and decreases back after 5 min waiting time. Increase in J_{SC} means that the longer I leave the solution, the better the dissociation of excitons. Improved vertical phase separation is surmised to be the reason. Notwithstanding high J_{SC} , series resistance (R_S) increases after 10 min of the waiting time to decrease FF, which undercuts the PCE. The solution left in air for a long time being oxidised is suspected to be the reason.

Table 1 also shows that the light-soaking time reduces as the waiting time increases. Ultimately, it decreases down to less than 1 min when the waiting time is 20 min. The corresponding J–V curves under 1 sun during the light-soaking time show the S-curves appearing in the beginning and disappearing gradually (Figure 1a–e). The dynamic inflection phenomenon can be explained by distribution of oxygen within the device. The initial oxygen concentration is determined by the oxygen solubility of each layer.^[67] Waited solution leads to less defect states at the interface of

the ETL and changes the electric field distribution of the device. As it is reported that electron trap sites caused by oxygen at the interface of the ETL are the major contribution to the S-curve, shorter light-soaking time indicates that during the waiting time the electrons are desorbed from the ETL interface.^[460] Other possibility is the decomposition of organic impurities on ETL by waited solution improving the morphology of the P3HT:PCBM heterojunction.^[461,462] Proposed mechanisms are illustrated in Figure 2.

Table 1. Air-processed inverted OSC device performance of a selected data set, their light-soaking time with different pre-spin coating initiation waiting times and related statistical

Type	Pre-spin waiting time	V_{oc} (V)	J_{sc} (mA cm ⁻²)	FF	R_s (Ω cm ²)	R_{sh} (Ω cm ²)	η (%)	Light-soaking time (s)
Inverted	0 min (ref.)	0.61	9.19	0.57	10.8	1.88E+4	3.15	1250
		0.60±0.01	9.13±0.16	0.52±0.04			2.87±0.24	
Inverted	2 min	0.62	9.15	0.57	10.7	2.98E+5	3.23	650
		0.61±0.01	9.17±0.16	0.56±0.04			3.09±0.09	
Inverted	5 min	0.62	9.46	0.61	6.3	1.28E+5	3.54	475
		0.62±0	9.26±0.42	0.59±0.02			3.38±0.22	
Inverted	10 min	0.61	9.09	0.59	12.3	3.79E+5	3.33	175
		0.62±0.01	9.78±0.24	0.59±0.02			3.22±0.19	
Inverted	20 min	0.61	9.86	0.46	17.6	2.36E+4	2.78	50
		0.61±0.01	9.34±0.45	0.50±0.04			2.86±0.16	
Normal	0 min (ref.)	0.64	0.64	0.64	-	-	3.59	30
		0.63±0.01	0.63±0.01	0.62±0.03			3.14±0.21	

analysis of five data sets under AM1.5G illumination (100 mW cm⁻²).

The optical property of devices fabricated using different waiting times was studied. In Figure 3, the picture above shows that there are apparent colour differences according to the waiting time. The colour deepened as the waiting time increases. I suspected thickness difference caused by leaving solution in air which might evaporate solvent, increasing concentration of the solutions. However, my measurements using a profilometer showed that the thicknesses of the photoactive layers of all devices were around 350 nm and no particular trend was observed. Next, I measured their optical spectra using a UV-vis absorption spectrometer. Figure 3 shows that there is neither significant difference nor a trend in the absorption. It is still not fully understood why they happen to exhibit such different colours.

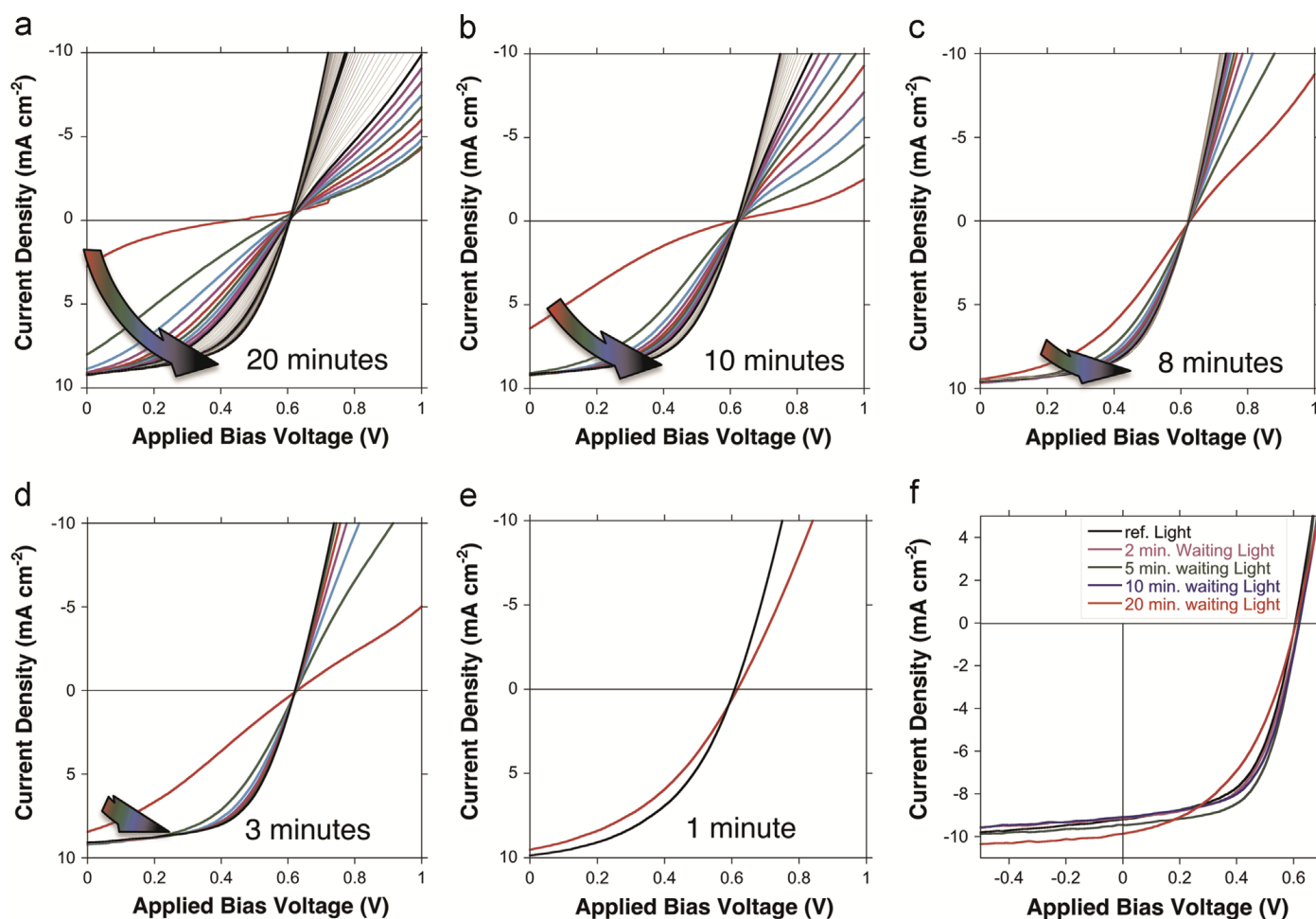


Figure 1. J - V curves of devices with different waiting times upon light activation with AM1.5G illumination (100 mW cm^{-2}) demonstrating the light-soaking time difference. The time delay between curves is approximately 30 s (a) reference device, (b) waiting time 2 min, (c) waiting time 5 min, (d) waiting time 10 min, (e) waiting time 20 min, and (f) overall devices.

The vertical phase separation in the polymer blend is related to difference in surface energy. Since P3HT has a lower surface energy than PCBM, it tends to accumulate at the surface in order to reduce the overall energy.^[463] A water contact angle test was conducted on photoactive layers with different waiting times to verify the vertical phase separation.^[464] Figure 4 shows the contact angle of water drops on ITO/TiO₂/P3HT:PCBM samples after thermal annealing. The measured contact angles can be used to estimate the surface energy using the extended Girifalco–Good–Fowkes–Young (GGFY) equation.^[465,466] However, it is unnecessary to derive the exact surface energy values, rather a simple comparison of the contact angles suffices my analysis. Figure 4 shows that the contact angle increases with the waiting time.

The reference device shows an average of 98.3° . It is slightly lower than the commonly reported values.^[464] With 5 min waiting time, the contact angle increases by around 3° and with 10 min waiting time, it increases by 7° to 105.3° . There is no significant difference between 10min waiting time and 20min waiting time. This indicates that either the vertical phase separation has been saturated at some point after 10 min waiting time or the organic molecules have been oxidised. This trend indicates that there are more P3HT with lower surface energy on the surface of the active layer as the waiting time increases.^[62] Consequently, the amount of non-continuous pathways of P3HT is reduced which decreases the carrier accumulation and the carrier recombination in the photoactive layer.^[467,468]

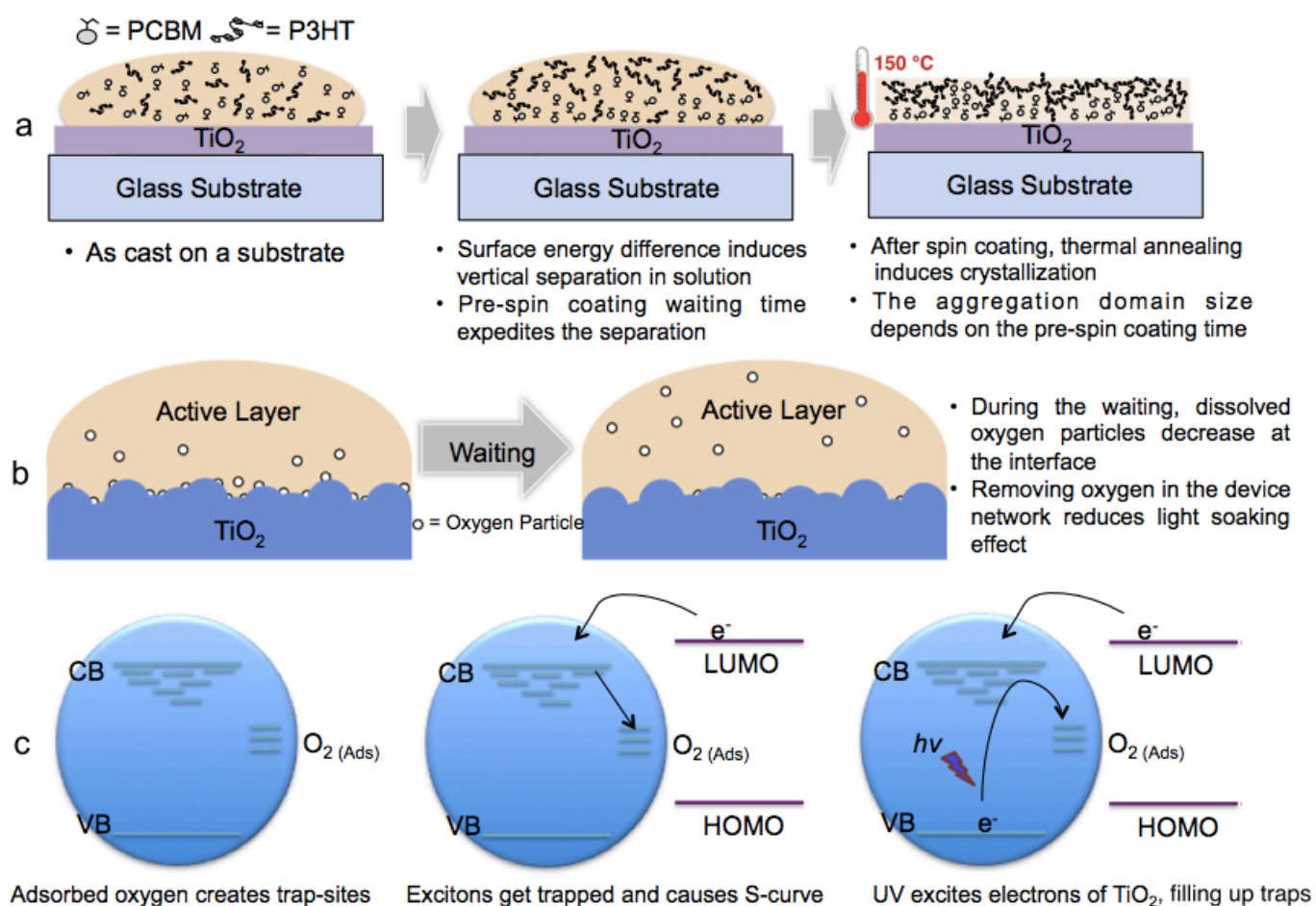


Figure 2. Graphical illustration of the two effects taking place in an inverted OSC during the waiting time. (a) vertical phase separation, (b) oxygen distribution within the photoactive layer and ELT interface, and (c) more detailed illustration of an interaction between TiO₂ surface and adsorbed oxygen that leads to the light-soaking effect.

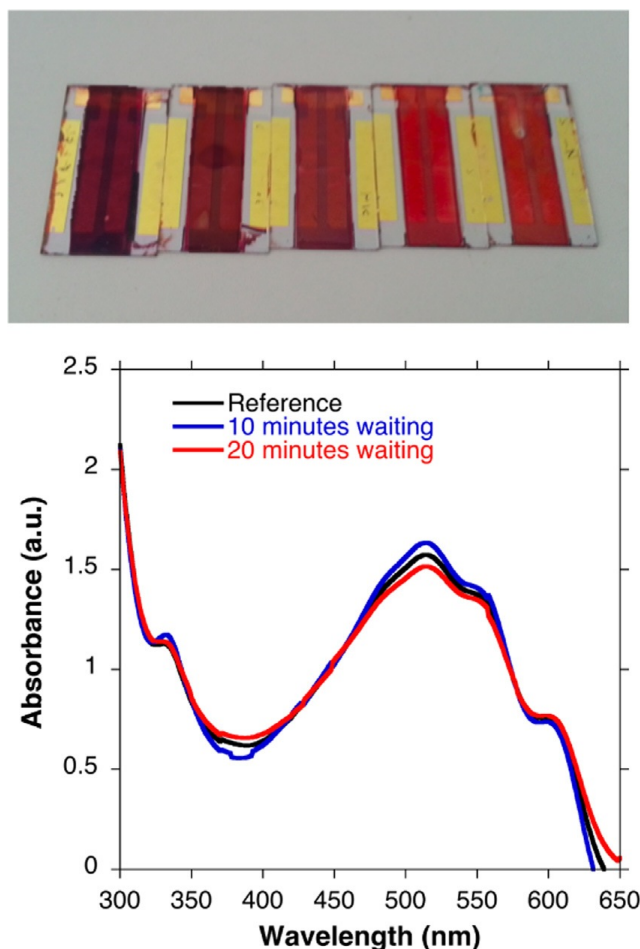


Figure 3. A picture showing the colour differences in photoactive layers of the devices with different waiting times (above) and UV-vis absorption spectra of thermally annealed ITO/TiO₂/P3HT:PCBM where the ITO/TiO₂ absorption has been subtracted (below).

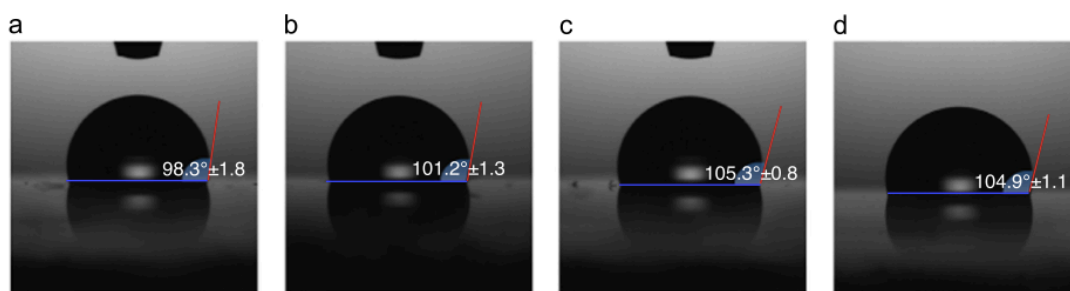


Figure 4. Water contact angle tests on ITO/TiO₂/P3HT:PCBM samples with (a) no waiting time, (b) 5 min waiting time, (c) 10 min waiting time, and (d) 20 min waiting time.

XPS has been used to study the composition of the photoactive layer surface. The weight or molar ratio of the components can be calculated directly from the peak intensities of individual elements in XPS.^[196,469,470] Using C/S atomic ratios obtained from the XPS spectra, I tried to obtain information on the surfaces of P3HT:PCBM films with different waiting times.

The peaks around 164 eV binding energy are assigned to the thiophene S atoms in P3HT and the peaks around 285 eV binding energy are assigned to the alkyl C atoms in PCBM. According to my data in Figure 5, with increase in the waiting time, both components decrease in intensity. If we look at the C/S atomic ratio, it does not change significantly. Therefore, the evidence is not strong enough to deduce any conclusion from this. With the short mean free path of photoelectrons, the probing depth is only 6–8 nm. Especially in this case, with 30° take-off angle, the probing depth was around 2 nm. The inaccuracy of the XPS measurement might have occurred from such shallow depth analysis, as the size of one PCBM is greater than 1 nm. In addition, the difference in vertical phase separation produced by my method may not be as great as the difference observed in the slow-and-fast growth study reported before.^[196]

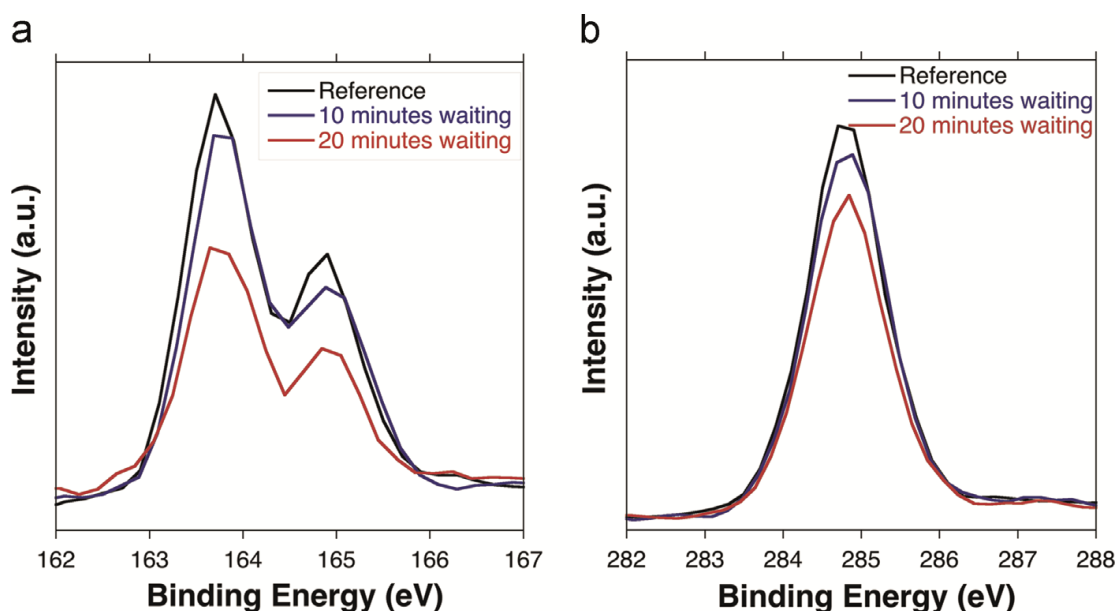


Figure 5. (a) The XPS peaks assigned to the thiophene S atoms in P3HT and (b) the XPS peaks assigned to the alkyl C atoms in PCBM both according to the waiting time.

AFM was employed to observe any morphological change owing to the vertical phase separation. When the P3HT:PCBM blends on TiO₂ films are observed, it is difficult to distinguish clearly from the images and the r.m.s. roughness values (Figure 6a–c). However, after selectively dissolving away the fullerene phase by OT, the difference between the samples with different waiting times are clearer (Figure 6d–f). The r.m.s. roughness increases from 2.9 of reference to 3.1 for 10 min waiting

time and to 3.7 for 20 min waiting time. The difference is even more clearly demonstrated in 3D images where a large proportion of PCBM is rinsed away in the reference sample unlike the rest. (Figure 6g–i).

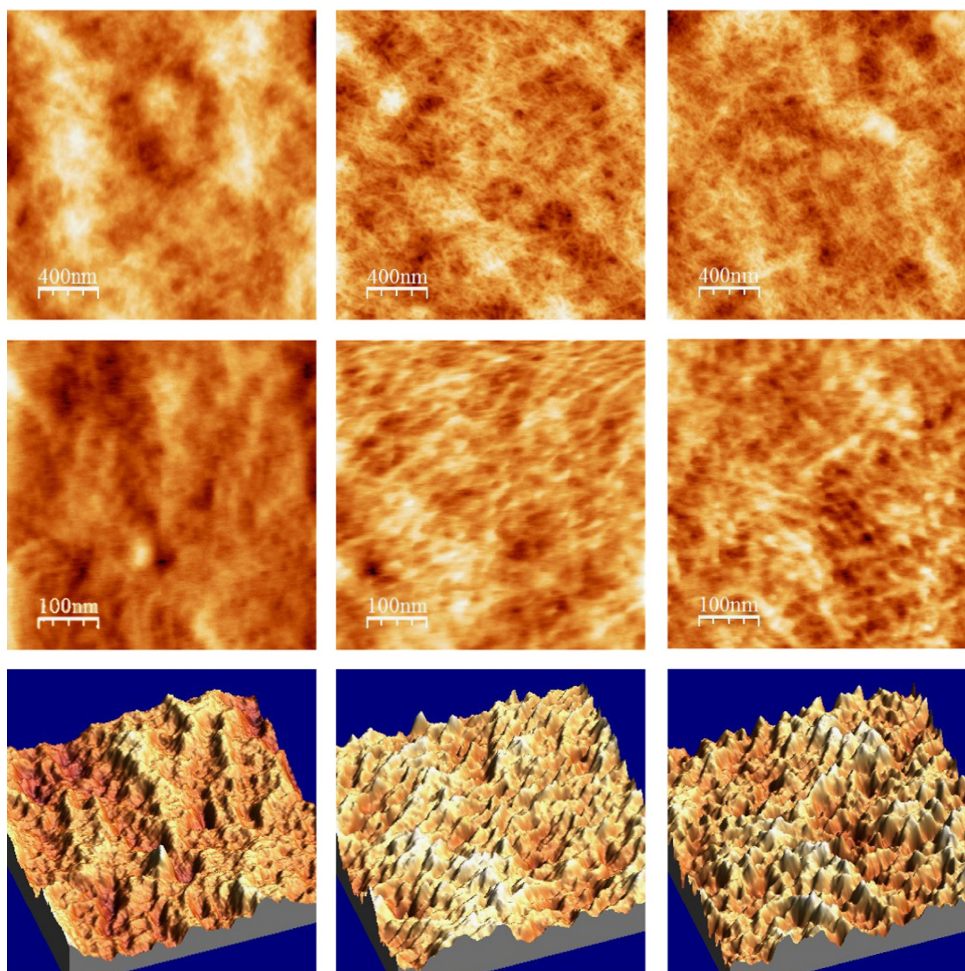


Figure 6. AFM images of P3HT:PCBM on ITO/TiO₂ substrates with (a) no waiting time, (b) 10 min waiting time, and (c) 20 min waiting time. Also AFM 2D and 3D images after PCBM of the photoactive layers have been washed with OT for (d) and (g) for no waiting time, (e) and (h) for 10 min waiting time, and (f) and (i) for 20 min waiting time.

The maximum exciton generation rate and the exciton dissociation probability in the P3HT:PCBM absorption layers of the samples with different waiting times were estimated from the J – V characteristics. Figure 7 shows the external photocurrent density (J_{ph}) as a function of the effective applied voltage ($V_{\text{eff}} = V_0 - V$) where J_{ph} is difference of the current density under illumination and dark conditions, and V_0 is the voltage at which $J_{\text{ph}} = 0 \text{ mA cm}^{-2}$. The external photocurrent density could be expressed as below:^[471,472]

$$J_{\text{ph}} = qG_{\text{max}} PL$$

where q is the electronic charge, G_{\max} is the maximum exciton generation rate, P is the exciton dissociation probability, and L is the thickness of the absorption layer. When the effective applied voltage is larger than 3 V ($V_{\text{eff}} > 3$ V), the full saturation photocurrent density (J_{sat}) was obtained. It indicates that all excitons are dissociated in the absorption layer. This indicates that the exciton dissociation probability is near to 1 and the Eq. (1) can be rewritten as $J_{\text{sat}} = qG_{\max}L$. The estimated G_{\max} of the samples leads us to the values of P to be 93.7%, 92.9%, 94.1%, and 96.6% for the reference, 2 min waiting time, 10 min waiting time, and 20 min waiting time, respectively, at a short-circuit condition. The increase in P of the samples is attributed to the extra PCBM and the non-continuous P3HT at the interface of the ETL, which improves the charge transfer rate and reduces carrier recombination in the absorption layer.

Figure 8 shows the incident photon to current efficiency (IPCE) as a function of the wavelength, which further evidences my findings. As shown in Figure 4, the IPCEs of the waited samples are larger than the reference. This means that there are more exciton generations followed by better charge collections. Moreover, the 20 min sample shows relatively higher increase in the 500 nm region which is responsible for the P3HT charge extraction. This, I suspect, is due to the fact that the non-continuous P3HT pathway has been reduced.

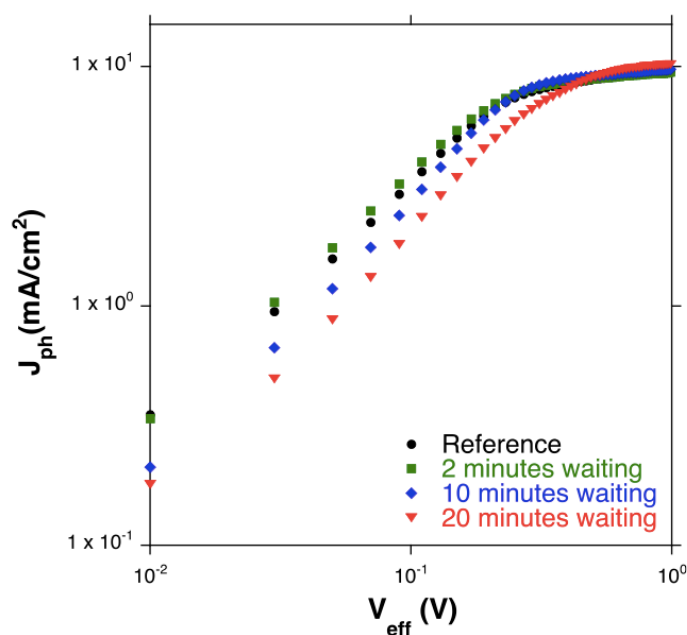


Figure 7. The external photocurrent density as a function of the effective applied voltage for the reference sample, 2 min waiting time, 10 min waiting time, and 20 min waiting time.

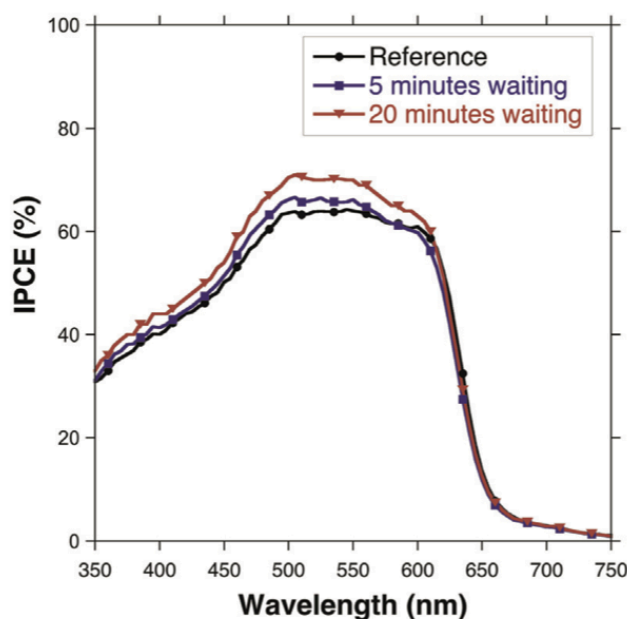


Figure 8. IPCE as a function of wavelength for the reference and the samples with different waiting times.

To ascertain the contribution of charge recombination in the loss mechanism for the photocurrent, the light intensity dependence of the normalised J_{SC} under illumination is plotted in Figure 9a. The experimental data are fitted with a formula:

$$J_{SC} = k \times LI^{\alpha}$$

J_{SC} vs. function of light intensity tells us about the space-charge build up. It has been predicted that $\alpha = 1$ when the photocurrent is determined by the generation rate of electron–hole pairs upon photon absorption, while it can be below 1, when a low mobility donor is used, active layer has a poor morphology, or the photocurrent is limited by the formation of space-charge regions due to unbalanced charge transport for electrons and holes as it prevents the efficient extraction of one carrier.^[473] α should be 1 in general bilayer device and bulk heterojunction. In this experiment, $\alpha = 1.05$ for the reference device, the 2 min waiting sample, and the 5 min waiting sample; and $\alpha = 1.04$ for both the 10 min and the 20 min waiting samples. This suggests that there is no space-charge limitation effect and the initial geminate pair separation is very efficient in all conditions. Thus none of the sample’s insulating oxides is acting as a barrier for charge transport nor the photoactive layer possesses low mobility.

The ideal factor, $\eta_{id} = 1$, can be expressed as the following formula:

$$\eta_{id} = q/kT \times dV_{OC}/d\ln(LI)$$

The ideality factor increases from 1, as more trap states are present. An ideality factor of 2 is indicative of Shockley–Read–Hall recombination (trap assisted recombination). This offers information on the recombination rate within the photoactive layer. Figure 9b shows that the increase in V_{OC} is large for the 20 min waiting sample, which can be attributed to a low recombination rate of the photo-generated charges in these structures, thus slow depletion excitons. This again supports my hypothesis that the phase separation improves for better charge extraction as I leave the cast solution longer. Yet, the decrease in FF is ascribed to the increased R_s , which probably originates from oxidation of the photoactive layer in air.

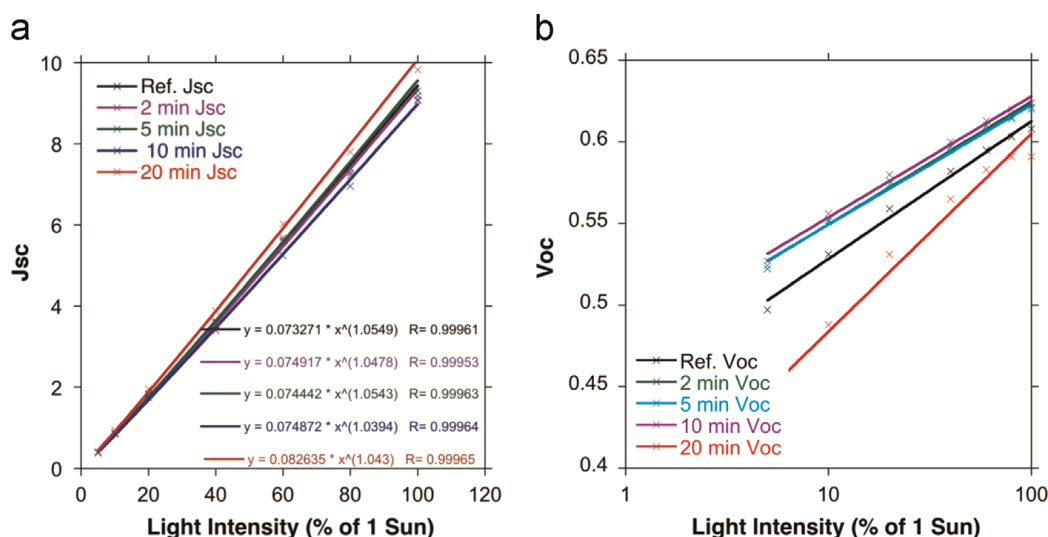


Figure 9. (a) J_{sc} and (b) V_{oc} as a function of light intensity for the reference and the samples with different waiting times.

Devices were fabricated in different conditions using different samples. Firstly, the waiting effect in nitrogen condition was checked by fabricating P3HT:PCBM based OSCs inside a glove box. I expected no light-soaking improvement but the vertical phase separation to still take place. According to Table 2, neither the PCE improvement nor the light-soaking time trends are clear. Therefore no light-soaking improvement has taken place. Yet, also no clear difference in PCE means that the vertical phase separation might have been too subtle to manifest observable difference.

Second, the same devices but using ZnO instead of TiO₂ were fabricated in air.

Some claim that the light-soaking mechanism and origin of ZnO is different from those of TiO₂, not to mention inherently shorter light-soaking time for ZnO. The Table 3 shows that the PCE improvement is not as dramatic as TiO₂ based devices and the light-soaking improvement is unclear which is probably due to intrinsically short light-soaking time. However, the trends in each photovoltaic parameter follow my hypothesis.

Lastly, I used a different acceptor material to check versatility of the waiting effect. MIF which is 56- π bis-functionalised fullerene where one adduct is an indene group and the other is methanediyl group was used in place of PCBM and inverted OSCs were fabricated in air with different waiting times.^[459] The Table 4 shows that MIF based devices behave the same way as the PCBM based devices. Therefore, it is proven that the waiting effect does not only work for PCBM but also for another fullerene derivative too.

Table 2. Nitrogen-processed inverted OSC device performance and their light-soaking time with different pre-spin coating initiation waiting times under AM1.5G illumination (100 mW cm⁻²).

Pre-spin waiting time	V_{OC} (V)	J_{SC} (mA cm ⁻²)	FF	η (%)	Light-soaking time (s)
0 min	0.62	9.71	0.56	3.33	480
5 min	0.61	9.91	0.57	3.41	840
10 min	0.60	9.55	0.56	3.25	660
20 min	0.60	9.51	0.57	3.33	175

Table 3. Air-processed inverted OSC device performance using ZnO and their light-soaking time with different pre-spin coating initiation waiting times under AM1.5G illumination (100 mW cm⁻²).

Pre-spin waiting time	V_{OC} (V)	J_{SC} (mA cm ⁻²)	FF	η (%)	Light-soaking time (s)
0 min	0.61	8.62	0.56	3.33	280
2 min	0.61	8.89	0.58	3.16	170
5 min	0.62	8.86	0.58	3.22	200
10 min	0.63	8.93	0.60	3.34	60
20 min	0.62	9.08	0.49	2.76	60

Table 4. Air-processed inverted OSC device performance using MIF and their light-soaking time with different pre-spin coating initiation waiting times under AM1.5G illumination (100 mW cm⁻²).

Pre-spin waiting time	V_{OC} (V)	J_{SC} (mA cm ⁻²)	FF	η (%)
0 min	0.77	6.42	0.44	2.18
5 min	0.79	6.04	0.55	2.61
10 min	0.77	6.72	0.58	3.00
20 min	0.77	5.57	0.53	2.27

13.5 Conclusion

In conclusion, I discovered that the pre-spin coating initiation of photoactive solution waiting time induces two favourable effects for air-processed inverted OSCs. One of the effects is the control of the vertical phase separation and another is desorption of oxygen at the interface of the ETL. Principles of these effects were evidenced by the analytical techniques. The optimised waiting time was found to be around 5–10 min and a PCE of an air-processed inverted OSC reached as high as a normal type OSC which was fabricated inside a glove box. I believe this study can play an important role in understanding the OSC devices and anticipate this facile method being utilised in scale-up of air-processed solar technologies.

CHAPTER 14

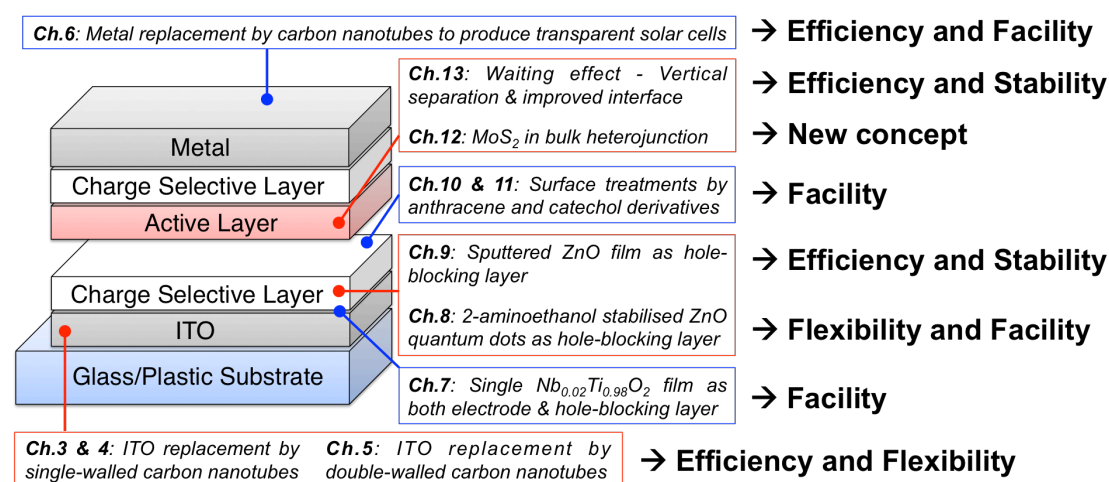
CONCLUSION AND OUTLOOK

The mainspring of the thesis was to understand the mechanisms behind interfaces of charge conductive and selective layers which lead to improvement of the four key criteria (efficiency, flexibility, facility, and stability) of the next-generation solar cells (Inset). From Chapter 3 to 6, carbon nanotube films were used as electrodes and their interfaces were studied. A variety of doping and interface modification methods were harnessed to achieve high efficiency and flexibility. In Chapter 7, I introduced a new metal oxide electrode, which can function as both charge conductive and selective by interface change to achieve facility of the solar cell fabrication. In Chapter 8 and 9, the conventional charge selective layer, ZnO was deposited in a novel fashion to enhance all of the four fronts. Surface modification using surfactants were discussed in Chapter 10 and 11. Interface investigation was extended even to the active layers in Chapter 12 and 13. Since this thesis is a collection of related individual researches rather than a single project which begets a single conclusion, I have provided a table below which summarises conclusions of individual chapters.

Chapter	Conclusion
3	Single-walled carbon nanotube successfully replaced ITO and thermally annealed MoO _x layer functioned as both dopant and charge selective layer. Flexible and high performing ITO-free organic solar cells were demonstrated.
4	Single-walled carbon nanotube successfully replaced ITO in perovskite solar cells. I discovered MoO _x layer is incompatible with perovskite solar cells due to energy level mismatch and introduced two novel ways of doping via diluted nitric acid and PEDOT:PSS modification. Although flexible and high performing ITO-free perovskite solar cells were demonstrated, carbon nanotube showed a slight energy level mismatch.
5	Application of solution-processed double-walled carbon nanotube as an electrode to replace ITO in organic solar cells was successfully demonstrated. I compared the mechanical and electronic properties of double-walled and single-walled nanotubes and discovered that inner-nanotube of the double-walled carbon nanotube does not produce defect sites under nitric acid doping as evidenced by higher solar cell efficiency.
6	Single-walled carbon nanotube replaced metal in organic solar cells and transparent window-like and metal-free organic solar cells were produced. In order to enhance the overall performance, novel methods of doping carbon nanotubes that are laminated from top were introduced for the first time.
7	Niobium-doped titanium oxide was used as an electrode to replace ITO, and moreover ozone-treated niobium-doped titanium oxide was used as both an electrode and a charge selective layer in inverted organic solar cells. It was found that ozone treatment oxidised the surface of niobium-doped titanium oxide film, turning it into semi-conductor.
8	I develop a new way of forming ZnO nano particles by using amino-2-ethanol as

	stabilisers which could form a film by a simple spin coating without applying thermal annealing in inverted organic solar cells.
9	High pressure-sputtered ZnO films showed higher efficiency than the sol-gel ZnO films.
10	I successfully modified the surface of metal oxide by anthracene compounds which enhanced the efficiency of solar cells by filling up the reactive sites of the oxide film.
11	I successfully modified the surface of metal oxide layers by catechol compounds which attracted fullerene acceptors to the surface to enhance organic solar cell efficiency.
12	I Introduce MoS ₂ as electron acceptors in organic solar cells by using carbon nanotube. MoS ₂ functioned as electron acceptor in a bulk heterojunction for the first time.
13	A vertical separation in a bulk heterojunction in inverted organic solar cells was successfully induced and better contact in active layer was achieved as proven by reduced light-soaking effect.

In summary, different materials and interfaces in the charge selective and conductive layers have been studied in depth and their applications successfully demonstrated advancements in terms of power conversion efficiency and versatility. This work is especially significant for the charge conductive and selective layers are applicable not only in photovoltaics, but in other electronic devices too. I look forward to science and technology discussed in dissertation contributing greatly to the academic community.



Inset. An illustration of how each project this thesis contributed to completing the initial objectives.

REFERENCES

- [1] J. L. Miller, *Phys. Today* **2014**, DOI 10.1063/PT.5.7058.
- [2] N. Armaroli, V. Balzani, *Angew. Chemie Int. Ed.* **2007**, *46*, 52.
- [3] A. Demirbas, *Energy Sources, Part B Econ. Planning, Policy* **2007**, *3*, 41.
- [4] R. E. H. Sims, H.-H. Rogner, K. Gregory, *Energy Policy* **2003**, *31*, 1315.
- [5] N. S. Lewis, D. G. Nocera, *Proc. Natl. Acad. Sci.* **2006**, *103*, 15729.
- [6] G. W. Crabtree, N. S. Lewis, *Phys. Today* **2007**, *60*, 37.
- [7] N. L. Panwar, S. C. Kaushik, S. Kothari, *Renew. Sustain. Energy Rev.* **2011**, *15*, 1513.
- [8] I. B. Fridleifsson, *Renew. Sustain. Energy Rev.* **2001**, *5*, 299.
- [9] P. Michalak, J. Zimny, *Renew. Sustain. Energy Rev.* **2011**, *15*, 2330.
- [10] A. J. Ragauskas, *Science* **2006**, *311*, 484.
- [11] F. Manzano-Agugliaro, A. Alcaide, F. G. Montoya, A. Zapata-Sierra, C. Gil, *Renew. Sustain. Energy Rev.* **2013**, *18*, 134.
- [12] K. S. Gallagher, *Daedalus* **2013**, *142*, 59.
- [13] S. Ruiz Romero, A. Colmenar Santos, M. A. Castro Gil, *Renew. Energy* **2012**, *43*, 322.
- [14] J. K. Kaldellis, M. Kapsali, E. Kaldelli, E. Katsanou, *Renew. Energy* **2013**, *52*, 197.
- [15] G. Turner, *Bloom. New Energy Financ.* <https://www.bnef.com/insightdownload/7526/pdf> (11 April 2014) **2013**.
- [16] M. Z. Jacobson, M. A. Delucchi, *Sci. Am.* **2009**, *301*, 58.
- [17] M. Z. Jacobson, *Energy Environ. Sci.* **2009**, *2*, 148.
- [18] N. S. Lewis, G. Crabtree, *Basic Research Needs for Solar Energy Utilization: Report of the Basic Energy Sciences Workshop on Solar Energy Utilization, April 18-21, 2005*, US Department Of Energy, Office Of Basic Energy Science, **2005**.
- [19] J. Y. Tsao, M. E. Coltrin, M. H. Crawford, J. A. Simmons, *Proc. IEEE* **2010**, *98*, 1162.
- [20] T. R. Cook, D. K. Dogutan, S. Y. Reece, Y. Surendranath, T. S. Teets, D. G. Nocera, *Chem. Rev.* **2010**, *110*, 6474.
- [21] D. J. Des Marais, *Science* **2000**, *289*, 1703.
- [22] M. A. Green, *Prog. Photovoltaics Res. Appl.* **2009**, *17*, 183.
- [23] L. Dou, J. You, J. Yang, C.-C. Chen, Y. He, S. Murase, T. Moriarty, K. Emery, G. Li, Y. Yang, *Nat. Photonics* **2012**, *6*, 180.
- [24] Y. Liu, X. Wan, F. Wang, J. Zhou, G. Long, J. Tian, J. You, Y. Yang, Y. Chen, *Adv. Energy Mater.* **2011**, *1*, 771.
- [25] G. Dennler, M. C. Scharber, C. J. Brabec, *Adv. Mater.* **2009**, *21*, 1323.
- [26] S.-S. Li, C.-W. Chen, *J. Mater. Chem. A* **2013**, *1*, 10574.
- [27] C. W. Tang, *Appl. Phys. Lett.* **1986**, *48*, 183.
- [28] M. Pope, C. E. Swenberg, *Electronic Processes in Organic Crystals and Polymers*, Oxford University Press, **1999**.
- [29] S. R. Forrest, *Nature* **2004**, *428*, 911.
- [30] J. C. Hummelen, B. W. Knight, F. LePeq, F. Wudl, J. Yao, C. L. Wilkins, *J. Org. Chem.* **1995**, *60*, 532.
- [31] *Science* **1992**, *258*, 1474.
- [32] S. Morita, A. A. Zakhidov, K. Yoshino, *Solid State Commun.* **1992**, *82*, 249.
- [33] N. S. Sariciftci, L. Smilowitz, A. J. Heeger, F. Wudl, *Synth. Met.* **1993**, *59*, 333.
- [34] M. Hiramoto, H. Fujiwara, M. Yokoyama, *J. Appl. Phys.* **1992**, *72*, 3781.
- [35] J. J. M. Halls, C. A. Walsh, N. C. Greenham, E. A. Marseglia, R. H. Friend, S. C. Moratti, A. B. Holmes, *Nature* **1995**, *376*, 498.
- [36] G. Yu, J. Gao, J. C. Hummelen, F. Wudl, A. J. Heeger, *Science* **1995**, *270*, 1789.
- [37] G. Li, V. Shrotriya, J. Huang, Y. Yao, T. Moriarty, K. Emery, Y. Yang, *Nat. Mater.* **2005**, *4*, 864.
- [38] W. Ma, C. Yang, X. Gong, K. Lee, A. J. Heeger, *Adv. Funct. Mater.* **2005**, *15*, 1617.
- [39] C. Piliago, T. W. Holcombe, J. D. Douglas, C. H. Woo, P. M. Beaujuge, J. M. J. Fréchet, *J. Am. Chem. Soc.* **2010**, *132*, 7595.
- [40] T.-Y. Chu, J. Lu, S. Beaupré, Y. Zhang, J.-R. Pouliot, S. Wakim, J. Zhou, M. Leclerc, Z. Li, J. Ding, Y. Tao, *J. Am. Chem. Soc.* **2011**, *133*, 4250.
- [41] J. Seo, S. Park, Y. Chan Kim, N. J. Jeon, J. H. Noh, S. C. Yoon, S. Il Seok, *Energy Environ. Sci.* **2014**, *7*, 2642.
- [42] M. M. Wienk, J. M. Kroon, W. J. H. Verhees, J. Knol, J. C. Hummelen, P. A. van Hal, R. A. J. Janssen, *Angew. Chemie* **2003**, *115*, 3493.
- [43] F. Padinger, R. S. Rittberger, N. S. Sariciftci, *Adv. Funct. Mater.* **2003**, *13*, 85.
- [44] Z. Bao, A. Dodabalapur, A. J. Lovinger, *Appl. Phys. Lett.* **1996**, *69*, 4108.
- [45] D. Mühlbacher, M. Scharber, M. Morana, Z. Zhu, D. Waller, R. Gaudiana, C. Brabec, *Adv. Mater.* **2006**, *18*, 2884.
- [46] J. Peet, J. Y. Kim, N. E. Coates, W. L. Ma, D. Moses, A. J. Heeger, G. C. Bazan, *Nat. Mater.* **2007**, *6*, 497.
- [47] N. Blouin, A. Michaud, M. Leclerc, *Adv. Mater.* **2007**, *19*, 2295.
- [48] S. H. Park, A. Roy, S. Beaupré, S. Cho, N. Coates, J. S. Moon, D. Moses, M. Leclerc, K. Lee, A. J. Heeger, *Nat. Photonics* **2009**, *3*, 297.
- [49] Y. Liang, Y. Wu, D. Feng, S.-T. Tsai, H.-J. Son, G. Li, L. Yu, *J. Am. Chem. Soc.* **2009**, *131*, 56.
- [50] H.-Y. Chen, J. Hou, S. Zhang, Y. Liang, G. Yang, Y. Yang, L. Yu, Y. Wu, G. Li, *Nat. Photonics* **2009**, *3*, 649.
- [51] S. C. Price, A. C. Stuart, L. Yang, H. Zhou, W. You, *J. Am. Chem. Soc.* **2011**, *133*, 4625.
- [52] H. Zhou, L. Yang, A. C. Stuart, S. C. Price, S. Liu, W. You, *Angew. Chemie* **2011**, *123*, 3051.
- [53] M.-S. Su, C.-Y. Kuo, M.-C. Yuan, U.-S. Jeng, C.-J. Su, K.-H. Wei, *Adv. Mater.* **2011**, *23*, 3315.
- [54] J. Yang, R. Zhu, Z. Hong, Y. He, A. Kumar, Y. Li, Y. Yang, *Adv. Mater.* **2011**, *23*, 3465.
- [55] Y. Sun, C. J. Takacs, S. R. Cowan, J. H. Seo, X. Gong, A. Roy, A. J. Heeger, *Adv. Mater.* **2011**, *23*, 2226.
- [56] C. M. Amb, S. Chen, K. R. Graham, J. Subbiah, C. E. Small, F. So, J. R. Reynolds, *J. Am. Chem. Soc.* **2011**, *133*, 10062.
- [57] M. Lenes, G. J. a H. Wetzelaer, F. B. Kooistra, S. C. Veenstra, J. C. Hummelen, P. W. M. Blom, *Adv. Mater.* **2008**, *20*, 2116.
- [58] S. E. Shaheen, C. J. Brabec, N. S. Sariciftci, F. Padinger, T. Fromherz, J. C. Hummelen, *Appl. Phys. Lett.* **2001**, *78*,

- 841.
- [59] F. Zhang, K. G. Jespersen, C. Björström, M. Svensson, M. R. Andersson, V. Sundström, K. Magnusson, E. Moons, A. Yartsev, O. Inganäs, *Adv. Funct. Mater.* **2006**, *16*, 667.
- [60] E. Pavlopoulou, G. Fleury, D. Deribew, F. Cousin, M. Geoghegan, G. Hadziioannou, *Org. Electron.* **2013**, *14*, 1249.
- [61] L.-M. Chen, Z. Xu, Z. Hong, Y. Yang, *J. Mater. Chem.* **2010**, *20*, 2575.
- [62] N. Schmerl, G. Andersson, *Phys. Chem. Chem. Phys.* **2011**, *13*, 14993.
- [63] M. Campoy-Quiles, T. Ferenczi, T. Agostinelli, P. G. Etchegoin, Y. Kim, T. D. Anthopoulos, P. N. Stavrinou, D. D. C. Bradley, J. Nelson, *Nat. Mater.* **2008**, *7*, 158.
- [64] K. M. Coakley, B. S. Srinivasan, J. M. Ziebarth, C. Goh, Y. Liu, M. D. McGehee, *Adv. Funct. Mater.* **2005**, *15*, 1927.
- [65] L. H. Nguyen, H. Hoppe, T. Erb, S. Günes, G. Gobsch, N. S. Sariciftci, *Adv. Funct. Mater.* **2007**, *17*, 1071.
- [66] M. M. Mandoc, W. Veurman, J. Sweelssen, M. M. Koetse, P. W. M. Blom, *Appl. Phys. Lett.* **2007**, *91*, 073518.
- [67] Y. Kim, S. A. Choulis, J. Nelson, D. D. C. Bradley, S. Cook, J. R. Durrant, *Appl. Phys. Lett.* **2005**, *86*, 063502.
- [68] V. D. Mihailetschi, H. Xie, B. de Boer, L. M. Popescu, J. C. Hummelen, P. W. M. Blom, L. J. A. Koster, *Appl. Phys. Lett.* **2006**, *89*, 012107.
- [69] P. Vanlaeke, G. Vanhoyland, T. Aernouts, D. Cheyns, C. Deibel, J. Manca, P. Heremans, J. Poortmans, *Thin Solid Films* **2006**, *511-512*, 358.
- [70] K. Kim, J. Liu, D. L. Carroll, *Appl. Phys. Lett.* **2006**, *88*, 181911.
- [71] M. Glatthaar, M. Riede, N. Keegan, K. Sylvester-Hvid, B. Zimmermann, M. Niggemann, A. Hinsch, A. Gombert, *Sol. Energy Mater. Sol. Cells* **2007**, *91*, 390.
- [72] C. S. Kim, S. S. Lee, E. D. Gomez, J. B. Kim, Y.-L. Loo, *Appl. Phys. Lett.* **2009**, *94*, 113302.
- [73] F. Verbakel, S. C. J. Meskers, R. A. J. Janssen, *Appl. Phys. Lett.* **2006**, *89*, 102103.
- [74] M. R. Lilliedal, A. J. Medford, M. V. Madsen, K. Norrman, F. C. Krebs, *Sol. Energy Mater. Sol. Cells* **2010**, *94*, 2018.
- [75] S. Chambon, E. Destouesse, B. Pavageau, L. Hirsch, G. Wantz, *J. Appl. Phys.* **2012**, *112*, 94503.
- [76] R. A. Marsh, C. Groves, N. C. Greenham, *J. Appl. Phys.* **2007**, *101*, 083509.
- [77] S. Trost, K. Zilberberg, A. Behrendt, A. Polywka, P. Görrn, P. Reckers, J. Maibach, T. Mayer, T. Riedl, *Adv. Energy Mater.* **2013**, *3*, 1437.
- [78] Y. Berredjem, N. Karst, A. Boulmouk, A. Drici, J. C. Bernède, *Eur. Phys. J. Appl. Phys.* **2007**, *40*, 163.
- [79] I. Morasero, *Sol. Energy Mater. Sol. Cells* **2004**, *85*, 51.
- [80] M. O. Reese, M. S. White, G. Rumbles, D. S. Ginley, S. E. Shaheen, *Appl. Phys. Lett.* **2008**, *92*, 053307.
- [81] M. Vogel, S. Doka, C. Breyer, M. C. Lux-Steiner, K. Fostiropoulos, *Appl. Phys. Lett.* **2006**, *89*, 163501.
- [82] D. Gupta, M. Bag, K. S. Narayan, *Appl. Phys. Lett.* **2008**, *92*, 93301.
- [83] J. Nelson, J. Kirkpatrick, P. Ravirajan, *Phys. Rev. B* **2004**, *69*, 035337.
- [84] N.-G. Park, *J. Phys. Chem. Lett.* **2013**, *4*, 2423.
- [85] A. Kojima, K. Teshima, Y. Shirai, T. Miyasaka, *J. Am. Chem. Soc.* **2009**, *131*, 6050.
- [86] J.-H. Im, C.-R. Lee, J.-W. Lee, S.-W. Park, N.-G. Park, *Nanoscale* **2011**, *3*, 4088.
- [87] H.-S. Kim, C.-R. Lee, J.-H. Im, K.-B. Lee, T. Moehl, A. Marchioro, S.-J. Moon, R. Humphry-Baker, J.-H. Yum, J. E. Moser, M. Grätzel, N.-G. Park, *Sci. Rep.* **2012**, *2*, 591.
- [88] M. M. Lee, J. Teuscher, T. Miyasaka, T. N. Murakami, H. J. Snaith, *Science* **2012**, *338*, 643.
- [89] U. Bach, D. Lupo, P. Comte, J. E. Moser, F. Weissortel, J. Salbeck, H. Spreitzer, M. Grätzel, **1998**, *395*, 583.
- [90] S. D. Stranks, G. E. Eperon, G. Grancini, C. Menelaou, M. J. P. Alcocer, T. Leijtens, L. M. Herz, A. Petrozza, H. J. Snaith, *Science* **2013**, *342*, 341.
- [91] J. H. Heo, S. H. Im, J. H. Noh, T. N. Mandal, C.-S. Lim, J. A. Chang, Y. H. Lee, H. Kim, A. Sarkar, M. K. Nazeeruddin, M. Grätzel, S. Il Seok, *Nat. Photonics* **2013**, *7*, 486.
- [92] J. H. Noh, S. H. Im, J. H. Heo, T. N. Mandal, S. Il Seok, *Nano Lett.* **2013**, *13*, 1764.
- [93] J. Burschka, N. Pellet, S.-J. Moon, R. Humphry-Baker, P. Gao, M. K. Nazeeruddin, M. Grätzel, *Nature* **2013**, *499*, 316.
- [94] M. Liu, M. B. Johnston, H. J. Snaith, *Nature* **2013**, *501*, 395.
- [95] Q. Chen, H. Zhou, Z. Hong, S. Luo, H.-S. Duan, H.-H. Wang, Y. Liu, G. Li, Y. Yang, *J. Am. Chem. Soc.* **2014**, *136*, 622.
- [96] K. Wojciechowski, M. Saliba, T. Leijtens, A. Abate, H. J. Snaith, *Energy Environ. Sci.* **2014**, *7*, 1142.
- [97] S. H. Im, J.-H. Heo, H. J. Han, D. Kim, T. Ahn, *Energy Environ. Sci.* **2015**, *8*, 1602.
- [98] T. Kojima, A. Teshima, K. Shirai, Y. Miyasaka, *J. Am. Chem. Soc.* **2009**, *131*, 6050.
- [99] M. D. McGehee, *Nat. Mater.* **2014**, *13*, 845.
- [100] S. Kazim, M. K. Nazeeruddin, M. Grätzel, S. Ahmad, *Angew. Chemie Int. Ed.* **2014**, *53*, 2812.
- [101] J. H. Noh, S. H. Im, J. H. Heo, T. N. Mandal, S. Il Seok, *Nano Lett.* **2013**, *13*, 1764.
- [102] C. Li, X. Lu, W. Ding, L. Feng, Y. Gao, Z. Guo, *Acta Crystallogr. Sect. B Struct. Sci.* **2008**, *64*, 702.
- [103] H. J. Snaith, *J. Phys. Chem. Lett.* **2013**, *4*, 3623.
- [104] N. K. McKinnon, D. C. Reeves, M. H. Akabas, *J. Gen. Physiol.* **2011**, *138*, 453.
- [105] B. N. Cohen, *J. Gen. Physiol.* **1992**, *100*, 373.
- [106] J.-H. Im, J. Chung, S.-J. Kim, N.-G. Park, *Nanoscale Res. Lett.* **2012**, *7*, 353.
- [107] T. M. Koh, K. Fu, Y. Fang, S. Chen, T. C. Sum, N. Mathews, S. G. Mhaisalkar, P. P. Boix, T. Baikie, *J. Phys. Chem. C* **2014**, *118*, 16458.
- [108] P. Umari, E. Mosconi, F. De Angelis, *Sci. Rep.* **2014**, *4*, 4467.
- [109] K. Liang, D. B. Mitzi, M. T. Prikas, *Chem. Mater.* **1998**, *10*, 403.
- [110] L. Etgar, P. Gao, Z. Xue, Q. Peng, A. K. Chandra, B. Liu, M. K. Nazeeruddin, M. Grätzel, *J. Am. Chem. Soc.* **2012**, *134*, 17396.
- [111] M. D. McGehee, *Nature* **2013**, *501*, 323.
- [112] I. C. Smith, E. T. Hoke, D. Solis-Ibarra, M. D. McGehee, H. I. Karunadasa, *Angew. Chemie Int. Ed.* **2014**, *53*, 11232.
- [113] N. Kawano, M. Koshimizu, K. Asai, *J. Phys. Chem. C* **2012**, *116*, 22992.
- [114] K. Ema, M. Inomata, Y. Kato, H. Kunugita, M. Era, *Phys. Rev. Lett.* **2008**, *100*, 257401.
- [115] H. S. Rauschenbach, *Solar Cell Array Design Handbook - The Principles and Technology of Photovoltaic Energy Conversion*, Van Nostrand Reinhold Co., New York, **1980**.
- [116] A. Fahrenbruch, R. Bube, *New York* **1983**.
- [117] P. Schilinsky, *J. Appl. Phys.* **2004**, *95*, 2816.
- [118] I. Riedel, V. Dyakonov, *Phys. status solidi* **2004**, *201*, 1332.
- [119] Y.-J. Cheng, S.-H. Yang, C.-S. Hsu, *Chem. Rev.* **2009**, *109*, 5868.

- [120] Y. Liang, L. Yu, *Polym. Rev.* **2010**, *50*, 454.
- [121] Y. Liang, L. Yu, *Acc. Chem. Res.* **2010**, *43*, 1227.
- [122] Y. Zhang, J. Zou, H.-L. Yip, K.-S. Chen, D. F. Zeigler, Y. Sun, A. K.-Y. Jen, *Chem. Mater.* **2011**, *23*, 2289.
- [123] F. He, W. Wang, W. Chen, T. Xu, S. B. Darling, J. Strzalka, Y. Liu, L. Yu, *J. Am. Chem. Soc.* **2011**, *133*, 3284.
- [124] E. E. Havinga, W. ten Hoeve, H. Wynberg, *Synth. Met.* **1993**, *55*, 299.
- [125] Q. T. Zhang, J. M. Tour, *J. Am. Chem. Soc.* **1997**, *119*, 5065.
- [126] J. Hou, H.-Y. Chen, S. Zhang, G. Li, Y. Yang, *J. Am. Chem. Soc.* **2008**, *130*, 16144.
- [127] H.-Y. Chen, J. Hou, A. E. Hayden, H. Yang, K. N. Houk, Y. Yang, *Adv. Mater.* **2010**, *22*, 371.
- [128] M. C. Scharber, D. Mühlbacher, M. Koppe, P. Denk, C. Waldauf, A. J. Heeger, C. J. Brabec, *Adv. Mater.* **2006**, *18*, 789.
- [129] D. Chen, F. Liu, C. Wang, A. Nakahara, T. P. Russell, *Nano Lett.* **2011**, *11*, 2071.
- [130] V. Shrotriya, G. Li, Y. Yao, C.-W. C. Chu, Y. Yang, *Appl. Phys. Lett.* **2006**, *88*, 73508.
- [131] M. D. Irwin, D. B. Buchholz, A. W. Hains, R. P. H. Chang, T. J. Marks, *Proc. Natl. Acad. Sci.* **2008**, *105*, 2783.
- [132] K. X. Steirer, P. F. Ndione, N. E. Widjonarko, M. T. Lloyd, J. Meyer, E. L. Ratcliff, A. Kahn, N. R. Armstrong, C. J. Curtis, D. S. Ginley, J. J. Berry, D. C. Olson, *Adv. Energy Mater.* **2011**, *1*, 813.
- [133] C.-P. Chen, Y.-D. Chen, S.-C. Chuang, *Adv. Mater.* **2011**, *23*, 3859.
- [134] L. S. Hung, C. W. Tang, M. G. Mason, *Appl. Phys. Lett.* **1997**, *70*, 152.
- [135] S. K. M. Jönsson, E. Carlegrim, F. Zhang, W. R. Salaneck, M. Fahlman, *Jpn. J. Appl. Phys.* **2005**, *44*, 3695.
- [136] C. Lee, *Synth. Met.* **1997**, *91*, 125.
- [137] G. E. Jabbour, B. Kippelen, N. R. Armstrong, N. Peyghambarian, *Appl. Phys. Lett.* **1998**, *73*, 1185.
- [138] H.-H. Liao, L.-M. Chen, Z. Xu, G. Li, Y. Yang, *Appl. Phys. Lett.* **2008**, *92*, 173303.
- [139] J. Y. Kim, S. H. Kim, H. H. Lee, K. Lee, W. Ma, X. Gong, A. J. Heeger, *Adv. Mater.* **2006**, *18*, 572.
- [140] J. Gilot, I. Barbu, M. M. Wienk, R. A. J. Janssen, *Appl. Phys. Lett.* **2007**, *91*, 113520.
- [141] K. Lee, J. Y. Kim, S. Park, S. Kim, S. Cho, A. J. Heeger, *Adv. Mater.* **2007**, *19*, 2445.
- [142] M.-H. Park, J.-H. Li, A. Kumar, G. Li, Y. Yang, *Adv. Funct. Mater.* **2009**, *19*, 1241.
- [143] H.-L. Yip, S. K. Hau, N. S. Baek, H. Ma, A. K.-Y. Jen, *Adv. Mater.* **2008**, *20*, 2376.
- [144] F. Huang, H. Wu, Y. Cao, *Chem. Soc. Rev.* **2010**, *39*, 2500.
- [145] T.-F. Guo, S.-C. Chang, S. Pyo, Yang, *Langmuir* **2002**, *18*, 8142.
- [146] Z. He, C. Zhong, X. Huang, W.-Y. Wong, H. Wu, L. Chen, S. Su, Y. Cao, *Adv. Mater.* **2011**, *23*, 4636.
- [147] D. Liu, T. L. Kelly, *Nat. Photonics* **2013**, *8*, 133.
- [148] J. A. Christians, R. C. M. Fung, P. V. Kamat, *J. Am. Chem. Soc.* **2014**, *136*, 758.
- [149] P. Docampo, J. M. Ball, M. Darwich, G. E. Eperon, H. J. Snaith, *Nat. Commun.* **2013**, *4*, 2761.
- [150] O. Malinkiewicz, A. Yella, Y. H. Lee, G. M. Espallargas, M. Graetzel, M. K. Nazeeruddin, H. J. Bolink, *Nat. Photonics* **2013**, *8*, 128.
- [151] C. Roldán-Carmona, O. Malinkiewicz, A. Soriano, G. Mínguez Espallargas, A. Garcia, P. Reinecke, T. Kroyer, M. I. Dar, M. K. Nazeeruddin, H. J. Bolink, *Energy Environ. Sci.* **2014**, *7*, 994.
- [152] J. T.-W. Wang, J. M. Ball, E. M. Barea, A. Abate, J. a. Alexander-Webber, J. Huang, M. Saliba, I. Mora-Sero, J. Bisquert, H. J. Snaith, R. J. Nicholas, *Nano Lett.* **2014**, *14*, 724.
- [153] B. J. Kim, D. H. Kim, Y.-Y. Lee, H.-W. Shin, G. S. Han, J. S. Hong, K. Mahmood, T. K. Ahn, Y.-C. Joo, K. S. Hong, N.-G. Park, S. Lee, H. S. Jung, *Energy Environ. Sci.* **2015**, *8*, 916.
- [154] J. You, Z. Hong, Y. (Michael) Yang, Q. Chen, M. Cai, T.-B. Song, C.-C. Chen, S. Lu, Y. Liu, H. Zhou, Y. (Michael) Yang, *ACS Nano* **2014**, *8*, 1674.
- [155] M. Yang, D. Kim, H. Jha, K. Lee, J. Paul, P. Schmuki, *Chem. Commun.* **2011**, *47*, 2032.
- [156] X. Lü, X. Mou, J. Wu, D. Zhang, L. Zhang, F. Huang, F. Xu, S. Huang, *Adv. Funct. Mater.* **2010**, *20*, 509.
- [157] T. Nikolay, L. Larina, O. Shevaleevskiy, B. T. Ahn, *Energy Environ. Sci.* **2011**, *4*, 1480.
- [158] K. Zilberberg, F. Gasse, R. Pagui, A. Polywka, A. Behrendt, S. Trost, R. Heiderhoff, P. Görrn, T. Riedl, *Adv. Funct. Mater.* **2014**, *24*, 1671.
- [159] R. S. Sanchez, V. Gonzalez-Pedro, J.-W. Lee, N.-G. Park, Y. S. Kang, I. Mora-Sero, J. Bisquert, *J. Phys. Chem. Lett.* **2014**, *5*, 2357.
- [160] J. Yun, W. Wang, T. S. Bae, Y. H. Park, Y.-C. Kang, D.-H. Kim, S. Lee, G.-H. Lee, M. Song, J.-W. Kang, *ACS Appl. Mater. Interfaces* **2013**, *5*, 9933.
- [161] S. Bae, H. Kim, Y. Lee, X. Xu, J.-S. Park, Y. Zheng, J. Balakrishnan, T. Lei, H. Ri Kim, Y. Il Song, Y.-J. Kim, K. S. Kim, B. Özyilmaz, J.-H. Ahn, B. H. Hong, S. Iijima, *Nat. Nanotechnol.* **2010**, *5*, 574.
- [162] H. Park, S. Chang, X. Zhou, J. Kong, T. Palacios, S. Gradečak, *Nano Lett.* **2014**, *14*, 5148.
- [163] D. M. Sun, C. Liu, W. C. Ren, H. M. Cheng, *Small* **2013**, *9*, 1188.
- [164] Y. H. Kim, L. Müller-Meskamp, A. A. Zakhidov, C. Sachse, J. Meiss, J. Bikova, A. Cook, A. A. Zakhidov, K. Leo, *Sol. Energy Mater. Sol. Cells* **2012**, *96*, 244.
- [165] M. F. L. De Volder, S. H. Tawfick, R. H. Baughman, A. J. Hart, *Science* **2013**, *339*, 535.
- [166] U. N. Maiti, W. J. Lee, J. M. Lee, Y. Oh, J. Y. Kim, J. E. Kim, J. Shim, T. H. Han, S. O. Kim, *Adv. Mater.* **2014**, *26*, 40.
- [167] Z. Wu, Z. Chen, X. Du, J. M. Logan, J. Sippel, M. Nikolou, K. Kamaras, J. R. Reynolds, D. B. Tanner, A. F. Hebard, A. G. Rinzler, *Science* **2004**, *305*, 1273.
- [168] D. Angmo, F. C. Krebs, *J. Appl. Polym. Sci.* **2013**, *129*, 1.
- [169] O. Inganäs, *Nat. Photonics* **2011**, *5*, 201.
- [170] K. Goto, T. Kawashima, N. Tanabe, *Sol. Energy Mater. Sol. Cells* **2006**, *90*, 3251.
- [171] W. H. Baek, M. Choi, T. S. Yoon, H. H. Lee, Y. S. Kim, *Appl. Phys. Lett.* **2010**, *96*, 8.
- [172] K. S. Yeo, S. Nakao, Y. Hirose, T. Hasegawa, Y. Matsuo, *Org. Electron.* **2013**, *14*, 1715.
- [173] A. De Sio, K. Chakanga, O. Sergeev, K. von Maydell, J. Parisi, E. von Hauff, *Sol. Energy Mater. Sol. Cells* **2012**, *98*, 52.
- [174] A. Aprilia, P. Wulandari, V. Suendo, Herman, R. Hidayat, A. Fujii, M. Ozaki, *Sol. Energy Mater. Sol. Cells* **2013**, *111*, 181.
- [175] D. Ginley, H. Hosono, D. C. Paine, *Handbook of Transparent Conductors*, Springer Science & Business Media, **2010**.
- [176] M. W. Rowell, M. A. Topinka, M. D. McGehee, H.-J. Prall, G. Denmler, N. S. Sariciftci, L. Hu, G. Gruner, *Appl. Phys. Lett.* **2006**, *88*, 233506.
- [177] R. A. Hatton, A. J. Miller, S. R. P. Silva, *J. Mater. Chem.* **2008**, *18*, 1183.

- [178] S. Iijima, T. Ichihashi, *Nature* **1993**, 363, 603.
- [179] Y. Zhou, L. Hu, G. Grüner, *Appl. Phys. Lett.* **2006**, 88, 123109.
- [180] C. Lim, D.-H. Min, S.-B. Lee, *Appl. Phys. Lett.* **2007**, 91, 243117.
- [181] Z. Wu, *Science* **2004**, 305, 1273.
- [182] H. Park, S. Chang, J. Jean, J. J. Cheng, P. T. Araujo, M. Wang, M. G. Bawendi, M. S. Dresselhaus, V. Bulović, J. Kong, S. Gradečak, *Nano Lett.* **2013**, 13, 233.
- [183] I. Jeon, K. Cui, T. Chiba, A. Anisimov, A. G. Nasibulin, E. I. Kauppinen, S. Maruyama, Y. Matsuo, *J. Am. Chem. Soc.* **2015**, 137, 7982.
- [184] T. Kuwabara, H. Sugiyama, M. Kuzuba, T. Yamaguchi, K. Takahashi, *Org. Electron.* **2010**, 11, 1136.
- [185] A. A. K. A. Kyaw, D. D. H. Wang, V. Gupta, J. Zhang, S. Chand, G. C. Bazan, A. J. Heeger, *Adv. Mater.* **2013**, 25, 2397.
- [186] A. Kaskela, A. G. Nasibulin, M. Y. Timmermans, B. Aitchison, A. Papadimitratos, Y. Tian, Z. Zhu, H. Jiang, D. P. Brown, A. Zakhidov, E. I. Kauppinen, *Nano Lett.* **2010**, 10, 4349.
- [187] A. G. Nasibulin, A. Kaskela, K. Mustonen, A. S. Anisimov, V. Ruiz, S. Kivistö, S. Rackauskas, M. Y. Timmermans, M. Pudas, B. Aitchison, M. Kauppinen, D. P. Brown, O. G. Okhotnikov, E. I. Kauppinen, *ACS Nano* **2011**, 5, 3214.
- [188] H.-C. Liao, C.-H. Lee, Y.-C. Ho, M.-H. Jao, C.-M. Tsai, C.-M. Chuang, J.-J. Shyue, Y.-F. Chen, W.-F. Su, *J. Mater. Chem.* **2012**, 22, 10589.
- [189] A. S. Riad, S. A. Mahmoud, A. A. Ibrahim, *Phys. B Condens. Matter* **2001**, 296, 319.
- [190] 'Ra & RMS Surface Roughness Calculation - Surface Finish Formulas | Harrison Electropolishing L.P.', can be found under <http://www.harrisonep.com/electropolishing-ra.html>, n.d.
- [191] S. L. Hellstrom, M. Vosgueritchian, R. M. Stoltenberg, I. Irfan, M. Hammock, Y. B. Wang, C. Jia, X. Guo, Y. Gao, Z. Bao, *Nano Lett.* **2012**, 12, 3574.
- [192] J. Du, S. Pei, L. Ma, H.-M. M. Cheng, *Adv. Mater.* **2014**, 26, 1958.
- [193] Y. Liang, Z. Xu, J. Xia, S.-T. Tsai, Y. Wu, G. Li, C. Ray, L. Yu, *Adv. Mater.* **2010**, 22, E135.
- [194] Z. He, C. Zhong, S. Su, M. Xu, H. Wu, Y. Cao, *Nat. Photonics* **2012**, 6, 593.
- [195] A. G. Nasibulin, A. Ollikainen, A. S. Anisimov, D. P. Brown, P. V. Pikhitsa, S. Holopainen, J. S. Penttilä, P. Helistö, J. Ruokolainen, M. Choi, E. I. Kauppinen, *Chem. Eng. J.* **2008**, 136, 409.
- [196] Z. Xu, L.-M. Chen, G. Yang, C.-H. Huang, J. Hou, Y. Wu, G. Li, C.-S. Hsu, Y. Yang, *Adv. Funct. Mater.* **2009**, 19, 1227.
- [197] G. Mestl, P. Ruiz, B. Delmon, H. Knozinger, *J. Phys. Chem.* **1994**, 98, 11269.
- [198] E. Kymakis, G. Klapsis, E. Koudoumas, E. Stratakis, N. Kornilios, N. Vidakis, Y. Franghiadakis, *Eur. Phys. J. Appl. Phys.* **2006**, 36, 257.
- [199] A. Kumar, N. Rosen, R. Devine, Y. Yang, *Energy Environ. Sci.* **2011**, 4, 4917.
- [200] Y. S. Eo, H. W. Rhee, B. D. Chin, J.-W. Yu, *Synth. Met.* **2009**, 159, 1910.
- [201] H. B. Michaelson, *J. Appl. Phys.* **1977**, 48, 4729.
- [202] H. E. Unalan, P. Hiralal, D. Kuo, B. Parekh, G. Amaratunga, M. Chhowalla, *J. Mater. Chem.* **2008**, 18, 5909.
- [203] H. Tanaka, T. Yasuda, K. Fujita, T. Tsutsui, *Adv. Mater.* **2006**, 18, 2230.
- [204] T. P. T. Tyler, R. R. E. Brock, H. J. Karmel, T. J. Marks, M. C. Hersam, *Adv. Energy Mater.* **2011**, 1, 785.
- [205] R. V. Salvatierra, C. E. Cava, L. S. Roman, A. J. G. Zarbin, *Adv. Funct. Mater.* **2013**, 23, 1490.
- [206] K. Cui, A. S. Anisimov, T. Chiba, S. Fujii, H. Kataura, A. G. Nasibulin, S. Chiashi, E. I. Kauppinen, S. Maruyama, *J. Mater. Chem. A* **2014**, 2, 11311.
- [207] G. D. M. R. Dabera, K. D. G. I. Jayawardena, M. R. R. Prabhath, I. Yahya, Y. Y. Tan, N. A. Nismy, H. Shiozawa, M. Sauer, G. Ruiz-Soria, P. Ayala, V. Stolojan, A. A. D. T. Adikaari, P. D. Jarowski, T. Pichler, S. R. P. Silva, *ACS Nano* **2013**, 7, 556.
- [208] S. Kim, J. Yim, X. Wang, D. D. C. Bradley, S. Lee, J. C. DeMello, *Adv. Funct. Mater.* **2010**, 20, 2310.
- [209] J. M. Lee, J. S. Park, S. H. Lee, H. Kim, S. Yoo, S. O. Kim, *Adv. Mater.* **2011**, 23, 629.
- [210] U. N. Maiti, W. J. Lee, J. M. Lee, Y. Oh, J. Y. Kim, J. E. Kim, J. Shim, T. H. Han, S. O. Kim, *Adv. Mater.* **2014**, 26, 40.
- [211] J. M. Lee, J. Lim, N. Lee, H. Il Park, K. E. Lee, T. Jeon, S. A. Nam, J. Kim, J. Shin, S. O. Kim, *Adv. Mater.* **2015**, 27, 1519.
- [212] W. J. Lee, U. N. Maiti, J. M. Lee, J. Lim, T. H. Han, S. O. Kim, *Chem. Commun.* **2014**, 50, 6818.
- [213] Z. Li, S. A. Kulkarni, P. P. Boix, E. Shi, A. Cao, K. Fu, S. K. Batabyal, J. Zhang, Q. Xiong, L. H. Wong, N. Mathews, S. G. Mhaisalkar, *ACS Nano* **2014**, 8, 6797.
- [214] J.-Y. Jeng, Y.-F. Chiang, M.-H. Lee, S.-R. Peng, T.-F. Guo, P. Chen, T.-C. Wen, *Adv. Mater.* **2013**, 25, 3727.
- [215] J. T.-W. Wang, J. M. Ball, E. M. Barea, A. Abate, J. A. Alexander-Webber, J. Huang, M. Saliba, I. Mora-Sero, J. Bisquert, H. J. Snaith, R. J. Nicholas, *Nano Lett.* **2014**, 14, 724.
- [216] D. Liu, T. L. Kelly, *Nat. Photonics* **2013**, 8, 133.
- [217] T. Leijtens, G. E. Eperon, S. Pathak, A. Abate, M. M. Lee, H. J. Snaith, *Nat. Commun.* **2013**, 4, 1.
- [218] N. J. Jeon, J. H. Noh, Y. C. Kim, W. S. Yang, S. Ryu, S. Il Seok, *Nat. Mater.* **2014**, 13, 897.
- [219] H. J. Snaith, A. Abate, J. M. Ball, G. E. Eperon, T. Leijtens, N. K. Noel, S. D. Stranks, J. T.-W. Wang, K. Wojciechowski, W. Zhang, *J. Phys. Chem. Lett.* **2014**, 5, 1511.
- [220] Z. Zhou, Z. Wang, Y. Zhou, S. Pang, D. Wang, H. Xu, Z. Liu, N. P. Padture, G. Cui, *Angew. Chemie Int. Ed.* **2015**, 54, 9705.
- [221] I. Jeon, J. W. Ryan, T. Nakazaki, K. S. Yeo, Y. Negishi, Y. Matsuo, *J. Mater. Chem. A* **2014**, 2, 18754.
- [222] H. Park, Y. Shi, J. Kong, *Nanoscale* **2013**, 5, 8934.
- [223] X. Yang, J. Loos, *Macromolecules* **2007**, 40, 1353.
- [224] Z.-S. Wang, H. Kawauchi, T. Kashima, H. Arakawa, *Coord. Chem. Rev.* **2004**, 248, 1381.
- [225] W. Jaegermann, A. Klein, T. Mayer, *Adv. Mater.* **2009**, 21, 4196.
- [226] C. V. Thompson, *Annu. Rev. Mater. Res.* **2012**, 42, 399.
- [227] D. W. Shin, J. H. Lee, Y. H. Kim, S. M. Yu, S. Y. Park, J. B. Yoo, *Nanotechnology* **2009**, 20, 475703.
- [228] Y. Jia, A. Cao, X. Bai, Z. Li, L. Zhang, N. Guo, J. Wei, K. Wang, H. Zhu, D. Wu, P. M. Ajayan, *Nano Lett.* **2011**, 11, 1901.
- [229] Y.-R. Shin, I.-Y. Jeon, J.-B. Baek, *Carbon N. Y.* **2012**, 50, 1465.
- [230] A. Godoy, L. Cattin, L. Toumi, F. R. Díaz, M. A. del Valle, G. M. Soto, B. Kouskoussa, M. Morsli, K. Benchouk, A. Kheil, *Sol. Energy Mater. Sol. Cells* **2010**, 94, 648.

- [231] M. Shiraishi, M. Ata, *Carbon N. Y.* **2001**, *39*, 1913.
- [232] J. Meyer, P. R. Kidambi, B. C. Bayer, C. Weijtens, A. Kuhn, A. Centeno, A. Pesquera, A. Zurutuza, J. Robertson, S. Hofmann, *Sci. Rep.* **2014**, *4*, 5380.
- [233] C. Wang, I. Irfan, X. Liu, Y. Gao, *J. Vac. Sci. Technol. B, Nanotechnol. Microelectron. Mater. Process. Meas. Phenom.* **2014**, *32*, 040801.
- [234] P. Liu, X. Liu, L. Lyu, H. Xie, H. Zhang, D. Niu, H. Huang, C. Bi, Z. Xiao, J. Huang, Y. Gao, *Appl. Phys. Lett.* **2015**, *106*, 193903.
- [235] L. Zuo, Z. Gu, T. Ye, W. Fu, G. Wu, H. Li, H. Chen, *J. Am. Chem. Soc.* **2015**, *137*, 2674.
- [236] Y. Zhao, A. M. Nardes, K. Zhu, *Appl. Phys. Lett.* **2014**, *104*, 213906.
- [237] I. Jeon, T. Chiba, C. Delacou, Y. Guo, A. Kaskela, O. Reynaud, E. I. Kauppinen, S. Maruyama, Y. Matsuo, *Nano Lett.* **2015**, *15*, 6665.
- [238] H. Park, S. Chang, M. Smith, S. Gradečak, J. Kong, *Sci. Rep.* **2013**, *3*, 1581.
- [239] S. Lee, J.-S. Yeo, Y. Ji, C. Cho, D.-Y. Kim, S.-I. Na, B. H. Lee, T. Lee, *Nanotechnology* **2012**, *23*, 344013.
- [240] L. Gomez De Arco, Y. Zhang, C. W. Schlenker, K. Ryu, M. E. Thompson, C. Zhou, *ACS Nano* **2010**, *4*, 2865.
- [241] H. Park, P. R. Brown, V. Bulović, J. Kong, *Nano Lett.* **2012**, *12*, 133.
- [242] S. Won, Y. Hwangbo, S.-K. Lee, K.-S. Kim, K.-S. Kim, S.-M. Lee, H.-J. Lee, J.-H. Ahn, J.-H. Kim, S.-B. Lee, *Nanoscale* **2014**, *6*, 6057.
- [243] P. You, Z. Liu, Q. Tai, S. Liu, F. Yan, *Adv. Mater.* **2015**, *27*, 3632.
- [244] Y. Wang, S. W. Tong, X. F. Xu, B. Özyilmaz, K. P. Loh, *Adv. Mater.* **2011**, *23*, 1514.
- [245] H. Dai, *Nanotube Growth and Characterization*, Springer Berlin Heidelberg, Berlin, Heidelberg, **2001**.
- [246] J. Wang, G. Yin, Y. Shao, S. Zhang, Z. Wang, Y. Gao, *J. Power Sources* **2007**, *171*, 331.
- [247] M. Asgari, E. Lohrasbi, *ISRN Electrochem.* **2013**, *2013*, 1.
- [248] S. P. Somani, P. R. Somani, M. Umeno, E. Flahaut, *Appl. Phys. Lett.* **2006**, *89*, 223505.
- [249] J.-F. Colomer, L. Henrard, P. Launois, G. Van Tendeloo, A. A. Lucas, P. Lambin, *Chem. Commun.* **2004**, 2592.
- [250] L. Ci, Z. Zhou, D. Tang, X. Yan, Y. Liang, D. Liu, H. Yuan, W. Zhou, G. Wang, S. Xie, *Chem. Vap. Depos.* **2003**, *9*, 119.
- [251] R. R. Bacsa, E. Flahaut, C. Laurent, A. Peigney, S. Aloni, P. Puech, W. S. Bacsa, *New J. Phys.* **2003**, *5*, 131.
- [252] W. Z. Li, J. G. Wen, M. Sennett, Z. F. Ren, *Chem. Phys. Lett.* **2003**, *368*, 299.
- [253] T. Sugai, H. Yoshida, T. Shimada, T. Okazaki, H. Shinohara, *Nano Lett.* **2003**, *3*, 769.
- [254] J. L. Hutchison, N. A. Kiselev, E. P. Krinichnaya, A. V. Krestinin, R. O. Loutfy, A. P. Morawsky, V. E. Muradyan, E. D. Obratsova, J. Sloan, S. V. Terekhov, D. N. Zakharov, *Carbon N. Y.* **2001**, *39*, 761.
- [255] Y. Saito, T. Nakahira, S. Uemura, *J. Phys. Chem. B* **2003**, *107*, 931.
- [256] S. Bandow, M. Takizawa, K. Hirahara, M. Yudasaka, S. Iijima, *Chem. Phys. Lett.* **2001**, *337*, 48.
- [257] R. R. Bacsa, C. Laurent, A. Peigney, W. S. Bacsa, T. Vaugien, A. Rousset, *Chem. Phys. Lett.* **2000**, *323*, 566.
- [258] Y. Zhao, Z. Xie, C. Qin, Y. Qu, Y. Geng, L. Wang, *Sol. Energy Mater. Sol. Cells* **2009**, *93*, 604.
- [259] W. Ren, F. Li, J. Chen, S. Bai, H.-M. Cheng, *Chem. Phys. Lett.* **2002**, *359*, 196.
- [260] S. C. Lyu, T. J. Lee, C. W. Yang, C. J. Lee, *Chem. Commun.* **2003**, *12*, 1404.
- [261] K. Mukhopadhyay, A. Koshio, N. Tanaka, H. Shinohara, *Jpn. J. Appl. Phys.* **1998**, *37*, L1257.
- [262] K. Mukhopadhyay, A. Koshio, T. Sugai, N. Tanaka, H. Shinohara, Z. Konya, J. B. Nagy, *Chem. Phys. Lett.* **1999**, *303*, 117.
- [263] A. Okamoto, T. Kawakubo, T. Hiraoka, T. Okazaki, T. Sugai, H. Shinohara, *Mol. Cryst. Liq. Cryst.* **2002**, *387*, 93.
- [264] T. Hiraoka, T. Kawakubo, J. Kimura, R. Taniguchi, A. Okamoto, T. Okazaki, T. Sugai, Y. Ozeki, M. Yoshikawa, H. Shinohara, *Chem. Phys. Lett.* **2003**, *382*, 679.
- [265] R. Saito, R. Matsuo, T. Kimura, G. Dresselhaus, M. S. Dresselhaus, *Chem. Phys. Lett.* **2001**, *348*, 187.
- [266] B. Shan, K. Cho, *Phys. Rev. B* **2006**, *73*, 081401.
- [267] D. W. Zhang, X. D. Li, S. Chen, F. Tao, Z. Sun, X. J. Yin, S. M. Huang, *J. Solid State Electrochem.* **2010**, *14*, 1541.
- [268] E. Flahaut, R. Bacsa, A. Peigney, C. Laurent, *Chem. Commun.* **2003**, 1442.
- [269] E. Kymakis, G. A. J. Amaratunga, *J. Appl. Phys.* **2006**, *99*, 084302.
- [270] E. Kymakis, E. Koudoumas, I. Franghiadakis, G. A. J. Amaratunga, *J. Phys. D: Appl. Phys.* **2006**, *39*, 1058.
- [271] M. Freitag, Y. Martin, J. A. Misewich, R. Martel, P. Avouris, *Nano Lett.* **2003**, *3*, 1067.
- [272] D. Stewart, F. Léonard, *Phys. Rev. Lett.* **2004**, *93*, 107401.
- [273] S. Lu, B. Panchapakesan, *Nanotechnology* **2006**, *17*, 1843.
- [274] A. Fujiwara, Y. Matsuoka, H. Suematsu, N. Ogawa, K. Miyano, H. Kataura, Y. Maniwa, S. Suzuki, Y. Achiba, *Jpn. J. Appl. Phys.* **2001**, *40*, L1229.
- [275] J. Wei, J.-L. Sun, J.-L. Zhu, K. Wang, Z. Wang, J. Luo, D. Wu, A. Cao, *Small* **2006**, *2*, 988.
- [276] J.-L. Sun, J. Wei, J.-L. Zhu, D. Xu, X. Liu, H. Sun, D.-H. Wu, N.-L. Wu, *Appl. Phys. Lett.* **2006**, *88*, 131107.
- [277] J. Wei, Y. Jia, Q. Shu, Z. Gu, K. Wang, D. Zhuang, G. Zhang, Z. Wang, J. Luo, A. Cao, D. Wu, *Nano Lett.* **2007**, *7*, 2317.
- [278] S. Iijima, C. Brabec, A. Maiti, J. Bernholc, *J. Chem. Phys.* **1996**, *104*, 2089.
- [279] D. J. Lipomi, B. C.-K. Tee, M. Vosgueritchian, Z. Bao, *Adv. Mater.* **2011**, *23*, 1771.
- [280] H. J. Park, T. Xu, J. Y. Lee, A. Ledbetter, L. J. Guo, *ACS Nano* **2011**, *5*, 7055.
- [281] A. Henemann, *Renew. Energy Focus* **2008**, *9*, 14.
- [282] R. Zhu, A. Kumar, Y. Yang, *Adv. Mater.* **2011**, *23*, 4193.
- [283] R. F. Bailey-Salzman, B. P. Rand, S. R. Forrest, *Appl. Phys. Lett.* **2006**, *88*, 3.
- [284] G.-M. Ng, E. L. Kietzke, T. Kietzke, L.-W. Tan, P.-K. Liew, F. Zhu, *Appl. Phys. Lett.* **2007**, *90*, 103505.
- [285] J. Huang, G. Li, Y. Yang, *Adv. Mater.* **2008**, *20*, 415.
- [286] Y.-Y. Lee, K.-H. Tu, C.-C. Yu, S.-S. Li, J.-Y. Hwang, C.-C. Lin, K.-H. Chen, L.-C. Chen, H.-L. Chen, C.-W. Chen, *ACS Nano* **2011**, *5*, 6564.
- [287] T. Ameri, G. Dennler, C. Waldauf, H. Azimi, A. Seemann, K. Forberich, J. Hauch, M. Scharber, K. Hingerl, C. J. Brabec, *Adv. Funct. Mater.* **2010**, *20*, 1592.
- [288] W. Gaynor, J.-Y. Lee, P. Peumans, *ACS Nano* **2010**, *4*, 30.
- [289] A. Colsmann, A. Puetz, A. Bauer, J. Hanisch, E. Ahlswede, U. Lemmer, *Adv. Energy Mater.* **2011**, *1*, 599.
- [290] R. R. Lunt, V. Bulovic, *Appl. Phys. Lett.* **2011**, *98*, 113305.
- [291] J. Meiss, F. Holzmueller, R. Gresser, K. Leo, M. Riede, *Appl. Phys. Lett.* **2011**, *99*, 193307.
- [292] A. Bauer, T. Wahl, J. Hanisch, E. Ahlswede, *Appl. Phys. Lett.* **2012**, *100*, 073307.

- [293] X. Xia, S. Wang, Y. Jia, Z. Bian, D. Wu, L. Zhang, A. Cao, C. Huang, *J. Mater. Chem.* **2010**, *20*, 8478.
- [294] J. Du, S. Pei, L. Ma, H. M. Cheng, *Adv. Mater.* **2014**, *26*, 1958.
- [295] L. J. A. Koster, V. D. Mihailetschi, R. Ramaker, P. W. M. Blom, *Appl. Phys. Lett.* **2005**, *86*, 123509.
- [296] M. A. Green, *Solid. State. Electron.* **1981**, *24*, 788.
- [297] G. Bunea, K. Wilson, Y. Meydbray, M. Campbell, D. De Ceuster, in *2006 IEEE 4th World Conf. Photovolt. Energy Conf.*, IEEE, **2006**, pp. 1312–1314.
- [298] A. Cravino, *Appl. Phys. Lett.* **2007**, *91*, 243502.
- [299] B. Qi, J. Wang, *J. Mater. Chem.* **2012**, *22*, 24315.
- [300] R. Steim, F. R. Kogler, C. J. Brabec, *J. Mater. Chem.* **2010**, *20*, 2499.
- [301] N. Yamada, T. Hitosugi, J. Kasai, N. L. H. Hoang, S. Nakao, Y. Hirose, T. Shimada, T. Hasegawa, *J. Appl. Phys.* **2009**, *105*, 123702.
- [302] Z. M. Jarzebski, *Phys. Status Solidi* **1982**, *13*, 13.
- [303] T. Hitosugi, N. Yamada, S. Nakao, Y. Hirose, T. Hasegawa, *Phys. status solidi* **2010**, *207*, 1529.
- [304] T. Koida, M. Kondo, *Appl. Phys. Lett.* **2006**, *89*, 3.
- [305] D. Morris, Y. Dou, J. Rebanc, C. E. J. Mitchell, R. G. Egdell, D. S. L. Law, A. Vittadini, M. Casarin, *Phys. Rev. B* **2000**, *61*, 13445.
- [306] S. Lee, J. H. Noh, H. S. Han, D. K. Yim, D. H. Kim, J.-K. Lee, J. Y. Kim, H. S. Jung, K. S. Hong, *J. Phys. Chem. C* **2009**, *113*, 6878.
- [307] Y.-H. Chen, L.-Y. Lin, C.-W. Lu, F. Lin, Z.-Y. Huang, H.-W. Lin, P.-H. Wang, Y.-H. Liu, K.-T. Wong, J. Wen, D. J. Miller, S. B. Darling, *J. Am. Chem. Soc.* **2012**, *134*, 13616.
- [308] G. Chen, H. Sasabe, Z. Wang, X.-F. Wang, Z. Hong, Y. Yang, J. Kido, *Adv. Mater.* **2012**, *24*, 2768.
- [309] J. Min, H. Zhang, T. Stubhan, Y. N. Luponosov, M. Kraft, S. A. Ponomarenko, T. Ameri, U. Scherf, C. J. Brabec, *J. Mater. Chem. A* **2013**, *1*, 11306.
- [310] W. L. Leong, S. R. Cowan, A. J. Heeger, *Adv. Energy Mater.* **2011**, *1*, 517.
- [311] C. M. Reich, A. Kaiser, J. T. S. Irvine, *Fuel Cells* **2001**, *1*, 249.
- [312] A. Folli, J. Z. Bloh, A. Lecaplain, R. Walker, D. E. Macphee, *Phys. Chem. Chem. Phys.* **2015**, *17*, 4849.
- [313] P. Hervé, L. K. J. Vandamme, *Infrared Phys. Technol.* **1994**, *35*, 609.
- [314] N. M. Ravindra, P. Ganapathy, J. Choi, *Infrared Phys. Technol.* **2007**, *50*, 21.
- [315] S. Mohri, Y. Hirose, S. Nakao, N. Yamada, T. Shimada, T. Hasegawa, *J. Appl. Phys.* **2012**, *111*, 093528.
- [316] H. Nogawa, T. Hitosugi, A. Chikamatsu, S. Nakao, Y. Hirose, T. Shimada, H. Kumigashira, M. Oshima, T. Hasegawa, *Jpn. J. Appl. Phys.* **2010**, *49*, 041102.
- [317] N. Beatham, P. A. Cox, R. G. Egdell, A. F. Orchard, *Chem. Phys. Lett.* **1980**, *69*, 479.
- [318] A. Kotani, Y. Toyozawa, *J. Phys. Soc. Japan* **1974**, *37*, 912.
- [319] G. K. Wertheim, *Chem. Phys. Lett.* **1979**, *65*, 377.
- [320] T. T. Nguyen, V. N. Tran, T. C. Bach, *Mater. Chem. Phys.* **2014**, *144*, 114.
- [321] K.-C. Ok, Y. Park, K.-B. Chung, J.-S. Park, *J. Phys. D. Appl. Phys.* **2013**, *46*, 295102.
- [322] T. Matsushima, Y. Kinoshita, H. Murata, *Appl. Phys. Lett.* **2007**, *91*, 253504.
- [323] Y. Matsuo, J. Hatano, T. Kuwabara, K. Takahashi, *Appl. Phys. Lett.* **2012**, *100*, 063303.
- [324] P. P. Boix, J. Ajuria, I. Etxebarria, R. Pacios, G. Garcia-Belmonte, J. Bisquert, *J. Phys. Chem. Lett.* **2011**, *2*, 407.
- [325] M. Bolognesi, A. Sánchez-Díaz, J. Ajuria, R. Pacios, E. Palomares, *Phys. Chem. Chem. Phys.* **2011**, *13*, 6105.
- [326] T. Kuwabara, T. Nakashima, T. Yamaguchi, K. Takahashi, *Org. Electron.* **2012**, *13*, 1136.
- [327] M. M. A. Ibrahim, H. H.-Y. Wei, M.-H. M. Tsai, K.-C. K. Ho, J.-J. Shyue, C. W. Chu, *Sol. Energy Mater. Sol. Cells* **2013**, *108*, 156.
- [328] S. Alem, J. Lu, R. Movileanu, T. Kololuoma, A. Dadvand, Y. Tao, *Org. Electron.* **2014**, *15*, 1035.
- [329] Y. Santo, I. Jeon, K. Sheng Yeo, T. Nakagawa, Y. Matsuo, *Appl. Phys. Lett.* **2013**, *103*, 73306.
- [330] K.-F. Lin, H.-M. Cheng, H.-C. Hsu, L.-J. Lin, W.-F. Hsieh, *Chem. Phys. Lett.* **2005**, *409*, 208.
- [331] M. Tian, M. Furuki, I. Iwasa, Y. Sato, L. S. Pu, S. Tatsuura, *J. Phys. Chem. B* **2002**, *106*, 4370.
- [332] W. Tress, K. Leo, M. Riede, *Adv. Funct. Mater.* **2011**, *21*, 2140.
- [333] Y. Ho Huh, B. Park, I. Hwang, *J. Appl. Phys.* **2014**, *115*, 124504.
- [334] A. Wagenpfahl, D. Rauh, M. Binder, C. Deibel, V. Dyakonov, *Phys. Rev. B* **2010**, *82*, 115306.
- [335] Y. Sun, J. J. H. Seo, C. J. C. Takacs, J. Seifert, A. J. Heeger, *Adv. Mater.* **2011**, *23*, 1679.
- [336] G. Wei, S. Wang, K. Renshaw, M. E. Thompson, S. R. Forrest, *ACS Nano* **2010**, *4*, 1927.
- [337] G. Chen, H. Sasabe, Z. Wang, X. Wang, Z. Hong, J. Kido, Y. Yang, *Phys. Chem. Chem. Phys.* **2012**, *14*, 14661.
- [338] J. You, C.-C. Chen, L. Dou, S. Murase, H.-S. Duan, S. A. Hawks, T. Xu, H. J. Son, L. Yu, G. Li, Y. Yang, *Adv. Mater.* **2012**, *24*, 5267.
- [339] C. E. Small, S. Chen, J. Subbiah, C. M. Amb, S.-W. Tsang, T.-H. Lai, J. R. Reynolds, F. So, *Nat. Photonics* **2011**, *6*, 115.
- [340] A. Roy, S. H. Park, S. Cowan, M. H. Tong, S. Cho, K. Lee, A. J. Heeger, *Appl. Phys. Lett.* **2009**, *95*, 013302.
- [341] A. Gadisa, Y. Liu, E. T. Samulski, R. Lopez, *ACS Appl. Mater. Interfaces* **2012**, *4*, 3846.
- [342] F. C. Krebs, *Sol. Energy Mater. Sol. Cells* **2009**, *93*, 394.
- [343] S. K. Hau, H.-L. Yip, N. S. Baek, J. Zou, K. O'Malley, A. K.-Y. Jen, *Appl. Phys. Lett.* **2008**, *92*, 253301.
- [344] S. K. Hau, H.-L. Yip, H. Ma, A. K.-Y. Jen, *Appl. Phys. Lett.* **2008**, *93*, 233304.
- [345] J. Hu, Z. Wu, H. Wei, T. Song, B. Sun, *Org. Electron.* **2012**, *13*, 1171.
- [346] C. Zhang, H. You, Z. Lin, Y. Hao, *Jpn. J. Appl. Phys.* **2011**, *50*, 082302.
- [347] M. D. Barankin, E. Gonzalez II, A. M. Ladwig, R. F. Hicks, *Sol. Energy Mater. Sol. Cells* **2007**, *91*, 924.
- [348] K.-S. Shin, H.-J. Park, B. Kumar, K.-K. Kim, S.-G. Ihn, S.-W. Kim, *J. Mater. Chem.* **2011**, *21*, 12274.
- [349] H. Cheun, C. Fuentes-Hernandez, Y. Zhou, W. J. Potscavage, S.-J. Kim, J. Shim, A. Dindar, B. Kippelen, *J. Phys. Chem. C* **2010**, *114*, 20713.
- [350] C. Klingshirn, *Phys. status solidi* **2007**, *244*, 3027.
- [351] Y. Jouane, S. Colis, G. Schmerber, P. Kern, A. Dinia, T. Heiser, Y.-A. Chapuis, *J. Mater. Chem.* **2011**, *21*, 1953.
- [352] Y.-S. Park, K.-H. Choi, H.-K. Kim, *J. Phys. D. Appl. Phys.* **2009**, *42*, 235109.
- [353] W. Shin, T. Yasuda, G. Watanabe, Y. S. Yang, C. Adachi, *Chem. Mater.* **2013**, *25*, 2549.
- [354] Y. Jouane, S. Colis, G. Schmerber, A. Dinia, P. Lévesque, T. Heiser, Y.-A. Chapuis, *Org. Electron.* **2013**, *14*, 1861.
- [355] J.-H. Lee, B. Hong, Y. S. Park, *Thin Solid Films* **2013**, *547*, 3.
- [356] Y. Jouane, S. Colis, G. Schmerber, A. Dinia, P. Bazylewski, G. S. Chang, Y.-A. Chapuis, *Thin Solid Films* **2015**, *576*,

- 23.
- [357] F. Zhu, X. Chen, J. Zhou, Z. Lu, Y. Chen, S. Huang, Z. Sun, *Mater. Res. Express* **2014**, *1*, 025020.
- [358] J.-C. Wang, W.-T. Weng, M.-Y. Tsai, M.-K. Lee, S.-F. Horng, T.-P. Perng, C.-C. Kei, C.-C. Yu, H.-F. Meng, *J. Mater. Chem.* **2010**, *20*, 862.
- [359] S. Chen, J. R. Manders, S.-W. Tsang, F. So, *J. Mater. Chem.* **2012**, *22*, 24202.
- [360] S. Flickyngerova, K. Shtereva, V. Stenova, D. Hasko, I. Novotny, V. Tvarozek, P. Sutta, E. Vavrinsky, *Appl. Surf. Sci.* **2008**, *254*, 3643.
- [361] G. Fang, D. Li, B.-L. Yao, *J. Cryst. Growth* **2003**, *247*, 393.
- [362] O. Game, U. Singh, A. A. Gupta, A. Suryawanshi, A. Banpurkar, S. Ogale, *J. Mater. Chem.* **2012**, *22*, 17302.
- [363] H. Park, Y. Shi, J. Kong, *Nanoscale* **2013**, *5*, 8934.
- [364] S.-H. Liao, H.-J. Jhuo, Y.-S. Cheng, S.-A. Chen, *Adv. Mater.* **2013**, *25*, 4766.
- [365] H. W. Kim, N. H. Kim, *Mater. Sci. Eng. B* **2003**, *103*, 297.
- [366] J. Lee, D. Lee, D. Lim, K. Yang, *Thin Solid Films* **2007**, *515*, 6094.
- [367] J. A. Thornton, *J. Vac. Sci. Technol.* **1974**, *11*, 666.
- [368] M. Yamagishi, S. Kuriki, P. K. Song, Y. Shigesato, *Thin Solid Films* **2003**, *442*, 227.
- [369] N. Sekine, C.-H. Chou, W. L. Kwan, Y. Yang, *Org. Electron.* **2009**, *10*, 1473.
- [370] M. Yuste, R. Escobar Galindo, I. Caretti, R. Torres, O. Sánchez, *J. Phys. D: Appl. Phys.* **2012**, *45*, 025303.
- [371] W. Ma, C. Yang, X. Gong, K. Lee, A. J. Heeger, *Adv. Funct. Mater.* **2005**, *15*, 1617.
- [372] N. Sekine, C.-H. Chou, W. L. Kwan, Y. Yang, *Org. Electron.* **2009**, *10*, 1473.
- [373] G. Li, C. Chu, V. Shrotriya, J. Huang, Y. Yang, *Appl. Phys. Lett.* **2006**, *88*, 253503.
- [374] L.-M. Chen, Z. Hong, G. Li, Y. Yang, *Adv. Mater.* **2009**, *21*, 1434.
- [375] W. J. E. Beek, M. M. Wienk, M. Kemerink, X. Yang, R. A. J. Janssen, *J. Phys. Chem. B* **2005**, *109*, 9505.
- [376] F. C. Krebs, T. Tromholt, M. Jørgensen, M. Jorgensen, *Nanoscale* **2010**, *2*, 873.
- [377] H. Oh, J. Krantz, I. Litsov, T. Stubhan, L. Pinna, C. J. Brabec, *Sol. Energy Mater. Sol. Cells* **2011**, *95*, 2194.
- [378] M. T. Lloyd, C. H. Peters, A. Garcia, I. V. Kauvar, J. J. Berry, M. O. Reese, M. D. McGehee, D. S. Ginley, D. C. Olson, *Sol. Energy Mater. Sol. Cells* **2011**, *95*, 1382.
- [379] O. Pachoumi, C. Li, Y. Vaynzof, K. K. Banger, H. Sirringhaus, *Adv. Energy Mater.* **2013**, *3*, 1428.
- [380] L. Guo, S. Yang, C. Yang, P. Yu, J. Wang, W. Ge, G. K. L. Wong, *Appl. Phys. Lett.* **2000**, *76*, 2901.
- [381] S. Mahamuni, B. Bendre, V. Leppert, C. A. Smith, D. Cooke, S. H. Risbud, H. W. H. Lee, *Nanostructured Mater.* **1996**, *7*, 659.
- [382] J. J. Cavaleri, D. E. Skinner, D. P. Colombo, R. M. Bowman, *J. Chem. Phys.* **1995**, *103*, 5378.
- [383] S. Sakohara, M. Ishida, M. A. Anderson, *J. Phys. Chem. B* **1998**, *102*, 10169.
- [384] R. Lindsay, E. Michelangeli, B. G. Daniels, T. V. Ashworth, A. J. Limb, G. Thornton, A. Gutiérrez-Sosa, A. Baraldi, R. Lariciprete, S. Lizzit, *J. Am. Chem. Soc.* **2002**, *124*, 7117.
- [385] H. Li, L. K. Schirra, J. Shim, H. Cheun, B. Kippelen, O. L. A. Monti, J.-L. Bredas, *Chem. Mater.* **2012**, *24*, 3044.
- [386] P. Winget, L. K. Schirra, D. Cornil, H. Li, V. Coropceanu, P. F. Ndione, A. K. Sigdel, D. S. Ginley, J. J. Berry, J. Shim, H. Kim, B. Kippelen, J.-L. Brédas, O. L. A. Monti, *Adv. Mater.* **2014**, *26*, 4711.
- [387] D. C. Look, G. C. Farlow, P. Reunchan, S. Limpijumnong, S. B. Zhang, K. Nordlund, *Phys. Rev. Lett.* **2005**, *95*, 225502.
- [388] C. E. Small, S. Chen, J. Subbiah, C. M. Amb, S.-W. Tsang, T.-H. Lai, J. R. Reynolds, F. So, *Nat. Photonics* **2011**, *6*, 115.
- [389] Y. Zhao, Z. Xie, C. Qin, Y. Qu, Y. Geng, L. Wang, *Sol. Energy Mater. Sol. Cells* **2009**, *93*, 604.
- [390] S. Na, S. Oh, S. Kim, D. Kim, *Org. Electron.* **2009**, *10*, 496.
- [391] Y.-J. Cheng, C.-H. Hsieh, Y. He, C.-S. Hsu, Y. Li, *J. Am. Chem. Soc.* **2010**, *132*, 17381.
- [392] C.-H. Hsieh, Y.-J. Cheng, P.-J. Li, C.-H. Chen, M. Dubosc, R.-M. Liang, C.-S. Hsu, *J. Am. Chem. Soc.* **2010**, *132*, 4887.
- [393] P. Schulz, L. L. Kelly, P. Winget, H. Li, H. Kim, P. F. Ndione, A. K. Sigdel, J. J. Berry, S. Graham, J.-L. Brédas, A. Kahn, O. L. A. Monti, *Adv. Funct. Mater.* **2014**, *24*, 7381.
- [394] F. Huang, H. Wu, D. Wang, W. Yang, Y. Cao, *Chem. Mater.* **2004**, *16*, 708.
- [395] H. Wu, F. Huang, J. Peng, Y. Cao, *Org. Electron.* **2005**, *6*, 118.
- [396] H. Wu, F. Huang, Y. Mo, W. Yang, D. Wang, J. Peng, Y. Cao, *Adv. Mater.* **2004**, *16*, 1826.
- [397] K. Kondo, A. Suzuki, M. Akita, M. Yoshizawa, *Angew. Chemie* **2013**, *52*, 2308.
- [398] K. Kondo, M. Akita, T. Nakagawa, Y. Matsuo, M. Yoshizawa, *Chem. - A Eur. J.* **2015**, *21*, 12741.
- [399] A. Suzuki, K. Kondo, M. Akita, M. Yoshizawa, *Angew. Chem. Int. Ed. Engl.* **2013**, *52*, 8120.
- [400] L. Chen, P. Degenaar, D. D. C. Bradley, *Adv. Mater.* **2008**, *20*, 1679.
- [401] I. Jeon, Y. Matsuo, Jeon II, Y. Matsuo, I. Jeon, Y. Matsuo, *Sol. Energy Mater. Sol. Cells* **2015**, *140*, 335.
- [402] V. I. Arkhipov, P. Heremans, E. V. Emelianova, G. J. Adriaenssens, H. Bäessler, *Appl. Phys. Lett.* **2003**, *82*, 3245.
- [403] R. H. Friend, R. W. Gymer, A. B. Holmes, J. H. Burroughes, R. N. Marks, C. Taliani, D. D. C. Bradley, D. A. Dos Santos, J. L. Brdas, M. Lgdlund, W. R. Salaneck, *Nature* **1999**, *397*, 121.
- [404] M. Scharber, D. Mühlbacher, M. Koppe, P. Denk, C. Waldauf, A. J. Heeger, C. J. Brabec, *Adv. Mater.* **2006**, *18*, 789.
- [405] H. Ishii, K. Sugiyama, E. Ito, K. Seki, *Adv. Mater.* **1999**, *11*, 605.
- [406] J. K. Lee, W. L. Ma, C. J. Brabec, J. Yuen, J. S. Moon, J. Y. Kim, K. Lee, G. C. Bazan, A. J. Heeger, *J. Am. Chem. Soc.* **2008**, *130*, 3619.
- [407] N. Koch, *ChemPhysChem* **2007**, *8*, 1438.
- [408] S. Lacher, Y. Matsuo, E. Nakamura, *J. Am. Chem. Soc.* **2011**, *133*, 16997.
- [409] Y.-Y. Lai, Y.-J. Cheng, C.-S. Hsu, *Energy Environ. Sci.* **2014**, *7*, 1866.
- [410] Y. Matsuo, K. Kanaizuka, K. Matsuo, Y.-W. Zhong, T. Nakae, E. Nakamura, *J. Am. Chem. Soc.* **2008**, *130*, 5016.
- [411] D. Hirayama, K. Takimiya, Y. Aso, T. Otsubo, T. Hasobe, H. Yamada, H. Imahori, S. Fukuzumi, Y. Sakata, *J. Am. Chem. Soc.* **2002**, *124*, 532.
- [412] A. Kira, T. Umeyama, Y. Matano, K. Yoshida, S. Isoda, J. K. Park, D. Kim, H. Imahori, *J. Am. Chem. Soc.* **2009**, *131*, 3198.
- [413] Y. Matsuo, M. Maruyama, *J. Nanosci. Nanotechnol.* **2012**, *12*, 6869.
- [414] T. P. Chou, Q. Zhang, G. Cao, *J. Phys. Chem. C* **2007**, *111*, 18804.
- [415] B. A. Borgias, S. R. Cooper, Y. B. Koh, K. N. Raymond, *Inorg. Chem.* **1984**, *23*, 1009.
- [416] J. Moser, S. PUNCHIHEWA, P. P. Infelta, M. Graetzel, *Langmuir* **1991**, *7*, 3012.

- [417] S. K. Hau, Y.-J. Cheng, H.-L. Yip, Y. Zhang, H. Ma, A. K.-Y. Jen, *ACS Appl. Mater. Interfaces* **2010**, *2*, 1892.
- [418] S. K. Hau, H.-L. Yip, O. Acton, N. S. Baek, H. Ma, A. K.-Y. Jen, *J. Mater. Chem.* **2008**, *18*, 5113.
- [419] Z. A. Page, Y. Liu, V. V. Duzhko, T. P. Russell, T. Emrick, *Science* **2014**, *346*, 441.
- [420] M. K. Nazeeruddin, S. M. Zakeeruddin, R. Humphry-Baker, M. Jirousek, P. Liska, N. Vlachopoulos, V. Shklover, C.-H. Fischer, M. Grätzel, *Inorg. Chem.* **1999**, *38*, 6298.
- [421] M. Montalti, S. Wadhwa, W. Y. Kim, R. A. Kipp, R. H. Schmehl, *Inorg. Chem.* **2000**, *39*, 76.
- [422] Y. Liu, J. I. Dadap, D. Zimdars, K. B. Eisenthal, *J. Phys. Chem. B* **1999**, *103*, 2480.
- [423] C. R. Rice, M. D. Ward, M. K. Nazeeruddin, M. Grätzel, *New J. Chem.* **2000**, *24*, 651.
- [424] K. L. Purvis, G. Lu, J. Schwartz, S. L. Bernasek, *J. Am. Chem. Soc.* **2000**, *122*, 1808.
- [425] T. Ichiki, Y. Matsuo, E. Nakamura, *Chem. Commun.* **2013**, *49*, 279.
- [426] W. U. Huynh, J. J. Dittmer, A. P. Alivisatos, *Science* **2002**, *295*, 2425.
- [427] A. Splendiani, L. Sun, Y. Zhang, T. Li, J. Kim, C.-Y. Chim, G. Galli, F. Wang, *Nano Lett.* **2010**, *10*, 1271.
- [428] K.-K. Liu, W. Zhang, Y.-H. Lee, Y.-C. Lin, M.-T. Chang, C.-Y. Su, C.-S. Chang, H. Li, Y. Shi, H. Zhang, C.-S. Lai, L.-J. Li, *Nano Lett.* **2012**, *12*, 1538.
- [429] K. F. Mak, C. Lee, J. Hone, J. Shan, T. F. Heinz, *Phys. Rev. Lett.* **2010**, *105*, 136805.
- [430] D. J. Li, U. N. Maiti, J. Lim, D. S. Choi, W. J. Lee, Y. Oh, G. Y. Lee, S. O. Kim, *Nano Lett.* **2014**, *14*, 1228.
- [431] S. Najmaei, Z. Liu, P. M. Ajayan, J. Lou, *Appl. Phys. Lett.* **2012**, *100*, 013106.
- [432] B. Streetman, S. Banerjee, *Solid State Electronic Devices*, Prentice Hall, **2000**.
- [433] R. H. Friend, R. W. Gymer, A. B. Holmes, J. H. Burroughes, R. N. Marks, C. Taliani, D. D. C. Bradley, D. A. Dos Santos, J. L. Brdas, M. Lgdlund, W. R. Salaneck, *Nature* **1999**, *397*, 121.
- [434] Q. H. Wang, K. Kalantar-Zadeh, A. Kis, J. N. Coleman, M. S. Strano, *Nat. Nanotechnol.* **2012**, *7*, 699.
- [435] T. Shimada, F. S. Ohuchi, B. A. Parkinson, *Jpn. J. Appl. Phys.* **1994**, *33*, 2696.
- [436] T. Fujimori, A. Morelos-Gómez, Z. Zhu, H. Muramatsu, R. Futamura, K. Urita, M. Terrones, T. Hayashi, M. Endo, S. Young Hong, Y. Chul Choi, D. Tománek, K. Kaneko, *Nat. Commun.* **2013**, *4*, 2162.
- [437] Y. H. Lee, X. Q. Zhang, W. Zhang, M. T. Chang, C. T. Lin, K. D. Chang, Y. C. Yu, J. T. Wang, C. S. Chang, L. J. Li, T. W. Lin, *Adv. Mater.* **2012**, *24*, 2320.
- [438] A. M. van der Zande, P. Y. Huang, D. A. Chenet, T. C. Berkelbach, Y. You, G.-H. Lee, T. F. Heinz, D. R. Reichman, D. A. Muller, J. C. Hone, *Nat. Mater.* **2013**, *12*, 554.
- [439] F. K. Perkins, A. L. Friedman, E. Cobas, P. M. Campbell, G. G. Jernigan, B. T. Jonker, *Nano Lett.* **2013**, *13*, 668.
- [440] Y. Li, H. Wang, L. Xie, Y. Liang, G. Hong, H. Dai, *J. Am. Chem. Soc.* **2011**, *133*, 7296.
- [441] R. Fivaz, E. Mooser, *Phys. Rev.* **1967**, *163*, 743.
- [442] D. C. Olson, S. E. Shaheen, R. T. Collins, D. S. Ginley, *J. Phys. Chem. C* **2007**, *111*, 16670.
- [443] K. M. Coakley, M. D. McGehee, *Appl. Phys. Lett.* **2003**, *83*, 3380.
- [444] Y. Yoon, K. Ganapathi, S. Salahuddin, *Nano Lett.* **2011**, *11*, 3768.
- [445] B. Radisavljevic, A. Radenovic, J. Brivio, V. Giacometti, A. Kis, *Nat. Nanotechnol.* **2011**, *6*, 147.
- [446] Y. Zhang, J. Ye, Y. Matsushashi, Y. Iwasa, *Nano Lett.* **2012**, *12*, 1136.
- [447] H. Qiu, L. Pan, Z. Yao, J. Li, Y. Shi, X. Wang, *Appl. Phys. Lett.* **2012**, *100*, 123104.
- [448] H. Hwang, H. Kim, J. Cho, *Nano Lett.* **2011**, *11*, 4826.
- [449] M. Shanmugam, T. Bansal, C. A. Durcan, B. Yu, *Appl. Phys. Lett.* **2012**, *100*, 153901.
- [450] M. S. Arnold, J. D. Zimmerman, C. K. Renshaw, X. Xu, R. R. Lunt, C. M. Austin, S. R. Forrest, *Nano Lett.* **2009**, *9*, 3354.
- [451] S. Ren, M. Bernardi, R. R. Lunt, V. Bulovic, J. C. Grossman, S. Gradečak, *Nano Lett.* **2011**, *11*, 5316.
- [452] C. B. Roxlo, *J. Vac. Sci. Technol. A Vacuum, Surfaces, Film.* **1987**, *5*, 555.
- [453] T. Li, G. Galli, *J. Phys. Chem. C* **2007**, *111*, 16192.
- [454] F.-C. Li, B. Yu, J.-J. Wei, Y. Kawaguchi, *Turbulent Drag Reduction by Surfactant Additives*, John Wiley & Sons Singapore Pte. Ltd., Singapore, **2011**.
- [455] X. Gu, W. Cui, H. Li, Z. Wu, Z. Zeng, S.-T. Lee, H. Zhang, B. Sun, *Adv. Energy Mater.* **2013**, *3*, 1262.
- [456] P. J. Brown, D. S. Thomas, A. Köhler, J. S. Wilson, J.-S. Kim, C. M. Ramsdale, H. Sirringhaus, R. H. Friend, *Phys. Rev. B* **2003**, *67*, 064203.
- [457] X. Zhang, Z. Yu, C. Wang, D. Zarrouk, J.-W. T. Seo, J. C. Cheng, A. D. Buchan, K. Takei, Y. Zhao, J. W. Ager, J. Zhang, M. Hettick, M. C. Hersam, A. P. Pisano, R. S. Fearing, A. Javey, *Nat. Commun.* **2014**, *5*, 2983.
- [458] J. L. Bahr, J. M. Tour, *J. Mater. Chem.* **2002**, *12*, 1952.
- [459] Y. Matsuo, J. Kawai, H. Inada, T. Nakagawa, H. Ota, S. Otsubo, E. Nakamura, *Adv. Mater.* **2013**, *25*, 6266.
- [460] V. D. Mihailetchi, H. Xie, B. de Boer, L. M. Popescu, J. C. Hummelen, P. W. M. Blom, L. J. A. Koster, *Appl. Phys. Lett.* **2006**, *89*, 012107.
- [461] T. Wu, T. Lin, J. Zhao, H. Hidaka, N. Serpone, *Environ. Sci. Technol.* **1999**, *33*, 1379.
- [462] J. Yang, C. Chen, H. Ji, W. Ma, J. Zhao, *J. Phys. Chem. B* **2005**, *109*, 21900.
- [463] S. Y. Heriot, R. A. L. Jones, *Nat. Mater.* **2005**, *4*, 782.
- [464] M. D. Clark, M. L. Jespersen, R. J. Patel, B. J. Leever, *ACS Appl. Mater. Interfaces* **2013**, *5*, 4799.
- [465] D. B. Mahadik, A. Venkateswara Rao, V. G. Parale, M. S. Kavale, P. B. Wagh, S. V. Ingale, S. C. Gupta, *Appl. Phys. Lett.* **2011**, *99*, 104104.
- [466] H. Kobayashi, M. J. Owen, *Die Makromol. Chemie* **1993**, *194*, 1785.
- [467] X. Yang, J. Loos, S. C. Veenstra, W. J. H. Verhees, M. M. Wienk, J. M. Kroon, M. A. J. Michels, R. A. J. Janssen, *Nano Lett.* **2005**, *5*, 579.
- [468] L. Zhang, X. Xing, L. Zheng, Z. Chen, L. Xiao, B. Qu, Q. Gong, *Sci. Rep.* **2014**, *4*, 5071.
- [469] M. Kwoka, L. Ottaviano, M. Passacantando, S. Santucci, J. Szuber, *Appl. Surf. Sci.* **2006**, *252*, 7730.
- [470] W. Song, S. K. So, J. Moulder, Y. Qiu, Y. Zhu, L. Cao, *Surf. Interface Anal.* **2001**, *32*, 70.
- [471] D. Chi, S. Qu, Z. Wang, J. Wang, *J. Mater. Chem. C* **2014**, *2*, 4383.
- [472] V. D. Mihailetchi, L. J. A. Koster, J. C. Hummelen, P. W. M. Blom, *Phys. Rev. Lett.* **2004**, *93*, 216601.
- [473] V. D. Mihailetchi, J. Wildeman, P. W. M. Blom, *Phys. Rev. Lett.* **2005**, *94*, 126602.